The German Section of the Combustion Institute (CI)

Deutsche Vereinigung für Verbrennungsforschung (DVV)

32.
Deutscher Flammentag
2025

15. - 17.09.2025

Paderborn

Inhaltsverzeichnis:

Titel *Seite*

Stickoxidemissionen bei der Wasserstoffverbrennung: physikalische und messtechnische Aspekte

J. Leicher*, A. Giese

*joerg.leicher@gwi-essen.de

Gas- und Wärme-Institutt Essen e.V., Hafenstrasse 101, 45356 Essen, Deutschland

Abstract

Wasserstoff (aus nachhaltigen Quellen) wird in einem dekarbonisierten Energiesystem der Zukunft eine wesentliche Rolle spielen. Die Verbrennung von Wasserstoff ist eine wichtige Dekarbonisierungsoption, etwa für die Bereitstellung von Hochtemperatur-Prozesswärme, wird aber auch im Kraftwerkssektor relevant sein, um Regelleistung bereitzustellen und die Versorgungssicherheit zu gewährleisten.

Wasserstoff unterscheidet sich in seinen verbrennungstechnischen Eigenschaften deutlich von Erdgas oder anderen konventionellen Brennstoffen. Ein wesentlicher Unterschied ist die adiabate Verbrennungstemperatur, und damit verbunden das Potential zur stärkeren Bildung von Stickoxiden (NO_X) bei der Verbrennung, verglichen mit der Erdgasverbrennung. Der dominante Bildungsmechanismus für die NO_X-Emissionen ist jedoch nach wie vor die thermische NO_X-Bildung, weswegen viele etablierte Primärmaßnahmen zur NO_X-Minderung mit Wasserstoff prinzipiell ähnlich effektiv funktionieren wie mit Erdgas.

Neben diesen physikalischen Aspekten hat der Brennstoffwechsel jedoch auch Auswirkungen darauf, wie NO_X-Emissionen heute quantifiziert und Grenzwerte festgelegt werden. In Europa ist es üblich, Schadstoffemissionen anhand der Konzentrationen im trockenen Abgas bei einem definierten Rest-Sauerstoffgehalt zu bewerten. Beim Vergleich des Emissionsverhaltens von Wasserstoff z. B. mit Erdgas führt dies zu erheblichen Verzerrungen, da die Verbrennung von Wasserstoff zu höheren Wasserdampfkonzentrationen im Abgas führt und gleichzeitig weniger Abgas (bei gleicher Feuerungsleistung und Luftzahl) gebildet wird.

Der Beitrag betrachtet die Auswirkungen eines Brennstoffwechsels von Erdgas zu Wasserstoff im Hinblick auf die NO_X-Emissionen in technischen Verbrennungsprozessen und ihre Bewertung. Die Auswirkungen verschiedener Bewertungsmetriken werden anhand von Beispielen diskutiert.

Einleitung

In den letzten Jahren ist Wasserstoff neben „grünem“ Strom immer mehr als zweiter zentraler Energieträger eines klimaneutralen Energiesystems der Zukunft in den Fokus gerückt. Wasserstoff und seine Derivate, etwa Ammoniak, erlauben den globalen Transport und die langfristige Speicherung großer Energiemengen, gleichzeitig ist die Verbrennung von Wasserstoff und seinen Derivaten eine vielversprechende Dekarbonisierungsoption, vor allem für Prozesse und Anwendungen in der Thermoprozesstechnik aber z. B. auch im Flug- oder Schiffsverkehr.

Aus Sicht der Verbrennung ist Wasserstoff, verglichen etwa mit Erdgas, ein sehr andersgearteter Brennstoff. Diese Eigenheiten müssen beim Einsatz von Wasserstoff (oder, in einem Zwischenschritt, auch Erdgas-Wasserstoff-Gemischen) berücksichtigt werden, da bei technischen Verbrennungsprozessen neben den Treibhausgasemissionen nach wie vor auch Anforderungen wie etwa Effizienz, Flexibilität und Dynamik oder auch Schadstoffemissionen eine große Rolle spielen. Für Verbrennungsprozesse in der Thermoprozesstechnik kommen Aspekte der Produktqualität hinzu.

Für großtechnische gasbefeuerte Verbrennungsanwendungen stehen im Hinblick auf die Schadstoffemissionen oft die Stickoxide (NO_X) oft im Vordergrund, während bei der häuslichen Verwendung der Fokus meist eher auf Kohlenmonoxid (CO) liegt. Gerade im Hinblick auf die NO_X-Bildung kann die Verbrennung von Wasserstoff aufgrund der höheren lokalen Verbrennungstemperaturen eine Herausforderung sein.

Grundsätzlich können Stickoxide durch verschiedene Mechanismen bei einem Verbrennungsprozess gebildet werden, etwa durch die Umsetzung von im Brennstoff gebundenem Stickstoff (Brennstoff-NO_X), die thermische NO_X-Bildung, den Lachgas-Mechanismus (N_2O-Mechanismus) oder durch den Prompt-NO-Mechanismus [1]. Bei den meisten technischen Verbrennungsprozessen liegt der Großteil der NO_X-Emissionen in der Form von NO vor, welches dann in der Atmosphäre zu NO_2 weiter oxidiert. Für gasförmiger Brennstoffe ist in der Regel die thermische NO_X-Bildung der dominante Bildungspfad, sofern im Brenngas keine stickstoffhaltigen Verbindungen wie NH_3 oder HCN enthalten sind, während gerade bei festen Brennstoffen wie Kohle oder Biomasse meist die NO-Bildung durch im Brennstoff gebundenen Stickstoff der maßgebliche Mechanismus ist. Auch bei der NH_3-Verbrennung spielt dieser Brennstoff-Stickstoff-eine zentrale Rolle**.**
Der Mechanismus der thermischen NO_X-Bildung ist gut verstanden und lässt sich durch die folgenden Reaktionsgleichungen beschreiben, wobei die erste Gleichung aufgrund der hohen notwendigen Aktivierungsenergie geschwindigkeitsbestimmend ist:

$$\begin{aligned} N_2 + O &\leftrightarrow NO + N \\ N + O_2 &\leftrightarrow NO + O \\ N + OH &\leftrightarrow NO + H \end{aligned} \qquad (1)$$

Die hohe benötigte Aktivierungsenergie erklärt sich dadurch, dass bei der thermischen NO_X-Bildung zuerst die Dreifach-Bindung des sehr stabilen Stickstoff-Moleküls (N_2) aufgebrochen werden muss, um die NO-Bildung einzuleiten. Daher ist die thermische NO_X-Bildung exponentiell temperaturabhängig (vgl. **Abbildung 1, links** für eine prinzipielle Darstellung) und führt erst bei hohen Temperaturen zu signifikanten NO-Konzentrationen. Weitere Einflussgrößen sind das Sauerstoff-Angebot im System (**Abbildung 1, rechts**), die Aufenthaltszeit im heißen Bereich und der anliegende Druck. Daher treten die maximalen NO-Konzentrationen auch nicht bei der maximalen Verbrennungstemperatur auf, sondern dort, wo sowohl hohe Temperaturen als auch ausreichend Sauerstoff zur Verfügung stehen. Die adiabate Verbrennungstemperatur von Wasserstoff unter stöchiometrischen Bedingungen ist bei der Verbrennung mit Luft etwa 150 °C höher als die von Erdgas, wodurch bei der H_2-Verbrennung mit Luft potentiell höhere NO_X-Emissionen auftreten können als bei einer vergleichbaren Erdgasverbrennung. Da aber nach wie vor die thermische Stickoxidbildung der dominante Bildungspfad ist, sind typische Primärmaßnahmen zur NO_X-Minderung bei der Verbrennung von Gasen, beispielsweise Brennstoff- und/oder Luftstufung, Abgasrezirkulation oder auch die flammenlose Oxidation, immer noch effektiv [2], [3], [4], [5]. Die Reaktionsgleichungen (1) zeigen auch, dass die eigentliche Verbrennung lediglich die Temperaturen bereitstellt, die zum Aufbrechen des N_2-Moleküls notwendig sind, aber chemisch nicht in die NO_X-Bildung eingreift.

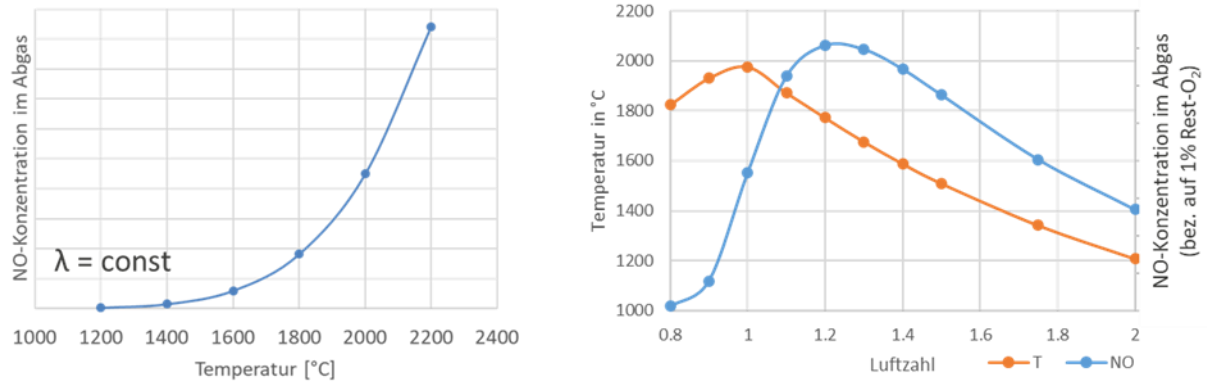

Abbildung 1: Links: prinzipieller Zusammenhang zwischen thermischer NO-Bildung und Temperatur (λ = konst.); rechts: (adiabate) Verbrennungstemperatur und NO-Konzentration als Funktion der Luftzahl. (Quelle: GWI)

NO_X-Emissionen bei der Verbrennung von H_2-reichen Brenngasen

Die zu erwartenden NO_X-Emissionen sind bei einem Brennstoffwechsel jedoch nicht allein von den Brennstoffen selbst abhängig. Mindestens genauso wichtig sind die eingesetzten Verbrennungstechnologien, wobei der Unterschied zwischen vorgemischter und nicht-vorgemischter Verbrennung in diesem Kontext besonders relevant ist.

Nicht-vorgemischte Verbrennungsprozesse sind in vielen großtechnischen Anwendungen, von Dampferzeugern bis hin zu Industrieöfen in der Metall- oder Glasindustrie, Stand der Technik. Diese Form der Verbrennung zeichnet sich dadurch aus, dass der Großteil der Wärmefreisetzung (und somit auch die maximalen Verbrennungstemperaturen) bei lokal ungefähr stöchiometrischen Bedingungen in der Flammenfront erfolgt, und somit weitaus unabhängiger von der global anliegenden Luftzahl λ_{global} ist. Dies ist ein zentraler Unterschied zur vorgemischten Verbrennung, wie man sie etwa in vielen Heizungssystemen im Haushalt, aber auch in modernen Gasturbinen im Kraftwerkssektor findet: da hier Brennstoff und Luft gemischt werden, bevor sie in den eigentlichen Brennraum eintreten, entspricht in diesem Fall die lokale Luftzahl λ_{lokal} in der Flammenfront der globalen Luftzahl (**Abbildung 2**).

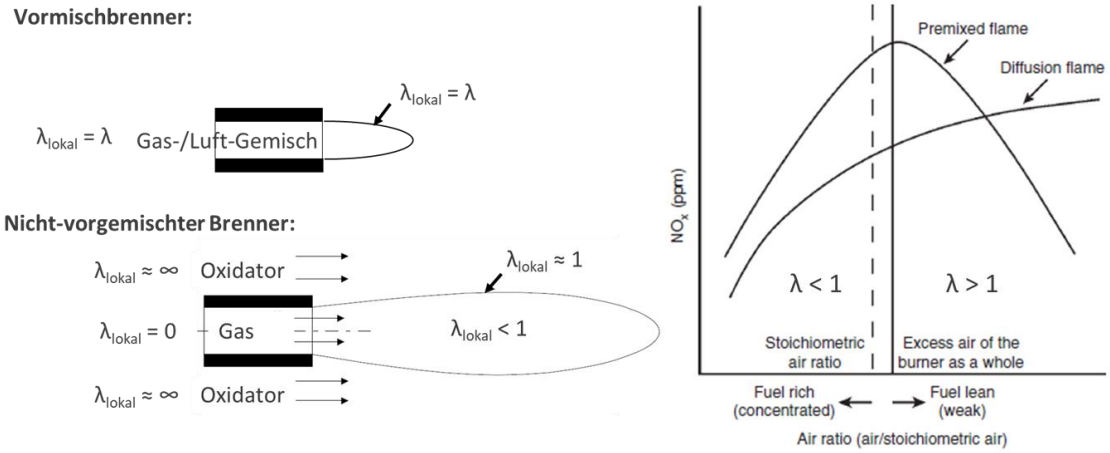

Abbildung 2: Prinzipdarstellung von vorgemischten und nicht-vorgemischten Verbrennungsprozessen (links, Quelle: GWI) und Auswirkungen der Verbrennungsform auf die NO_X-Bildung [6]

Die Auswirkungen dieser verschiedenen Brennertechnologien auf die thermische Stickoxid-Bildung beim Wechsel von Erdgas zu Erdgas-Wasserstoff-Gemischen bzw. reinem Wasserstoff sind erheblich. Da bei der nicht-vorgemischten Verbrennung die Hauptreaktionen im Wesentlichen bei Stöchiometrie stattfinden, führt der Brennstoffwechsel zu höheren lokalen Temperaturen in der Reaktionsfront, und somit zu verstärkter NO_X-Bildung, unabhängig von der globalen Luftzahl des Verbrennungsprozesses. **Abbildung 3** zeigt die Auswirkungen einer Wasserstoffbeimischung anhand von Prüfstandsmessungen des „HyGlass"-Projekts [7], in dem u. a. die Auswirkungen einer Wasserstoff-Beimischung bzw. des Wechsels zu reinem Wasserstoff auf die nicht-vorgemischten Verbrennungsprozesse in der Glasindustrie untersucht wurden. Die Messungen wurden an einem Hochtemperatur-Prüfstand des GWI für eine in der Glasindustrie typische Underport-Konfiguration bei konstanten Betriebsbedingungen ($P = 500$ kW; $\lambda = 1{,}1$; $T_{Luft} = 1.250$ °C) durchgeführt. Mit höheren H_2-Gehalten im Brenngas ergeben sich unter diesen Bedingungen deutlich höhere NO_X-Konzentrationen im Abgas. Für Gasgebläsebrenner

in Industriekesseln oder andere typische Industriebrenner zeigen sich ähnliche Effekte [2], [8].

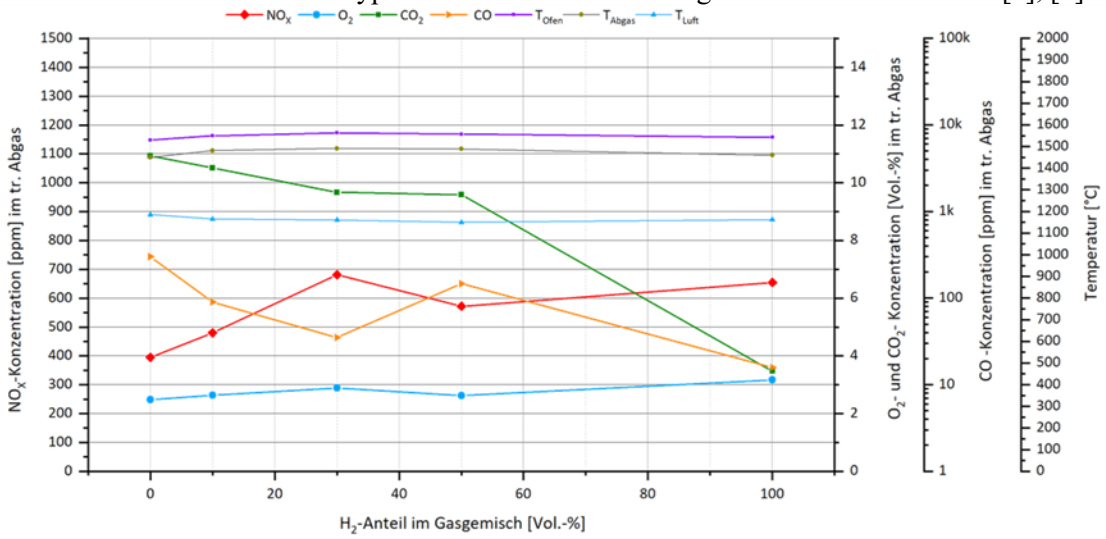

Abbildung 3: Auswirkungen der H_2-Beimischung in Erdgas auf einen Brenner aus der Glasindustrie [7].

Die Wasserstoff-Beimischung oder auch der Wechsel zu reinem Wasserstoff sind jedoch nicht zwangsweise mit höheren NO_X-Emissionen bei einer nicht-vorgemischten Verbrennung verbunden, wie etwa CFD-Studien eines oxy-fuel-befeuerten Aluminiumschmelzofens zeigen [5]. Im Rahmen der Simulationen wurde der Betrieb des 3,5 MW-Ofens sowohl mit Erdgas als auch mit Wasserstoff bei ansonsten gleichen Randbedingungen untersucht. Das in diesen Simulationen verwendete Erdgas enthielt etwa 0.8 Vol.-% N_2, zudem wurde dem Sauerstoff in beiden Fällen 1 Vol.-% N_2 beigemischt, um Unreinheiten im Sauerstoff und den Effekt von Falschluft abzubilden. Beim Vergleich ergaben etwa 40 % niedrigere NO_X-Emissionen beim Wasserstoffbetrieb, verglichen mit der Erdgasverbrennung. Im Kontext der Oxy-Fuel-Verbrennung ist das Angebot an Stickstoff im System der begrenzende Faktor der NO_X-Bildung. Da bei der Wasserstoffverbrennung in Summe weniger N_2 in den Ofen eingebracht wurde, lassen sich die niedrigeren NO_X-Emissionen hiermit physikalisch plausibel erklären.
Beim Brennstoffwechsel in einer Vormischverbrennung ist hingegen maßgeblich für die NO_X-Bildung, ob die globale Luftzahl konstant bleibt oder nicht. Da Wasserstoff bzw. Erdgas-Wasserstoff-Gemische einen geringeren minimalen Luftbedarf für die vollständige Verbrennung aufweisen als Erdgas, wird sich die Luftzahl beim Brennstoffwechsel hin zu magereren Gemischen verschieben, wenn dieser Effekt nicht bewusst ausgeregelt wird. Dies ist die Ursache, warum bei Untersuchungen zum Einfluss der Wasserstoff-Beimischung in Erdgas auf häusliche Gasgeräte die gemessenen NO_X-Konzentrationen in der Regel sinken. Durch die Verschiebung hin zu höheren Luftzahlen nehmen die lokalen Temperaturen in der Flamme ab, wodurch die Stickoxid-Bildung reduziert wird. Dieser Effekt zeigt sich selbst bei Gasgeräten, die mit einer Verbrennungsregelung ausgerüstet sind. Die Regelung dieser Geräte basiert meist auf einer Ionisationsstrommessung, die für schwankende Erdgasbeschaffenheiten hervorragend funktioniert, aber bei der Beimischung von Wasserstoff an ihre Grenzen stößt [9], [10], [11]. Dies gilt vor allem im Volllastbetrieb.

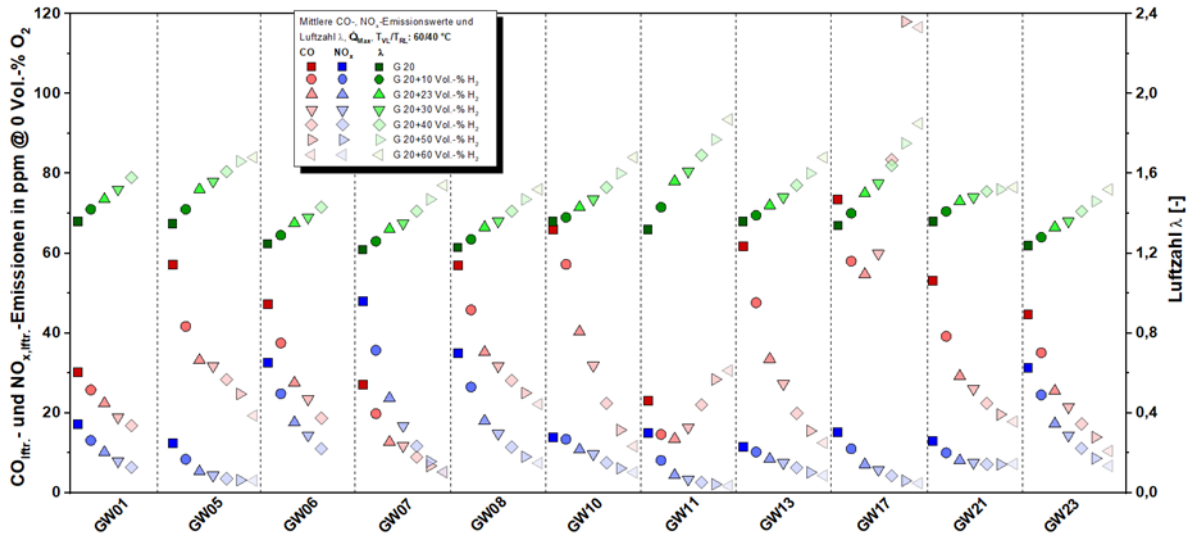

Abbildung 4: Luftzahl, CO- und NO_X-Konzentrationen bei verschiedenen Brennwertgeräten bei H_2-Beimischung [11]

Diese Situation für Verbrennungsprozesse bei Gasheizungen lässt sich jedoch nicht auf Gasturbinen übertragen, obwohl es sich in beiden Fällen meist um vollvorgemischte Verbrennungsprozesse handelt. Bei Gasturbinen werden in der Regel sowohl die Leistung als auch die Luftzahl des Verbrennungsprozesses brennstoffabhängig ausgeregelt, so dass höhere Wasserstoffgehalte höhere lokale Temperaturen und somit auch eine verstärkte NO_X-Bildung zur Folge haben. Dieser Effekt, vor allem in Verbindung mit den deutlich höheren Verbrennungsgeschwindigkeiten von Wasserstoff im Vergleich zu Erdgas, stellt eine erhebliche Herausforderung für moderne Gasturbinen dar, die meist ihre niedrigen Emissionen meist durch den Einsatz einer mageren vorgemischten Verbrennung erreichen. Dieser Ansatz dürfte für Brennstoffe mit hohen H_2-Gehalten nur schwer realisierbar sein, so dass hier andere Verbrennungskonzepte untersucht werden [12].
Die dargestellten Beispiele zeigen, wie unterschiedlich sich der Einsatz von Erdgas-Wasserstoff-Gemischen oder auch der Wechsel zu reinem Wasserstoff als Brennstoff auch auf die Stickoxid-Emissionen auswirken können.

Bewertung von Schadstoff-Emissionen bei wasserstoffreichen Brennstoffen
Neben den physikalischen Auswirkungen, die höhere Wasserstoffanteile auf die NO_X-Bildung in Verbrennungsprozessen haben können, ergeben sich zusätzlich Fragen, wie Emissionswerte bei sehr unterschiedlichen Brennstoffen wie etwa Erdgas und Wasserstoff überhaupt sinnvoll verglichen und bewertet werden können. Grundsätzlich ist es das Ziel von Grenzwerten für Emissionen, die emittierten Massenströme, etwa von Stickoxiden, zu begrenzen. Aus Gründen der Handhabung werden Grenzwerte in Deutschland und Europa jedoch üblicherweise in Form von Schadstoffkonzentrationen, bezogen auf das trockene Abgasvolumen und normiert auf einen Referenz-Sauerstoffgehalt, angegeben, üblicherweise in Einheiten wie [ppm] oder [mg/m^3]. Dies hat vor allem praktische Gründe: Konzentrationen sind erheblich einfacher im Abgas eines großtechnischen Verbrennungsprozess zu erfassen als die emittierten Speziesmassenströme. Die Nutzung trockener Abgaskonzentrationen ist auf Beschränkungen der Messtechnik zurückzuführen. Viele Messzellen können durch den Kontakt mit Wasser Schaden nehmen, zudem kann es Querempfindlichkeiten geben. Daher werden Gasproben üblicherweise getrocknet, d. h., das im Abgas enthaltene Wasser wird auskondensiert, bevor die Probe dem Analysator zugeführt wird.
Solange die eingesetzten Brennstoffe sich in ihrer Zusammensetzung nicht deutlich unterscheiden, ist eine solche Begrenzung der Emissionen durch geeignete Grenzwerte für trockene Konzentrationen im Abgas sinnvoll. Sie stößt jedoch an ihre Grenzen, wenn die Brennstoffe (oder die Oxidatoren, etwa im Kontext der Oxy-Fuel-Verbrennung [13], [14]) sich in ihren Zusammensetzungen deutlich unterscheiden.
Der Wasserdampfanteil im Abgas ist sowohl von den Zusammensetzungen von Brennstoff und Oxidator als auch von der Luftzahl abhängig. So besteht das Abgas einer stöchiometrischen CH_4-Luft-

Verbrennung (λ = 1) rechnerisch zu etwa 17,4 Vol.-% aus H_2O, bei einer Oxy-Fuel-Verbrennung jedoch zu knapp 67 Vol.-%. Bei der stöchiometrischen H_2-Luft-Verbrennung hingegen liegt die Wasserdampfkonzentration bei 34 Vol.-%, bei der Oxy-Fuel-Verbrennung sogar quasi bei 100 Vol.-%. Hinzu kommt, dass sich die produzierten Abgasmengen bei Erdgas und Wasserstoff ebenfalls unterscheiden. Bei einer stöchiometrischen Verbrennung von Methan mit Luft wird eine Abgasmenge von 1.054 m^3/MWh freigesetzt, bei der Verbrennung von Wasserstoff lediglich 961 m^3/MWh. Das bedeutet, dass selbst wenn die emittierten Massenströme einer Schadstoffspezies (in [mg/s]) völlig identisch wären, sich allein aufgrund der veränderten Abgasmengen und Wassserdampfanteile eine Veränderung in den trockenen Spezieskonzentrationen ergeben würde.
Für die Bewertung von Schadstoffemissionen wie etwa NO_X hat dies erhebliche Folgen in Bezug auf die Vergleichbarkeit von Emissionen und damit verbunden die Einhaltung von Grenzwerten, gerade bei Gasen mit hohen H_2-Anteilen. Dies wird in den **Abbildungen 5** und **6** veranschaulicht. **Abbildung 4** zeigt dabei Ergebnisse einer Reihe von CFD-Simulationen, die im Rahmen des COSIMa-Projekts [15] entstanden sind und die Oxy-Fuel Verbrennung von Erdgas H und Wasserstoff vergleichen. Dem Sauerstoff wurde bei den Simulationen 1 Vol.-% N_2 beigemischt, um immer eine Stickstoffquelle im System zu haben, das Erdgas enthielt ebenfalls etwa 1 Vol.-% N_2. Betrachtet man die (trockenen) NO-Konzentrationen in beiden Fällen, scheint es, als ob bei der H_2-Verbrennung deutlich mehr NO gebildet wird. Allerdings zeigen die Massenströme und auch die feuchten NO-Konzentrationen, dass bei der H_2-Verbrennung tatsächlich deutlich geringere NO-Emissionen anfallen. Dies wurde auch durch Messungen im semi-industriellen Maßstab, die im Rahmen des Projekts durchgeführt wurden, bestätigt (Abbildung 6, rechts).

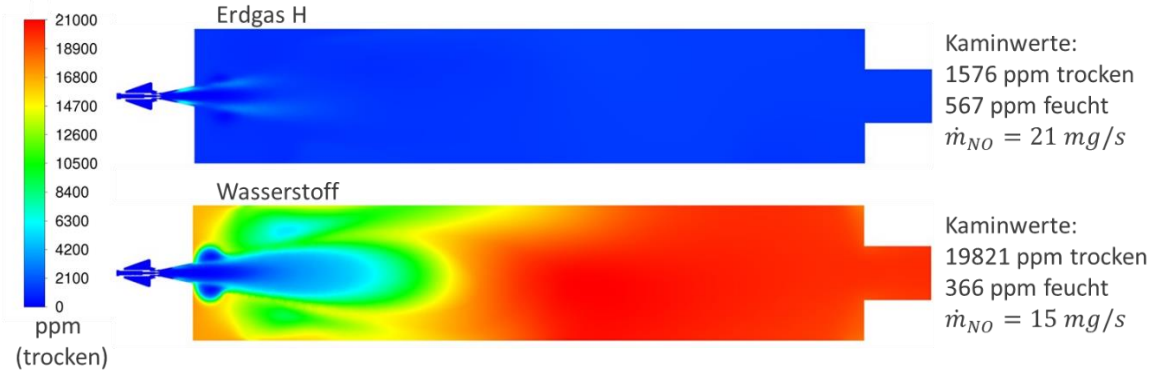

Abbildung 5: NO-Verteilungen bei der Oxy-Fuel-Verbrennung von Erdgas H und H_2 (P = 320 kW, λ = 1,02), ermittelt mit Hilfe von CFD-Simulationen.

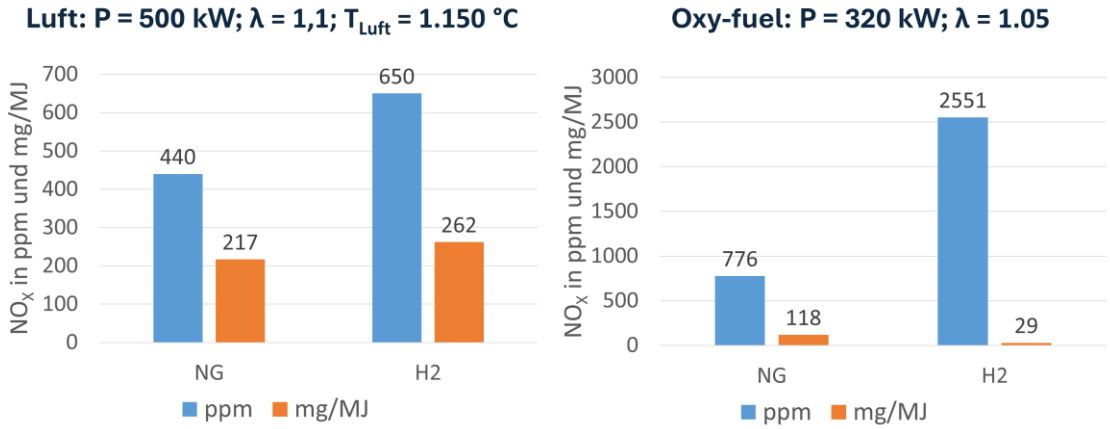

Abbildung 6: Vergleich der NO_X-Emissionen in [ppm] (im trockenen Abgas) und in [mg/MJ]. Messdaten aus den HyGlass (links)- und COSIMa-Projekten (rechts) [7], [15]

Vergleiche der Schadstoffemissionen anhand etablierter Metriken wie etwa der Spezieskonzentration im trockenen Abgas in Einheiten wie [ppm] oder [mg/m^3] führen somit zu erheblichen Verzerrungen. Andere Ansätze erscheinen hier besser geeignet [16], [17], etwa der Bezug des emittierten

Schadstoffmassenstroms auf die Feuerungsleistung mit Hilfe von Einheiten wie [mg/MJ] oder [mg/kWh]. Solche, in Regelwerk und Literatur durchaus bekannten Einheiten erlauben einen konsistenten Vergleich der Schadstoffemissionen, die beim Einsatz unterschiedlicher Brennstoffe oder selbst elektrischer Beheizungssysteme anfallen. Die vorhandene Messtechnik zur Erfassung der Schadstoffkonzentrationen kann dabei genutzt werden, die ermittelten Werre müssen lediglich mit Hilfe leicht bestimmbarer Stoffgrößen wie dem volumetrischen Heizwert H_i und dem minimalen trockenen spezifischem Abgasvolumen $V_{Abg,tr,min}$ anhand der z. B. in EN676 [18] vorgegebenen Gleichung umgerechnet werden:

$$NO_X\left[\frac{mg}{MJ}\right] = NO_x[ppm] \cdot 2{,}056 \cdot \frac{21}{21 - O_{2,\,gem}} \cdot \frac{V_{Abg,tr,min}}{H_i} \qquad (2)$$

Alternativ wäre auch der Bezug der Schadstoffemission auf eine Produktionsmenge [mg/$t_{Produkt}$] möglich, was durchaus diskutiert wird und z. B. in der TA Luft [19] für manche Prozesse bereits vorgeschrieben wird. Allerdings werden hierbei zwangsläufig die Schadstoffemissionen an die Prozesseffizienz gekoppelt, was Anlagenbetreibern u. U. die Freiheit nimmt, z. B. eine niedrigere Prozesseffizienz in Kauf zu nehmen, um Schadstoffemissionen zu reduzieren. Zudem stellt sich die Frage, wie beispielsweise mit dem nicht-produzierenden Haltebetrieb von Anlagen umgegangen werden soll.

Zusammenfassung

Bei allen Bemühungen zur Dekarbonisierung von energieintensiven industriellen Fertigungsprozessen und thermischen Kraftwerken müssen weitere wesentliche Aspekte des Anlagenbetriebs nach wie vor beachtet werden. Dies gilt u. a. auch für die Emissionen von Schadstoffen wie etwa Stickoxiden, die gerade beim Wechsel zu regenerativen Brennstoffen wie etwa Wasserstoff oder Ammoniak verstärkt gebildet werden können und für die strenge Emissionsgrenzwerte gelten.

Hierbei müssen neben den veränderten Brennstoffeigenschaften auch die Auswirkungen der eingesetzten Verbrennungstechnik berücksichtigt werden. So führt der Brennstoffwechsel von Erdgas zu Wasserstoff nicht zwangsläufig zu höheren Stickoxidemissionen, wie Beispiele aus der Oxy-Fuel-Verbrennung und der häuslichen Gasanwendung demonstrieren. Zudem muss überdacht werden, wie Schadstoffemissionen bei sehr unterschiedlichen Energieträgern sinnvoll und konsistent quantifiziert und limitiert werden können. Etablierte Einheiten wie [ppm] oder [mg/m^3] können nicht ohne Weiteres zum Vergleich des Emissionsverhaltens bei chemisch sehr unterschiedlichen Brennstoffen verwendet werden.

Ein Lösungsansatz, Schadstoffemissionen bei sehr unterschiedlichen Brennstoffen (oder sogar bei einer elektrischen Beheizung) physikalisch plausibel zu vergleichen, ist der Bezug auf die Feuerungs- bzw. Heizleistung, etwa in Einheiten wie [mg/MJ] oder [mg/kWh], wie in diesen Beitrag anhand einiger Beispiele aus aktuellen Forschungsprojekten gezeigt wird.

Quellen

[1] Warnatz, J., Maas, U., Dibble, R. W., *Verbrennung: Physikalisch-Chemische Grundlagen, Modellierung und Simulation, Experimente, Schadstoffentstehung*, 3. Aufl. Springer-Verlag, 2001.

[2] Dreizler, D., „Auswirkung von Wasserstoffbeimischung im Erdgas auf Gebläsebrenner“, 6. Forum Feuerungstechnik, München, 2019.

[3] Sankowski, L., Wünning, C., Kaiser, H., Schmitz, N., Pfeifer, H., „Experimentelle Untersuchungen zur Verbrennung von Wasserstoff und Erdgas-Wasserstoff-Gemischen in einem vorindustriellen Hochgeschwindigkeitsbrenner im Flammen- und flammlosen Betrieb“, 31. Deutscher Flammentag zur Nachhaltigen Verbrennung, Berlin, 2023.

[4] Astesiano, D., Bissoli, M., Della Rocca, A:, Malfa, E., Wuppermann, C., „Flexible hydrogen heating technologies, with low environmental impact“, *Matériaux & Techniques*, Vol. 111, 2023, doi: 10.1051/mattech/2023018.

[5] Leicher, J., „Hydrogen for industrial process heating: challenges and opportunities“, Keynote Lecture, IFRF TOTeM "Hydrogen for Decarbonization", Paris, Frankreich, 2022.

[6] Mullinger, P., Jenkins, B., *Industrial and Process Furnaces - Principles, Design and Operation*, 2. Aufl. Elsevier Applied Science Publishers Ltd, 2014.
[7] „HyGlass - Wasserstoffnutzung in der Glasindustrie als Möglichkeit zur Reduzierung von CO2-Emissionen und des Einsatzes erneuerbarer Gase – Untersuchung der Auswirkungen auf den Glasherstellungsprozess und Analyse der Potenziale in NRW“, Gas- und Wärme-Institut Essen e.V. / Bundesverband Glasindustrie e.V., Essen, PRO 0087 A, 2023.
[8] Gitzinger, H.-P-. Schröder, L., Rieken, M., „Veränderungen durch Wasserstoff beim Betrieb von Rekuperator-, Impuls- und Flachflammenbrennern“, *Prozesswärme*, Nr. 1, S. 40–45, 2022.
[9] Leicher, J., Schaffert, J., Tali, E., Oberschelp, L., Cigarida, H., Burmeister, F:, Albus, R., Schweitzer, J., Milin, P., „Wasserstoffeinspeisung in das Erdgasnetz auf Gasgeräte in Haushalt und Gewerbe in der EU - Ergebnisse des THyGA-Projekts“, 31. Deutscher Flammentag für Nachhaltige Verbrennung, Berlin, 2023.
[10] Schweitzer, J., „Self-regulated gas boilers able to cope with gas quality variation: State of the art and performances“, gehalten auf der EGATEC 2019, Groningen, Niederlande, 2019.
[11] Leicher, J., Giese, A., Görner, K., „Wasserstoff als Brennstoff: Stickoxidemissionen in technischen Verbrennungsprozessen“, 55. Kraftwerkstechnisches Kolloquium, Dresden, 2023.
[12] Noble, D., Wu, D., Emerson, B., Sheppard, S., Lieuwen, T., Angello, L., „Assessment of Current Capabilities and Near-Term Availability of Hydrogen-Fired Gas Turbines Considering a Low-Carbon Future“, *Journal of Engineering for Gas Turbines and Power*, Bd. 143, Nr. 4, 2021, doi: 10.1115/1.4049346.
[13] Baukal, C.E., Eleazer, P.B., „Quantifying NOx for Industrial Combustion Processes“, *Journal of the Air & Waste Management Association*, Vol. 48, No. 1, pp. 52–58, 1998, doi: 10.1080/10473289.1998.10463664.
[14] Schemberg, S., „NOx Emissionen verschiedener Brennersysteme im Hinblick auf die zu erwartenden Änderungen der TA Luft 2017“, 8. gwi-Praxistagung „Effiziente Brennertechnik für Industrieöfen“, Essen, 2017.
[15] „COSIMa“, NRW.Energy4Climate. [Online]. Verfügbar unter: https://www.energy4climate.nrw/industrie-produktion/praxisbeispiele-industrietransformation/cosima
[16] Leicher, J., Giese, A., Görner, K., „Vergleichbarkeit von Stickoxid-Emissionen bei wasserstoffreichen Brenngasen“, *Prozesswärme*, Nr. 1, S. 52–56, 2023.
[17] Schmitz, N., Sankowski, L., Busson, E., Echterhof, T., Pfeifer, H., „NOx Emission Limits in a Fuel-Flexible and Defossilized Industry - Quo Vadis?“, *Energies*, Vol. 16, No. 15, 2023, doi: 10.3390/en16155663.
[18] „DIN EN 676:2021-09 Gebläsebrenner für gasförmige Brennstoffe“, Deutsches Institut für Normung, 2021.
[19] *Neufassung der Ersten Allgemeinen Verwaltungsvorschrift zum Bundes-Immissionsschutzgesetz (Technische Anleitung zur Reinhaltung der Luft - TA Luft)*. 2021.

Numerical and experimental investigation of an additively manufactured H_2-capable gas burner in EAF relevant conditions

Christian Goßrau[1*], Johannes Willkomm[2], Fabian Krause[3]
Manfred Wirsum[1], Johannes Henrich Schleifenbaum[2], Hans-Jürgen Odenthal[3]

*gossrau@ikdg.rwth-aachen.de

[1] *Institut für Kraftwerkstechnik, Dampf und Gasturbinen (IKDG), RWTH Aachen University, Mathieustraße 9, 52074 Aachen, Deutschland*
[2] *Lehrstuhl für Digital Additive Production (DAP), RWTH Aachen University, Campus-Boulevard 73, 52074 Aachen, Deutschland*
[3] *SMS group GmbH, Am SMS Campus 1, 41069 Mönchengladbach, Germany*

Abstract
For the decarbonisation of the steel industry, electric steelmaking using scrap is the most important technology with 80 % less greenhouse gases than the blast furnace route. Since the electric arc furnace (EAF) is usually equipped with supplemental diffusion burners, there are numerous efforts to replace natural gas with hydrogen. However, high H_2 contents significantly change the combustion process due to the very different combustion properties, which places high demands on the burner design. Additive manufacturing (AM) opens new ways for burner design regarding gas/water routing. To cope with the high thermal load, the prototype is additively manufactured using powder bed fusion of metals using a laser (PBF-LB/M) with a new, pure copper powder (copper content > 99.5 %).

This study presents the numerical and experimental investigation and the design optimisation of an additively manufactured, small-scale 450 kW burner prototype in EAF relevant conditions. Good agreement has been shown between simulation results and closed-furnace test measurements when the extraction process via lance is also modelled. Preliminary investigations of the base burner design have shown that changes to the EAF gas composition and temperature have a minor and moderate impact on flame topology. Increasing the amount of H_2 in the fuel mixture results in shorter detachment distance and slower chemical conversion, thus causing flame elongation. The flame topology is impacted moderately (CH_4) and negligibly (H_2) by geometry alteration, as the high flow momentum dominantly impacts jet flame stabilisation. Biggest lever for altering flame topology is found by changing the mixing section length l_{ms}, with best comparability of H_2 and CH_4 operation evident when reducing l_{ms}, with a mean total deviation of 15 - 16 %.

Introduction

The recycling of scrap in the electric arc furnace (EAF) accounts for approximately one third of the produced world's crude steel and can be adjusted well to local requirements. Compared to the blast furnace route, the EAF route cuts down energy (- 30 %) and material (iron: - 1.5 t, carbon: - 0.65 t [1]) requirements as well as CO_2 emissions (- 80 % [2]). Figure 1 shows the design of an alternating current (AC) EAF consisting of hydraulic tilting platform, lower and upper shell, power supply, gantry system and burner system [3]. EAFs have tapping weights of 5 - 320 t, and the electrical energy required for melting and superheating is approx. 320 $\mathrm{kWh/t_{crude\ steel}}$ with tap-to-tap times of about 40 min. The EAF process can be distinguished in four main steps: (1) charging, (2) processing, (3) post-processing, and (4) tapping. In (1-2), the furnace is filled with recyclable scrap and the melting takes place. During post-processing (3), the melt is super-heated and refined. In the last step (4), the molten scrap is tapped and the whole cycle starts again. While the main amount of energy required is introduced by electricity and converted into heat by the electric arcs, a small amount is added to the furnace as chemical energy. The melting power is highest below the electric arcs in the furnace centre, so cold spots may occur near the walls so that melt and slag can build-up. Depending on the EAF size, up to six combined gas burner-injector systems can be installed to assist in melting, superheating and decarburizing the hot melt by

oxygen injection. Until today, such burners are operated with hydrocarbon fuels. According to the 2015 Paris Climate Agreement, carbon dioxide emissions must be reduced to limit global warming to less than 2°C by 2035 compared to pre-industrial levels. Hydrogen is considered as suitable future energy carrier and is currently integrated into the steel industry (e.g., reducing agent in pig iron production or in fossil-energy-operated plants) in first projects. However, climate-neutral production, transport, and storage of large quantities of H_2 requires significant energy and financial resources. Therefore, full H_2 availability to steel plants remains uncertain, necessitating fuel-flexible systems.

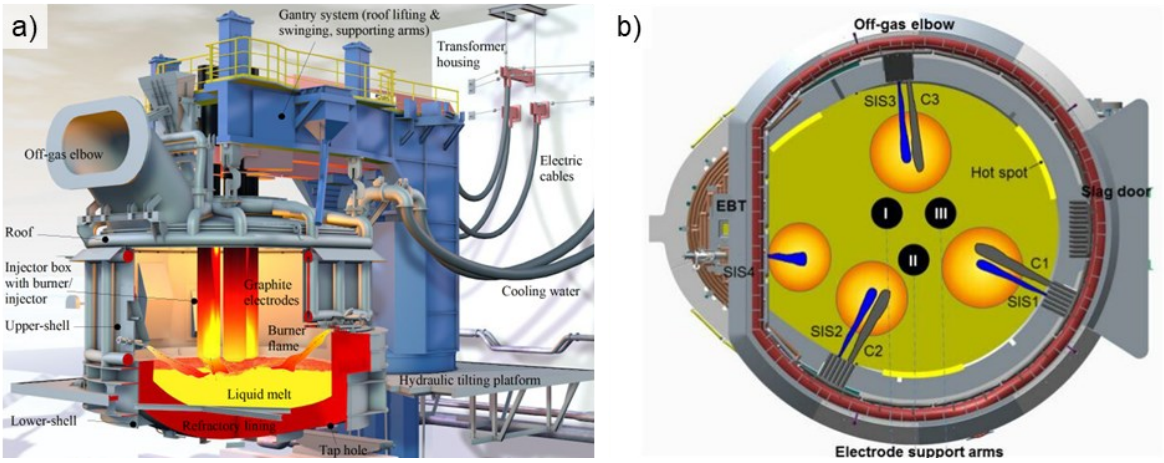

Figure 1. a) Design of an AC EAF with three burner-injector systems [4], b) arrangement of combined burner/injector system (*SIS*) in a 120 t EAF [5]

Some aspects related to the unique properties of H_2 need to be considered. The density and volumetric heating value of H_2 are only about one-eighth and one-third, respectively, of those of CH_4 [6]. Thus, the fuel switch to H_2 requires up to 3.3 times the fuel volume for the same thermal power. Hydrogen is extremely volatile due to its high diffusion coefficient [6] and has a high reactivity and flame speeds with O_2 [7]. In addition, H_2 leaks through even small gaps and diffuses slightly in materials (i.e., higher risk of H_2 embrittlement) due to its low density and low viscosity, necessitating suitable material choice and manufacturing process. Consequently, the burner design must be adapted to cope with the properties of H_2. Here, additive manufacturing (AM) can make valuable contributions in designing complex cooling and gas ducts as well as complex nozzle geometries. Thereby, fuel-flexible burners can be optimized to enhance their performance in terms of flame stability, emissions, and safety.

Burner operation and additive manufacturing

This study focuses on a 450 kW burner-injector system for application in EAFs, as shown in Figure 2. Its monolithic architecture integrates more than 40 conventionally manufactured components into a single part, reducing material usage (- 58 %), manufacturing complexity and effort. The burner consists of a central oxygen nozzle (on) and a coaxial fuel nozzle (fn). An inner and outer water duct are implemented for cooling due to thermal load by hot gases and furnace radiation. The design is enabled by PBF-LB/M using pure copper (*Cu01*) [8], which is selected due to its high thermal conductivity, mechanical strength and H_2 resistance. Despite the challenges of processing copper with standard infrared laser systems due to its low absorptivity, a patented post-treatment of *Cu01* allows for stable processing on an *EOS M290* system with a laser power below 400 W, achieving relative part densities above 99.5 % and surface roughness values of Sa = 4.84 µm. In a four-stage process development, suitable exposure parameters were determined for bulk, upskin, and downskin areas. Following appropriate heat treatment, a thermal conductivity of up to 360 W/(m·K) is obtained [4, 9].

During each EAF cycle, the burner works in three different modes: a) shrouding mode, b) burner mode, and c) injector mode [10]. While the shrouding mode is operated during charging (1) and tapping (4), the burner mode and injector mode are operated in the processing (2) and post-processing mode (3), respectively. The burner mode is the one most affected by the switch from natural gas to hydrogen and is therefore the focus of this study. In this mode, O_2 and fuel are fed unmixed through the burner, i.e. mixing and ignition take place inside the furnace. The central convergent-divergent nozzle is designed

in such a way that a compression shock forms, and O_2 exits the burner at high subsonic speeds (CH_4: 221 m/s, H_2: 188 m/s). The fuel is always found with subsonic conditions, but also at high jet velocities (CH_4: 34 m/s, H_2: 114 m/s). As consequence, an elongated flame forms, which assists in scrap melting in cold spots and overall melting pattern homogenisation of the furnace.

Figure 2. Additively manufactured 450 kW burner with gas/water routing in operation mode

Experimental and numerical setup

The burner prototype was tested at the *Gas- und Wärme-Institut* (GWI) in Essen, Germany and is numerically investigated with *ANSYS FLUENT 22 R2*, with post-processing performed using *Python*. In a previous study, free-fire tests were carried out under ambient conditions to provide an initial assessment of the burner mode's flame topology [4]. For this study, closed-furnace tests of the burner in fuel-flexible operation (P = 450 kW, ϕ = 1) were carried out and are assessed numerically. The burner was mounted in a furnace and supplied with O_2 and NG-H_2 mixtures. The combustion takes place in a gas environment composed of combustion products at high temperatures. The operation of the burner is monitored by temperature and species measurements at various locations. Due to the high thermal conductivity of the material and the high amount of cooling water, the burner was cooled sufficiently.

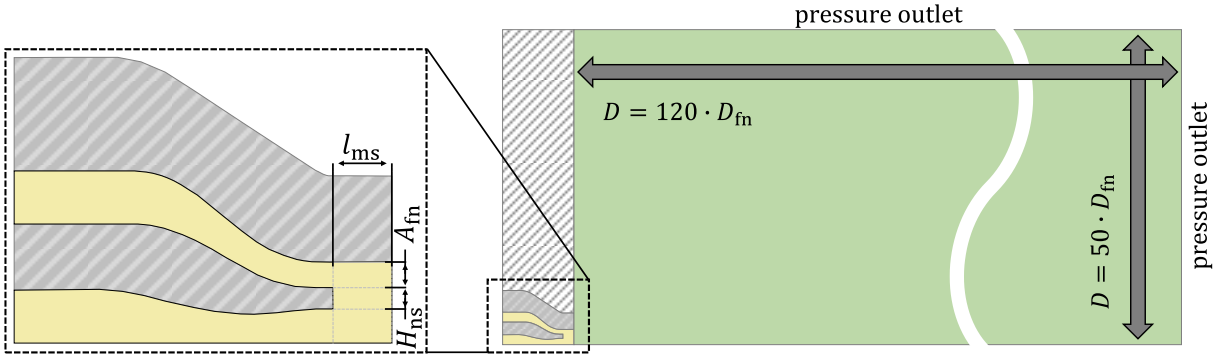

Figure 3. Base burner design and numerical domain

Due to the rotational-symmetric character of the flames, the flow field and chemical conversion are numerically investigated on a 2D axisymmetric domain. The length and diameter of the combustion domain are 120 and 50 times the fuel nozzle exit diameter D_{fn}. All gases enter the domain at 15 C and natural gas is considered as pure CH_4 for simplicity. The O_2 mass flow rate is given by the stoichiometric ratio (ϕ = 1). The outflow surfaces are characterized by pressure outlet conditions, and combustion takes place under atmospheric pressure. The equations for mass, momentum, energy, and species are solved using the Reynolds-averaged Navier-Stokes (RANS) solver. Discretisation is done by the second-order differencing scheme for the pressure equation and the second-order upwind scheme for all other equations. The pressure-based coupled solver and the pseudo-transient method are used. The SST k-ω model is used for turbulence and the EDC model is used for turbulence-chemistry modelling, since it is found to be a satisfactory hypothesis for H_2-CH_4 combustion [11, 12]. The chemical conversion is calculated for fine turbulent structures by the species transport model with volumetric reactions by integrating the chemistry at constant pressure. The in-situ adaptive tabulation (ISAT) model is applied to ease computational effort. The *DRM22* mechanism is used to reflect the main combustion characteristics of both fuels accurately with reasonable computational effort. Combustion of CH_4 / H_2 with O_2 results in very high combustion temperatures (~ 3000 K). Without external heat sink, the completion of chemical conversion is impeded in a dissociation equilibrium. Gas extraction by lance results in rapid cooling, which artificially accelerates heat dissipation and dissolves the dissociation equilibrium. This significantly impacts the gas composition measurements, especially in the vicinity of the flame. Therefore, the numerical results are exported to *Python* for correction of the simulation

results. For this purpose, a reactor network consisting of modules from *Cantera* [13] is used to model the continuous cooling of the gas to ambient temperature in finite time.

To address the impact of design on flame topology, three variation parameters are studied: fuel nozzle flow area A_{fn}, nozzle separation height H_{ns}, and mixing section length l_{ms} (cf. Figure 3). Compared to the base design ($A_{\mathrm{fn}} = 402.1$ mm^2, $H_{\mathrm{ns}} = 4$ mm, $l_{\mathrm{ms}} = 15$ mm), A_{fn} (min | max: 201.1 | 603.2 mm^2) and H_{ns} (min |max: 2 | 6 mm) are changed by 50 % and l_{ms} (min | max: 0 |30 mm) is either omitted or doubled. The angles of the oxygen and fuel nozzle remain unchanged, as these are crucial for the injector mode. The flame contour ($x_{\mathrm{fc}}|y_{\mathrm{fc}}$) is characterised by the local OH concentration equal to 50 % of its global maximum. The flame topology is evaluated using four parameters: flame height $FH = \max(x_{\mathrm{fc}})$, flame base $FB = \min(x_{\mathrm{fc}})$, flame length $FL = FH - FB$, and flame width $FW = \max(y_{\mathrm{fc}})$. The deviation of each parameter p for a design change $dev_{\mathrm{a,r}}^{p}$ is assessed as the absolute difference between the parameter of the altered (a) burner case with H_2 $p_{\mathrm{a}}^{\mathrm{H_2}}$ and of the reference (r) burner case with CH_4 $p_{\mathrm{r}}^{\mathrm{CH_4}}$, normalised by $p_{\mathrm{r}}^{\mathrm{CH_4}}$:

$$dev_{\mathrm{a,r}}^{p} = \left|\left(p_{\mathrm{a}}^{\mathrm{H_2}} - p_{\mathrm{r}}^{\mathrm{CH_4}}\right)/p_{\mathrm{r}}^{\mathrm{CH_4}}\right| \tag{1}$$

The reference burner case is defined in two ways for different design goals: (b) base design, and (a) altered design, with 100 % CH_4. Case (b) reflects the goal of burner operation with mainly H_2, thus achieving similarity to the base burner design with CH_4. Case (a) reflects the goal of fuel-flexible burner operation, thus achieving similarity between flame topologies of both fuels. To assess comparability of flame topology, each parameter deviation is multiplied with a weighting factor w according to their relevance (*FH*: 4, *FB*: 3, *FL*: 2, *FW*: 1). The average weighted deviation for each design change $dev_{\mathrm{a,r}}$ is assessed as the sum of individual weighted parameter deviations $dev_{\mathrm{a,r}}^{p}$ referenced to the sum of weighting factors:

$$dev_{\mathrm{a,r}} = \sum_p \left(w_p \cdot dev_{\mathrm{a,r}}^{p}\right)/\sum_p w_p \tag{2}$$

During the EAF operation, gas atmosphere conditions are very specific to the melting process. Therefore, two exemplary EAF processes with different gas compositions (cf. Figure 4) from literature [14] are used. The burner is not operated during charging of scrap, post-processing and tapping of the melt. The most dominant species are CO, CO_2, H_2 and N_2, while O_2 and H_2O are only minor.

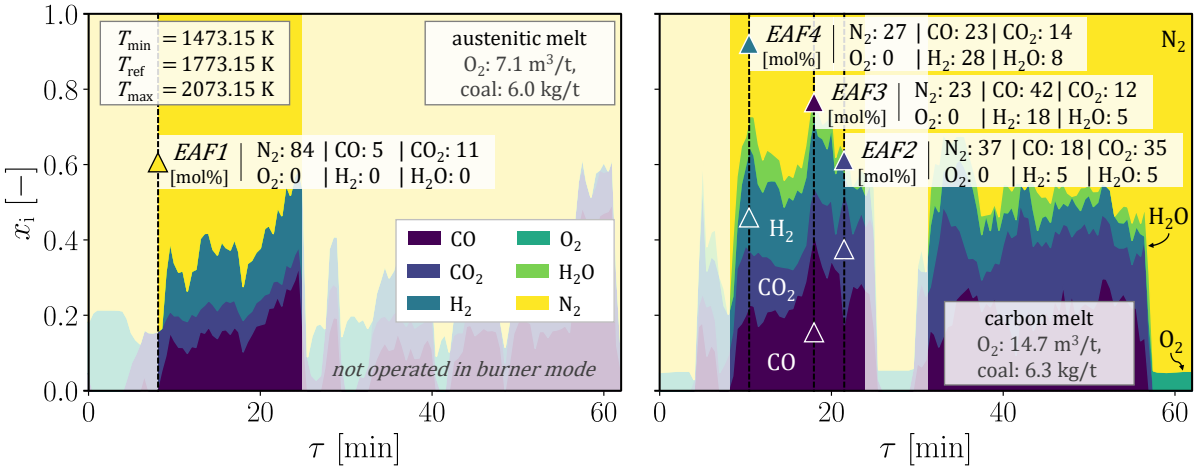

Figure 4. Furnace gas composition for two EAF melts (left: austenitic (O_2: 7.1 m^3/t, coal: 6.0 kg/t), right: carbon (O_2: 14.7 m^3/t, coal: 6.3 kg/t) [14]) and derived characteristic gas conditions (*EAF1-4*)

Four characteristic furnace conditions (*EAF1-4*) are derived from the two EAF runs (cf. Figure 4) for the assessment of burner operation change during the EAF process, with each case characterised by maximum concentration of the dominant species: N_2 in *EAF1*, CO_2 in *EAF2*, CO in *EAF3,* H_2 in *EAF4*. All characteristic gas compositions yield high concentrations of CO (5 – 37 mol.%) and CO_2

(11 – 35 mol.%) without the presence of O_2. Since measurement data for the two EAF processes [14] only includes gas composition, a temperature range of 1473.15 – 2073.15 K is assumed.

Validation of numerical setup

The CFD simulations are validated with emission measurements of the natural gas combustion in the closed-furnace. The measurement data (*EXP*) as well as the numerical results without (*CFD*) and with correction of the extraction lance cooling (*CFD+*) are shown in Figure 5 along the axis and radially offset by 0.05 m. The impact of extraction lance cooling is evident from the large difference between experiments and uncorrected simulations, particularly in the vicinity of the flame. The emissions of the experiments and the corrected simulations agree very well for large parts of the furnace chamber. Significant deviations only occur close to the burner (≤ 0.5 m). While CO and CO_2 measurements indicate a chemical conversion as downstream, the O_2 concentration decreases closer to the burner. Due to the rotationally symmetrical character of the flame in free-fire tests [4] and in simulations, the same topology is also generally concluded for the furnace tests. Accordingly, the O_2 concentration must increase opposingly along the axis until approaching pure O_2. The deviation is therefore attributed to the measurement uncertainty. Exhaust gas extraction using a lance is an invasive process with direct influence on the flow field and on combustion. In addition, the lance positioning is subject to inaccuracy (approx. 0.02 m), which makes measurements on the centre axis difficult.

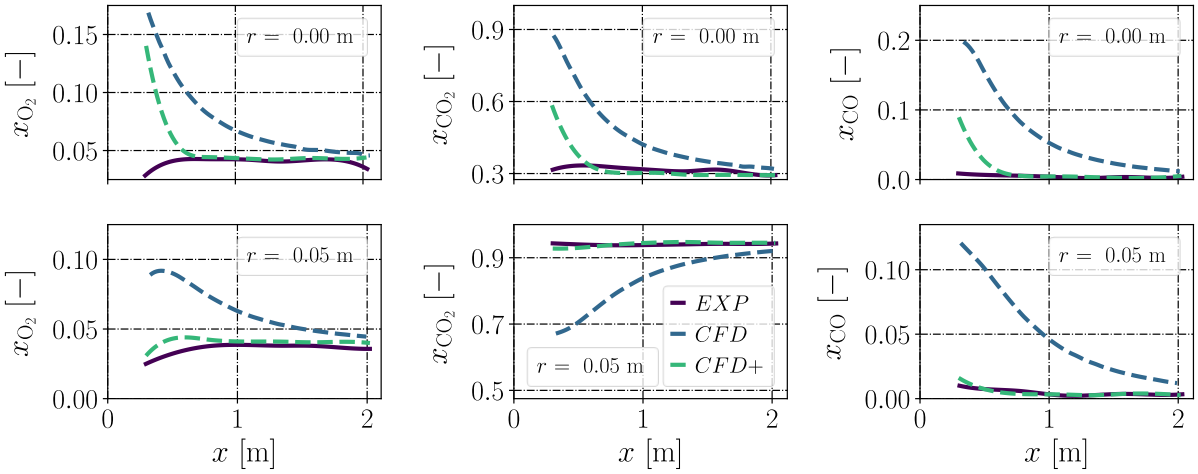

Figure 5. Experimental (*EXP*) and numerical (*CFD*: without correction, *CFD+*: with correction) species concentrations along the axis (r = 0.00 m) and radially offset (r = 0.05 m)

Base burner design

This section assesses the changes to flame microstructure and topology of the base design for altered furnace gas condition (*EAF1-4*, T_{EAF} = 1473.15 – 2073.15 K) and fuel composition (x_{H_2} =0 – 1). The flame topology of the base design is shown in Figure 6 for both CH_4 and H_2 in all furnace environments for T_{EAF} = 1773.15 K. In all cases, the flame detaches from the burner surface and combustion takes place inside the furnace. Due to the increased distance from the nozzle, the mixing of oxygen and fuel is enhanced. In addition, surrounding EAF gas is admixed to the fuel jet, thereby affecting combustion in two ways: (1) As reactive species (i.e., H_2) entrain, the overall reactivity increases, and the flame moves upstream and shortens. (2) As non-reactive species entrain at substantially lower temperatures (~ 1773.15 K) than the flame temperature (~ 3000 K), the flame moves downstream and becomes prolonged due to the decreased reactivity. In general, (1) dominates in the vicinity of the flame and (2) in the downstream part of the flame. Consequently, the flame detachment is reduced, which shortens the effective mixing length of fuel and furnace gas, and the flame is prolonged.

However, the general reactivity and impact of both effects differ depending on the fuel composition. The CH_4 flames are characterised as partially premixed with moderate dilution, since the prolonged effective mixing length of fuel and furnace gas and the lower CH_4 jet impulse leads to greater entrainment of furnace gas. Consequently, the flames stabilise further downstream and spread outwards more radially, and the chemical conversion occurs over a wider volume. This effect is more pronounced at lower H_2 concentrations in the furnace gas ($x_{H_2,EAF1} < x_{H_2,EAF2} < x_{H_2,EAF3} < x_{H_2,EAF4}$). The H_2

flames are characterised as non-premixed with minor dilution, since the shortened effective mixing length of fuel and furnace gas and the higher H_2 jet impulse leads to impeded entrainment of furnace gas. Consequently, the flames stabilise further upstream and spread outwards less radially, and the chemical conversion occurs in the H_2/O_2 mixing layer. The H_2 flames are less depending on EAF gas condition, since entrainment of additional H_2 has only neglectable impact on the overall reactivity.

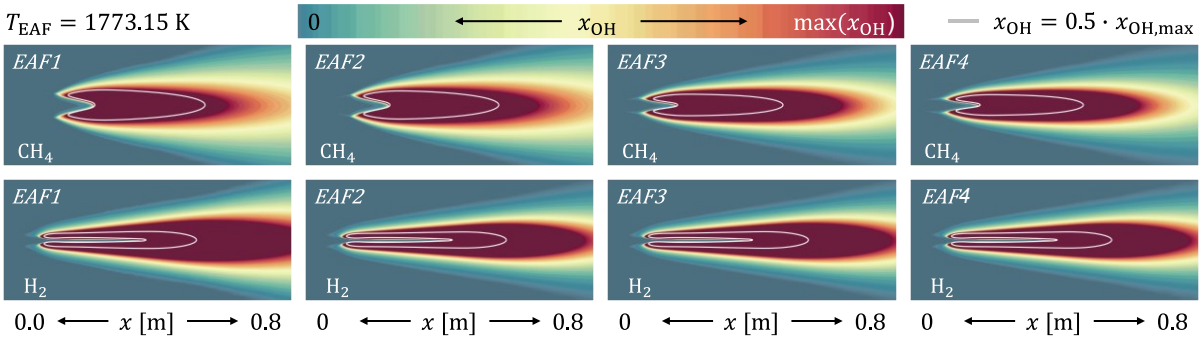

Figure 6. Flame topology indicated by OH concentration ($x_{OH} = 0.5 \cdot x_{OH,max}$) with CH_4 and H_2 for altered EAF gas conditions (*EAF1-4*, T_{EAF} = 1773.15 K)

The impact of altered EAF temperature (*EAF1-4*, T_{EAF} = 1473.15 – 2073.15 K) on flame topology is shown in Figure 7 by relating each topology parameter to its value at reference temperature (T_{EAF} = 1773.15 K). The relative flame topology parameters are shown for CH_4 and H_2 in all EAF environments with the base design. Following the previous conclusions, H_2 flames (up to ± 7 %) are less impacted by changes in EAF gas condition than CH_4 flames (up to ± 79 %). For CH_4 flame, largest changes are found when the temperature is increased by 300 K from 1473.15 K, while further increase in temperature up to 2073.15 K yields less change. The increase of EAF temperature (1473.15 to 2073.15 K) results in a decrease of *FB* (≤ 60 %), *FH* (≤ 34 %), *FL* (≤ 23 %) and *FW* (≤ 48 %). The greatest influence on flame topology is found with *EAF1* (≤ 60 %), whilst it is more moderate (≤ 53 %) with *EAF2-4*. The impact of gas temperature is therefore increasingly evident in flames with prolonged lift and flame length, hence enhanced effective mixing length of fuel and furnace gas (i.e., *EAF1*, cf. Figure 6). For H_2 flames, the increase of EAF temperature (1473.15 to 2073.15 K) results in a decrease of *FB* (≤ 3 %) as well an increase in *FH* (≤ 8 %), *FL* (≤ 11 %) and *FW* (≤ 13 %). Again, as the deviations are small and all flames are impacted in the same manner, the H_2 flame topologies are comparable at the same temperature with different EAF gas composition (*EAF1-4*). For simplicity, the remainder of the study assumes a constant EAF temperature of 1773.15 K.

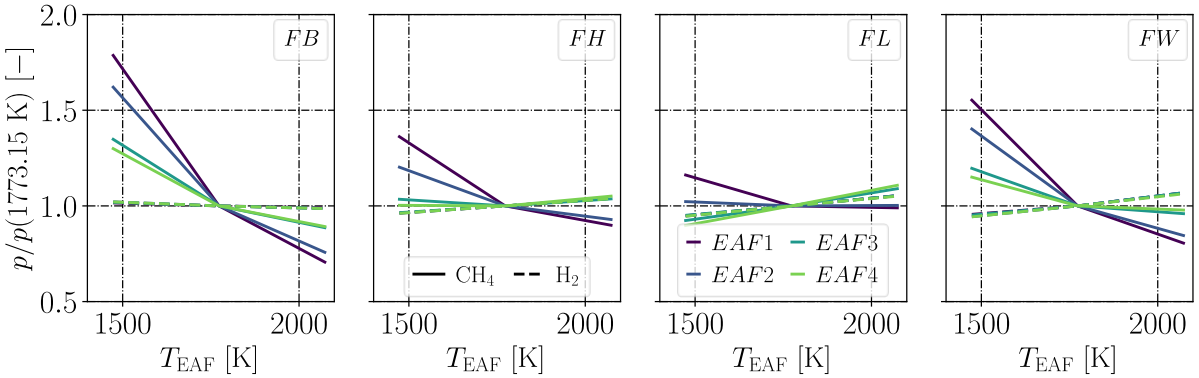

Figure 7. Flame topology changes by altered EAF gas temperature (T_{EAF} = 1473.15 – 2073.15 K) for the base burner design operated with CH_4 and H_2, and different EAF gas compositions (*EAF1-4*)

The flame topology parameters for changing EAF gas composition are shown in Figure 8 for the operation of the base design with CH_4 and H_2, quantitively reflecting the trends observed in Figure 7. For CH_4, all topology parameters decrease when moving from *EAF1* to *EAF4*, following the trend of increasing H_2 concentration in the furnace gas. For *EAF3-4*, however, flame topology is comparable with minor deviations (≤ 5 %). Due to the admixture of H_2 from the furnace, the reactivity significantly increases, and the flame base *FB* moves upstream (≤ 30 %). With reduced lift, less EAF gas is admixed,

resulting in a further increase of reactivity. Consequently, also the flame height *FH* decreases, though more moderately (≤ 14 %). With the stronger absolute reduction of *FH*, the flame length *FL* decreases (≤ 7 %). With increasing reactivity and reduced entrainment, the flame width *FW* decreases from *EAF1* to *EAF4* by 32 %. The H_2 flames are less affected by the change in EAF atmosphere due to their high inherent reactivity. Consequently, the flame base *FB* only minorly increases by 1 % compared to its minimum (*EAF1*: 12 mm). With moderately increasing flame height *FH* (≤ 4 %), also the flame length *FL* increases (≤5 %). The flame width *FW* decreases only minorly by up to 5 %.

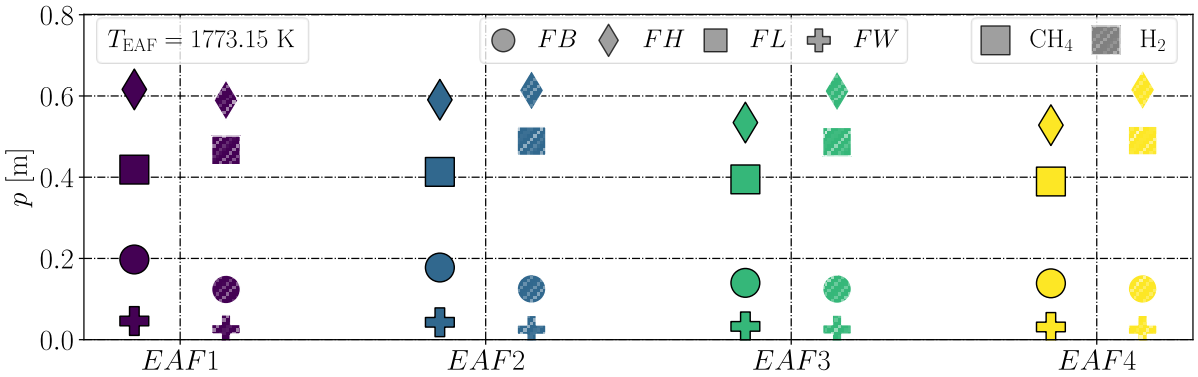

Figure 8. Change in flame topology parameters p by altered EAF gas conditions (*EAF1-4*) with CH_4 and H_2 for the base design

The flame topology parameters for altered fuel composition are shown in Figure 9 for the base burner design in *EAF1-4*. The admixture of H_2 has the same qualitative impact on the flame topology in all furnace gas conditions. For increasing H_2 content, there is a continuous decrease in *FB* (≤ 37 %) and *FW* (≤ 44 %), whilst *FH* (≤ 17 %) and *FL* (≤ 26 %) increase again after initially decreasing for up to 25 - 65 vol.% H_2. Due to the increasing reactivity with H_2 admixture, the reaction starts further upstream, and the flame moves towards the nozzle (min. distance: 0.12 m). The reduction in flame lift results in decreased entrainment of furnace gas, thereby enhancing reactivity and reducing the flame width *FW*. Up to 25 - 65 vol.% H_2, the increased reactivity also enhances chemical conversion while maintaining a premixed character, resulting in reduced flame height *FH*. Conversely, for higher H_2 contents, the reaction gradually shifts into the mixing layer between oxygen and fuel. Consequently, the flame shifts towards a more non-premixed type, which leads to impeded mixing and an extended flame height *FH*.

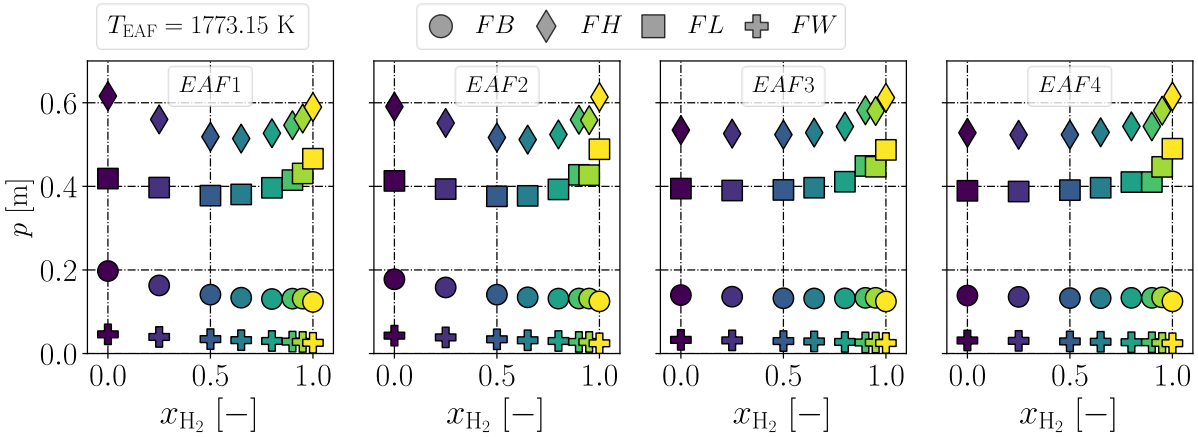

Figure 9. Change in flame topology parameters p by altered fuel composition (x_{H_2} = 0 – 1) with all EAF gas conditions (*EAF1-4*) for the base design

Altered burner designs

To incorporate the sensitivity of the burner design, the assessment of flame topology is carried out for all proposed burner design alterations. The qualitative and quantitative investigation is exemplarily conducted for *EAF1*. Finally, the evaluation of the impact of design alteration on flame topology is done coherently for all EAF operation conditions. Figure 10 shows the OH concentration as indicator for the

flame topology for all designs ($l_{ms}^{min|max}$, $A_{fn}^{min|max}$, $H_{ns}^{min|max}$) with both CH_4 and H_2. In general, altering the nozzle design has only moderate impact on flame topology. Consequently, the flame topologies of the altered designs have the same characteristics compared to the base design (cf. *Base burner design*). Therefore, the differences in flame topologies for fuel changes remain qualitatively the same.

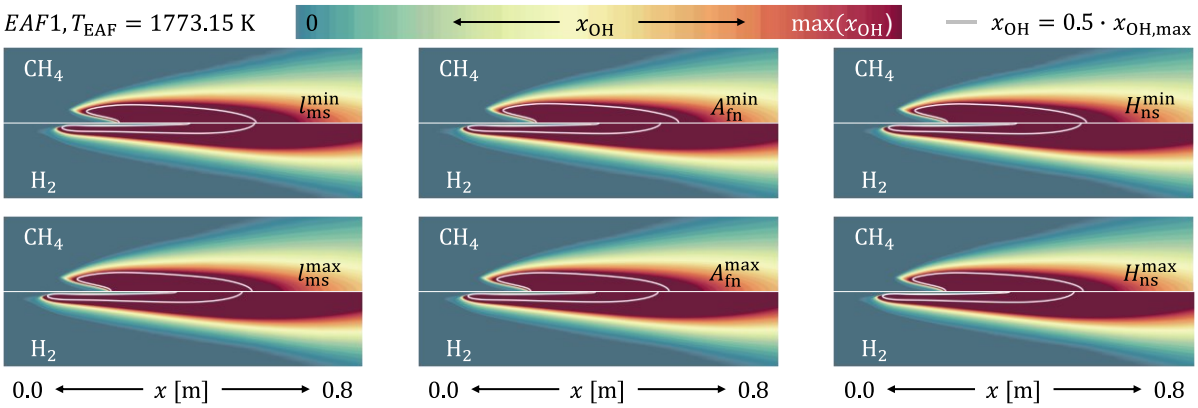

Figure 10. Flame topology indicated by OH concentration ($x_{OH} = 0.5 \cdot x_{OH,max}$) with CH_4 and H_2 for altered burner design (*EAF1*, T_{EAF} = 1773.15 K)

The changes in flame topology parameters p (*FB*, *FH*, *FL*, *FW*) for all design alterations compared to the base design in *EAF1* are shown in Figure 11. Following the observations for Figure 10, the changes of flame topology are moderate (≤ 16 %) compared to the base design. For CH_4 operation, changing the nozzle design has minor effect on the flame topology with a maximum deviation of 9 %. The highest increase of *FB* (+ 9 %) and *FW* (+ 4 %) is found for l_{ms}^{max} and l_{ms}^{min}. The highest increase of *FH* and *FL* is both found with 3 % for A_{fn}^{min}. For H_2 operation, changing the nozzle design has moderate effect on the flame topology with a maximum deviation of 16 %. Highest increase of *FB* (+ 16 %) and *FH* (+ 4 %) is found for l_{ms}^{min}. The highest increase of *FL* (+ 2 %) and *FW* (+ 23 %) is found for l_{ms}^{max}. Comparing H_2 operation with any design to CH_4 operation with the base design, the same *FH* is found for l_{ms}^{min}. The minimum deviation in *FB* (– 27 %), *FL* (+ 11 %) and *FW* (– 43 %) is found for l_{ms}^{min}, A_{fn}^{max} and l_{ms}^{max}. Comparing H_2 operation to CH_4 operation with any design, a minimum deviation of 1 % in *FH* is evident with l_{ms}^{min}. The minimum deviation in *FB* (– 30 %), *FL* (+ 10 %) and *FW* (– 43 %) is found for l_{ms}^{min}, A_{fn}^{min} and H_{ns}^{max}.

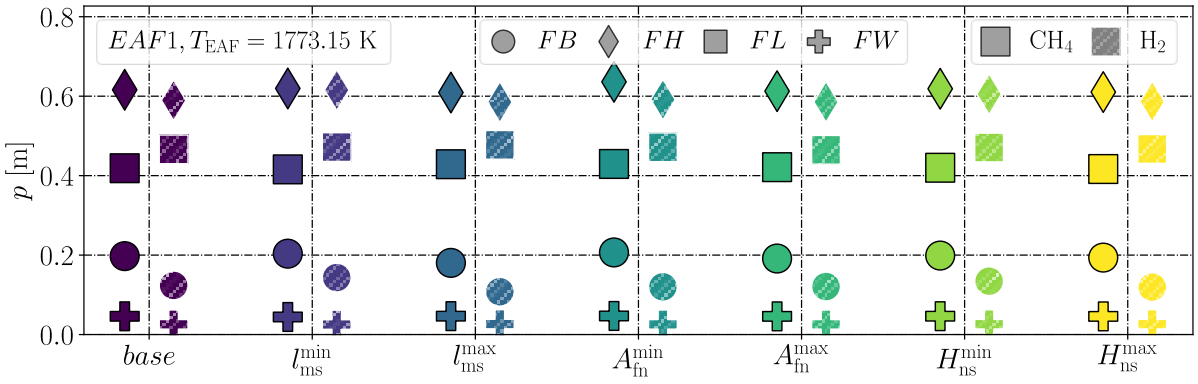

Figure 11. Flame topology changes compared to the reference design by altered burner design

The flame topology deviations by the design alterations for each EAF gas condition and the sum across all EAF gas conditions are shown in Table 1. The changes are thereby evaluated by the weighted sum of the individual deviations for both comparison cases: (b) base design with CH_4 ($dev_{a,b}$), and (a) altered design with CH_4 ($dev_{a,a}$).

Table 1. Weighted sum of flame topology parameter deviation for each altered burner design referenced to the base design $\boldsymbol{dev}_{\mathbf{a,b}}$ and to the altered design $\boldsymbol{dev}_{\mathbf{a,a}}$ with CH_4 operation

EAF	$dev_{\mathrm{a,b}}$							$dev_{\mathrm{a,a}}$						
	base	l_{ms}		A_{fn}		H_{ns}		*base*	l_{ms}		A_{fn}		H_{ns}	
		min	max	min	max	min	max		min	max	min	max	min	max
1	18	14	21	20	19	17	19	18	15	20	20	18	18	19
2	16	15	19	18	17	15	17	16	16	18	19	16	16	17
3	17	16	20	18	17	15	18	17	16	19	20	17	16	18
4	20	15	23	20	20	17	20	20	16	20	22	19	17	20
All	18	15	21	19	18	16	18	18	16	19	20	18	17	18

For case (b), the comparison of flame topology to the base burner design with CH_4 ($dev_{\mathrm{a,b}}$), the base design and all design changes with H_2 yield comparable mean deviations (14 – 23 %). For case (a), the comparison of flame topology to the respective altered burner design with CH_4 ($dev_{\mathrm{a,a}}$), the base design and all design changes with H_2 yield comparable mean deviations (15 – 22 %). For all furnace gas conditions (*EAF1-4*), reducing the mixing length ($l_{\mathrm{ms}}^{\mathrm{min}}$) yields the smallest deviations in (b) and (a). For (b) in *EAF3* and (a) in *EAF3-4*, reducing the nozzle separation height ($H_{\mathrm{ns}}^{\mathrm{min}}$) yields similar results. For all furnace gas conditions, increasing the mixing section length ($l_{\mathrm{ms}}^{\mathrm{max}}$) in (b) and reducing the fuel nozzle flow are ($A_{\mathrm{fn}}^{\mathrm{min}}$) yields the highest deviations. By concluding all the mean deviations for all furnace gas conditions, the best design can be derived for the entire EAF process. For influencing the flame topology, altering l_{ms} has the highest lever with a difference in total mean deviation by 6 % and 3 % in (b) and (a). Altering H_{ns} (1 – 2 %) and A_{fn} (1 – 2 %) has a smaller lever. For (b), best (15 %) and worst (21 %) similarity is found for reducing ($l_{\mathrm{ms}}^{\mathrm{min}}$) and vice versa increasing ($l_{\mathrm{ms}}^{\mathrm{max}}$) the mixing section length. For (a), best (16 %) and worst (20 %) similarity is found for reducing the mixing length ($l_{\mathrm{ms}}^{\mathrm{min}}$) and the fuel nozzle flow area ($A_{\mathrm{fn}}^{\mathrm{min}}$).

Conclusion and Outlook

The operation of a small-scale, additively manufactured 450 kW burner prototype with both natural gas and hydrogen was investigated experimentally in closed furnace test and numerically in different electric arc furnace (EAF) atmospheres. Simulations have shown good qualitative agreement with closed-furnace test measurements. However, exhaust gas cooling and subsequent reaction progress in the extraction lance must be considered. Based on this, the operation of the base burner design has been analysed preliminarily for four gas atmospheres of exemplary EAF runs:

- Changing the EAF gas composition has moderate and minor impact on CH_4 and H_2 flames.
- Increasing the EAF temperature notably impacts CH_4 flames only, generally resulting in the flame being closer to the nozzle and the reaction zone being elongated and narrowed.
- With increasing H_2 in the fuel mixture, the flame base moves towards the nozzle with moderately and notably increasing flame height and length.

In addition, the impact of design changes on the nozzle section of the burner was analysed by varying three geometric parameters (fuel nozzle flow area A_{fn}, nozzle separation height H_{ns}, and mixing section length l_{ms}):

- Flame topology is impacted moderately (CH_4) and minorly (H_2) by design changes, hence chemical reaction and flame formation is mainly influenced by the high momentum of the jets.
- Altering l_{ms} has the highest lever ($\Delta dev_{(\mathrm{b})-(\mathrm{a})}$ = 3 -6 %) on flame topology, while altering H_{ns} ($\Delta dev_{(\mathrm{b})-(\mathrm{a})}$ = 1 – 2 %) and A_{fn} ($\Delta dev_{(\mathrm{b})-(\mathrm{a})}$ = 1 – 2 %) have reduced lever.
- Best comparability of H_2 and CH_4 operation is found for reducing l_{ms} in all cases.

The findings show moderate potential for flame topology improvement, mostly by reducing the mixing length. However, the impact of this alteration on the different burner modes (i.e., shrouding and injector mode [4]) must also be evaluated, especially since the latter is highly sensitive to changes in nozzle geometry. Additionally, the thermal resistance and cooling capability must be assessed to ensure the

burner's longevity. The demonstration of fuel-flexible operation is subject of ongoing work and a test campaign in an EAF is planned. The required upscaled burner (in MW scale) will also be preliminarily investigated in laboratory environment, resulting additional validation data. The results will further demonstrate the burner's capability to ensure the process requirements with fuel-flexible operation.

Acknowledgments
The authors gratefully acknowledge the financial support of the German Federal Ministry of Education and Research (BMBF) as part of the project *SupplHyInno Rhineland: Technology demonstration of hydrogen industrial gas burners in steel production (HyInnoBurn2),* Funding reference: 03ZU2115JA, 02/2025 – 01/2028.

Literature

[1] Meier T.: *Modellierung und Simulation des Elektrolichtbogenofens*, Dissertation, RWTH Aachen University, 2016.
[2] Stahlinstitut VDEh / WV Stahl: *Jahrbuch Stahl 2017*, Verlag Stahleisen, Düsseldorf, ISBN: 3-514-00825-6, 2017.
[3] Odenthal H.-J., Kemminger A., Krause F., Sankowski L., Uebber N., Vogl N.: *Review on modeling and simulation of the electric arc furnace (EAF)*, steel research international, 89, 1-36, 2017.
[4] Goßrau C., Willkomm J., Krause F., Wirsum M., Schleifenbaum J., Odenthal H.-J.: *Additive manufacturing, numerical simulation and experimental investigation of a diffusion gas burner with H_2 fuel-flexibility*, 31. Deutscher Flammentag, 2023.
[5] Odenthal H.-J., Bader J., Nörthemann R., Reifferscheid M., Klioutchnikov I., Olivier H.: *The optimized SIS injector for EAF applications*, AISTech - Iron and Steel Technology Conference Proceedings. 1, 2014.
[6] Gas- und Wärme-Institut Essen e.V.: *gwi-Arbeitsblätter*, Vulkan-Verlag, Essen, ISBN: 3-8027-2475-5, 2012.
[7] Chen X., Qingming L., Qi J., Zonglei M., Yang S., Jinxiang H., Hongrong M.: *The characteristics of flame propagation in hydrogen/oxygen mixtures*, International Journal of Hydrogen Energy, Volume 47, Issue 17, 2022.
[8] Infinite Flex: 3D Printing Solutions, https://infinite-flex.de/3d-printing, 30.09.2022.
[9] Krause F., Kemminger A., Odenthal H.-J., Willkomm J., Schleifenbaum J., Goßrau C., Wirsum, M., Cameron F., Ren Y., Pitsch H.: *Design, simulation and testing of additive manufactured hydrogen burners used in the EAF*, 9th European Oxygen Steelmaking Conference, 6th European Conference on Clean Technologies, 2022.
[10] Odenthal H.-J., Bader J., Nörthemann R., Reifferscheid M., Klioutchnikov I., Olivier H.: *The optimized SIS injector for EAF applications*, Association for Iron & Steel Technology Conference, 1, 1-12, 2014.
[11] Tang G., Chen Y., Silaen A., Krotov Y., Riley M., Zhou C.: *Effects of fuel input on coherent jet length at various ambient temperatures*, Applied Thermal Engineering, 153, 513-523, 2019.
[12] Yan S., Tang G. Zhou C., Guo X.: *Computational Fluid Dynamics Modeling of Combustion Characteristics of a CH_4 / O_2 Combustor in a Copper Anode Furnace*, ACS Omega, 4, 12449-12458, 2019.
[13] Goodwin D. G., Moffat H. K., Schoegl I., Speth R.L., Weber B. W.: *Cantera: An object-oriented software toolkit for chemical kinetics, thermodynamics, and transport processes*. https://www.cantera.org, Version 3.1.0, doi:10.5281/zenodo.14455267, 2024.
[14] Kirschen M., Velikorodov V., Pfeifer H., Kühn R., Lenz S., Loh J., Schäfers K.: *Off-gas measurements at the EAF primary dedusting system*, 8th European Electric Steelmaking Conference, 2005.

Optimisation of air preheating in cement rotary kilns using IR cameras

N. Bodendiek*, A. Schall, S. Schäfer

*nils.bodendiek@vdz-online.de

VDZ Technology gGmbH, Toulouser Allee 71, 40476 Düsseldorf, Germany

Abstract

The cement industry is striving to further reduce the amount of fuel and electrical energy required for the clinker burning process, thereby lowering operating costs and CO_2 emissions. Optimising air preheating through heat recovery in the clinker cooler is a key lever in this effort. Every reduction in thermal energy losses at the cooler results in a 1.5-fold reduction in the total losses of the kiln system [1]. In a research project conducted by the VDZ, a new approach using infrared cameras is being pursued, in which the temperature distribution of the clinker bed surface in the cooler is recorded and unfavourable conditions such as uneven clinker distribution are identified.

Operational tests carried out to date in two cement plants have shown that the selected IR camera system is capable of continuously recording measurement data on an industrial clinker cooler over a period of several weeks. Extensive evaluation of the camera data and other operating data from the plant enabled continuous assessment of the condition inside the cooler. In parallel with the evaluation, the control variables of the clinker cooler were specifically varied during the operational tests. This resulted in a more uniform clinker bed temperature in the clinker cooler and an improvement in various kiln operating and product parameters.

Description of the clinker burning process

The raw materials (limestone, marl, clay, etc.) are finely ground and fed into the kiln system in a dry state (Figure 1).

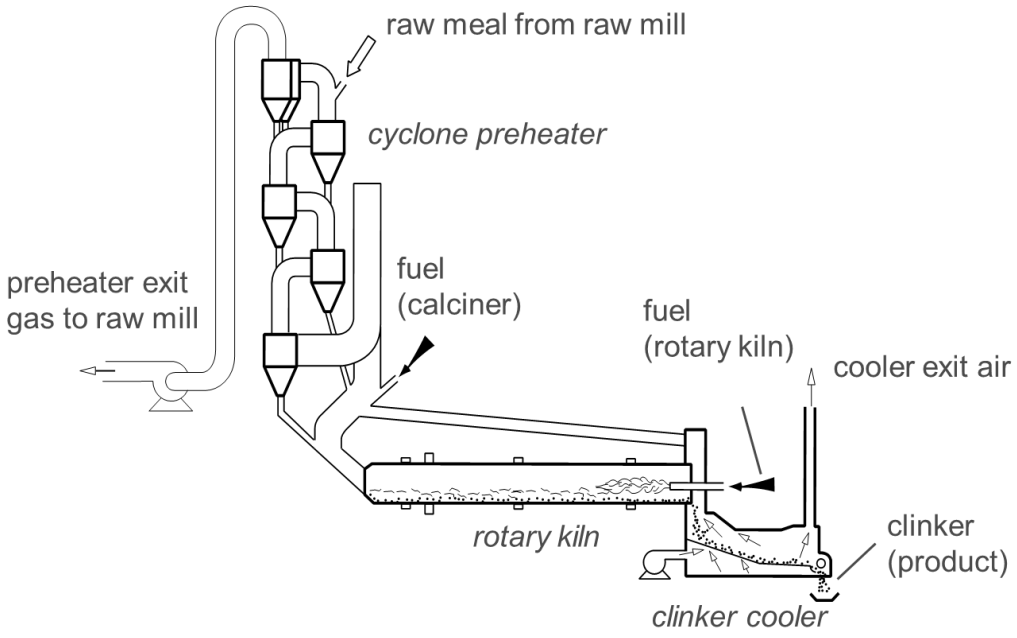

Figure 1. Rotary kiln plant with preheater, calciner and grate cooler

In the preheater, the raw meal is heated to approximately 850 °C by the counterflowing exhaust gas and then calcined at this temperature. The meal is then heated to 1450 °C in the rotary kiln and burned to form cement clinker. The chemical and mineralogical reactions that take place during this process lead to the formation of clinker phases, which are essential for the hydraulic properties of the cement. While still in the kiln, the clinker is cooled to a temperature of approx. 1200 °C in the so-called pre-cooling zone (between the sintering zone and the cooler). The clinker then enters the clinker cooler, where it is cooled to approx. 100 °C by cooling air. Some of the preheated cooling air is returned to the kiln as combustion air (secondary and tertiary air). In the final step, the burnt clinker is finely ground and processed together with a sulphate carrier to produce cement.

Among the various cooler designs, the grate cooler has now become the state of the art. The clinker is transported with the aid of various different transport mechanisms in the floor. When dropped into the cooler, the clinker first passes through the recuperation zone. The temperature control in this area is primarily designed to achieve optimum heat recovery. The efficiency of heat transfer in the clinker bed depends to a large extent on the height of the clinker bed, the granulometry of the clinker and the gas flow velocity [2, 3]. The aim is to achieve a sufficiently high clinker bed with even distribution of the clinker and clinker particle size across the entire width of the cooler, resulting in uniform flow resistance. Otherwise, local air breakthroughs occur, since the cooling air seeks the path of least resistance. As a result, the clinker is not cooled effectively and the cooling air is not heated effectively. However, perfect distribution of the clinker cannot be achieved in practice. The rotation of the kiln causes a separation of the clinker during discharge into the cooler. Clinker on the upturning side is consistently finer the than on the other. Manufacturers of clinker coolers developed countermeasures to correct this effect by offsetting the cooler centerline relative to the centerline to the kiln and a horse-shoe-shaped refractory assembly at the cooler inlet. However, the continuous fluctuations in the firing conditions inside the rotary kiln remain to be a challenge. These fluctuations are unavoidable because the process is designed as a counterflow process and is therefore prone to oscillation. The fluctuations result in uneven discharge from the kiln into the cooler, which leads to uneven distribution of the clinker across the width and length of the cooler [2, 4].

Measurement technology used

As part of the research project, two operational tests were carried out in two different cement plants. At the start of each test, an infrared camera from CMV Systems GmbH & Co. KG was installed in the recuperation area of the clinker cooler. The selected IR camera is suitable for measuring temperatures between 300 and 1000 °C. It is designed as a combustion chamber camera, i.e., the camera is installed in a water-cooled stainless steel probe housing (boroscope camera with optics, Figure 2).

Figure 2. IR camera in borescope design in removed state

The camera lens is kept free of dust and deposits by means of purge air. Compressed air is used as purge air. The camera is locked to the steel housing of the cooler by means of a probe holder. The probe is attached with a quick-release fastener and can be removed and reinstalled for maintenance purposes. A pin/ring system ensures that the probe is reinstalled in exactly the same position, maintaining a consistent field of view. This is essential for ensuring the comparability of continuous camera data and enabling long-term evaluations.

A lateral position halfway along the length of the clinker cooler proved to be a suitable measuring point. The camera was aligned precisely so that the field of view of the wide-angle lens covered the entire width and almost the entire length of the recuperation area (see Figure 3).

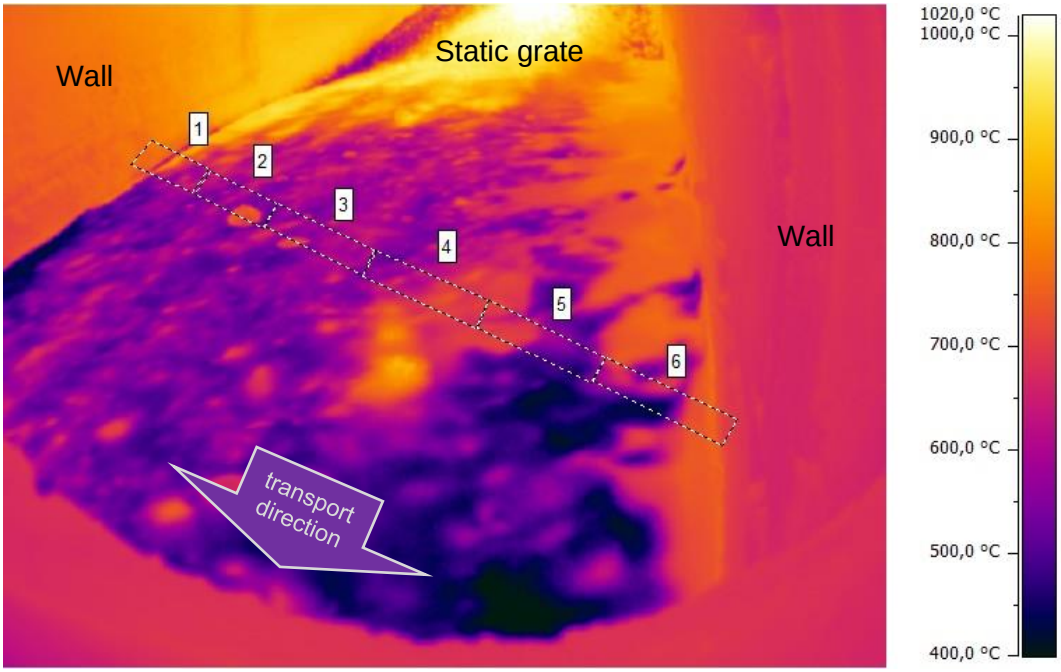

Figure 3. Field of view of the IR camera, view of the recuperation area of the clinker cooler A (shown is an image taken at low cooler temperature during kiln shut-down)

The camera data is transferred to the evaluation computer via a data cable. The frame rate is 25 Hertz. Evaluation software from DIAS Infrared GmbH is installed on the evaluation computer, which continuously records the infrared data from the camera and converts it into temperature data. An emissivity of 1 is used as standard for converting the data. Since the clinker bed and the walls in the clinker cooler are not black radiators, the actual emissivity values are below 1. The actual values were not determined during the operational measurements. However, the resulting measurement deviation is not particularly relevant in the context of the research project, as the evaluation of temperature gradients and trends is entirely sufficient for the project objectives. The measured temperature distribution in the visible range is displayed as a "live image" in the form of a false-colour image, in which each temperature is assigned a colour. The temperature/colour scale used in the tests can be seen on the right-hand side of Figure 3. The evaluation software allows evaluation zones (regions of interest, ROI) to be defined in the camera's field of view. Six elongated rectangles were defined as ROIs across the entire width of the clinker cooler. Using the evaluation software, the average temperatures in the ROIs were continuously calculated and stored as values of interest (VOI) in the form of a time series for further evaluation.

At both kiln systems, the IR camera recorded clinker surface data continuously. The test period lasted about two months. View obstruction by dust in the cooler was rare. When it occurred, it was brief and the data collection was not significantly affected. The selected camera positions were located in a less dusty part of the clinker cooler, which helped to reduce issues with high dust loads.

Results of the operational tests

After installing the IR camera system, a test program was carried out on the two rotary kiln systems. During this program, specific control variables of the clinker cooler were changed in several test settings. Each test setting was maintained for several days. The effects on the clinker bed in the cooler, on the operation of the entire kiln system, and on the clinker product were investigated by evaluating the data from the IR camera, other factory measurement data and clinker analyses. The primary objective was to determine the logical connection between the temperature signals from the IR camera and the operational control variables and, on this basis, to be able to design optimisation strategies for the cooler operation.

Starting from the initial state of normal kiln operation (test 1) at kiln system A, the clinker bed height was increased by 5% in the first step (test 2). The evaluation of the measurement data showed that this had no significant effect. Presumably, the height changes were too small, but larger changes were not feasible due to the operational constraints. In the second step, the stroke length of the outer push plates was additionally shortened by up to 30% (test 3). This measure caused the clinker bed to be pushed forward less at the areas on the side and thus to be more compacted there than in the middle area. The camera images and the evaluation of the VOI temperature values show that the temperature profile on the clinker bed has become significantly more uniform (Figures 4, 5 and 8). In addition, the evaluation of further plant measurements and clinker analyses showed that there was a significant temperature increase of approx. 30 °C in the sintering zone of the rotary kiln and that the free lime content of the burnt clinker decreased from 0.9 to 0.7 M.-%. Both indicate that, compared to the initial condition, heat recovery in the clinker cooler has improved. This led to a better preheating of the combustion air, which can be considered a very positive development.

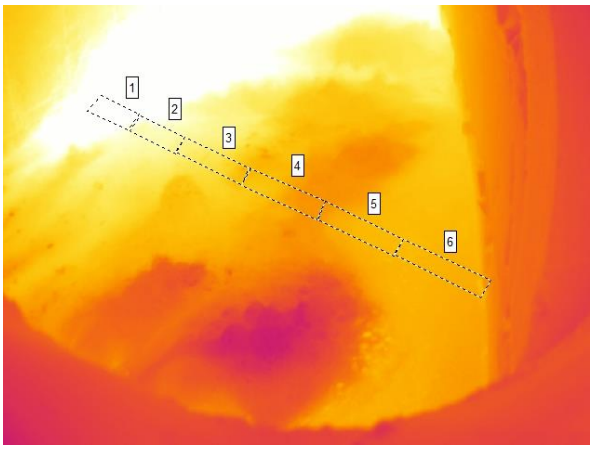

Figure 4. kiln system A; initial operating condition (test 1)

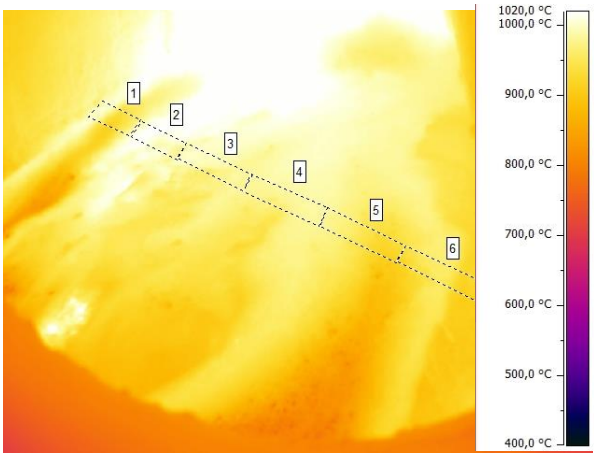

Figure 5. kiln system A, operating condition with stroke length of the outer push plates below ROI 1 and 6 reduced up to 30% (test 3)

In kiln system B, the normal operating condition was first recorded as the initial state (test 1). For the test the stroke length of the push plates on the right-hand side was gradually reduced to 50% compared to the standard setting (test 3). The camera images and the evaluation of the VOI temperature values show a clear equalisation of the temperature profile (Figures 6, 7 and 8**)**. Further measurement data, such as the temperatures in the sintering zone or clinker analysis values, are not yet available, as the operational test on kiln system B had not been completed at the time of publication.

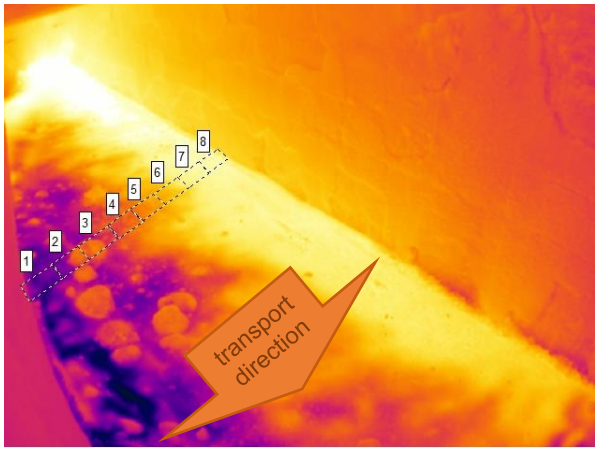

Figure 6. Kiln system B; initial operating condition (test 1)

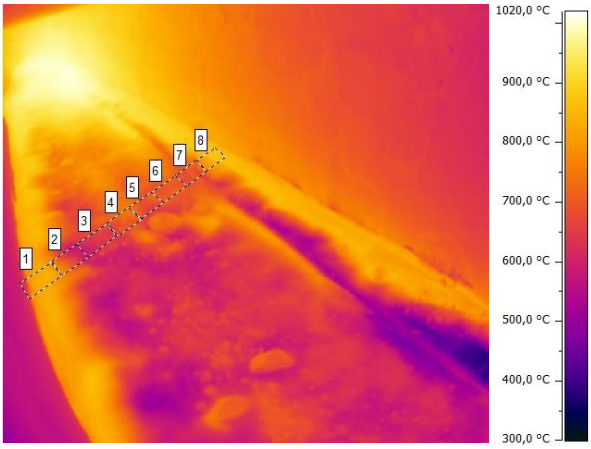

Figure 7. Kiln system B, operating condition with stroke length of the push plates below ROI 5 to 8 reduced to up to 50% (test 3)

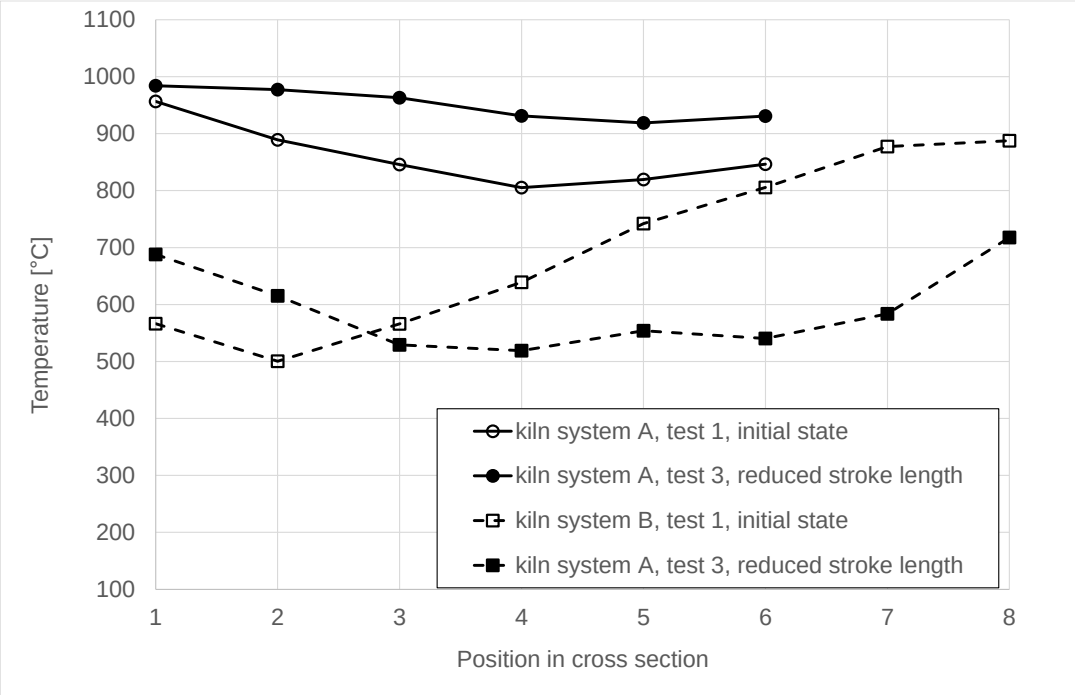

Figure 8. Temperature profiles across the cross-section/total width of the clinker bed (daily average values of the VOI on a day typical for the test)

Outlook

Once the operational tests have been completed, the test results will be used to derive general recommendations for optimising clinker cooler operation and to develop a control concept for integrating the measurement data into the cooler control system. In addition, an initial assessment of potential energy and CO_2 savings will be carried out.

Funding

The IGF project 22644 N is funded by the German Federal Ministry for Economic Affairs and Energy as part of the program for promoting the Industrial Joint Research (IGF) on the basis of a decision of the German Bundestag.

Literature

[1] Rosemann H., *Theoretische und betriebliche Untersuchungen zum Brennstoffenergieverbrauch von Zementdrehofenanlagen mit Vorcalcinierung*, Beton-Verlag, Düsseldorf, 1986.

[2] Føns M., *Optimization of clinker cooler performance with understanding of the heat exchanger challenges*, Cement international, 15, 56 – 61, 2, 2017.

[3] Bhatty, J.I.; Miller, F.M.; Kosmatka, S.H., *Innovations in portland cement manufacturing*, Portland Cement Association, Skokie, Illinois, USA, 2004.

[4] Harder, J., *Latest trends in clinker cooling*, ZKG International, 42 – 42, 3, 2011.

HYDROGEN IN SHOCKLESS EXPLOSION COMBUSTION FOR GAS TURBINES

C. Zenker[1*], M. Oevermann[1] , R. Klein[2], C. O. Paschereit[3]

*Christian.Zenker@b-tu.de

[1] *Institut für Mathematik, Brandenburgische Technische Universität Cottbus-Senftenberg, Platz der Deutschen Einheit 1, 03046 Cottbus, Deutschland*
[2] *Fachbereich Mathematik & Informatik, Freie Universität Berlin, Arnimallee 6, 14195 Berlin, Deutschland*
[3] *Chair of Fluid Dynamics, Hermann-Föttinger-Institut (HFI), Technische Universität Berlin, Müller-Breslau Str. 8, 10623 Berlin Deutschland*

Abstract

The *Shockless Explosion Combustion* (SEC) concept, introduced by Bobusch et al. (Combust. Sci. Technol., Vol. 186, (10-11), 2014), seeks to achieve constant volume combustion in gas turbines by using acoustic confinement to trigger close-to-homogeneous auto-ignition of small premixed fuel-air packets. The authors recently (Klein et al., ASME J. Eng. Gas. Turb. Pow., Vol. 147, 2025) presented a comprehensive computational study of a whole engine SEC-driven gas turbine model with detailed investigations of the highly unsteady reactive gas-dynamics inside the combustor. Thermodynamic cycle analyses have shown thermal efficiencies close to the theoretical Humphrey cycle for pressure gain combustion for compressor pressure ratios of 6:1 and 20:1. The study demonstrated the potential of an SEC-driven gas turbine to deliver substantial efficiency gains over classical gas turbines designs.

The study of Klein et al. utilizes a simple one-step Arrhenius type chemical reaction with parameters adjusted to mimic key parameters of real fuels such as ignition delay and heat release rate, which are essential for the resonant behavior of the SEC combustor. In this study we advance the study of Klein et al. by presenting results for an SEC-driven gas turbine using a detailed chemical reaction mechanism for hydrogen, which has been identified as a suitable fuel for pressure gain combustion. For a compressor pressure ratio of 6:1 a thermal efficiency of 47,3% is achieved for the engine operating in SEC mode compared to 38,4% thermal efficiency for the classical Brayton-Joule process. The investigations demonstrate the overall robustness of the SEC combustion mode.

Introduction

Pressure gain combustion (PGC) describes unsteady combustion processes where heat release increases the stagnation pressure. This is in contrast to conventional constant-pressure combustors, like those in the Brayton-Joule cycle, which always incur a pressure loss [5, 6]. By mimicking a constant-volume (Humphrey) cycle, PGC can use some of its heat release to compress the gas before reactions set in, thereby reducing the entropy production of the combustion process and boosting thermodynamic efficiency [6].

A theoretical study from Heiser and Pratt [7] analyzed different thermodynamic cycles, namely the constant pressure (CPC), constant volume (CVC), and pulsed detonation combustion (PDC), of which the last can be interpreted as a special form of CVC. They concluded that the ideal PDC cycle can reach a thermal efficiency above 40%. However, PDC suffers from drawbacks such as extreme pressure peaks, entropy generation via shock waves, and exergy losses [1].

To overcome these issues, Bobusch et al. [1] proposed an alternative approach to achieve a constant volume cycle called S*hockless Explosion Combustion* (SEC). According to this concept, a controlled homogeneous auto-ignition of the fuel-air mixture creates a smooth pressure rise without forming destructively strong shocks. The cyclic SEC process is fundamentally managed by standing pressure waves inside the combustor, which orchestrate the four key stages: wave establishment, filling with compressed air, fuel injection and mixture formation, and finally, homogeneous auto-ignition and exhaust [1, 2]. Since its conception, SEC has been investigated in numerous theoretical studies [9,10,11] with different approaches and levels of detail.

According to Klein et al. [2], developing an SEC-based gas turbine involves several challenges: (i) forming a stratified charge inside the combustor to promote nearly uniform auto-ignition, (ii) controlling pressure fluctuations to safeguard turbine components, (iii) achieving efficiency gains comparable to those expected from constant volume combustion, and (iv) designing a reliable one-way inlet valve. The authors address in [2] the first three challenges in a conceptual full engine simulation models that couple a quasi-onedimensional combustor with both zero- and two-dimensional representations of the compressor and turbine plena, alongside quasi-stationary turbo-machinery models for compressor and turbine. Their simulations reveal two distinct SEC modes - one with firing frequency close to the combustor's fundamental acoustic frequency and another about roughly twice that frequency. For compressor pressure ratios of 6:1 and 20:1, the system realizes an average pressure increase across the combustor by a factor of ca. 1.5. Assuming ideal performance of compressor and turbine, the SEC engine models demonstrate efficiency improvements of roughly 30 % and 18 % over their deflagration-based counterparts, reaching overall efficiencies of 52 % and 66 %, respectively. These values are in close agreement with predicted efficiencies for the Humphrey cycle. In addition, the thermodynamic cycle analysis in [2] suggests that further efficiency gains may be achievable with optimized plenum and combustor designs.

The study in [2] uses a simple one-step Arrhenius reaction model to capture key processes such as ignition delay and heat release, which are essential for the resonant behavior of the SEC combustor. However, real fuels feature many different time scales of different orders of magnitude leading to complex auto-ignition behavior which highly depends on local flow conditions.

This study builds upon the authors work presented in [2] and advances it by investigating the use of hydrogen as a potential fuel for SEC in gas turbines (see also [9,10]), employing the same modeling approach. The engine simulator couples standard thermodynamic models for turbomachinery components with zero-dimensional plena and a quasi-onedimensional combustor. However, it replaces the simple Arrhenius kinetics of [2] with the comprehensive hydrogen/oxygen kinetic model for high-pressure combustion from Burke et al. [3] to consider realistic detailed chemistry, thereby aiming to analyze the SEC concept's robustness w.r.t. details of the chemical heat release. The following analysis will present and discuss the resulting gas-dynamic processes and thermal efficiencies.

Gasturbine Model and Computational Representation

Klein et al. [2] created an idealized computational model to simulate a single-shaft gas turbine. This model can operate in two different modes: either in traditional turbulent premixed (constant pressure) deflagration mode or in (pressure gain) Shockless Explosion Combustion (SEC) mode. As described in detail in [2], the conceptual engine is comprised of five main components shown in Fig. 1: a quasi-

stationary compressor model, a compressor plenum, the combustor, a turbine plenum, and a quasi-stationary turbine model. The core of this setup is the combustor, which is modeled using a quasi-onedimensional (1D) framework. Within this framework, the reactive Navier-Stokes-Fourier equations are solved for the combustor tube incorporating a closure for turbulent transport and source terms that account for variable tube cross-sections. The two plena, preceding and following the combustor, are treated as zero-dimensional (0D) volumes. For these components, only the overall budgets for mass and energy are evaluated during the simulation. In the following we provide a brief overview for each component.

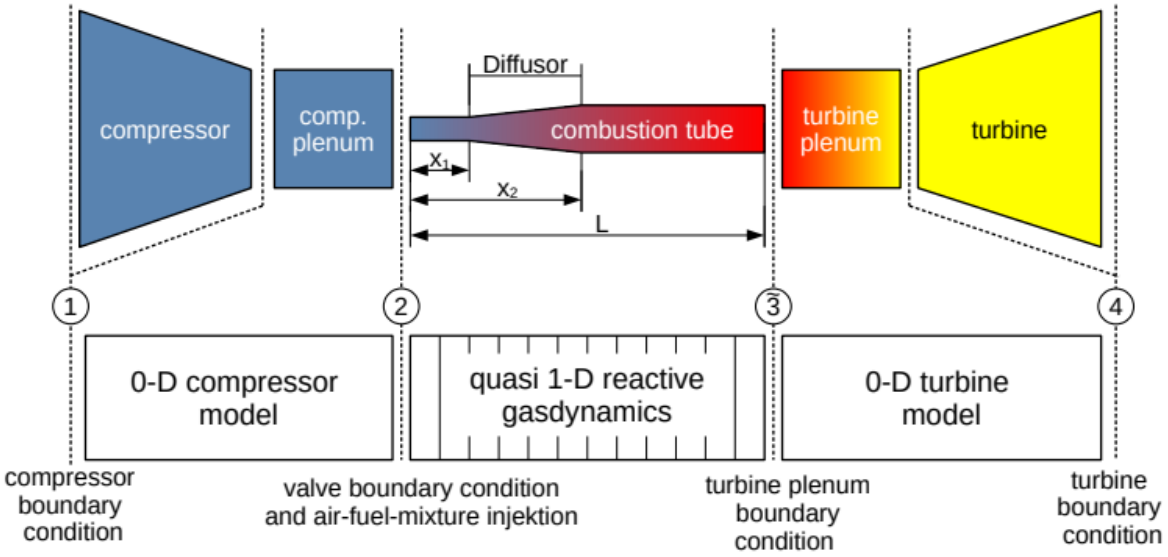

Figure 1 Upper Part: Sketch of the conceptual engine model adapted from [2]. Lower Part: Corresponding discretization of the conceptual model.

The turbine is modeled using standard stationary turbomachinery characteristics, operating under the assumption of a reduced mass flowrate

$$\frac{\dot{m}_\mathrm{T}\sqrt{T_{\tilde{3}}}}{p_{\tilde{3}}} = C_\mathrm{T} = \text{const.} \tag{1}$$

This approach is valid for sonic or near-sonic flow conditions at the turbine outlet. The turbine inlet pressure $p_{\tilde{3}}$ and temperature $T_{\tilde{3}}$ are derived from mass and energy balances in the turbine plenum assuming that the mean momentum is zero. The capacity of the turbine is defined by the product $C_\mathrm{T} A_\mathrm{T}$, where A_T is the turbine inlet cross-section and C_T is a constant characterizing the turbine size. This allows for the calculation of the mass flow rate per unit area $\dot{m}_\mathrm{T}$. Assuming an expansion of the working gas inside the turbine to ambient pressure p_4 in an ideal, adiabatic process, the outlet temperature can be calculated using the relation

$$\frac{T_4}{T_{\tilde{3}}} = \left(\frac{p_4}{p_{\tilde{3}}}\right)^{\frac{\gamma-1}{\gamma}}. \tag{2}$$

Here, γ is the isentropic exponent, defined as the ratio of the specific heat capacities at constant pressure c_p and constant volume c_v. The corresponding positions in the engine from indices $\tilde{3}$ and 4 are also given in circles in Figure 1 between the upper and lower part.

The turbine's power generation is by given by the enthalpy flux difference between turbine inlet and outlet:

$$P_{\mathrm{T}} = \dot{m}_{\mathrm{T}} A_{\mathrm{T}} \left(h_{\tilde{3}} - h_4 \right). \tag{3}$$

As demonstrated in [2], the model is capable of simulating the engine start-up process, during which the compressor's rotational speed is gradually increased until a target pressure ratio p_2/p_1 is achieved. Here, the indices 1 and 2 (cf. 1) refer to conditions at the compressor inlet (ambient conditions) and the compressor plenum outlet, respectively. For simplicity, in this study the start-up phase is omitted. Instead, the simulation begins directly with the desired pressure ratio already established. Assuming an ideal adiabatic compression, the temperature ratio across the compressor is

$$\frac{T_2}{T_1} = \left(\frac{p_2}{p_1} \right)^{\frac{\gamma - 1}{\gamma}} \tag{4}$$

Analogous to (3), the power input required to drive the compressor is determined by the enthalpy balance

$$P_{\mathrm{C}} = -\dot{m}_{\mathrm{C}} A_{\mathrm{C}} \left(h_2 - h_1 \right) \tag{5}$$

and the engine output power P_{out} for an assumed single-shaft engine is given by the difference between turbine power generation (3) and compressor power (5).

A onedimensional model is used to represent and simulate the unsteady combustion and gas-dynamical effects inside the combustor. Recharging at the combustor inlet is controlled by a diodic valve located at the interface between the compressor plenum and the combustor inlet. In deflagration mode, this valve remains open. However, in SEC mode, it opens and closes based on the pressure difference between compressor plenum and the pressure in the first grid cell of the combustor simulation model. The valve closes when the pressure at the combustor inlet exceeds the compressor plenum pressure and opens when it drops below. SEC mode also employs a cold air buffer to prevent the injected fuel from early uncontrolled ignition due to mixing with hot product gases from the previous cycle. Close-to-simultaneous auto-ignition of the injected fuel charge is achieved by adjusting the ignition delay time to the residence time via temperature stratification. The inlet temperature for each parcel of a charge is calculated such that its ignition delay matches that of the first parcel of the charge, corrected for the time difference of their injection times. To prevent unphysical negative ignition delays, a minimum delay threshold is enforced, and the required temperature is found using a damped Newton iteration. Some details are provided below.

A diffusor is integrated into the combustion tube. Its main purpose is to enhance the overall efficiency of the SEC cycle via i) amplification of backward propagating suction waves to enable reliable recharging against an increasing pressure between the compressor and turbine plena, ii) pressure/temperature amplification of backward propagating pressure waves to support autoignition and iii) weakening of flow pulsations due to strong pressure waves traveling downstream into the turbine plenum. For details we refer to [2]. The cross-sectional area of the diffusor in the combustion tube is given as:

$$A(x) = A_0 \begin{cases} 1, x \in [0, x_1] \\ 1 + (\alpha - 1) \dfrac{x - x_1}{x_2 - x_1}, x \in [x_1, x_2] \\ \alpha, x \in [x_2, L] \end{cases} \tag{6}$$

where A_0 represents the inflow cross-sectional area of the tube. Combined with the area ratio α, this allows to determine the outflow cross-sectional area $A_L = \alpha A_0$ at the exit of the tube. The diffusor section extends from position x_1 to x_2 (cf. 1).

Within the combustor the reactive quasi-onedimensional Navier-Stokes equations for multiple species are solved:

$$(\rho A)_t + (\rho u A)_x = 0, \tag{7}$$

$$(\rho u A)_t + \left(\left[\rho u^2 + p\right] A\right)_x = p A_x + \frac{4}{3} \nu_{\text{eff}} (\rho A u_x)_x, \tag{8}$$

$$(\rho E A)_t + \left(\left[\rho E + p\right] u A\right)_x = \lambda_{\text{eff}} (\rho A T_x)_x + D_{\text{eff}} \sum_s \left(h_s \rho A Y_{s,x}\right)_x, \tag{9}$$

$$\left(\rho A Y_s\right)_t + \left(\rho Y_s u A\right)_x = D_{eff} \left(\rho A Y_{s,x}\right)_x + \rho A \dot{\omega}_s, s = 1, \ldots, N_s - 1. \tag{10}$$

Here, ρ denotes density, u velocity, p pressure, T temperature, E total (mass-specific) energy (including kinetic and chemical energy), Y_s mass-fraction of species s, h_s (mass-specific) enthalpy of species s and $\dot{\omega}_s$ net production rate due to chemical reactions. We assume enhanced constant effective transport coefficients ν_{eff}, λ_{eff}, D_{eff} for kinematic viscosity, heat conductivity and mass-diffusivity to account for turbulence. To close the system, we consider the thermal equation of state for an ideal gas

$$p = \rho R_{\text{spec}} T, E = U + \frac{1}{2} u^2 \tag{11}$$

and the calorical equation of state

$$U = \sum_{k=1}^{N_s} Y_k u_k(T), u_k(T) = u_{k,\text{ref}} + \int_{T_{\text{ref}}}^{T} c_{v,k}(T')\,\mathrm{d}T', h_k(T) = h_{k,\text{ref}} + \int_{T_{\text{ref}}}^{T} c_{p,k}(T')\,\mathrm{d}T' \tag{12}$$

with total (mass-) specific internal energy $U = E - u^2/2$. Here, R_{spec} is the specific gas constant and the specific internal energy U of the mixture is the sum of the specific internal energies of each species weighted by their mass fractions. All caloric quantities and net production rates are computed from the reaction mechanism of Burke et al. [3] using the open-source software package Cantera [8]. Note that, since the gas is treated as calorically non-perfect (in contrast to [2]), the equations (2) and (4) for an adiabatic compression and expansion are only a good initial guess for an iteration to find the temperature ratio from the corresponding pressure ratio. However, a reversable adiabatic thermodynamic process for an ideal gas is governed by the fundamental equation

$$\mathrm{d}s = \frac{c_p}{T}\mathrm{d}T - R_{\text{spec}} \frac{\mathrm{d}p}{p} = 0, \tag{13}$$

which allows the iteration of the temperature for a given pressure ratio.

Ignition Delay time fitting for Charge Stratification

Appendix A of [2] outlines the control of ignition delay times τ_{ign} via temperature adjustments of the inflowing premixed gas. Using large activation energy asymptotics, the authors derive in [2] an analytical approximation for the ignition delay time as a function of initial temperature and fuel mass fraction of their simple one-step Arrhenius reaction model. Here, however, we utilize the complex

Burke et al. [3] reaction mechanism for hydrogen, which does not easily lend itself to such an analytical derivation. Therefore, we numerically compute ignition delay times over a relevant range of initial temperature and pressure values with the Burke et al. mechanism using Cantera and subsequently fit a polynomial to the data. Consistent with standard reaction kinetics, the relation for the ignition delay time is known to be of an Arrhenius-type

$$\tau_{\text{ign}} \propto \phi^{x} p^{y} \exp\left(\frac{E}{RT}\right), \tag{14}$$

which depends on the equivalence ratio ϕ, initial temperature T and pressure p. Following Zhao et al. [4], the influence of the equivalence ratio on the ignition delay time is less compared to the other two quantities. Therefore, we neglect this parameter dependence for the curve fitting and construct the following functional form for the ignition delay time:

$$\log_{10}\tau_{\text{ign}} = f\left(1/T, \log_{10} p\right) \tag{15}$$

We define the ignition delay time as the point at in time when the gradient of OH* concentration is maximal. Ignition delay times for a hydrogen/air mixture with equivalence ratio $\phi = 0.5$, a temperature range $T_0 \in (700\,\text{K}, 1100\,\text{K})$ and pressure $p \in (4\,\text{bar}, 8\,\text{bar})$ conditions are calculated. From this data, we perform a multivariate polynomial regression via linear regression to obtain a third-order polynomial fit in the form:

$$y = a_0 + b_0 x_1 + b_1 x_2 + c_0 x_1^2 + c_1 x_1 x_2 + c_3 x_2^2 + d_0 x_1^3 + d_1 x_1^2 x_2 + d_2 x_1 x_2^2 + d_3 x_2^3 \tag{16}$$

with $y = \log_{10}\tau_{\text{ign}}$, $x_1 = 1/T$ and $x_2 = \log_{10} p$. This polynomial exhibits a coefficient of determination of $R^2 = 0.99654$ and is depicted by the solid red line in Figure 2. For comparison, the original Cantera ignition delay times are included for $p = 4\,\text{bar}$ (blue, dash-dotted line), $p = 6\,\text{bar}$ (orange, dash-dotted line) and $p = 7\,\text{bar}$ (green, dotted line). The black dashed rectangle outlines the region of interest for our simulations which arranges in $T \in (980\ \text{K}, 1020\ \text{K})$ and $\tau_{\text{ign}} \in (2 \cdot 10^{-2}\ \text{s}, 5 \cdot 10^{-3}\ \text{s})$. Within this specific control region, the polynomial fit shows excellent agreement with the original data points.

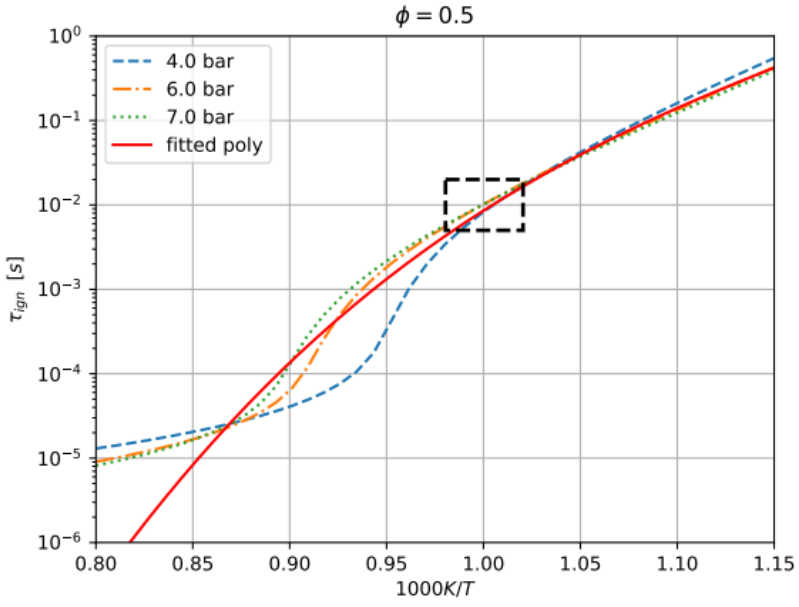

Figure 2. Polynomial fit from ignition delay time over inverse temperature for hydrogen/air mixture at equivalence ratio 0.5.

Results

We follow the simulation approach of Klein et al. [2], for their small-to-medium engine setup with a compressor pressure ratio of 6:1. We used the parameters from their Table 1 (cf. Table 1 below) as a starting point and ran simulations with the Burke et al. [3] hydrogen/oxygen reaction mechanism.

To achieve stable SEC operation, a few key adjustments compared to [2] are adopted the turbine's cross-sectional area are doubled and the air buffer duration is increased. As in [2], the fuel mixture's equivalence ratio is reduced to achieve an average turbine plenum temperature of approximately 1800 K in SEC mode. This resulted in injecting a lean mixture with an equivalence ratio $\phi_{\mathrm{SEC}}=0.5$. Factoring in dilution from the fresh air buffer during an inlet period, the simulation effectively operates with a mean equivalence ratio $\phi_{\mathrm{SEC},av}=0.355$. The complete set of parameters is detailed in Table 1.

Table 1. Mathematical models used for the corresponding physical processes and parameter settings

Physical Process	Mathematical Model
Reference Values	$T_{\mathrm{ref}}=300\,\mathrm{K}$, $p_{\mathrm{ref}}=10^5\,\mathrm{Pa}$, $R_{\mathrm{spec,ref}}=287.4\,\mathrm{J/kg\,K}$, $\rho_{\mathrm{ref}}=p_{\mathrm{ref}}/\left(R_{\mathrm{spec,ref}}T_{\mathrm{ref}}\right)=1.16\,\mathrm{kg/m^3}$, $l_{\mathrm{ref}}=1\,\mathrm{m}$, $u_{\mathrm{ref}}=\sqrt{\left(p_{\mathrm{ref}}/\rho_{\mathrm{ref}}\right)}=294\,\mathrm{m/s}$, $t_{\mathrm{ref}}=l_{\mathrm{ref}}/u_{\mathrm{ref}}=3.4\times10^{-3}\,\mathrm{s}$
	combustor: $D=5\,\mathrm{cm}$, $A_0=\pi D^2/4$
Turbulent transport	$\nu_{\mathrm{eff}}=0.44\,\mathrm{m^2/s}$, $Pr=Sc=1:D_{\mathrm{eff}}=\nu_{\mathrm{eff}}$, $\lambda_{\mathrm{eff}}=\nu_{\mathrm{eff}}\rho_{\mathrm{eff}}c_p$
Chemical model	hydrogen/oxygen kinetic model for high-pressure combustion from Burke et al. [3] with 11 Species and 27 reactions
	$\phi_{\mathrm{DEFL}}=0.4$, $\phi_{\mathrm{SEC}}=0.5$, air buffer time: 0.204 ms
Compressor	compressor exit area: $A_{\mathrm{exit,C}}/A_0=8$
Compressor plenum	torus with cross-sectional area: $A_{\mathrm{pl,C}}/A_0=4$, length: $L_{\mathrm{pl,C}}/l_{\mathrm{ref}}=5$
Combustor	parameter for the diffusor, see eq.(6): $\alpha=4$, $x_1=0.2\,\mathrm{m}$, $x_2=0.65\,\mathrm{m}$, $L=1\,\mathrm{m}$
Turbine plenum	torus with cross-sectional area: $A_{\mathrm{pl,T}}/A_0=8$, length: $L_{\mathrm{pl,T}}/l_{\mathrm{ref}}=5$
Turbine	cross-secctional area: $A_{\mathrm{entry}}/A_0=0.6104$, $C_{\mathrm{T}}\sqrt{R_{\mathrm{spec,ref}}}=0.5505$

Figure 3 shows key results from the SEC simulation. While in the upper left panel the compressor plenum (blue) stays constant at 6 bar, due the fixed pressure ratio, a pressure gain in the turbine plenum (red) to approx 6.1 bar can be seen, which qualitatively corroborates the results based on one-step Arrhenius kinetics in [2]. This stays in contrast to the classical deflagration combustion (not shown) which exhibits a design-inherent small pressure drop towards the turbine plenum consistent with the Brayton/Joule-cycle taking into account that the mean flow Mach number is low but non-zero.

As mentioned above, the inflow mixture's equivalence ratio was precisely adjusted to reach a target turbine plenum temperature of 1830 K, shown in the upper right panel with a red line. Due to the constant pressure ratio of the compressor the compressor plenum temperature remains constant at 487 K.

The lower-left panel of Figure 3 indicates that the compressor (blue line) consistently requires around 0.1 MW of power input. Conversely, the turbine (red line) generates more power, resulting in a higher extractable output power for the SEC mode, reaching 0.3 MW (the difference between turbine and compressor power).

Finally, the lower-right panel, represented by a red line, shows the thermal efficiency of the engine, calculated as the ratio of power output to mean chemical energy. As described in [2], we used a 0.34-second moving average window for efficiency, revealing a consistent overall efficiency of 47.3 %. Revealing that the efficiency for the Brayton-Joule cycle can be estimated only by the compressor plenum temperature as $\eta_{\mathrm{B/J}}=1-T_1/T_2=1-300/487=0.384$ (see for example [2]). The efficiency reached with the SEC is significantly higher than the estimated 38.4 %.

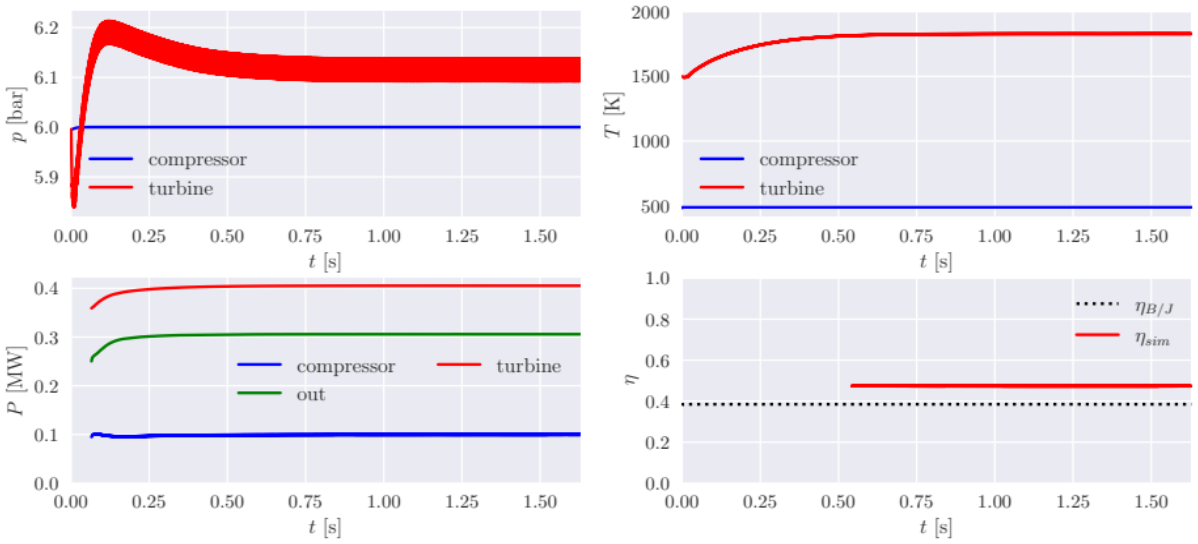

Figure 3: Selected time evolutions taken from the SEC simulation

As illustrated in Figure 4, the space-time diagrams span the period from t~1.5 s to t~1.505 s, thereby demonstrating the inherent near-periodicity of the Shockless Explosion Combustion (SEC) process. The diagrams illustrate, from right to left, the normalized mass fraction of hydrogen, the Mach number, the temperature, and a scaled pressure. In view of the substantial pressure range, which extends from approximately 4 bar (during fuel mixture filling) to 20 bar (post-ignition), the visualization method employed by Klein et al. [2] has been adopted. The scaled pressure $\sqrt{\log(p/\mathrm{Pa})}$ is displayed rather than the raw pressure itself. This transformation facilitates the distinction of phenomena within the combustor. Specifically, the red colouring is indicative of pressure waves that are propagating in the rightward direction following the combustion of the fuel mixture. These waves subsequently reflect at the open end as suction waves, which then transition from green to dark blue as they travel back towards the inflow section of the tube. The value range of the scalar field is centred such that its midpoint corresponds to the $\sqrt{\log(6\,\mathrm{bar}/\mathrm{bar})}$, which is approximately 1.34.

Consider, for instance, the period commencing at t=1.501 s. A filling phase is already underway, indicated by the blue coloring of the pressure scalar field, signifying that the combustor pressure is below that of the compressor plenum. As a consequence, fresh air at approximately 500 K enters the combustor. This air buffer is followed by a temperature-stratified hydrogen/air mixture initially entering at 970 K and raised until 985 K. Doing so implies that the ignition delay is reduced from 15.2 ms to 14.4 ms. It is notable that the pressure dependence of the ignition delay time is minimal within this temperature range (cf. Figure 2). Furthermore, these ignition delay times of 15 ms are significantly longer than the firing period of approximately 1.33 ms (corresponding to 750 Hz). While a typical pressure wave cycle (a left-to-right and back traversal, as seen in Figure 2's pressure field) normally takes 2.66 ms, a double-firing mode has been established, as discussed in detail in Klein et al. [2].

However, as revealed by the pressure and temperature fields, the fuel/air mixture ignites in a nearly auto-homogeneous manner at approximately t=1.5018 ms. This is preceded by a weak pressure wave (around 7 bar) originating from right to left, exiting the diffusor at 1.5015 ms (as indicated by near zero values in the Mach number plot). This weak pressure wave's passage is also evident through its effect on temperature, elevating it to approximately 1150 K. Merely fractions of a second after this weak pressure wave reaches the combustor inlet on the left, the inflow valve closes. Subsequently, the pressure transitions to deep red and the temperature field to yellow, triggering the ignition of the entire mixture. From Figure 2, it can be deduced that at $p=7\,\mathrm{bar}$ and $T=1150\,\mathrm{K}$, the mixture's ignition delay time is approximately 0.026 ms. This implies that the weak pressure wave or the associated preheating is sufficient to exploit the substantial, two orders of magnitude decrease in ignition delay times. Following the mixture's ignition, the pressure wave propagates to the right, and the ensuing suction wave initiates another filling period.

Analysis of the Mach number plot in Figure 4 reveals that the combustor consistently operates within the subsonic regime. While the highest Mach numbers are observed during the near-homogeneous auto-ignition of the fuel/air mixture, the integrated diffusor effectively damps these elevated flow Mach number. As a result, the flow at the combustor exit maintains at a Mach number below 0.5.

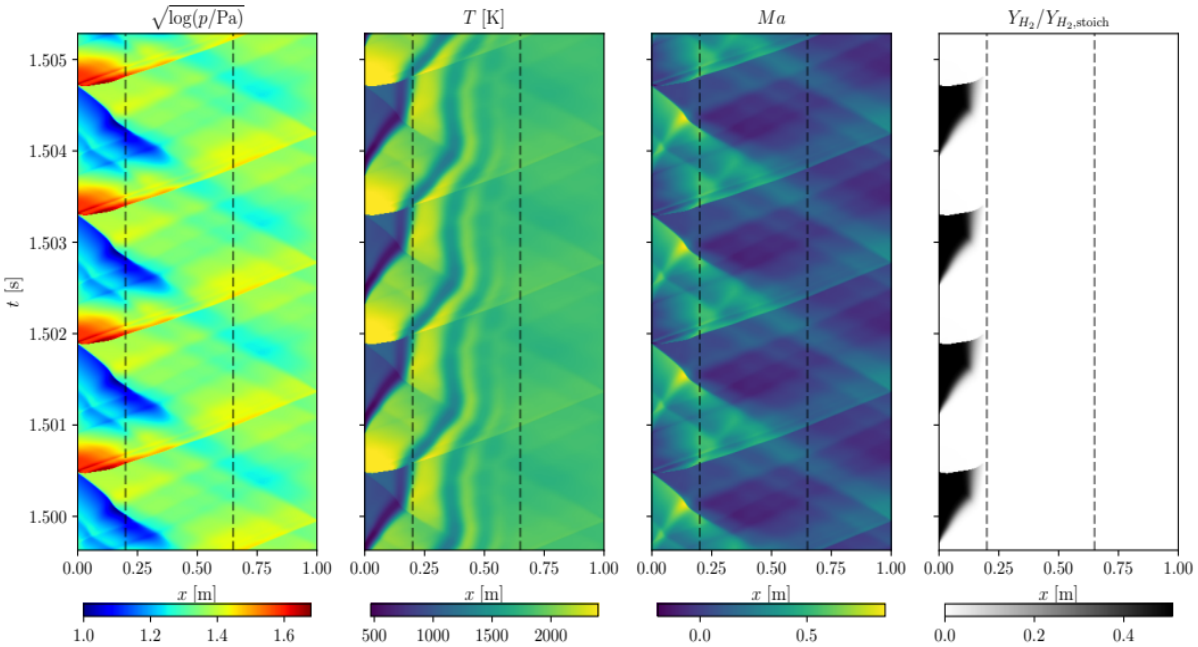

Figure 4: Space-time diagrams for the SEC simulation, where the black dashed lines indicate the beginning and end of the diffusor section.

Summary

This research investigates the feasibility of using hydrogen as a fuel in Shockless Explosion Combustion (SEC) for gas turbines, a Pressure Gain Combustion (PGC) method designed to significantly boost efficiency by mimicking the Humphrey cycle. Unlike conventional Brayton-Joule cycle engines, which come with neither a pressure rise upon combustion nor an overall pressure gain across the combustor, an SEC-driven system achieves both a local pressure rise before and during combustion, and an overall pressure gain between compressor and turbine plenum. Significant efficiency gains relative to the classical Brayton-Joule-cycle of about 23% have been demonstrated in a simplified quasi-onedimensional full engine simulation model.

The study employed a full engine computational model, notably incorporating the detailed hydrogen/oxygen kinetic mechanism of Burke et al. [3]. Ignition delay times for charge stratification were numerically computed and fitted to a polynomial. The combustor design included a diodic valve, air buffer, and a diffusor, with specific adaptations for hydrogen operation (doubled turbine area, increased air buffer duration at a 6:1 compressor pressure ratio as compared to the corresponding setup from Klein et al. [2]).

Simulations confirmed a pressure gain in the turbine plenum, characteristic of the Humphrey cycle. Turbine plenum temperature was maintained at ~1800 K by adjusting the equivalence ratio ($\phi_{\mathrm{SEC},av}=0.355$, averaged with air buffer). Crucially, overall SEC efficiency with hydrogen reached approximately 47.3 %, which is significantly higher than 38.4 % of a classical Brayton-Joule cycle for the same operation point. Spatio-temporal analysis revealed a nearly-periodic cycle of homogeneous auto-ignition, initiated by a weak pressure wave that preheats the mixture, enabling rapid and near-simultaneous ignition.

Future work could involve a parameter study to further investigate the pressure gain observed in the turbine plenum. Additionally, a detailed analysis of the internal thermodynamic processes, e.g. by following individual mass parcels as in [2], would provide deeper insights into the sources of

efficiency gains and losses. From a computational perspective, incorporating a simpler hydrogen reaction mechanism, such as the recently proposed by Merino et al. [12], holds significant promise for reducing CPU-time. This would be particularly advantageous for increasing domain dimensions, like extending the simulation to a 2D representation of the turbine plena as seen in [2].

Acknowledgements
The authors thank Deutsche Forschungsgemeinschaft for funding under grant CRC 1029 "Substantial efficiency increase in gas turbines through direct use of coupled unsteady combustion and flow dynamics," Project No. 200291049, subprojects A03 and C01.

Literatur

[1] Bobusch B. C., Berndt P., Paschereit C. O., Klein R.: *Shockless Explosion Combustion: An Innovative Way of Efficient Constant Volume Combustion in Gas Turbines,* Combustion Science and Technology, 186(10–11), 1680–1689, 2014, https://doi.org/10.1080/00102202.2014.935624

[2] Klein R., Nadolski M., Zenker C., Oevermann M., Paschereit C. O.: *Pressure Gain Combustion for Gas Turbines: Analysis of a Fully Coupled Engine Model,* ASME. J. Eng. Gas Turbines Power, 147(2): 021003, 2025, https://doi.org/10.1115/1.4066348

[3] Burke M.P., Chaos M., Dryer Y. Ju, F.L., Klippenstein S.J.: *Comprehensive H2/O2 kinetic model for high-pressure combustion,* Int. J. Chem. Kinet., 44: 444-474, 2011, https://doi.org/10.1002/kin.20603

[4] Zhao, Z., Chen, Z. & Chen, S: *Correlations for the ignition delay times of hydrogen/air mixtures,* Chin. Sci. Bull, 56, 215–221, 2011, https://doi.org/10.1007/s11434-010-4345-3

[5] Paxson Dan: *Pressure-Gain Combustion for Gas Turbines*, INSPIRE Capstone Symposium, Florence, Italy, 2024 https://ntrs.nasa.gov/citations/20240010842, last visited 15.07.2025

[6] Zheng R., Gong E., Li, J., Yao, Q., Nie, Z.: *Performance Analysis of Wave Rotor Combustor Integration into Baseline Engines: A Comparative Study of Pressure-Gain and Work Cycles*, Energies, 17, 2074, 2024, https://doi.org/10.3390/en17092074

[7] Heiser W. H and Pratt D. T.: *Thermodynamic cycle analysis of pulse detonation engines,* J. Propul. Power, 18(1):68–76, 2002

[8] Goodwin D. G., Moffat H. K., Schoegl I., Speth R. L., and Weber B. W., *Cantera: An Object-oriented Software Toolkit for Chemical Kinetics*, Thermodynamics and Transport Processes (Version 3.1.0) [Computer software], 2024, https://doi.org/10.5281/zenodo.14455267

[9] Stathopoulos P.: *An alternative architecture of the Humphrey cycle and the effect of fuel type on its efficiency,* Energy Sci Eng.,8:3702–3716, 2020, https://doi.org/10.1002/ese3.776

[10] Berndt P., Klein R.: *Modeling the kinetics of the Shockless Explosion Combustion*, Combustion and Flame, Volume 175, 16-26, 2017, https://doi.org/10.1016/j.combustflame.2016.06.029.

[11] Tornow, G., Klein, R.: *A 1D Multi-Tube Code for the Shockless Explosion Combustion,* In: King, R. (eds) Active Flow and Combustion Control 2018, Notes on Numerical Fluid Mechanics and Multidisciplinary Design, vol 141, Springer, Cham., 2019, https://doi.org/10.1007/978-3-319-98177-2_20

[12] Millán-Merino A., Boivin P: *A new single-step mechanism for hydrogen combustion*, Combustion and Flame, Vol. 268, 113641, 2024, https://doi.org/10.1016/j.combustflame.2024.11364

CFD-Simulation einer H_2 - Feuerung in Industriekesseln

W.Timm[1], B. Zimmermann[1]

[1] *Power Service Solutions GmbH, Schifferstraße 80, 47059 Duisburg*

Abstract

Wasserstoff wird für verschiedene Anwendungen als Ersatz für fossile Brennstoffe geplant. Durch seine hohe Reaktivität entstehen jedoch verschiedenste Herausforderungen bei der Umrüstung bestehender Anlagen. Bei der Power Service Solutions GmbH wurden verschiedene Konzepte untersucht, um erdgasgefeuerte Anlagen in Zukunft mit Wasserstoff zu betreiben. Dazu wurden auch diverse CFD-Simulationen durchgeführt.

Zur Validierung wird zunächst eine vermessene H_2-Laborflamme [1] mittels CFD simuliert, um die Temperatur und den NO_x-Gehalt zu bestimmen. Dabei kommt ein reduzierter Mechanismus zum Einsatz [2], der nur die wesentlichen Reaktionen der Oxidation von Wasserstoff berücksichtigt.

Diese Modellierung wird auf verschiedene industrielle Anlagen übertragen, die im Rahmen einer Studie untersucht bzw. bereits gebaut wurden. Bei großtechnischen Anlagen besteht zusätzlich die Herausforderung, dass durch die Komplexität der Strömung mehrerer Brenner oftmals Modifikationen am Turbulenzmodell zur Kalibrierung der Turbulenz-Chemie-Interaktion gemacht werden müssen [3,4]. Die gemessenen Werte für NO_x bzw. die Rauchgastemperatur werden zur Modellkalibrierung herangezogen. Es werden verschiedene Lastfälle für H_2 und Erdgas/H_2 als Mischfeuerung am Beispiel industrieller Dampferzeuger unterschiedlicher Größen und Leistung betrachtet.

Es zeigt sich, dass die reine Wasserstofffeuerung im Hinblick auf die NO_x-Produktion durch eine Rauchgasrezirkulation gesteuert werden kann. Hierbei kommen verschiedene Brennertypen mit unterschiedlicher Rauchgasrückführung zum Einsatz.

Im Vergleich zur reinen Erdgasflamme bzw. Mischfeuerung sind bei der reinen H_2-Feuerung allerdings höhere Rezirkulationsgasmengen erforderlich, da durch die besonderen Eigenschaften der Wasserstofflamme (v.a. Temperatur, hohe Geschwindigkeit) die Bildung von thermischen NOx-Emissionen begünstigt wird.

1. Einleitung

Im Zuge der Umstellung von fossilen Brennstoffen auf alternative Energiequellen ist insbesondere die Verbrennung von Wasserstoff in den Fokus der industriellen Energieerzeugung gerückt. Erste Umrüstungen von bestehenden Anlagen von Erdgas auf Wasserstoff finden vermehrt statt bzw. werden auf Machbarkeit untersucht. Mit seiner hohen Verbrennungstemperatur stellt Wasserstoff allerdings auch eine Herausforderung für die Einhaltung von NOx-Grenzwerten dar. Hier kommt CFD-Simulationen als Werkzeug zur Vorab-Analyse von Feuerungskonzepten eine besondere Bedeutung zu. Ziel der vorliegenden Studie ist die Entwicklung eines Konzepts zur numerischen Simulation von Flammen in Wasserstoff- bzw. Wasserstoff/Erdgas-Feuerungen, das belastbare Vorhersagen zur Temperaturverteilung und NOx-Emissionen machen kann, wobei aber gleichzeitig der Rechenaufwand in realistischem Rahmen bleiben soll.
Zunächst wird ein Versuchsbrenner nachgebildet, der aufgrund reproduzierbarer Laborbedingungen eine genaue Simulation der Strömungsverhältnisse bei gleichbleibenden Brennstoff- und Verbrennungsluftmassenströmen ermöglicht. Hierdurch ist eine zielgerichtete Auswahl einer Verbrennungskinetik möglich, da Störeinflüsse weitgehend ausgeschaltet sind. Es wird der am IMFT in

Toulouse [1] entwickelte HYLON (Hydrogen Low NOx)-Brenner betrachtet, der in Abbildung 1 dargestellt ist.

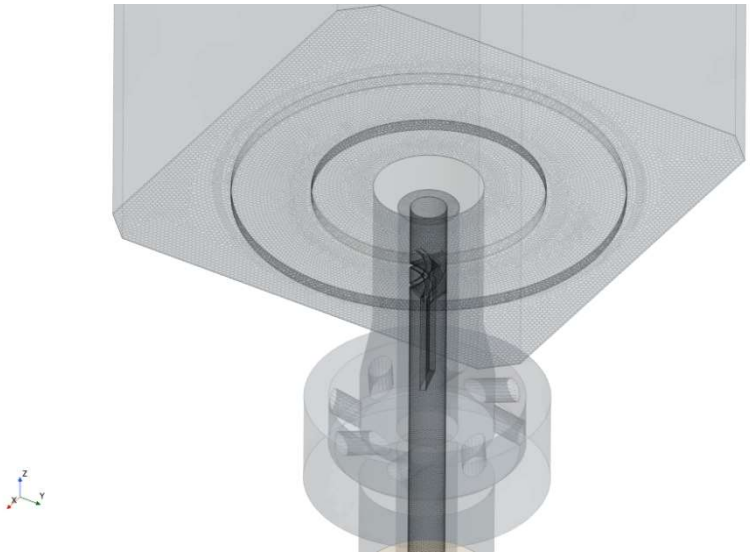

Abbildung 1. Geometrie des HYLON-Brenners [1], [10]

Dieser im Rahmen des TNF-Workshops als CAD-Geometrie mit Messwerten für Temperaturen und NOx-Werten zur Verfügung gestellte Brenner [10] ermöglicht die Realisierung verschiedener Flammenformen. Zum einen kann eine direkt am Brenner anliegende Flamme (Flamme A) mit einer thermischen Leistung von P_{th} = 4 kW erzeugt werden, ebenso ist eine abgelöste, aber hydrodynamisch stabilisierte Flamme (Flamme L) mit einer Leistung von 10 kW möglich [1]. Diese zwei Flammentypen zeichnen sich durch unterschiedliche Werte der NOx-Emissionen aus, so dass eine Auswahl eines geeigneten Turbulenz- bzw. Chemiemodells mitsamt zugehöriger Interaktion erfolgen kann, die beide Zustände möglichst gut abdeckt. Dieses Modell wird zur Simulation eines industriellen Dampferzeugers mit zwei Brennern, mit je 8 Gaslanzen verwendet, der bei einer thermischen Leistung von ~80 MW eine Dampfleistung von 100 t/h erreicht. Dieser ist als 3D CAD-Modell in der folgenden Abbildung dargestellt.

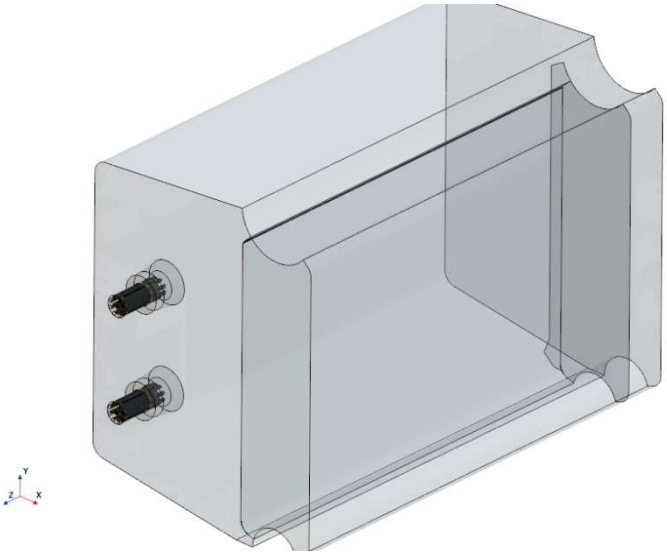

Abbildung 2. Geometrie des Dampferzeugers

Im Gegensatz zur Erdgasverbrennung kann der kinetische Mechanismus der Oxidation von Wasserstoff durch eine wesentlich geringere Anzahl an Einzelreaktionsschritten beschrieben werden, da keine langkettigen Verbindungen bzw. deren Zerlegung in verschiedenste Zwischenprodukte beschrieben werden muss. Selbst Methan braucht eine deutlich höhere Anzahl von Reaktionsschritten als reiner Wasserstoff. Dessen Verbrennungsmechanismus stellt im Grunde eine Untermenge der Reaktionen der Erdgasverbrennung dar, wie z.B. von Zettervall dargestellt [8]. Dieser beschreibt die Kinetik des H_2/O_2-Mechanismus als ein System von ca. 20 Einzelreaktionen in vier Untersystemen, wobei neben den beiden Ausgangsstoffen und dem Reaktionsprodukt Wasser die Zwischenprodukte bzw. -radikale HO_2, H_2O_2, OH, und O von Bedeutung sind. Die letzteren beiden sind wiederum entscheidende Faktoren für den Mechanismus der thermischen NOx-Bildung nach Zeldovich.
Zur Modellierung der Verbrennung von Erdgas bzw. Wasserstoff sowie NOx-Bildung wurden verschiedene Kinetiken entwickelt, die entweder als reduzierter Mechanismus die wesentlichen Zwischenreaktionen beschreiben z.B. in [2] oder als globaler Mechanismus direkt die Umsetzung der Ausgangsstoffe in die Endprodukte in wenigen Schritten formulieren [5,6,7,9]. Die aufwendigsten Systeme mit 50 oder mehr Spezien und Hunderten von Unterreaktionen stellen die leistungsfähigsten Kinetiken dar [11-13], benötigen jedoch auch den höchsten numerischen Aufwand. In der vorliegenden Studie wurde ein kombinierter Ansatz gewählt, bei dem nur die Verbrennung von Methan und Wasserstoff mit einem ausführlicheren Mechanismus beschrieben wird und die im Brenngas des industriellen Dampferzeugers enthaltenen längeren Kohlenwasserstoffe mit dem globalen Ansatz nach Jones und Lindstedt modelliert werden [6].

2. Simulation der HYLON-Flamme

Im Rahmen von Testrechnungen stellte sich heraus, dass zur Berechnung der NOx-Emissionen eine auf die Wasserstoffreaktionen reduzierte Version des San-Diego-Mechanismus [11] und die von Conaire et. al. [2] entwickelte Kinetik im Zusammenspiel mit dem ebenfalls an der Universität San Diego entwickelten NOx-Mechanismus vergleichbare Ergebnisse lieferten. Im Folgenden sind die Ergebnisse dargestellt, die mit dem San-Diego-Gesamtsystem aus Verbrennungs- und NOx-Kinetik erhalten wurden, da dieses den Vorteil einer konsistenten Datenbasis aus einer Quelle bietet. Für die Turbulenz-Chemie -Interaktion wird das Eddy-Dissipation-Concept Modell mit den bekannten Standardparametern zusammen mit einem elliptischen k-epsilon Modell verwendet. Aufgrund der vergleichsweisen einfachen Strömung mit relativ niedriger Reynoldszahl im Vergleich zu einer hochturbulenten Feuerraumströmung mit mehreren Brennern wird davon ausgegangen, dass dieser Ansatz zur Auswahl der NOx-Kinetik bzw. Verbrennungschemie komplett ausreichend ist, zumal eine detaillierte transiente Simulation mit bspw. einem LES-Modell bei einer realen Kesselgeometrie aus Gründen der Rechenzeit nicht praktikabel wäre. Der Einfluss der Strahlung wird durch das Diskrete-Ordinaten-Modell berücksichtigt.
Beim HYLON-Brenner wird ein zentraler Wasserstoffstrom über einen Drallkörper in eine ebenfalls drallbehaftete umgebende Oxidationsluftströmung geleitet. Beide Ströme haben jeweils Umgebungstemperatur. Eine genaue Beschreibung des Versuchsaufbaus kann [1] bzw. [10] entnommen werden. Die Hauptparameter der jeweiligen Flammenkonfiguration finden sich in Tabelle 1.

Tabelle 1. Parameter der Flammen A und L

Flamme	P_{th} [kW]	V_{H2} [m/s]	V_{Luft} [m/s]	T [°C]
A	3,89	13,6	11,4	25
L	9,73	34,0	28,5	25

Eine Möglichkeit zur Visualisierung der Flammenform besteht in der Methode der Chemolumineszenz, bei der die Verteilung der OH-Radikale optisch sichtbar gemacht wird, was in industriellem Maßstab z.B. bei Daurer et. al. [4] beschrieben wird und ebenfalls beim HYLON Versuchsaufbau zum Einsatz kommt. In Abbildung 3 und 4 ist dies für die beiden untersuchten Flammentypen dargestellt.

Ein Vergleich von gemessener und simulierter Verteilung der OH-Radikalkonzentration zeigt eine deutliche Übereinstimmung der Flammenform, so dass davon ausgegangen werden kann, dass beide Flammen im CFD-Modell prinzipiell richtig wiedergegeben werden.

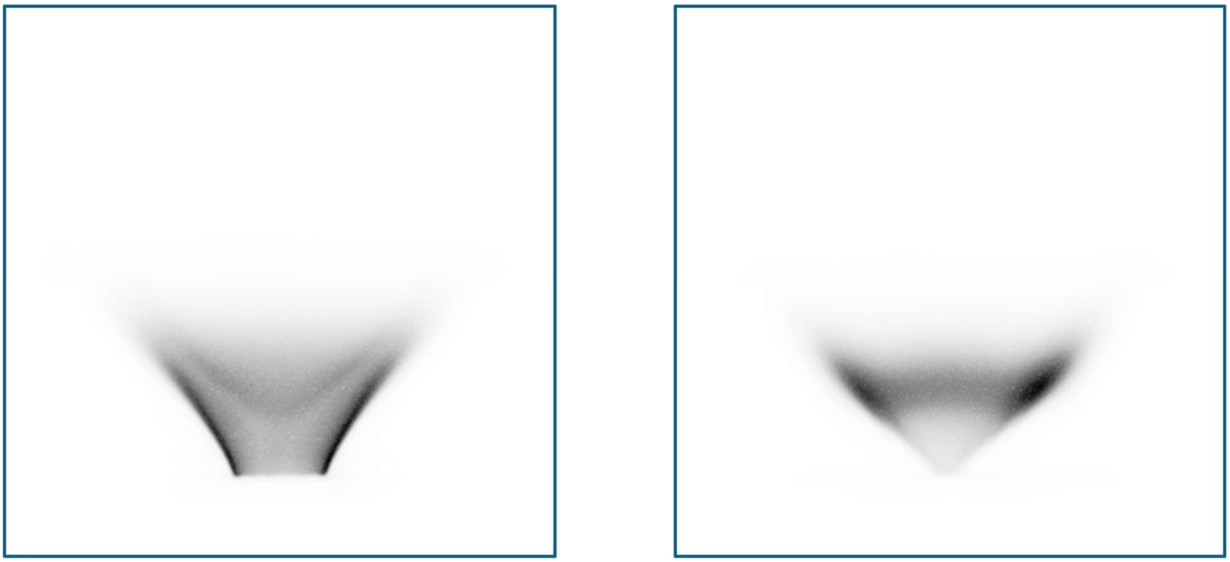

Abbildung 3. Flamme A (links) und L (rechts) in OH*-Radikalverteilungsdarstellung [1]

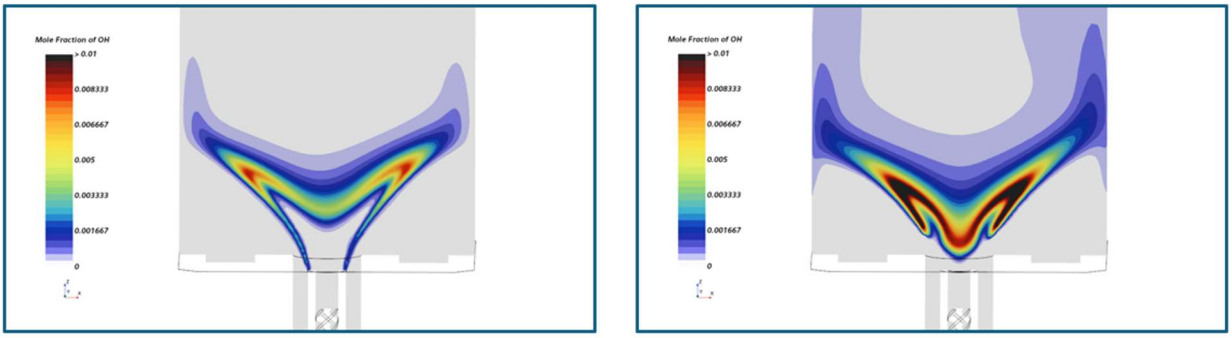

Abbildung 4. CFD-Simulation der OH*-Radikalkonzentration

Der grundsätzliche Unterschied in den beiden Flammentypen spiegelt sich auch in der Temperaturverteilung bzw. dem NOx-Verlauf wider. Die gemessene bzw. simulierte Temperatur sowie der NO-Wert am Auslass (ppm, wasserfrei) ist in der Tabelle 2 aufgeführt. (NO_2 wurde getrennt ermittelt, liegt aber in beiden Fällen auf vernachlässigbarem Niveau.)

Tabelle 2. Temperatur und NO-Emission der Flammen A und L am Austritt

Flamme	NO gemessen [ppm]	NO berechnet [ppm]	T gemessen [K]	T berechnet [K]
A	12,1	15,7	~1170	~1207
L	6,2	5,3	~1360	~1321

Es fällt auf, dass bei der Flamme mit höherer thermischer Leistung und Temperaturniveau ein deutlich niedrigerer NO-Wert vorliegt, was der Tatsache geschuldet sein dürfte, dass es in der heißesten Zone der Flamme zu anderen Verweilzeiten und Reaktionsraten im abgelösten Fall L aufgrund unterschiedlicher Rezirkulationsströmung kommt. Da dieses auf den ersten Blick unerwartete Ergebnis

der Messung auch in der Simulation genauso wiedergegeben wird, kann davon ausgegangen werden, dass das hier verwendete CFD-Modell Wasserstofflammen mit ausreichender Genauigkeit beschreibt. In den nachfolgenden Abbildungen 5 und 6 sind die Temperatur und NOx-verläufe für beide Flammen einander gegenübergestellt.

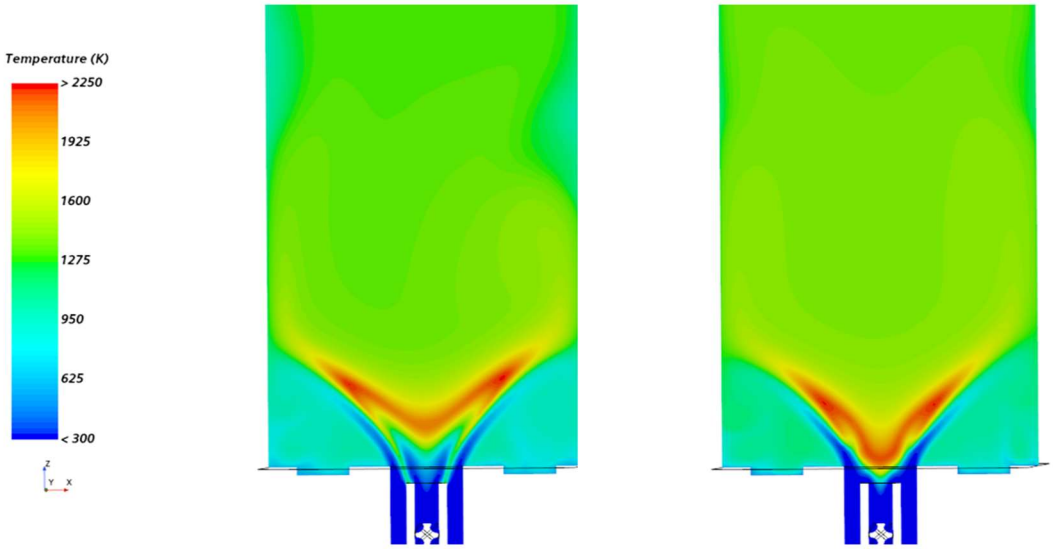

Abbildung 5. Temperaturverlauf von Flamme A (links) und L (rechts)

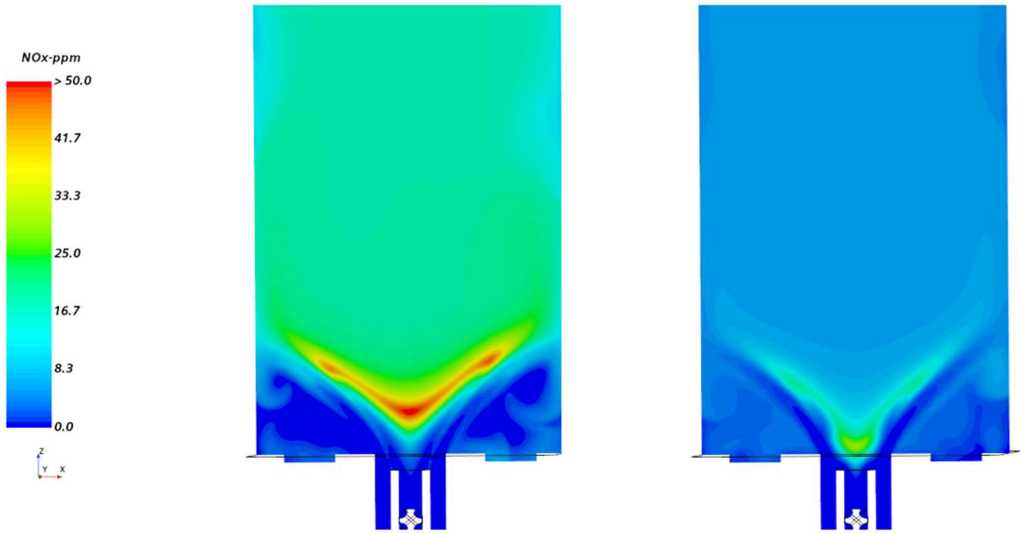

Abbildung 6. NOx-Verteilung von Flamme A (links) und L (rechts)

3. Simulation eines industriellen Dampferzeugers mit 80 MW thermischer Leistung

Aufgrund der guten Übereinstimmung des Modells mit den Messwerten des Laborbrenners werden die genutzten CFD-Modelle auch für die Simulation des hier vorgestellten Dampferzeugers genutzt, wobei aber noch einige Zusatzannahmen gemacht werden müssen. Im Gegensatz zu einem Laborbrenner ist auf industriellen Anlagen von einer nicht vernachlässigbaren Menge an Kohlenwasserstoffen selbst im Falle von scheinbar „reinem“ Wasserstoffbetrieb auszugehen. Außerdem bleibt Erdgas im Mischbetrieb weiter ein wichtiger Brennstoff, so dass in der Realität verschiedene Lastfälle mit variierendem

Wasserstoffanteil erfolgreich gefahren werden müssen. Bei den Abnahmetests der gezeigten Anlage wurden 4 Lastfälle mit steigendem Wasserstoffanteil geprüft, wobei Lastfall P1 reiner Erdgasbetrieb ist. In der Tabelle 3 sind die wesentlichen Betriebsparameter aufgeführt, sowie in der letzten Spalte der Mittelwert der gemessenen NOx-Werte im Rauchgas bezogen auf 3% Sauerstoff. Der Fall mit maximalem Wasserstoffanteil von 95 Vol. % enthält 5 Vol. % Erdgas, was aufgrund des Dichteunterschiedes zu einem immer noch signifikanten Beitrag des Erdgases zur thermischen Leistung führt. Um dies in der chemischen Kinetik zu berücksichtigen, werden die Methan-Reaktionen des San-Diego Mechanismus mitberücksichtigt und die Reaktionen höherer Kohlenwasserstoffe wie eingangs erwähnt in einer Ein-Schritt-Aufspaltung in CO und H_2 mit Lindstedt-Jones-Kinetik [6] modelliert.

Tabelle 3. Lastfälle des Dampferzeugers bei Abnahmetest

Lastfall	H_2-anteil [%]	Luftzahl	Rezi Mass. [%]	P_{th} [MW]	Dampf [t/h]	NOx gemessen [ppm tr.]
P1	0	1,11	5,3	73	94	43
P2	50	1,08	12,0	78	103	42
P3	75	1,07	16,2	77	102	42
P4	95	1,08	21,1	67	88	41

Die Limitierung des H_2-Anteils auf 95% ergibt sich bei dieser Anlage (Dampferzeuger einer Raffinerie) dadurch, dass als Betriebsmittel neben Erdgas ein sogenanntes „Rich Gas“ zur Verfügung steht, dass neben 95% Wasserstoff auch noch 0,6% Methan und jeweils ca. 1,6% Ethan und Propan und geringe Mengen höherer Kohlenwasserstoffe enthält. Der eigentliche Brennstoff wird durch die Mischung von Rich Gas und Erdgas bereitgestellt. Die Zusammensetzung des hier eingesetzten Erdgases ist in Tabelle 4 angegeben.

Tabelle 4. Zusammensetzung des Erdgases

Komponente	CH_4	C_2H_6	C_3H_8	C_4H_{10}	CO_2	N_2
Vol.-Anteil [%]	91,32	5,69	0,45	0,02	1,89	0,63

Bei den Emissionsmessungen wurden bei allen vier Lastfällen sehr ähnliche NOx-Werte festgestellt. Dies konnte dadurch erreicht werden, dass mit zunehmendem Wasserstoffanteil eine höhere Menge an Rauchgas rezirkuliert und der Verbrennungsluft beigemischt wurde. Für reines Erdgas ist bereits ein Rezi-Anteil von 5% ausreichend (Volumenstrom Rauchgas bezogen auf Frischluftvolumenstrom), wohingegen bei nahezu reinem Wasserstoff aufgrund der deutlich höheren Flammentemperatur ein Rezi-Anteil von 21% erforderlich ist. Ein Indiz für den Einfluss des Wasserstoffanteils auf die Flammentemperatur insbesondere im Brennernahbereich lieferten die Daten von Thermoelementen, die am unteren Brenner vorne an der Brennerkehle in 12 Uhr Position befestigt waren. Diese sind in der folgenden Abbildung zusammen mit der vom CFD-Modell berechneten Temperaturverteilung dargestellt.
Man erkennt deutlich, dass ein Unterschied von mehr als 200K bei Wasserstoffbetrieb im Vergleich zu reinem Erdgas vorliegt, was sich auch sehr gut mit den Daten der Messungen deckt. Auch die maximalen Temperaturen der eigentlichen Flamme sind bei Wasserstoffbetrieb höher, obwohl durch die Rauchgasbeimischung der Sauerstoffgehalt der Verbrennungsluft bereits deutlich abgesenkt ist.

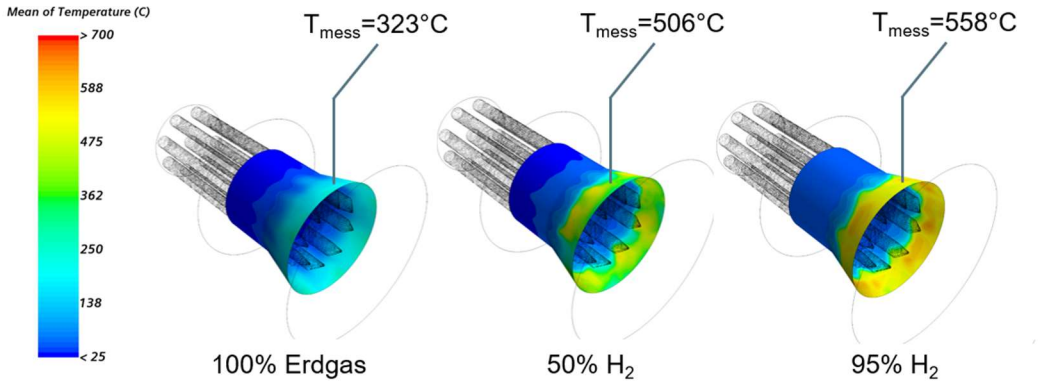

Abbildung 7. Temperatur der Brennerkehle in Abhängigkeit des H_2-Anteils

Eine Gegenüberstellung der Temperaturverteilung im Feuerraum auf zwei Schnittebenen für jeweils Erdgas- und Wasserstoffbetrieb findet sich in der folgenden Abbildung 8. Man erkennt, dass im Vergleich zu Erdgas die Wasserstoffflamme schlanker und etwas heißer ist, wobei die Temperaturerhöhung aufgrund der hier deutlich höheren Rauchgasrezirkulation vergleichsweise moderat ausfällt. Eine Testrechnung mit ebenfalls 5% Rauchgasrezirkulation zeigte sehr viel höhere Temperaturen bei doppelt so hohen NOx-Werten.

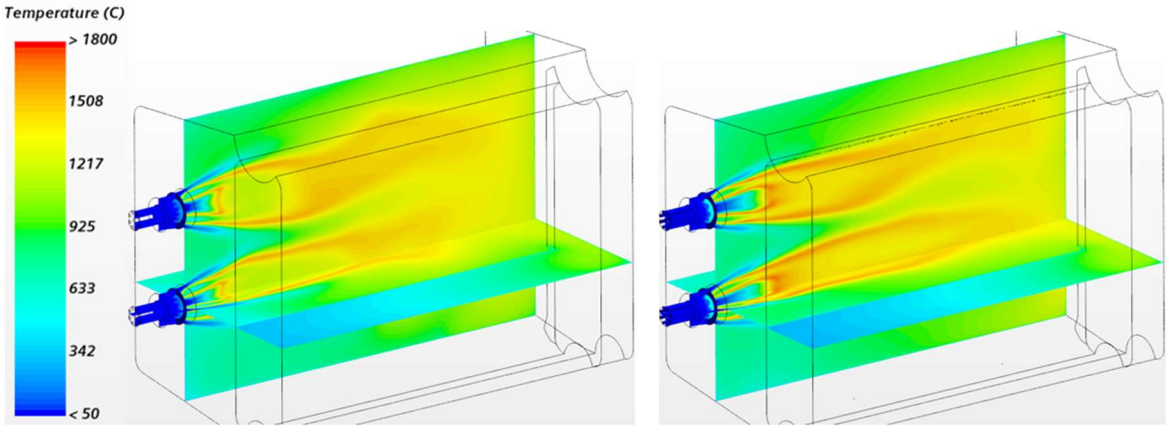

Abbildung 8. Flammentemperatur bei Erdgas- (P1, links) und Wasserstoffbetrieb (P4, rechts)

Für die Bildung von Stickoxiden ist die Gastemperatur natürlich ein entscheidender Faktor, der aber durch die Zumischung von sauerstoffarmem Rauchgas so reguliert wird, dass im Betrieb in allen Lastfällen ein Niveau von im Mittel 40 bis 43 ppm erreicht wurde, was auch vom verwendeten CFD-Modell gut wiedergegeben wurde. Eine Abweichung mit beim CFD-Modell etwas zu geringen NOx-Werten lag lediglich beim reinen Erdgasfall vor, was hier auf die Verwendung des San-Diego Mechanismus zurückzuführen sein dürfte, da dieser aufgrund seiner Performance für die Wasserstoffflamme des Laborbrenners ausgewählt wurde. Tatsächlich zeigte eine weitere Rechnung des Erdgasfalles mit dem Gri-Mech-2.11 Mechanismus, der gezielt auf Methanverbrennung hin optimiert wurde [13], höhere und realistischere Werte.
In Abbildung 9 ist die NOx-Verteilung der Fälle P1 und P4 im Vergleich dargestellt.

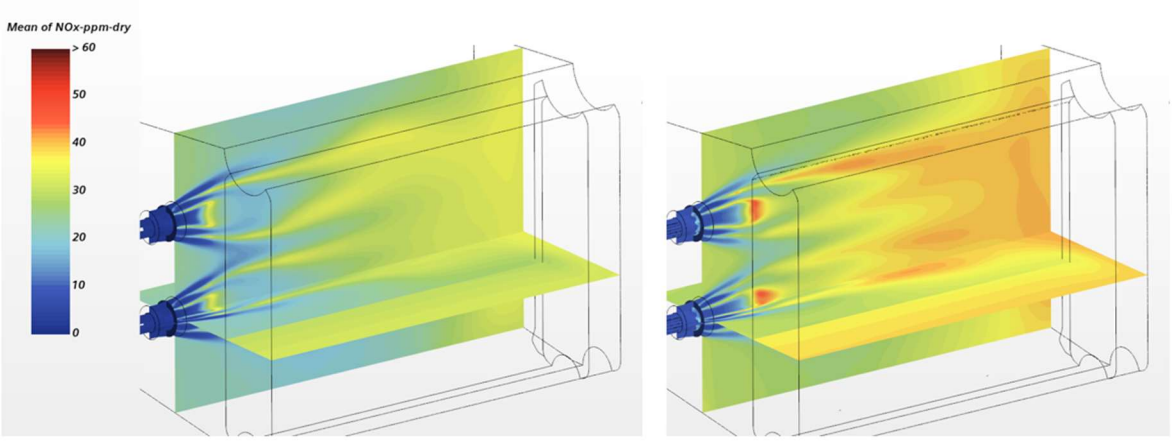

Abbildung 9. NOx-Verteilung bei Erdgas- (P1, links) und Wasserstoffbetrieb (P4, rechts)

Man kann erkennen, dass die Hauptzonen der NOx-Bildung erwartungsgemäß mit dem Temperaturverlauf korrelieren und in den Bereichen mit dem höchsten Brennstoffumsatz stattfinden. Da dieser wiederum durch die Rauchgasrezirkulation verzögert wird, liegen am hinteren Teil des Kessels große Bereiche mit ähnlicher NOx-Konzentration vor, da hier schon eine weitgehende Vermischung aller Komponenten stattgefunden hat. Das Diagramm in Abbildung 10 enthält alle aufgezeichneten Messwerte für die 4 Lastfälle und die zughörigen Werte des CFD-Modells.

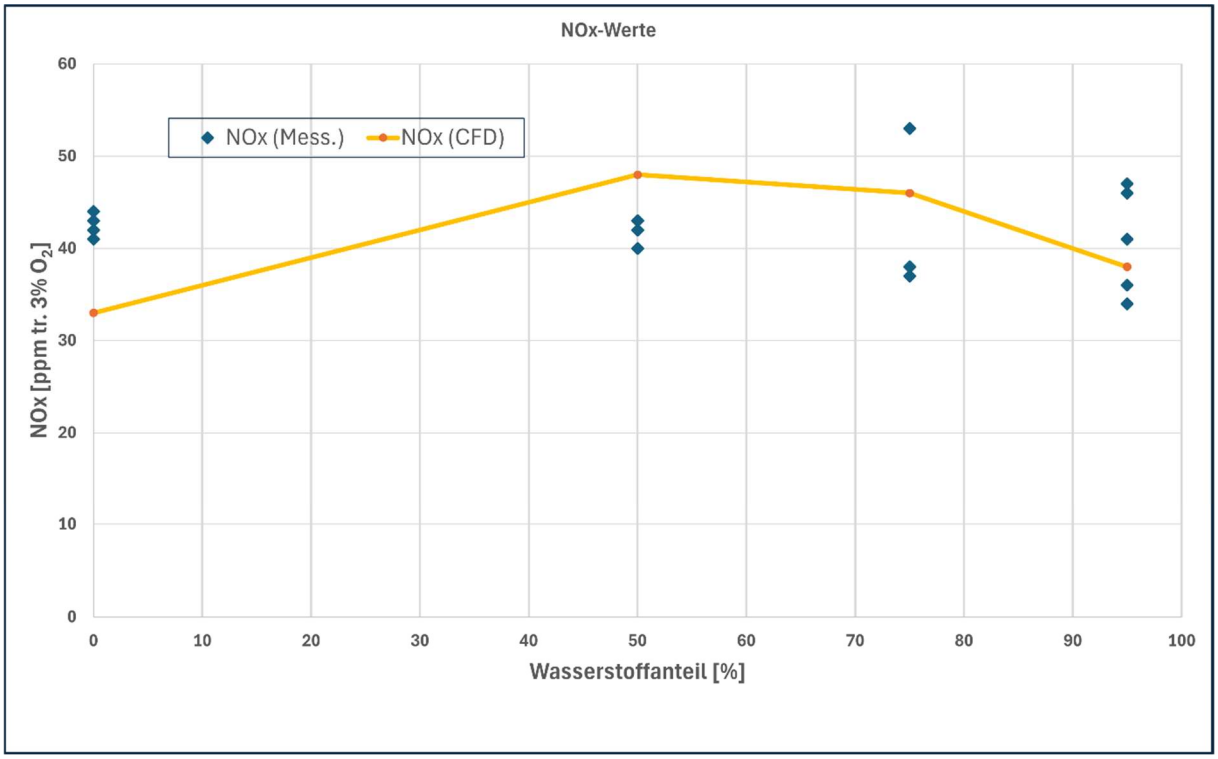

Abbildung 10. NOx-Messwerte und CFD-Werte über dem Wasserstoffanteil des Brenngases

Bei den Messwerten handelt es sich um punktuelle Einzelmessungen zu verschiedenen Zeitpunkten, die CFD-Werte geben den massenstromgemittelten Wert über dem Austrittsquerschnitt hinter dem Bündelbereich an. Wie bereits erwähnt, gibt es eine kleine Abweichung nach unten beim reinen Erdgasfall, wohingegen die NOx-Vorhersage des CFD-Modelles bei allen Fällen mit höherem Wasserstoffgehalt mit hinreichender Genauigkeit zutrifft.

4. Fazit

Es wurde gezeigt, dass die industrielle Verbrennung von Wasserstoff (bzw. Gemischen mit hohem Wasserstoffanteil) mit bestehender Brennertechnologie beherrschbar und auch simulationstechnisch in Bezug auf Temperaturverlauf und NOx-Emissionen reproduzierbar ist.
Der wichtigste Parameter zur Minderung der NOx-Emissionen ist die Menge des rezirkulierten Rauchgases, womit ein für verschiedene Lastfälle mit variierendem Wasserstoffgehalt gleichbleibend niedriger Level an NOx im Rauchgas sichergestellt werden kann.
Mittels CFD-Simulationen kann die benötigte Rauchgas-Rezirkulationsmenge korrekt vorhergesagt werden. Eine Modellauswahl, die die NOx-Bildung an einem genau vermessenen Laborbrenner reproduzieren konnte, ist auch auf eine großtechnische Anlage übertragbar.

Literatur

[1] Aniello A., Laera D., Marragou S. , Magnes H. , Selle L., Schuller T. , Poinsot T., *Experimental and numerical investigation of two flame stabilization regimes observed in a dual swirl H2-air coaxial injector*, Combustion and Flame, Volume 249, (March 2023).

[2] Conaire M. , Curran H. , Simmie J., Pitz W. , Westbrook C., *A Comprehensive Modeling Study of Hydrogen Oxidation* , Int. Journ. Chemical Kinetics 36, 603-622, (2004)

[3] Andreini A. ,Facchini B. , Innocenti A., Cerutti M., *Numerical analysis of a low NOx partially premixed burner for industrial gas turbine applications*, Energy Procedia 45, 1382-1391, (2014)

[4] Daurer G. , Schwarz S. , Demuth M. , Gaber C., Hochenauer C., *Experimental and numerical analysis of industrial-type low-swirl combustion of hydrogen enriched natural gas including OH* chemiluminescence imaging*, Int. Journ. Hydrogen Energy 80, 890-906, (2024)

[5] Marinov N., Westbrook C., Pitz W., *Detailed and global chemical kinetics model for hydrogen*,Transport phenomena in combustion 1, 118-129, (1996)

[6] Jones, W. P., & Lindstedt, R. P., *Global reaction schemes for hydrocarbon combustion*, Combustion and flame, *73*(3), 233-249, (1988)

[7] Leiser S., Schnell U., Scheffknecht G., *A kinetic homogeneous reaction model for oxy-fuel combustion,* 9th International Conference on Energy for Clean Environment. povoa de Varzim, Portugal. (July 2-5 2007)

[8] Zettervall, N. ,*Methodology for developing reduced reaction mechanisms, and their use in combustion simulations*, PhD Thesis, Department of Physics, Lund University, (2021)

[9] Si J., Wang G., Li P., Mi J., *Optimization of the Global Reaction Mechanism for MILD Combustion of Methane Using Artificial Neural Network*, Energy Fuels 34, 3805-3815, (2020)

[10] https://tnfworkshop.org/hydrogen-flames/

[11] https://web.eng.ucsd.edu/mae/groups/combustion/mechanism.html

[12] https://c3.universityofgalway.ie/combustionchemistrycentre/mechanismdownloads/

[13] http://combustion.berkeley.edu/gri-mech/

Dynamic Adaptation of the Air Split of a Gas Turbine Combustion Chamber for a Hybrid Energy System Application

S. Bellaire*, J. Zanger[1], A. Huber[1]

*sebastian.bellaire@dlr.de

[1] *Institute of Combustion Technology, German Aerospace Center (DLR), Pfaffenwaldring 38-40, 70569 Stuttgart, Germany*

Abstract

In this paper, the functionality of a newly designed orifice is investigated. The orifice is used to adjust the air split inside a gas turbine combustion chamber. Via this adjustment, the local air fuel ratio and therefore the combustion properties and emissions of a gas turbine can be optimized. This leads to many advantages in the stand-alone gas turbine operation. It enables the gas turbine to operate at an optimized air fuel ratio for all operating points, which especially benefits part load operating points, with normally relatively lean combustion conditions. With that, it is possible to enlarge the operating range of gas turbines. In operation regimes, where lean blow off occurs or the combustion conditions are unfavorable, an adaptation of the primary combustion air mass flow can be used to stabilize the flame and enable stable and clean gas turbine combustion. In addition to that, the orifice enables a broader fuel flexibility, since the local air split ratio can be adapted to the respective fuels. Additionally, it enables the integration of energy storage systems, such as high temperature energy storages, into the gas turbine system, which require the air split adjustment to fully utilize their advantages. Therefore, to research the operability of this orifice, an experimental investigation of such a hybrid energy system is carried out, to proof the impact of the orifice on the air split and the gas turbine operation and emissions.

Introduction

With the important and vast expansion of renewable energy production, its impact on the energy system rises. The energy production capabilities of most renewable energy systems vary strongly from the conventional energy systems. The mostly fluctuating energy production of the renewable energy systems are on their own not suitable for base load application. Therefore, energy storage systems are a promising solution to complement these renewable energy systems and maximize their impact on the energy market. Power-to-Heat-to-Power systems are auspicious solutions for this. Here, in times of low energy demand, low-cost green electric energy surplus can be stored as heat. In times of high energy demand, when the energy prices rise, the stored heat can be transformed back to electrical energy and sold on the energy market. This is possible for large-scale powerplants, as well as for smaller, decentralized energy systems. Agelidou et al. [1] introduced such a hybrid energy system consisting of a high temperature energy storage (HTES) and a gas turbine. The concept idea is to improve the gas turbine cycle by integrating a high temperature energy storage before the combustion chamber and to utilize green energy excess. Hereby, in times of green energy surplus, the produced energy is used to electrically heat up the HTES. The now converted energy can then be stored as heat. In times of high energy demand, the stored heat can then be used to further preheat the combustion air of the gas turbine, reducing or even negating the fuel demand of the gas turbine and therefore providing fast and reliable power and heat, while strongly reducing or even negating exhaust gas emissions (Figure 1).

In gas turbines, the incoming combustion air is split into primary air, which is mixed with fuel and takes place in the combustion, and secondary air, which is used as cooling and dilution air. With an increase of the combustion air temperature, the needed temperature rise in the combustion chamber is reduced. Therefore, an increase in combustion air temperature reduces the necessary fuel amount.

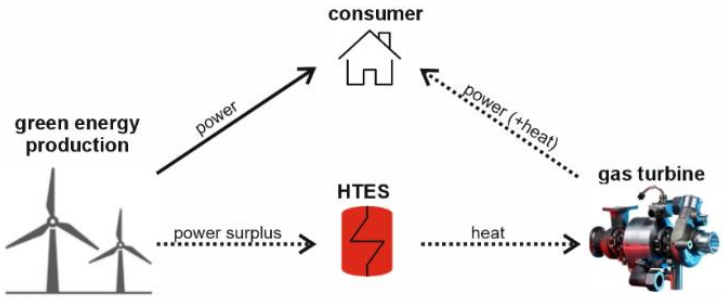

Figure 1: Schematic of a possible use case of the hybrid energy system (gas turbine image from [2])

However, without any additional adjustments, this reduced fuel amount affects the local air fuel ratio in the combustor and therefore has a strong impact on the combustion itself, which can lead to worsen exhaust gas emissions or even a lean-blow-off, impeding the gas turbine operation. Therefore, means to adjust this air split are needed, in order to adapt the air fuel ratio for the combustion and with that, to enable the gas turbine operation independently of the reduced fuel amount in the hybrid energy system. In the literature there are some means presented, to influence the air split. However, either they cannot be integrated in this system, because of their use of special elements (e.g. guiding vanes in [3]), have different focus (no air shifting towards a secondary air path [4]) or directly influence the mixing of air and fuel [5]. Therefore, an orifice is designed, which enables an adjustment of the air split by shifting primary air towards the secondary air path, thus being able to adapt the local fuel air ratio towards any fuel reduction, introduced through an increased combustion air temperature by the high temperature energy storage in the hybrid system. In this paper, the functionality of the designed orifice will be experimentally shown for a hybrid energy system demonstrator.

Technical Background

The standard micro gas turbine cycle is composed of six parts (Figure 2). Firstly, the compressor, which draws in and compresses ambient air. Then, the compressed air flows through the recuperator, where it is preheated before entering the combustion chamber. In order to reach the necessary turbine inlet temperature (TIT), fuel is injected into the compressed, preheated air and is ignited. The hot exhaust gas enters the turbine, where it is expanded, transferring mechanical energy to the turbine, which is connected to the compressor and uses part of the energy to power the compressor. The greater part of the energy is received by the generator, where it is transformed into electrical power. The still hot, but decompressed gas-mixture enters the recuperator, where it transfers heat to the incoming combustion air, which reduces the fuel demand and therefore increases the electrical efficiency of the gas turbine system. In order to maximize the energy output, a heat exchanger uses the remaining heat to warm up water, which can be used in industrial processes or in domestic applications.

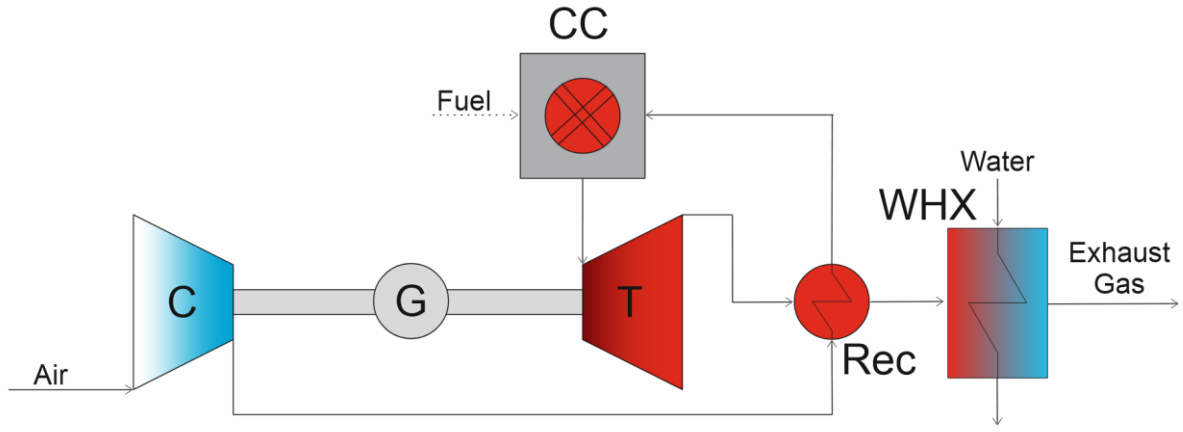

Figure 2: gas turbine system (derived from [1])

For a cost-efficient demonstration system, a MTT EnerTwin gas turbine with an electrical power output of up to 3 kW is installed. Its revolution speed ranges from 180.000 rpm up to 240.000 rpm, with an electrical efficiency of 16%, a total efficiency of 94% and a pressure ratio of up to 3:1 ([6]). The typical

air temperatures in the combustion chamber inlet range from 685 °C to 700 °C. Depending on the operating point and with that, the air mass flow, fuel is injected into the combustion chamber. The amount of fuel is controlled by the turbine outlet temperature (TOT), which is kept at 767 °C. Thereby, the turbine inlet temperatures (TIT) extends up to 970 °C. The power module consists of a single stage, single shaft turbomachinery with radial impellers with the generator located in between the compressor and turbine as illustrated in Figure 2. Further information about the EnerTwin can be found in [1].
For the MTT EnerTwin a jet stabilized (FLOX®) combustion chamber was designed and implemented by Seliger-Ost et al. [7]. A schematic representation of the combustion chamber is shown in Figure 3. Here, the incoming, compressed and preheated air is split into two air paths. Firstly, the primary air path, where the air gets distributed into six air/fuel nozzles, where the fuel is injected co-axially into the primary air. The air and fuel get technically premixed, before entering the combustion chamber with a high momentum, which leads to a recirculation zone inside the combustion chamber. This recirculation zone dilutes the incoming air/fuel mixture with flue gas, which leads to a homogenous temperature distribution without local temperature peaks, which is necessary for low NOx emissions ([8]). The greater part of the air enters the secondary air path, where it acts as cooling air for the combustion chamber before entering the flame tube as dilution air via the dilution holes. The far downstream position of the dilution holes prevents the direct participation of the secondary air in the combustion.

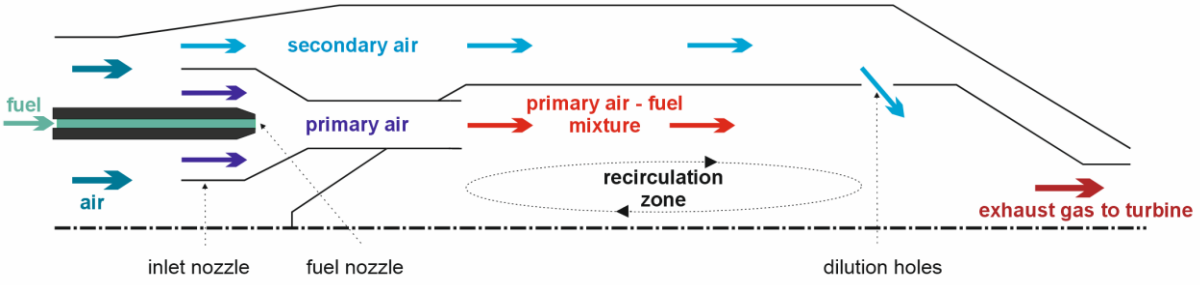

Figure 3: schematic representation of the air paths in the MTT combustion chamber

To quantify the air distribution between these two air paths, an air split S_d is defined in equation (1):

$$S_d = \frac{\dot{m}_{primary\ air}}{\dot{m}_{air}} = \frac{\dot{m}_{primary\ air}}{\dot{m}_{primary\ air} + \dot{m}_{secondary\ air}} \tag{1}$$

This air split is mainly geometry dependent and therefore approximately constant for the operating points of a combustion chamber. The combustion properties, especially regarding the emissions, are strongly influenced by the local air number λ_{local}, which is calculated in equation (2), using the primary air mass flow $\dot{m}_{primary\ air}$, the fuel mass flow $\dot{m}_{fuel}$ and the stochiometric air fuel ratio AFR_{st}:

$$\lambda_{local} = \frac{\dot{m}_{primary\ air}}{\dot{m}_{fuel} \cdot AFR_{st}} \tag{2}$$

Adjustable Orifice

Through the implementation of a HTES in the gas turbine system, the incoming combustion air can be further preheated, decreasing the necessary fuel amount of the gas turbine. However, the primary air mass flow stays approximately constant. This impacts the local air fuel ratio λ_{local} and therefore the combustion properties in the combustion chamber. This can lead from worsen exhaust gas emissions up to a lean blow off, which would impede the operability of the hybrid energy system.

Therefore, an adjustable orifice is presented, which can be implemented into the combustion chamber to adjust the air split. The orifice is put in front of the inlet nozzles of the flame tube. In the opened position (Figure 4 – left), the incoming air gets divided into 3 air paths: two primary air paths and the secondary air path. Using an actuator, the orifice can be axially moved towards the nozzle. With the conical shape of the orifice, the outer primary air path is getting more and more restricted, until the orifice and nozzle are in contact, completely blocking the outer primary air path (Figure 4 – right).

Additionally, the conical shape of the fuel supply nozzle also reduces the effective diameter of the inner primary air path. However, this path cannot be fully restricted, always leaving a minimal path for the primary air. Therefore, the axial movement of the orifice towards the nozzle leads to an increased pressure drop in theses air paths, which shifts parts of the primary air towards the secondary air path, adjusting the air split. Through that, the local lambda in the primary air zone can be adjusted to fit the optimal combustion conditions. This enables the application of the hybrid energy system consisting of a HTES and a gas turbine, since it is possible to balance out the reduced fuel amount by reducing the primary air mass flow and keeping the local lambda λ_{local} at an optimum. This enables the integration of the HTES into the gas turbine system, without impeding the gas turbine operation.

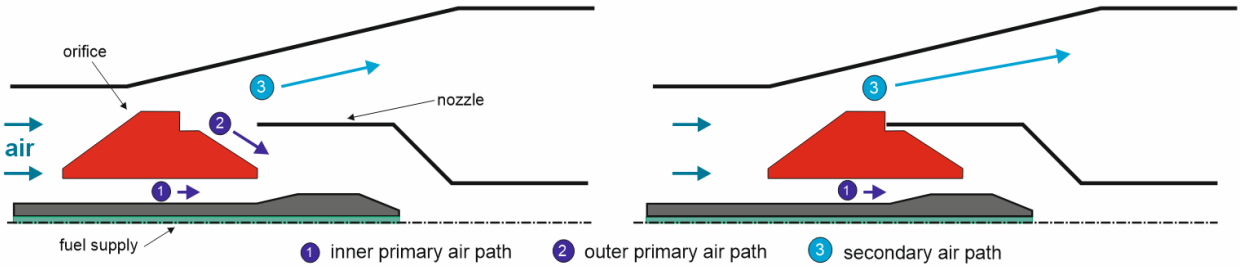

Figure 4: left: open primary air paths – right: restricted primary air paths

A patent regarding the orifice is submitted and currently in examination (German patent application number: DE 10 2024 116 456.5). Since the integration of the orifice integrates an additional body into the combustion chamber, it will influence the pressure loss over the combustion chamber, which plays an important role for the overall efficiency of the gas turbine. To minimize this effect, the orifice is designed to reduce its impact on the pressure loss as far as possible. Its impact is evaluated by the relative pressure loss over the combustion chamber Δp_{cc}, which is calculated by dividing the pressure difference $p_{diff,cc}$ by the combustion chamber pressure p_{cc} as seen in equation (3):

$$\Delta p_{cc} = \frac{p_{diff,cc}}{p_{cc}} \cdot 100\% \tag{3}$$

Air split calculation

In order to be able to quantify the influence of the orifice, a defined diameter reduction is integrated into the secondary air path of the combustion chamber (Figure 5 – display of the casing, without the flame tube). With this constriction, it is possible to derive the secondary air mass flow $\dot{m}_{secondary\ air}$, using the temperature of the secondary air flow (T_{sec}), the pressure and surface area before the constriction (p_{sec}, A_1), the pressure difference to a second measuring point in the constriction (Δp_{sec}), as well as the surface area in the constriction (A_2) and the universal gas constant R. In order to minimize local effects, the pressure sensors have multiple measurement points distributed circumferentially.

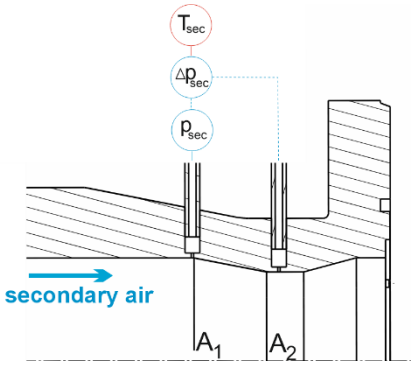

Figure 5: Instrumentation in the secondary air path (flame tube not shown)

$$\dot{m}_{secondary\ air} = \sqrt{\frac{2 \cdot \Delta p_{sec}}{R \cdot T_{sec} \cdot \left(\frac{1}{A_2^2 \cdot (p_{sec} - \Delta p_{sec})} - \frac{1}{A_1^2 \cdot p_{sec}}\right)}} \tag{4}$$

Experimental Testing

This paper investigates the performance of the newly designed orifice and its influence on the gas turbine operation, mimicking the boundary conditions of a hybrid energy system consisting of a gas turbine with an integrated high temperature energy storage. As fuel, natural gas from the local grid is used. The measurements were performed at steady-state combustion conditions, where each measurement point is time-averaged over 5 min.

Test rig

In order to investigate the influence of the HTES and the orifice on the gas turbine performance, a gas turbine test rig is used. The key component of the test rig is the MTT EnerTwin. The original combustion chamber of the MTT EnerTwin was replaced by a newly designed combustion chamber, which was optimized for the orifice implementation. This combustion chamber originated from the single-stage, FLOX® combustion chamber, developed by Seliger-Ost et al. [7].

In Figure 6 a simplified overview of the test rig and the positions of the most important sensors is presented. As shown, the HTES is not directly implemented into the test rig, but is modelled by an electrical heater, which preheats the combustion air to the necessary temperature levels to mimic the HTES. The heater allows for a more dynamic temperature adjustment of the incoming air, as well as a broader temperature range. The heater is an Osram flanged inline heater system, which allows for a maximum heating temperature of 871 °C. However, with the higher volume flows and the heat losses between heater and combustion chamber, only inlet temperatures of 750 °C up to 825 °C, depending on the air mass flow, are possible.

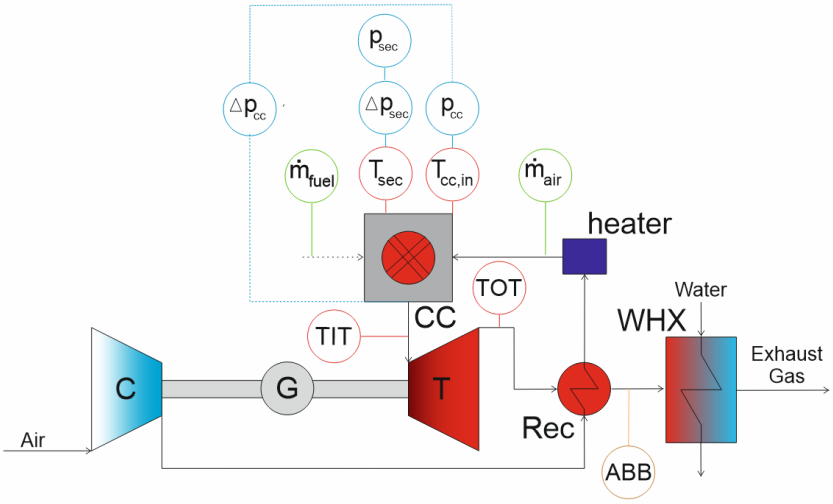

Figure 6: simplified overview of the main instrumentation

The temperatures of the incoming combustion air ($T_{cc,in}$), the secondary air mass flow (T_{sec}) and the turbine outlet and inlet temperatures (TOT, TIT) are measured by thermocouples of type N with tolerance class 1 (accuracy ± 2.4 K). The pressure sensors p_{cc}, p_{sec} and Δp_{cc} are "Althen pressure Transducers" with a range of 0 to 4 bar. p_{sec} is a "EE600" differential sensor with a range from 0 to 1000 Pa and an accuracy of 5 Pa. The natural gas mass flow $\dot{m}_{fuel}$ is controlled by a "Bronkhorst M54-RBD-99-V-C" with an inaccuracy of $\pm$ 0.5 %. The air mass flow is derived using a "SKI probe with an AccuFlo® Zero element" to increase its accuracy. The ABB exhaust gas analyzer has a sampling rate of 1 Hz. The measurement of NO, NO_2, CO and O_2 concentrations are measured by means of UV absorption ("Limas11 HW"), infrared photometry ("Uras26") and paramagnetism ("Magnos26") and a Vaisala HMT 338 humidity sensor [9]. Table 1 depicts the measured flue gases and their respective manufactures accuracies.

Species	**NO_2** ppm	**NO** ppm	**CO** ppm	**CO_2** vol.-%	**O_2** vol.-%	**H_2O** %rF
Range 1	0-10	0-10	0-10	0-5	0-5	-40 – 180 °C
Accuracy 1	0.1	0.1	0.1	0.05	0.025	$\pm\,(1.5 + 0.015 \cdot x)$
Range 2	10-20	10-20	10-100	5-20	5-15	
Accuracy 2	0.2	0.2	1.0	0.2	0.075	
Range 3	20-50	20-50	100-200		15-25	
Accuracy 3	0.5	0.5	2.0		0.125	
Range 4	50-200	50-200	200-500		25-100	
Accuracy 4	2.0	2.0	5.0		0.5	

Table 1: Measurement range and accuracy of the ABB exhaust gas analyzer

The exhaust gas measurements are corrected to a residual oxygen content of 15 vol.% and dry conditions. For the CO emissions, equation (5) describes the correction of the measured species concentration ($C_{meas,dry}$) by using the measured concentration of the residual oxygen content $C_{O2/vol.\%}$.

$$C_{corr/ppm} = C_{meas,dry/ppm}\frac{20.95 - 15}{20.95 - C_{O2/vol.\%}} \tag{5}$$

For species (such as NO and NO_2), which are measured wet ($C_{meas,wet/ppm}$), the correction considers the water content in the exhaust gas ($C_{H20/ppm}$), as shown in equation (6):

$$C_{corr/ppm} = C_{meas,wet/ppm}\frac{20.95 - 15}{20.95 - C_{O2/vol.\%}} \cdot \frac{1}{1 - (C_{H20/ppm} \cdot 0.0001 \cdot 0.01)} \tag{6}$$

As a data acquisition system, a Bachmann PLC was used, with a sampling rate of 1 Hz.

Test campaign

The test campaign investigates the influence of the orifice on the gas turbine operation, especially in regard to exhaust gas emissions. In Table 2 the main variables, as well as their ranges, are shown. Due to the long piping system of the test rig, there are some restrictions regarding gas turbine operation. Therefore, in this paper the influence of the orifice will be mainly investigated on the lower operation points. The orifice position describes the distance between the orifice and the nozzle, whereas a position of 0 mm describes the "closed position", with a completely restricted outer primary air path (Figure 4 – right), and the 14 mm the "open position" with a maximal retracted orifice and therefore a minimized influence on the air split.

	Unit	**Min**	**Max**
Rotational speed	rpm	180.000	210.000
Inlet temperature	°C	675	775
Orifice position	mm	0	14

Table 2: investigated boundary conditions of the main measurement campaign

Prior to the main measurements, preliminary investigations were conducted, in order to enable optimal measurement conditions for the main measurement campaign.

Definition of an effective inlet temperature

Based on the relatively long distance between the heater and the combustion chamber of around 1 m, the temperature profile at the combustion chamber inlet is not homogenous. The heat loss over the wall lead to the buildup of a temperature profile of the combustion chamber inlet with high temperatures in the middle and lower values at the wall (indicated by the temperature profile in Figure 7).

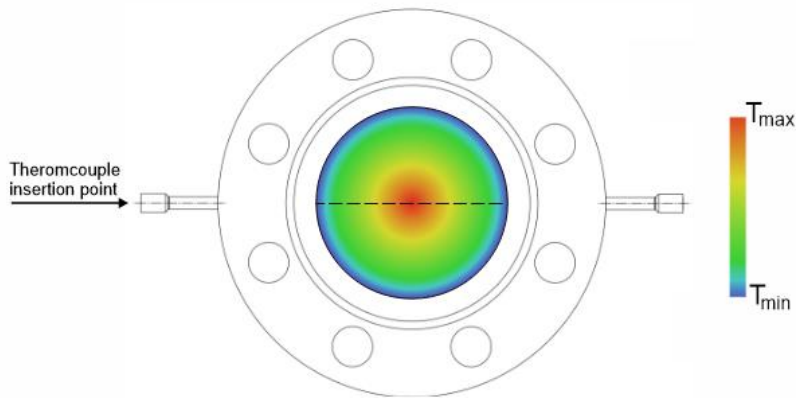

Figure 7: schematic temperature distribution of the air flow in the combustion chamber inlet

In a first step, the temperature profile of the incoming combustion air is investigated, in order to be able to extract one effective temperature value, which describes the temperature content of the air flow more precisely than the maximum temperature value in the middle flow. This value is then used as target value for an optimized reference of the temperature input of an integrated HTES.
Therefore, a thermocouple is inserted into the combustion chamber inlet, perpendicular to the air flow. The thermocouple is not fixed in place, but can be moved from wall to wall in order to be able to measure the temperature profile along the dotted axis of the round combustion chamber inlet, shown in Figure 7. The inlet diameter is $d_{cc,in} = 9.6\ cm$, and the measurement points are distributed between $\pm$ 3.6 cm from the middle flow. For different boundary conditions, the thermocouple is moved to these distinct positions on that axis, measuring the respective temperatures. The inlet temperature is varied between 700 °C and 825 °C. Additionally, the influence of rotational speed is investigated in the range from 180.000 rpm up to 225.000 rpm, which directly impacts the air mass flow through the gas turbine system. Both variations have minor effects on the temperature profile (<1 %) and are neglectable in comparison to the heat loss to the wall, which leads to a temperature drop of at least 2.5 % at the walls. Therefore, for a representative measurement point of 700 °C, a rotational speed variation is investigated. The measured temperatures at seven distinctive positions are shown in Figure 8. Based on these measurements, a polynomial function is generated, which describes the temperature profile over the diameter of the combustion chamber inlet. By calculating the root mean square (RMS) value of this temperature function an "effective temperature factor" is derived. This factor is then multiplied with the measured, maximum temperature in the middle of the flow, generating an "effective temperature", which is used as the target temperature value for the HTES coupling.

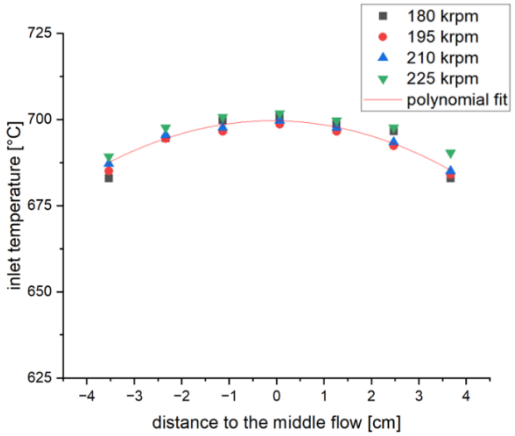

Figure 8: Polynomial fit for the temperature distribution in the combustion chamber inlet for different rotational speeds

Orifice performance

To evaluate the pressure loss over the combustion chamber in regard to the orifice positions, Figure 9 displays the relative pressure loss Δp_{cc} for different orifice positions for the rotational speeds of 180.000 and 210.00 rpm. As expected, the pressure loss is maximized for the closed position (0 mm), where the orifice restriction of the primary air path is the highest. Through increasing the distance between orifice and inlet nozzle, the adjusted pressure loss in the primary air path decreases strongly for the first 7 mm, with a shallower gradient later on. This behavior is based on the design of the orifice – nozzle interaction. The main interaction is designed for the shorter distances (between 0 and 7 mm), where the orifice has a strong impact on the air split. For the backmost positions (> 7 mm), the interaction between orifice and nozzle is minimized, which reduces the impact of the orifice in these regions, as seen for the pressure loss. However, the overall static pressure loss of 4.8 % up to 5.8 % are in a standard range for combustion chambers in gas turbines, enabling the general application of the orifice in gas turbine systems.

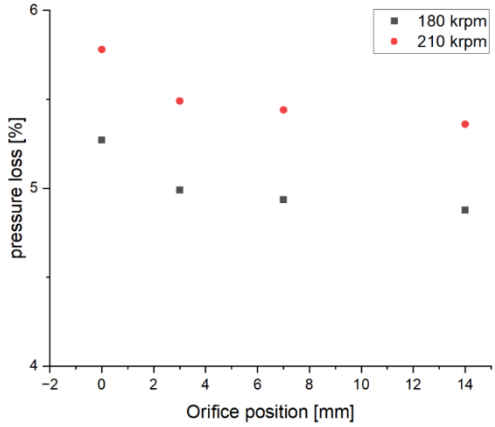

Figure 9: relative pressure loss over the combustion chamber in regard to orifice position

The main task of the orifice is to shift primary air towards the secondary air path, adjusting the air split. In Figure 10, the air split adjustment over different orifice positions is shown for two rotational speeds. Here, the effectiveness of the orifice in the design positions (between 0 and 7 mm) is clearly seen. In the closed position (0 mm), the air split is minimal. By increasing the distance towards the 7 mm position, the air split increases by 7.7 percentage points (52.7 %) for the 180.000 rpm case and 7.4 percentage points (60.6 %) for the 210.000 rpm case. Behind the 7 mm point, the air split roughly changes anymore, since the orifice-nozzle interaction is minimized.

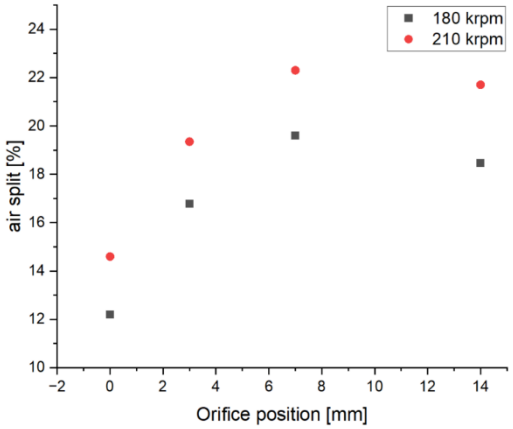

Figure 10: air split in regard to orifice position

In order to evaluate the influence of the successful air split adjustment of the orifice on the gas turbine operation, the exhaust gas emissions are investigated. Hereby, the application case with the emulated HTES is researched. The emission values for the rotational speeds of 180.000 rpm and 210.000 rpm and for different combustion chamber inlet temperatures (675 °C up to 775°C) are recorded and analyzed. In Figure 11 the NO_x emissions for both rotational speeds are pictured. For both rotational speeds, the opening of the orifice results in lower NO_x emissions. This is due to the decreased primary air path

restrictions and the so increased primary air mass flow in the open positions, which results in leaner fuel air mixtures, less hot spots and therefore less thermal NO_x production. In addition to that, the temperature increase of the incoming combustion air steadily decreases the respective NO_x emissions for each orifice position. Here, for each position, the air split is constant and the necessary fuel mass flow is reduced, resulting in leaner fuel air mixtures and therefore again lower NO_x emissions. For the 180.000 rpm case, all but 1 single measurement point are below the 37 ppm German legal limit for NO_x emissions. For the 210.000 rpm case all orifice positions, but the 0 mm position, are also below the legal limit. The closed position exceeds this limit for all, but the 775 °C case, showing the impact of the temperature increase of the combustor air through the heater and the respective fuel decrease.

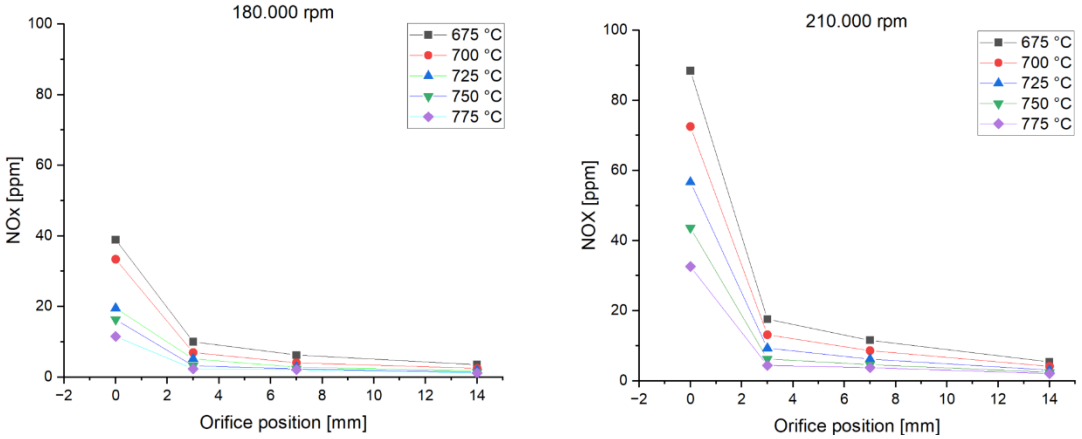

Figure 11: NO_x emissions in regard to orifice position for different inlet temperatures left: 180 krpm – right: 210 krpm

In Figure 12 the CO emissions for both rotational speeds are shown. Here, the influence of the orifice and especially the design points are apparent. The CO emissions in the design point (0 mm position) are extremely low (all below 16 ppm). However, through increasing the distance between orifice and nozzle, the CO emissions rise strongly for both rotational speeds. This is again based on the increased primary air mass flow and the higher air fuel ratio. The leaner conditions lead to reduced adiabatic flame temperatures, whereby the rates of the chemical reactions slow down and the residence time for the CO oxidation is not sufficient anymore, resulting in higher CO emissions. The German limits for the CO emissions are only met for the 0 mm case (for both rotational speeds). For the other positions, the CO emissions rise strongly. This is due to the strong influence of the air split adjustment.

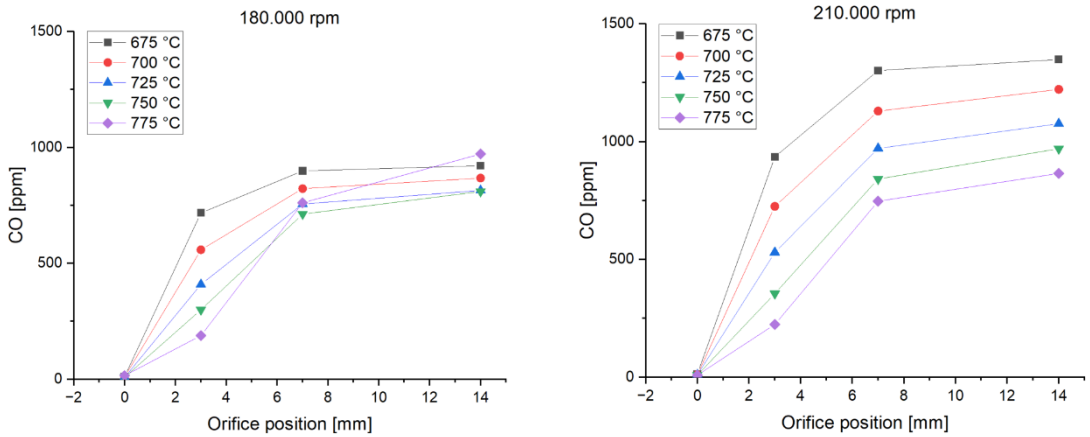

Figure 12: CO emissions in regard to orifice position for different inlet temperatures left: 180 krpm – right: 210 krpm

The influence of the increased temperature for the incoming air is clearly underlined as well. The increase in temperature and therefore the reduction of fuel, reduces the emissions strongly. However, since the NO_x and CO emissions behave opposed in regard to the orifice position, a sweet spot has to be found, where the CO and NO_x emissions both are at a preferable level.

Summary and Conclusion

In the present paper, an orifice was presented, which can be implemented into gas turbines to adjust the air split in the combustion chamber, in order to optimize the local air fuel ratio and therefore the exhaust gas emissions. The fundamental function of the orifice, as well as a demonstrator for an application case within a hybrid energy system - consisting of a high temperature energy storage and a gas turbine - were presented and investigated. Firstly, an effective temperature value for the test rig was experimentally defined, to enable an optimized mimicking of the temperature input of an integrated high temperature energy storage. Afterwards, the performance of the orifice itself was investigated. In a first step, the pressure loss over the combustion chamber for different boundary conditions was analyzed. It was shown, that the position of the orifice has an impact on the overall pressure loss. However, the pressure loss levels were on a reasonable level, thus enabling the application of the orifice in a gas turbine operation. To proof the functionality of the orifice, a mass flow measurement system was introduced into the combustion chamber, which enabled the measurement of the secondary air mass flow and thus the air split. The measurement showed the operability of the orifice in its design positions. The successful adjustment of the air split in the front region was also clearly seen in the exhaust gas emissions, which could be greatly modified, depending on the orifice position.

The correlation between orifice displacement and split adjustment is not linear. The foremost positions have the most impact on the adjustment. In a next step, the region between the 0 mm and 7 mm orifice position has to be investigated more closely. Here, the orifice-nozzle interaction is clearly discernible. For optimized emissions, an optimal orifice position has to be found for the different operating points. This optimal point seems to be in this front region. If this point would be outside this range, the air split range could be adjusted by enlarging or reducing the dilution hole diameters.

The investigation of the emulated HTES through the increased combustion air temperature levels has shown, that a decrease in fuel for these operating points results mainly in better emission values. However, since both NO_x and CO emissions behave contradictory regarding the orifice positions, sweet spots for the orifice position have to be found to optimize emissions. Nevertheless, it could be shown, that the orifice has an impact on the emissions and therefore works for the integration of the HTES in the gas turbine system. However, in the next measurement campaign, the optimal orifice positions depending on the boundary conditions will be investigated. From them, a matrix can be derived, to enable an automated repositioning for the orifice depending on the boundary conditions, resulting in an optimized air fuel ratio and exhaust gas emissions.

Acknowledgments

I would like to thank Nikhil Shinde for his big support during the measurement campaign.

References

[1] Agelidou, Eleni, Seliger-Ost, Hannah, Henke, Martin, Dreißigacker, Volker, Krummrein, Thomas, and Kutne, Peter. “The Heat-Storing Micro Gas Turbine—Process Analysis and Experimental Investigation of Effects on Combustion.” *Energies* Vol. 15 No. 17 (2022): p. 6289. DOI 10.3390/en15176289.

[2] Hohloch, M. “Hybrid power plant - concept for coupling MGT and SOFC.”. DLR (2019).

[3] Jungbauer Leopold. “Brennkammer für eine thermische Strömungsmaschine: Offenlegungsschrift.” DE 3819898 A1.

[4] Potesser Michael. “Brenner: Offenlegungsschrift.” DE 10 2007 005 256 A1.

[5] Huber, Andreas. “Offenlegungsschrift DE 10 2017 120 370 A1: Offenlegungsschrift.”.

[6] MTT Enertwin. “MTT EnerTwin Specifications.”, 2020. URL https://enertwin.com/wp-content/uploads/2021/02/en_enertwin_specifications_2020.pdf.

[7] Seliger-Ost, H., Kutne, P., Zanger, J., and Aigner, M. “Experimental Investigation of the Impact of Biogas on a 3 KW Micro Gas Turbine FLOX®-Based Combustor.”. *Proceedings of the ASME Turbo Expo: Turbomachinery Technical Conference and Exposition - 2020: Presented at the ASME Turbo Expo 2020: Turbomachinery Technical Conference and Exposition, September 21-25, 2020, Virtual, Online*.

[8] Zanger, J. “Experimentelle Charakterisierung eines atmosphärisch betriebenen, jet-stabilisierten Mikrogasturbinenbrenners für Erdgas.”. Stuttgart, Universität. DOI 10.18419/opus-8827.

[9] Seliger, H., Huber, A., and Aigner, M. “Experimental Investigation of a FLOX-Based Combustor For a Small-Scale Gas Turbine Based CHP System Under Atmospheric Conditions.”. *Proceedings of the ASME Turbo Expo: Turbine Technical Conference and Exposition - 2015: Presented at the ASME 2015 Turbo Expo: Turbine Technical Conference and Exposition, June 15 - 19, 2015, Montreal, Quebec, Canada*. DOI 10.1115/GT2015-43094.

Optimization and Atmospheric Experimental Investigation of a Jet Stabilized Micro Gas Turbine Combustor for the Use of Hydrogen

M. Hohloch[1*], T. Lingstädt[1] and P. Kutne[1]

*martina.hohloch@dlr.de

[1] *Institute of Combustion Technology, German Aerospace Center (DLR), Pfaffenwaldring 38-40, 70569 Stuttgart, Germany*

Abstract

In this study, the further development of the F400 combustor for the use of hydrogen and mixtures of hydrogen and natural gas is shown. The F400s, initially developed for the use of low calorific fuels like biogas and synthesis gas, has already demonstrated the capability to run on pure hydrogen and mixtures of hydrogen and natural gas. To further minimize the risk of flashback and to improve the combustor, different modifications have been implemented on both pilot and main stage. For the investigation, an atmospheric test rig was utilized. The test rig is equipped with an optically accessible flame tube to observe the combustion process. It offers the advantages of conducting parametric studies of the combustor independently from the MGT using diagnostic methods to analyze the combustion process itself. In the measurement campaign, two different modifications of the main stage were evaluated. For the assessment, especially the height above the burner, the shape of the flame and the emissions of NO_x were considered. For each configuration, a variation of the burner air number was conducted to determine the operating range for the MGT application. For all configurations, stable combustion of pure hydrogen could be achieved.

Introduction

In the future energy system, decentralized power and heat generation based on micro gas turbines (MGT) can play an important role. Regarding the need for heat and power, MGTs can reach high overall efficiencies. They can react flexibly to a varying demand, compensating for the volatile energy output of renewable sources like wind and PV. MGTs will be operated with renewable fuels like hydrogen, which can be produced from renewable power in times of high availability and used as chemical energy storage. Because of the limited availability of hydrogen, it would be favorable, if the combustor could also operate with mixtures of natural gas and hydrogen, without changing the combustion system.

At the DLR Institute of Combustion Technology, a combustor was developed for the use in a 100 kW_{el} MGT with a thermal power input of approximately 330 kW like the Turbec T100 or the Ansaldo AE-T100. The combustor, shown in Figure 1, combines a swirl-stabilized pilot stage with a main stage based on the jet-stabilized (FLOX®) combustion principle. It was originally designed for the use of low calorific fuels like biogas or synthesis gas [1,2]. First tests with hydrogen at atmospheric conditions [3] as well as in the MGT [4,5] revealed that the jet stabilized concept offers a great advantage for the use of hydrogen as it minimizes the risk of flashback. Therefore, in this study, the combustor was further optimized for hydrogen, focusing on a safe and stable operation at low emissions.

The measurement campaign was carried out at a single combustor test rig with optical access at atmospheric conditions, independently from the micro gas turbine. Therefore, it was possible to conduct different parametric studies decoupled from the boundary conditions of the real MGT. The flame tube made of quartz glass offers the possibility to apply optical measurement techniques like the OH* chemiluminescence. Hereby, especially for hydrogen combustion, important insights into the flame shape and position can be obtained.

Combustor

In an MGT, only part of the air is used for the combustion process. Figure 1 depicts the distribution of the air mass flow in the combustion chamber of the AE-T100 micro gas turbine. The preheated air from

the recuperator enters the combustion chamber on the right side. The major portion of the air (secondary air) is injected downstream of the combustion zone through the dilution air holes to decrease the temperature of the flue gas for the turbine. The smaller portion of the air (primary air) is used for the combustion. This air mass flow is split between the pilot stage (marked in orange) and the main stage (marked in blue).

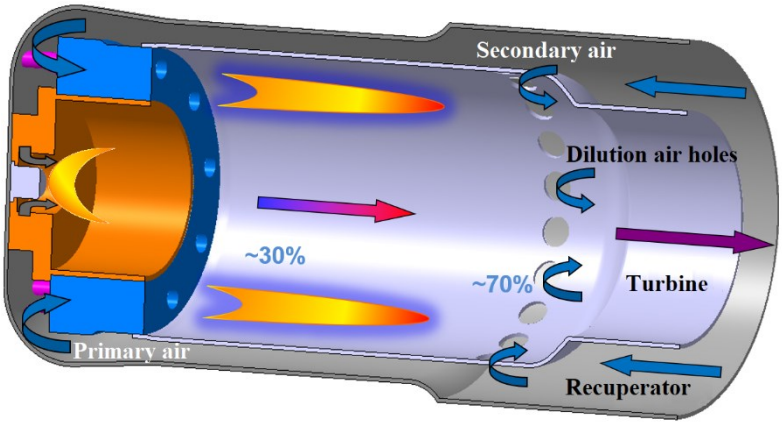

Figure 1. Combustion Chamber AE-T100 [6]

The combustor used in this study is a modified version of the F400s.3 described in detail in [3,6]. To improve the hydrogen-use in terms of safety and emissions, different modifications to this version were carried out resulting in versions F400h.1 and F400h.2. For both, the pilot stage is still based on the commonly used swirl stabilized concept. In the s.3 version, the pilot stage has both an axial and a tangential fuel injection. For the use of hydrogen, the tangential fuel injection was removed to prevent undefined backflow to the plenum of mixed fuel and air, potentially resulting in flame flashback. For the main stage in both h-versions, the nozzles were modified to remove the additional air injection and two different mixing lengths were tested. In version F400h.1, the mixing length was set to zero, offering the highest safety margin against flashback. In version F400h.2 a certain mixture of fuel and air was allowed. The sketches in Figure 2 show a scheme of the combustor.

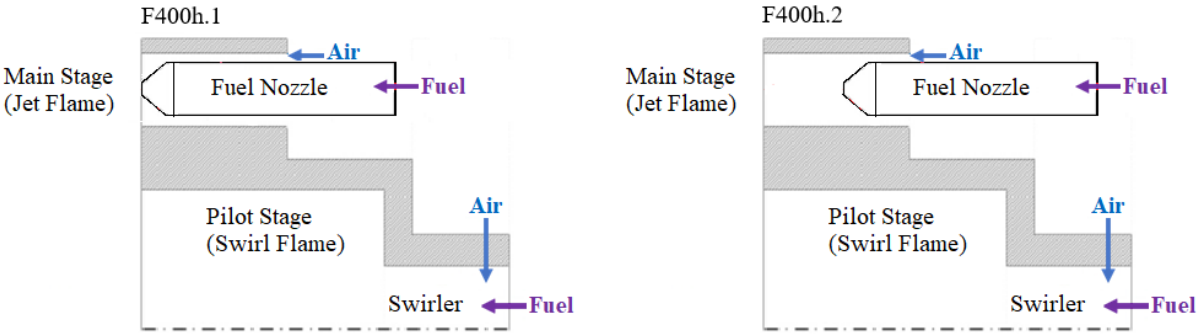

Figure 2. Combustor version F400h.1 and F400h.2 (modified from [2,3])

ATM test rig

To investigate the combustor independently of the micro gas turbine, a single combustor test rig, operated at atmospheric conditions, was used (see Figure 3). In the test rig, the operating conditions from the MGT are scaled by Mach number similarity to atmospheric conditions to keep the velocities (and hence similar pressure losses and residence times) constant. This results in a thermal power of approximately 80 kW for full load. The temperature of the air mass flow can be adjusted to the inlet conditions of the combustion chamber in the real MGT. As in a former measurement campaign, the influence of the secondary air on the combustion process was seen as negligible, it was not implemented for the present tests. Therefore, in this configuration of the test rig, only the primary air to the combustor

was used. The test rig is equipped with an optically accessible flame tube. This offers the possibility to analyze the shape and the position of the flame using OH* chemiluminescence.

At the atmospheric test rig, a variation of the air mass flow is used to account for different burner air numbers. The air mass flow was adjusted using a *Bronkhorst El-flow F-206BI* with a measurement uncertainty of ± 0.5 % plus 0.1 % full scale. The fuel composition was provided by hydrogen gas bundles and natural gas from the local grid. Using a *Bronkhorst El-Flow F-113AC* mass flow controller (uncertainty of ± 0.5 % plus 0.1 % full scale) for H_2 and a *Bronkhorst Cori-Flow M54* (uncertainty ± 0.5 %) for natural gas, the fuel composition was adjusted. The split of main to pilot burner was provided using a flow ratio controller based on a *Bronkhorst El-Press P-502C* pressure controller (uncertainty ± 0.5 %) and two *Bronkhorst El-Flow F-203AV* with an uncertainty of ± 0.5 % plus 0.1 % full scale.

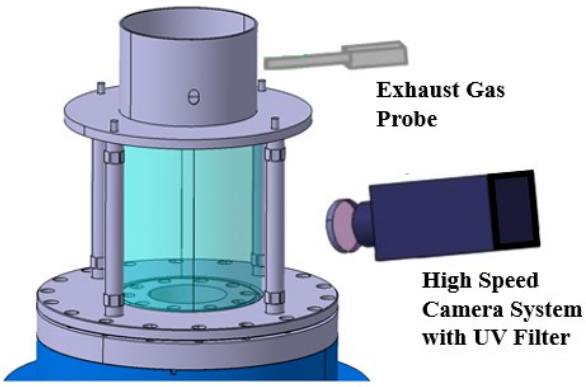

Figure 3. CAD scheme ATM test rig [3]

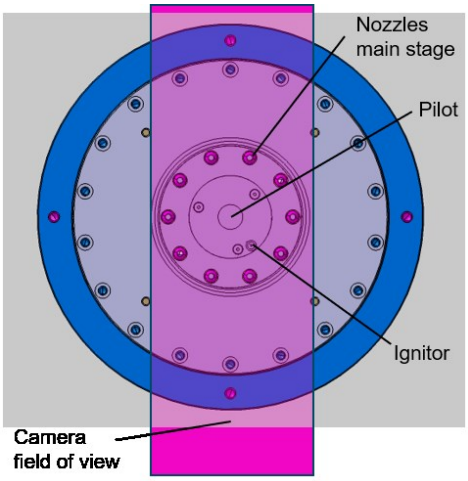

Figure 4. Field of view, shown in a horizontal section through the test rig [3]

The temperatures are measured using thermocouples type N with tolerance class 1 (accuracy ± 2.4 K). The probes are connected to a *Delphin Top message* data acquisition system (accuracy ± 0.1 % for thermocouples), operated at a sample rate of 1 Hz. For the evaluation of the combustor, the emissions in the exhaust gas stream are analyzed. The concentrations of CO, CO_2, NO, NO_2, the water content, and the residual oxygen content are continuously measured with a sample rate of 1 Hz using an *ABB* gas analyzer system (accuracies are given in Table 1). Here, NO_x was quantified using a UV photometer, CO and CO_2 using an IR photometer and the unburned hydrocarbons (UHC) using a flame ionization detector. The residual oxygen content was measured using a paramagnetic type analyzer. The water content was quantified using a *Vaisala HMT 338* sensor (uncertainty ± (1.5 + 0.015 · measured value) %RH).

Table 1: Ranges and accuracies of measured exhaust gas species

Species	**NO_2** ppm	**NO** ppm	**CO** ppm	**CO_2** vol.-%	**O_2** vol.-%	**UHC** mgC/m³
Range 1	0-10	0-10	0-10	0-5	0-5	0-10
Accuracy 1	0.1	0.1	0.1	0.05	0.025	0.2
Range 2	10-20	10-20	10-100	5-20	5-15	10-100
Accuracy 2	0.2	0.2	1.0	0.2	0.075	2
Range 3	20-50	20-50	100-200		15-25	100-2000
Accuracy 3	0.5	0.5	2.0		0.125	40
Range 4	50-200	50-200	200-500		25-100	2000-5000
Accuracy 4	2.0	2.0	5.0		0.5	100

For the presentation of the emissions, the common normalization method for gas turbine applications is used. The authors are aware that this causes a bias to the hydrogen combustion, as the differences to natural gas combustion is not considered well [6]. The emissions are referred to dry conditions and a residual oxygen content of 15 vol.-%. The normalization depends on the measurement method of the species. For wet measurements the correction is shown by Equation (1), where $C_{meas,wet}$ is the measured concentration of the species at wet conditions, C_{O2} is the residual oxygen content, C_{H2O} is the water content and C_{corr} is the corrected concentration.

$$C_{corr\ /ppm} = C_{meas,wet\ /ppm} \cdot \frac{20.95 - 15}{20.95 - C_{O2\ /vol.-\%}} \cdot \frac{1}{\left(1 - {C_{H2O}}/{10^6}\right)} \quad (1)$$

For species, already measured dry, the water correction can be deleted and Equation (2) results, where $C_{meas,dry}$ is the species measured in dry conditions.

$$C_{corr\ /ppm} = C_{meas,dry\ /ppm} \cdot \frac{20.95 - 15}{20.95 - C_{O2\ /vol.\%}} \quad (2)$$

The data shown in this work is time averaged for 100 s.

Experimental Setup

The main focus of this work was the investigation of hydrogen. In addition, one mixture of 50 m% H_2 and 50 m% natural gas with a lower heating value (LHV) of 66.5 MJ/kg was used.

The thermal power as well as the combustor inlet temperature were kept constant at MGT full load conditions for all measurements. The pilot split represents the ratio of fuel mass flow to the pilot to the overall fuel mass flow and is calculated using Equation (3). It was varied to investigate the influence of the pilot stage on the main stage. A second parameter variation was done on the burner air number, which is given in Equation (4), where AFR is the air fuel ratio. The burner air number represents the reciprocal value of the equivalence ratio.

$$S_{pilot} = \frac{\dot{m}_{fuel,pilot}}{\dot{m}_{fuel}} \quad (3) \qquad \lambda = \frac{1}{\phi} = \frac{\dot{m}_{air}}{\dot{m}_{air,stoichometric}} = \frac{\dot{m}_{air}}{\dot{m}_{fuel} \cdot AFR} \quad (4)$$

All settings are summarized in Table 2.

Table 2: Settings

Setting	Value / Range
Thermal power P	80 kW
Combustor inlet temperature T	600 °C
S_{pilot}	5 % – 30 %
λ	2.0 – 4.5

The optical access was used to apply the OH* chemiluminescence measurement. Here, the flame shape and position can be analyzed using the chemiluminescence signal emitted by the OH* radical [7]. This radical has a very short life time and is formed in the heat release zone. The chemiluminescence signal was detected using a *LaVision Imager Pro Plus 2M* intensified CCD camera equipped with a *CERCO* 2178 UV lens, a *Laser Components* high-transmission bandpass filter and *Schott* color glass filters. For all images, the gain was kept constant at a value of 75 %. The exposure time was varied according to the intensity from 100 to 350 µs. In Figure 4, a horizontal section through the combustion chamber is shown which depicts the field of view for the measurements. As OH* chemiluminescence is a line-of-sight technique, the flames from the 10 nozzles of the combustor appear as 6 flames in the images. For one average image, 500 single shots were taken and processed. Previously, the single shots were corrected for background noise and camera sensitivity. Finally, the images were cut and normalized to the combustion chamber dimensions. The images are all scaled to the common maximum. This was done using an inhouse code implemented in Davis software. To show the difference in exposure time, a scaling factor is given for each image, referring to the minimal exposure time for the campaign.

Results

For the investigation of the two versions of the combustor, different parametric studies were carried out. Firstly, a variation of the burner air number was carried out to analyze the optimal operation range. Both versions were compared regarding the influence of the mixing length. To determine the influence of the pilot on the main stage and the emissions, a variation of the split was carried out with the F400h.2. Finally, for the F400h.2 the fuel mixture specified in the experimental setup was tested at different burner air numbers.

Variation of burner air number for hydrogen operation

In Figure 5, the OH* chemiluminescence images for three different burner air numbers for the F400h.1 combustor are shown. On the right side, the corresponding NO_x emissions are plotted against the burner air number. It can be clearly seen, that the flames are highly lifted from the burner plate. This is due to the missing mixing section at the main stage, keeping the hydrogen shielded by the surrounding air flow. This configuration also leads to very high NO_x emissions. In addition, the emissions show, that the optimal operating point for the hydrogen combustor is located at higher burner air numbers, starting at 3.5. In the images, discrete single flames are visible corresponding to individual nozzles. The flames are short. Generally, with increasing burner air number, the flame height above burner increases as expected.

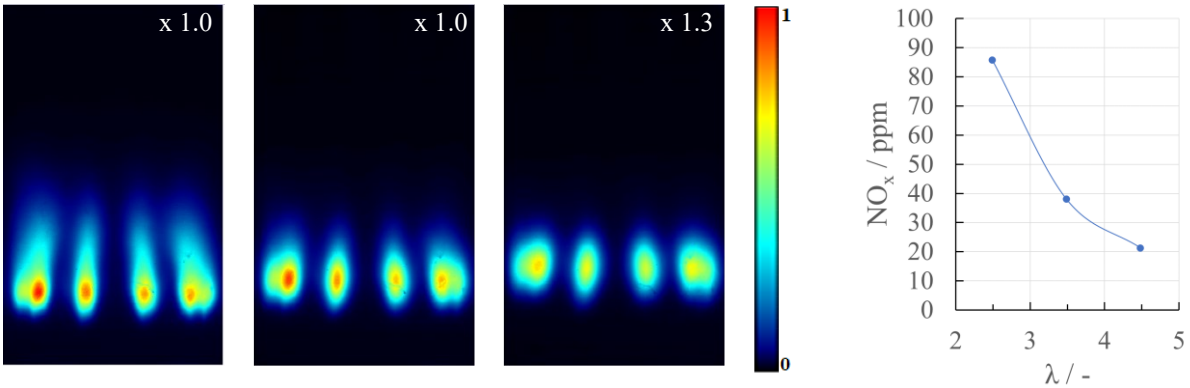

Figure 5. F400h.1 variation of burner air number for pure hydrogen and corresponding NO_x emissions

In Figure 6, the same parameter variation was carried out for the F400h.2 combustor. Here, the flames stabilize closer to the combustor plate, but are still lifted. For the hole campaign with this version, no flashback was observed. The flame length is larger compared to the first version. In the images, discrete single flames for every nozzle are visible. The height above burner increases with increasing burner air number. But this does not occur as remarkable as for the F400h.1(Figure 5).

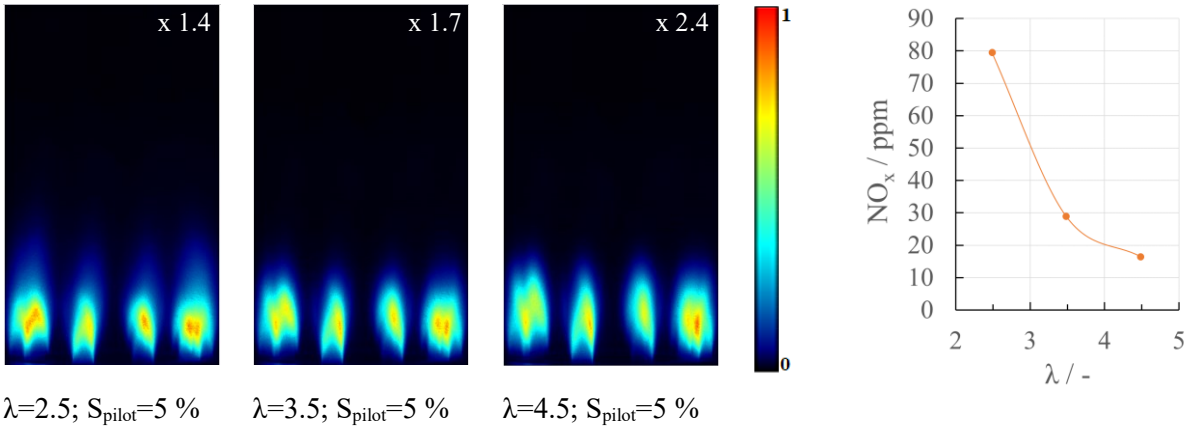

Figure 6. F400h.2 variation of burner air number for pure hydrogen and corresponding NO_x emissions

The effect of the pre-mixing of air and fuel is also visible in the emissions. They are reduced compared to the non-premixed F400h.1 version, but still not optimal. Here, for a burner air number higher than 3.5, the NO_x emissions are already lower than the German legal emission limit for natural gas combustion in micro gas turbines at 37 ppm [8].

The following investigations are all based on the F400h.2, as it turned out to be the more promising version for further improvements.

Variation of pilot split

In Figure 7, the influence of the pilot stage on the main stage was analyzed. Here, a parameter study was carried out on different pilot splits from 5 % up to 30 % at a constant burner air number of 4.5. The flames in all images are very similar. The height above burner and the flame length stay almost constant. As there is no optical access to the pilot, it is not possible to analyze the pilot flame itself.

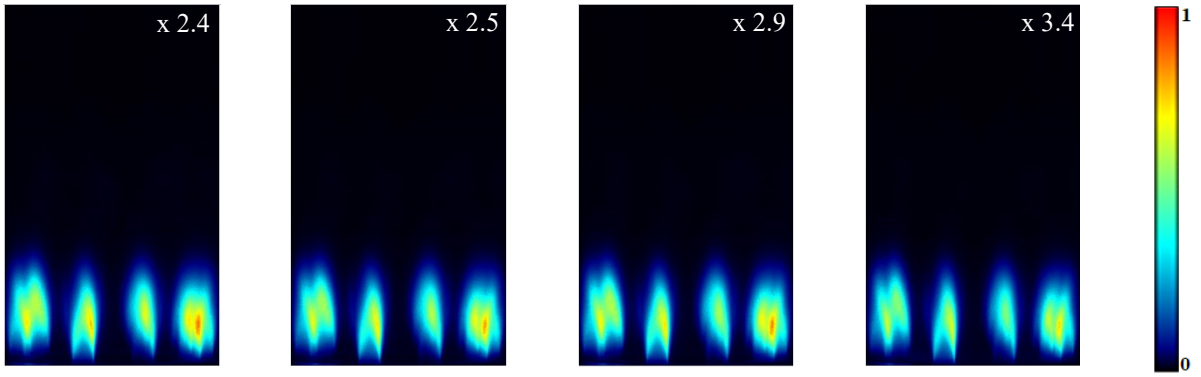

Figure 7. F400h.2 variation of pilot split for pure hydrogen

A clear influence can be seen in the NO_x emissions plotted against the pilot split in Figure 8. Here, the emissions increase with increasing mass flow to the pilot stage. This shows, that the pilot stage has a strong impact on the NO_x formation. For hydrogen combustion, the effect of the pilot stage on the flame stabilization of the main stage is almost negligible. Therefore, the pilot mass flow can be reduced significantly. However, due to thermal stress in the combustor head, it is not possible to completely switch of the pilot combustor. For start-up of the AE-T100 and to maintain the fuel flexibility, the pilot is still needed.

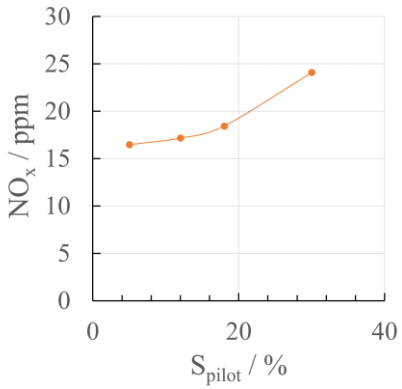

Figure 8. F400h.2: NO_x emissions for the pilot split variation with $\lambda = 4.5$

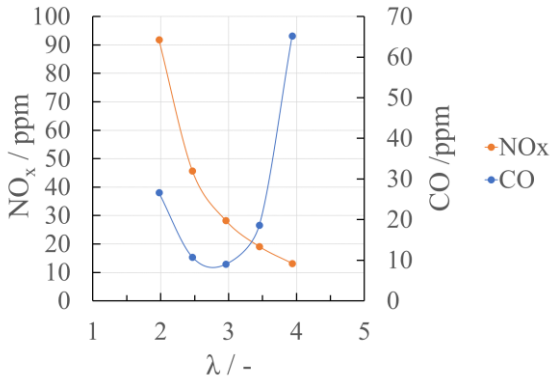

Figure 9. F400h.2: NO_x and CO emissions for the fuel mixture at different burner air numbers with $S_{pilot} = 5\%$

Variation of burner air number for the fuel mixture

For the investigation of the fuel flexibility, a mixture of hydrogen and natural gas was tested with the F400h.2 version. The mixture is a 50 m% hydrogen and 50 m% natural gas mixture, which corresponds

to 23.34 % natural gas and 72.66 % H_2 expressed in volumetric fractions. For this fuel mixture, the burner air number was varied from 2 to 4. Here, the emissions of NO_x and CO were analyzed (Figure 9). NO_x is measured at wet conditions and corrected by Equation (1). CO is already measured in dry conditions. Therefore, the correction was done according to Equation (2). With increasing burner air number, the NO_x emissions are decreasing due to the leaner conditions. The CO emissions show the common trend. At first, they are also decreasing with increasing burner air number. But for burner air numbers higher than 3, the conditions approach lean blow out, where CO emissions increase again. A burner air number of 4.5 was not feasible in this case due to limits in the air preheating device. In general, the emissions are within the legal limits for natural gas at burner air numbers from 3 to 3.5.

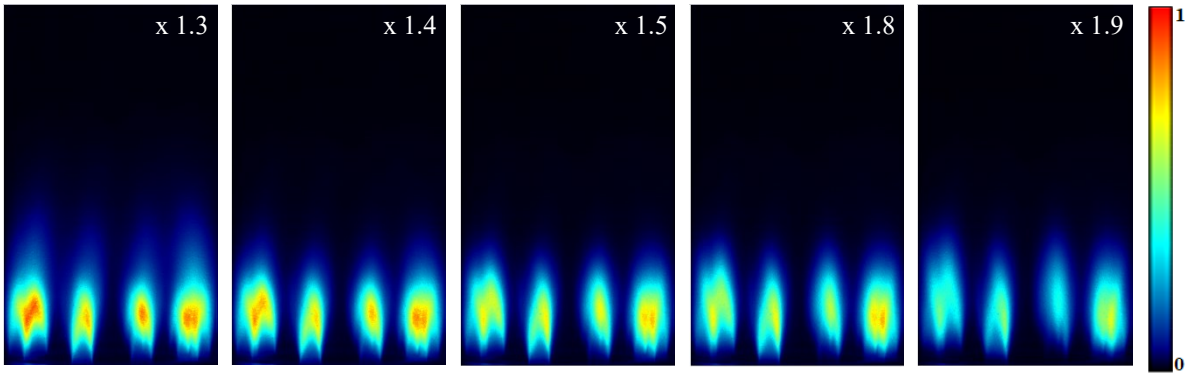

λ=2.0; S_{pilot}=5% λ=2.5; S_{pilot}=5% λ=3.0; S_{pilot}=5% λ=3.5; S_{pilot}=5% λ=4.0; S_{pilot}=5%

Figure 10. F400h.2 variation of burner air number for the fuel mixture

In Figure 10, the corresponding OH* chemiluminescence images are shown for the variation of the burner air number. Towards leaner conditions, the intensity decreases. Compared to pure hydrogen operation, the height above burner is increased, the flames are more lifted from the burner plate. With increasing burner air number, the height above burner increases only marginally.

The results from the hydrogen operation and the operation with the fuel mixture show, that it is possible to operate the combustor at one burner air number with both fuels, achieving acceptable emissions below the legal limits. Also, the OH* chemiluminescence images show for both cases a stable and lifted flame.

Summary and Conclusions

This study shows results from the further development of the F400s.3 combustor, which was originally developed for the use of a syngas mixture supplied by a wood gasifier. The combustor was modified for a safe use of both hydrogen, and mixtures of hydrogen and natural gas. Two different design versions, the F400h.1 and F400h.2 were introduced and tested in an atmospheric single combustor test rig. The main difference between the two versions was the premixing length in the nozzles of the main stage, before entering the combustion chamber. For both, a stable combustion was reached with pure hydrogen. Whereas the F400h.1 does not reach optimal emissions, lower emissions for NO_x could be reached with the F400h.2. For a burner air number higher than 3.5 the emissions are below the legal limit for natural gas combustion in a MGT. The influence of the pilot stage on the stabilization of the main stage was seen as negligible, whereas a strong influence on the emissions of NO_x was observed. Therefore, the pilot stage can be operated at a very low split of 5 %. Due to thermal stresses, it is undesirable to turn off the pilot stage completely. The F400h.2 showed its fuel flexibility at a fuel mixture of 50 m% H_2 and 50 m% natural gas. Here, low emissions could be reached at a burner air number of 3 to 3.5. It was proven, that with both fuels low emissions and at the same time stable combustion with the same combustor configuration could be reached.

The next steps are now further reduction of emissions and extension of the fuel flexibility of the combustor. Furthermore, the combustor has to be tested under real conditions in the MGT.

Acknowledgement
The authors would like to thank Stefan Fiedler and Timo Wagner for the support during the measurement campaign and Hannah Seliger-Ost and Jan Zanger for the support during the analysis.

References
[1] Zornek, Timo. “Entwicklung eines Holzgas-Brennkammersystems für die Mikrogasturbine Turbec T100.” (2019).
[2] Bower, Hannah E., Schwärzle, Andreas, Grimm, Felix, Zornek, Timo, and Kutne, Peter. “Experimental Analysis of a Micro Gas Turbine Combustor Optimized for Flexible Operation with Various Gaseous Fuel Compositions.” *Journal of Engineering for Gas Turbines and Power* Vol. 142 No. 031015 (2019): pp. 1–9. DOI 10.1115/1.4044901.
[3] Hohloch, M., Lingstädt, T., and Kutne, P. “Experimental Analysis of the Hydrogen Capability of a Fuel Flexible Jet Stabilized Syngas Micro Gas Turbine Combustor under Atmospheric Conditions.”. *Proceedings of the ASME Turbo Expo: Turbomachinery Technical Conference and Exposition - 2023: June 26-30, 2023, Boston MA*.
[4] Banihabib, Reyhaneh, Lingstädt, Timo, Wersland, Magnus, Kutne, Peter, and Assadi, Mohsen. “Development and testing of a 100 kW fuel-flexible micro gas turbine running on 100% hydrogen.” *International Journal of Hydrogen Energy* Vol. 49 (2024): pp. 92–111. DOI 10.1016/j.ijhydene.2023.06.317.
[5] Banihabib, Reyhaneh and Assadi, Mohsen. “A Hydrogen-Fueled Micro Gas Turbine Unit for Carbon-Free Heat and Power Generation.” *Sustainability* Vol. 14 No. 20 (2022): p. 13305. DOI 10.3390/su142013305.
[6] Hohloch, M., Seliger-Ost, H., and Kutne, P. “Experimental Investigation of the Fuel Flexibility of a Jet Stabilized Syngas Micro Gas Turbine Combustor Under Atmospheric Conditions.”. *31. Deutscher Flammentag.* Berlin, 27. - 28. September 2023.
[7] Dandy, D. S. and Vosen, S. R. “Numerical and Experimental Studies of Hydroxyl Radical Chemiluminescence in Methane-Air Flames.” *Combustion Science and Technology* Vol. 82 1-6 (1992): pp. 131–150.
[8] Bundesministerium für Umwelt, Naturschutz und nukleare Sicherheit. “Neufassung der Ersten Allgemeinen Verwaltungsvorschrift zum Bundes-Immissionsschutzgesetz (Technische Anleitung zur Reinhaltung der Luft – TA Luft).”, Gemeinsames Ministerialblatt, https://umweltmessung.com/wp-content/uploads/TA-Luft-2021-1.pdf (2021).

Development of flame monitoring methods for thermoacoustic instabilities in H_2 containing combustion

Y. John[1*], S. Eckart[2], C. Nailis[1] , D. Kuckelberg[1] , M. Juttu[2] , H. Krause[2]

*y.john@owi-aachen.de

[1] *OWI Science for Fuels (An-Institut der RWTH Aachen), Kaiserstraße 100, 52134 Herzogenrath,*

[2] *Institut für Wärmetechnik und Thermodynamik (GWA), Technische Universität Bergakademie Freiberg, Gustav-Zeuner-Straße 7, 09599 Freiberg*

Abstract

There is an increasing shift in the furnace industry from fossil-based energy carriers such as natural gas to renewable gases, such as hydrogen. Reports of preliminary tests of use of hydrogen-natural gas mixtures indicates the increasing interest of the industry to ramp up the fuel change in the future [1]. The increase of hydrogen in the fuel has shown to change flame response and acoustic output of the flame [2] which may under some conditions lead to thermoacoustic flame instabilities [3] and even flame extinction due to unfavourable interaction with the furnace environment and thermal and acoustic output of other combustors in the same furnace. In the current work, development of methods with the help of optical (in the visible and ultraviolet spectral ranges) and acoustic sensors to detect thermoacoustic instabilities for hydrogen-containing gas mixtures for the thermal processing industry is presented. Experiments were conducted using hydrogen-methane mixtures at a lab scale for the development of the method and subsequently at a scale closer to that of the industry. As part of the work at OWI, signal response of different sensors of different hydrogen-methane fuel ratios were investigated under laboratory conditions. The objective was to develop techniques to understand limits of sensors in detecting flame response when subjected to different amplitudes of external excitation and so develop methods for predicting possible flame instabilities such as blowoff or flashback.

Study at the laboratory scale

The study utilized raw signal data from a cost-effective microphone, two industrial flame monitoring systems, and an optical sensor (developed inhouse) capable of detection in both the ultraviolet (UV) and visible ranges. In this work the optical sensor capable of detection in the visible range will be further, for the sake of brevity, referred to as VIS sensor and likewise the other sensor capable of detection in the ultraviolet range as UV sensor. From literature studies, it can be seen that blending of hydrogen to natural gas (the current major fuel in the furnace industry) has an influence on the flame monitoring [4]. For the development of the method at the laboratory scale, two types of burners were used a premixed gauze stabilized flat flame burner and a non-premixed swirl-stabilized burner (Figure 1), both operating at a thermal power below 1 kW. The flames were externally acoustically excited with a loudspeaker using a sinusoidal wave at approximately 130 Hz. The choice is constrained to a particular range; the constraints here include audio sensitivity of the microphone and main frequency of electrically powered light and its harmonics. Additionally, the fact that the acoustic emissions of most furnace combustors lie in the lower frequency range was also considered. 130 Hz was then arbitrarily chosen within this range. Sensor data were recorded at a sampling rate of 48 kHz for approximately 30 seconds. A commercially available software (GNU Radio) was used to record the signals and FFT analyses were carried out for all the data with the help of a Python-code. Initially the premixed flame was acoustically excited at 42 Hz to verify that the visual, UV sensors and the microphone data are in agreement with each other.

To provoke flame instability, the input signal strength of the loudspeaker (measured in mV) is gradually increased which causes an increase in amplitude of the input sinusoidal signal. With increase in

amplitude of external excitation, the pressure fluctuations of the flame in both the burner types increase till a point is reached where the flame extinction is observed.

Before starting the experiments with flames, the repeatability of the recorded audio signal in the flat flame burner setup with increase in signal strength was verified with the help of multiple trials. Slight variations in the amplitudes of the audio signal were observed, but the overall qualitative trends are seen to be the same. The difference in conditions in the lab during the multiple trials is assumed to the reason for the variations.

Figure 1: Lab scale burners used: Premixed flat flame (left); Non premixed swirl flame (right)

During the experiments with flame, the mixture fraction of hydrogen in the methane-hydrogen mixture was gradually increased in both the burner types and the variation in sensor signal response is noted as the signal strength of loudspeaker is increased. An equivalence ratio of about 1 is always used for the different methane to hydrogen fractions. In Figure 2 the variation is shown for the case of the flat flame burner and the swirl burner. Each point in the figure results from an FFT analysis of the measurement. From the FFT spectrum, the 90^{th} percentile of the amplitude distribution was used as the value of each point. The 90^{th} percentile instead of the maximum value was used to account for external random noise which may distort the results. Additionally, each of the series of measurements (i.e. measurements with the same mixture fraction) was normalized using the maximum value of the corresponding series. From the resulting plot, a maximum value of amplitude is observed for all the measurements. From the analysis it can be observed that for increasing mixture fractions of hydrogen, a higher signal strength of external excitation is required to achieve this maximum. The increase of signal strength causes an amplification because of the flame and additionally a gradual decrease in the flame surface area on the gauze. The two opposing effects counterbalance each other such that a maximum is reached at a certain signal strength till flame blowoff occurs. The aforementioned maximum is seen to increase with higher H_2 molar fractions in the fuel mixture.

In the case of the swirl combustor (non-premixed case) a similar approach is followed as before. It is seen that the variation of the signal strength along with the different methane to hydrogen mixture fractions show quite similar quantitative trends. The variation of the VIS signal of the non-premixed case with different hydrogen to methane ratios is shown in Figure 3. The signals were captured using the raw signal of an industrial sensor. The values in this case are normalized using the maximum value of all the series of mixture fractions. It is seen that there is a light shift in the signal peak values depending on the mixture fraction. In the same figure, the frequency values in the FFT spectrum of the maximum amplitudes (f_{max}) shown on the left is plotted for every point. It is seen that for the case of the swirl stabilized burner, that although the burner being externally excited by the loudspeaker at 130 Hz, the frequency (f_{max}) does not always coincide with that of the excitation frequency. It is only at higher values of signal strengths does the maxima coincide with that of the excitation frequency. This behaviour is observed to differ to the case of the premixed burner.

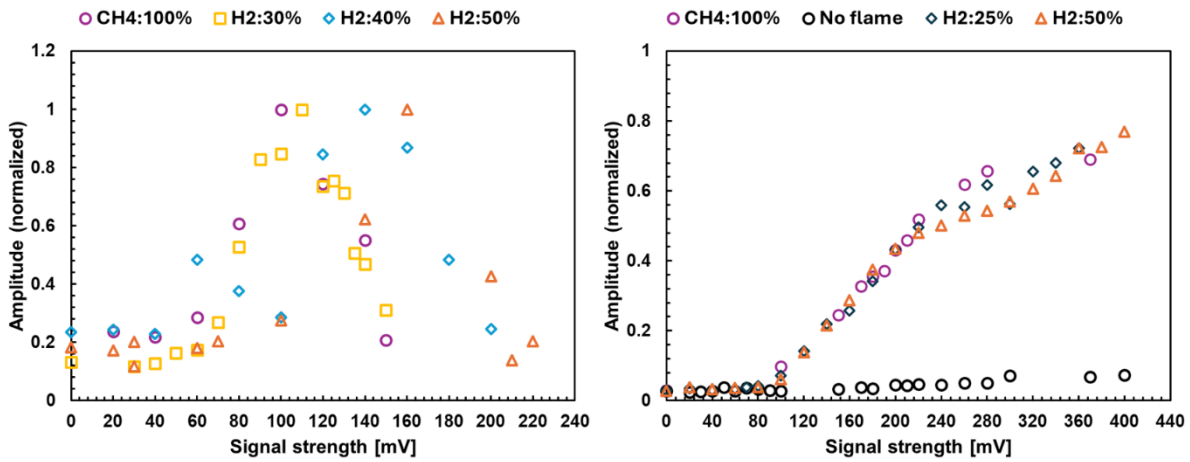

Figure 2: Amplification of acoustic signal with variation of H_2 mixture fractions: premixed case (left); non-premixed (right)

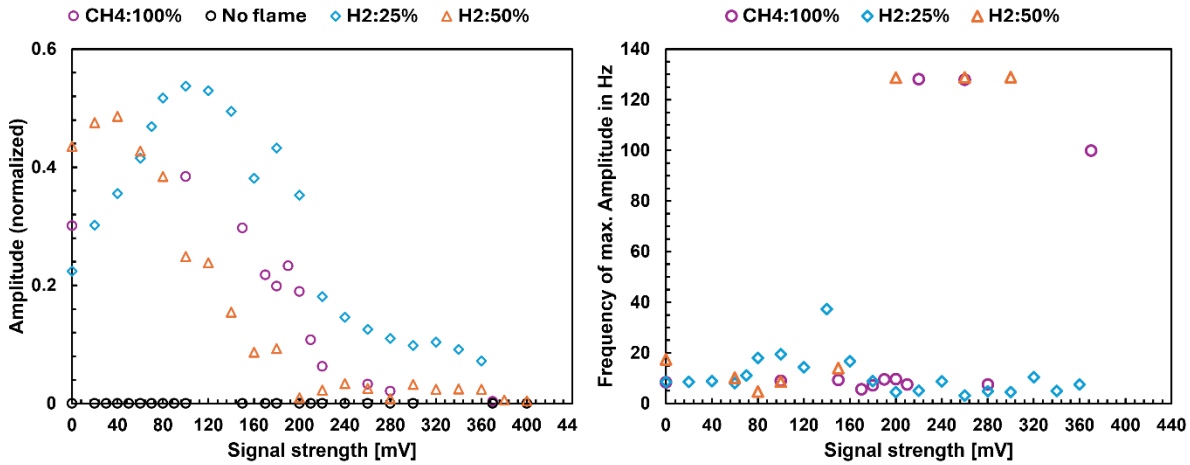

Figure 3: Variation of H2 fraction and input signal strength of the VIS signal (left) and frequency of the max. amplitude of the VIS signal (right) in the non-premixed case

Study of developed techniques on industrial scale burners

As part of the work, experiments were also conducted on a boiler at OWI fired by a partially premixed industrial burner. The boiler used for the experiments has four windows which allow optical access to the flame along its length. The positions of the inhouse sensors (UV and VIS) can be seen in Figure 4. The thermal power of the combustor can be varied between 15-35 kW and variation of H_2 in the fuel mixture in the current work was limited to a maximum of 35%.

For safety reasons, the flame was also monitored by the industrial combustor monitoring system, which is responsible for closing the fuel valves in case of absence of the flame. This in turn led to a limitation of the initially planned experimental matrix. To induce flame instabilities a gradual variation of the equivalence ratio is carried out till flame extinction was detected. The result of a particular case is shown in Figure 5; the fuel mixture of hydrogen and methane contains 35% H_2 and 15 kW thermal is produced with the parameters used. To induce instability, the equivalence ratio is gradually changed till a flame was no longer detected by the commercial flame monitoring system, which subsequently closed the valves. In the figure, it can be clearly seen that both the acoustic and optical sensors are able to clearly capture the change in flame behaviour. In both the plots at around 450 s, a sharp decay is seen in both signal amplitudes till the point where the flame is extinguished. The UV sensor used also showed similar signal response.

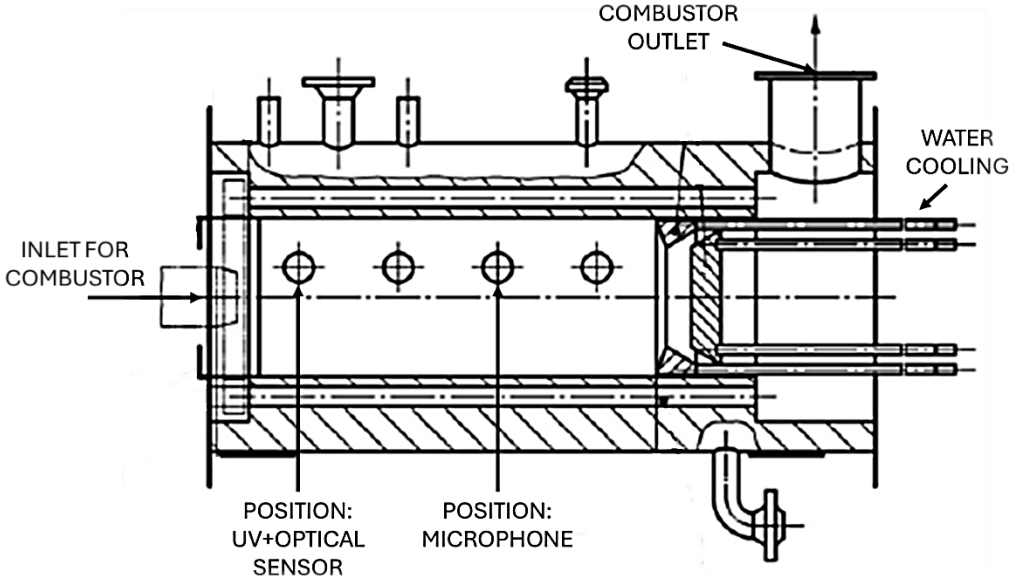

Figure 4: Boiler used for experiments at OWI

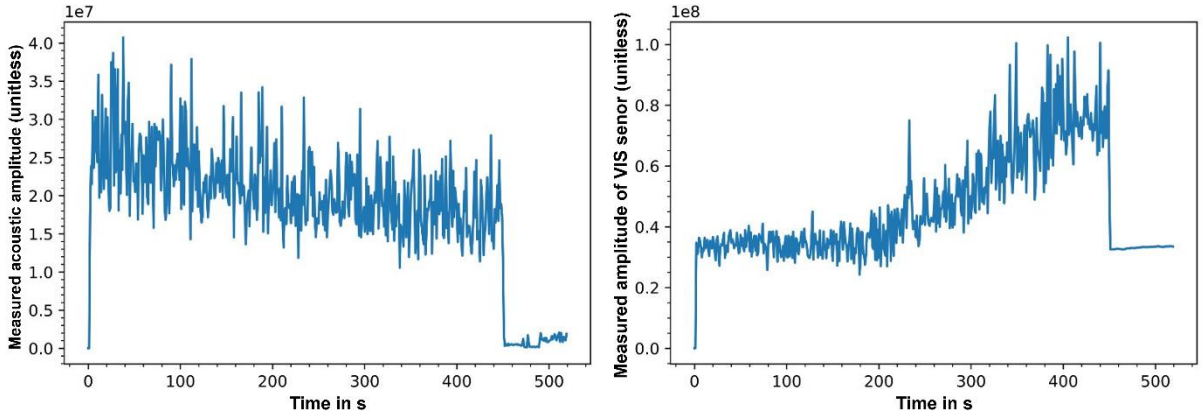

Figure 5: Amplitude of acoustic and VIS signals with time for a case with thermal power at 15 kW

Similar trends were seen also during an experimental campaign at the partner institute (GWA), where measurements were carried out on an experimental combustor setup. The maximum thermal power for the test rig for this work is 50 kW and the test rig was modified so that exhaust gas recirculation with N_2 was made possible. More information to the test rig can be found in the publication [5]. The air fuel ratio was held relatively constant close to the stoichiometric value and the hydrogen content was increased up to 100% hydrogen flame. Flame instability was induced mainly by variation of the N_2 recirculation rate. The recirculation rate is defined as the ratio of the volume flow rate of the recirculated gas (N_2) to the sum of the volume flow rates of the oxidizer (air) and recirculated gas. Along with detailed laser induced fluorescence measurements at GWA, the sensors mentioned above were also used to detect flame acoustic and optical emissions. The combined (UV+VIS) inhouse sensor was installed on the test rig with the help of an optical mount that protected the sensor from extreme temperatures. The microphone was additionally fixed in place with the help of a remote probe microphone [6], custom-made for the test rig. During the experiments, it was observed that the use of the VIS sensor was limited due to the resulting radiation which resulted in lack of contrast to the flame because of the extreme temperatures (~1600°C) in the chamber. The UV sensor however could capture changes in flame behaviour as was mentioned above in the case of the boiler. The results of an example case are shown in Figure 6, where the recirculation rate of N_2 was slowly increased in 1-minute increments till flame blow-off took place. During this run, the fuel rate was set to produce a thermal power of about 15 kW,

the fuel mixture additionally had a H_2:CH_4 ratio 75% H_2. After a phase of dynamic flame instability, flame extinction took place as the recirculation rate reached around 66%.

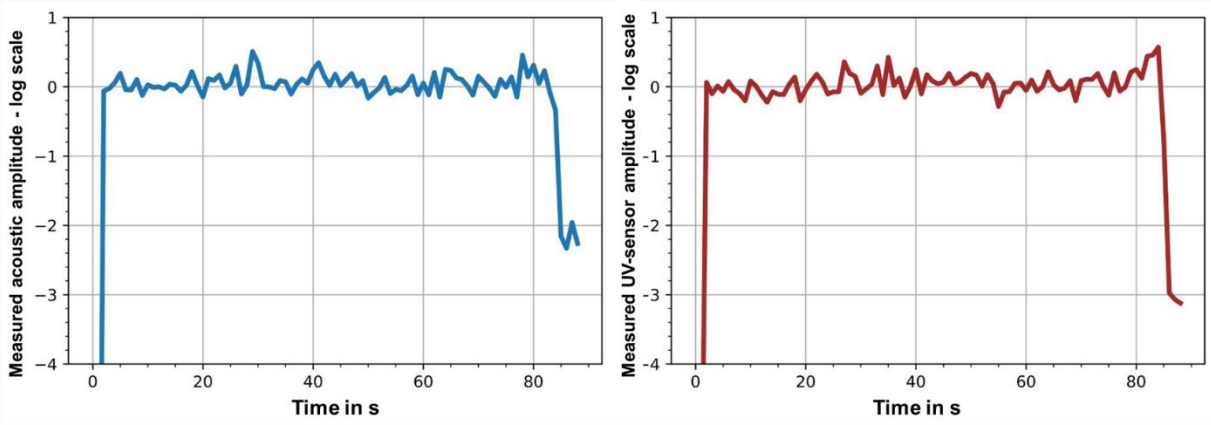

Figure 6: Amplitude of acoustic and UV signals with time for a case with thermal power at 15 kW

Summary

From the tests and methods developed at the laboratory scale and with the used sensors, clear qualitative trends could be observed with increasing mixture fractions. It could be clearly seen that variation of the fuel hydrogen content has implications on the acoustic and optical emissions of the flame. This in turn could mean that interactions with the chamber or furnace and with other flames (if present) could cause additional changes in flame behaviour in comparison to a pure methane/natural gas flame.

From the experimental results and the methods developed in this work, the authors believe that cost-effective optical and acoustic sensors can be useful for additional flame diagnostics relevant to industrial applications (in particular for the furnace industry). The effect of addition of hydrogen to the mixture and how this will affect flame stability, and its detection is however system specific and should be studied accordingly. From the results, it can also be postulated that a combination of acoustic and optical sensors will increase the probability of better recognizing instable conditions needed for active control.

References

[1] „BMWi - Die Nationale Wasserstoffstrategie“. [Online]. Verfügbar unter: https://www.bmwi.de/Redaktion/DE/Publikationen/Energie/die-nationale-wasserstoffstrategie.html

[2] J. G. Wäsle, „Vorhersage der Lärmemission turbulenter Vormischflammen“, PhD Thesis, 2007.

[3] I. Yilmaz, A. Ratner, M. Ilbas, und Y. Huang, „Experimental investigation of thermoacoustic coupling using blended hydrogen-methane fuels in a low swirl burner“, *International Journal of Hydrogen Energy*, Bd. 35, Nr. 1, S. 329–336, Jan. 2010, doi: 10.1016/j.ijhydene.2009.10.018.

[4] J. Ballester, R. Hernández, A. Sanz, A. Smolarz, J. Barroso, und A. Pina, „Chemiluminescence monitoring in premixed flames of natural gas and its blends with hydrogen“, *Proceedings of the Combustion Institute*, Bd. 32, Nr. 2, S. 2983–2991, Jan. 2009, doi: 10.1016/j.proci.2008.07.029.

[5] S. Eckart *u. a.*, „Conception of a pilot plant scaled optically accessible combustion chamber for determining the combustion properties of process, mixed and natural gases under the influence of external recirculation and changing wall conditions“.

[6] F. L. dos Santos, L. Botero-Bolívar, C. H. Venner, und L. D. de Santana, „Analysis of the remote microphone probe technique for the determination of turbulence quantities“, *Applied Acoustics*, Bd. 208, S. 109387, Juni 2023, doi: 10.1016/j.apacoust.2023.109387.

Optimization of blast furnace efficiency through Reactive Pulverized Coal Injection

Y. Höcker[1], R. Schott[1]

yannick.hoecker@hatch.com

[1] *Iron Making Technologies, Hatch Küttner GmbH, Alfredstraße 28, 45130 Essen, Germany*

Abstract

Pulverized coal injection (PCI) is an established method for reducing the total fuel costs of the blast furnace process. During the continuous thrive for optimization of this impact on the profitability, Hatch Küttner has developed the Reactive PCI technology. Targeting higher injection rates tolerated by the blast furnace process, the gasification and burnout of the injected coal has to be improved. Basic principle of Reactive PCI is the addition of a small amount of reactive gas to the transport gas of the dense-phase injection system. When entering the tuyere of the blast furnace (BF), the portion of reactive gas will cause an acceleration of the pulverized coal gasification. Thus, the PCI-rate can be increased while simultaneously decreasing the coke rate to enhance cost efficiency of the BF operation. Various gas mixtures available in steelworks can be considered as reactive gases, such as coke oven gas (COG), BF-top gas and converter off gas, but also pure gases like hydrogen or carbon monoxide. The potential of Reactive PCI has been analyzed using a proven procedure which has already been implemented for other PCI optimization techniques such as Oxycoal [1]. Simulations with an in-house CFD-raceway model show an earlier ignition of injected coal and indicate a possible increase in PCI-rate of approx. 10 % when Reactive PCI is applied. Combined with Oxycoal, even higher injection rates are achievable.

These promising results of the numerical simulations have been verified in industrial trials. Dense-phase pulverized coal injection with additional reactive gases has been tested successfully at one tuyere at a large-scale blast furnace BF#1 at thyssenkrupp steel Europe in Duisburg. Field measurements with pyrometers and a thermovision camera have confirmed the earlier ignition of the injected coal for different mixtures of reactive gases and enabled a qualitative analysis of the effect [2].

This article concludes with an evaluation of the economic benefit of Reactive PCI and Reactive Oxycoal resulting from achievable optimization of reducing agent consumptions. Therefore, the heat and mass balances of the BF process have been mathematically modelled based on an in-house BF mass and energy balance model [3] and the total fuel costs and possible cost reduction have been assessed for different injection technology scenarios with reference cost data for a representative exemplary blast furnace.

Introduction

The blast furnace process is still the dominant method to produce hot metal as part of the integrated steelmaking route. Main source of process energy and reducing agents is blast furnace coke. The production of coke is associated with high costs and CO_2 emissions. The substitution of expensive coke by injection of cost-efficient pulverized coal (PCI) is a well-established technique to reduce total fuel costs of the blast furnace. Additionally, minimizing the coke consumption of the blast furnace will improve the carbon footprint (scope 2) of the coking plant. Driven by constant pressure to maximize profitability and additional goals of the decarbonization program of the European steelmaking industry, the target of operators and technology owners is the continuous optimization of PCI-technology to achieve high injection rates with corresponding low coke rates.

The following will first address the key mechanisms and operating principles of pulverized coal injection at the blast furnace, before the latest development for optimization of the PCI-technology by use of reactive gases will be outlined. Based on this example, a methodology for assessing the technological and economic optimization potential is described, and the results for expected cost reduction are presented.

Pulverized coal injection

Figure 1 shows three different operating scenarios of the blast furnace process with PCI to illustrate interdependent mechanisms and limitations.

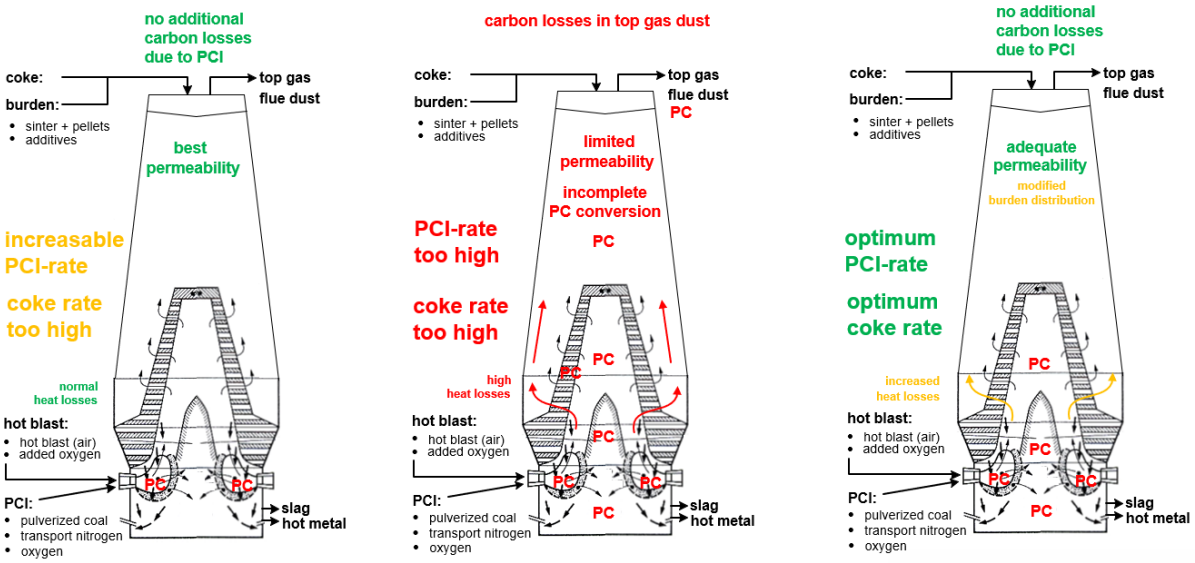

Figure 1. Mechanisms and limitations of the BF process using pulverized coal injection

The first scenario on the left shows a standard case for a blast furnace operated with PCI. Pulverized coal is injected into the tuyere and the coke rate is reduced according to the replacement ratio coke / coal. Hot blast parameters and oxygen input are adjusted to maintain constant hot metal production rate and raceway adiabatic flame temperature. The stability of the BF process is ensured by good permeability for reducing gases as injected pulverized coal particles are gasified completely within the tuyere and raceway without entering the coke bed [3]. However, there is optimizing potential left unexploited. The injection rate could still be increased.

An inefficient way of further increasing the pulverized coal injection rate is demonstrated in the second case of Figure 1. The injection rate into the BF has been increased beyond the capacity to gasify the injected PC within the lower part of the furnace. Unconverted pulverized coal is blocking the coke layer in the cohesive zone causing wall-bound flow of reducing gases, thus decreasing the reduction efficiency of the process. PC particles are even entering the upper part of the BF and leave the furnace as carbon losses in the top gas.

The targeted optimum operating scenario is shown on the right side of Figure 1. The burden and coke distribution of the blast furnace are modified to maintain an adequate permeability of the blast furnace process. The coke rate has been reduced to a possible minimum. The PCI rate has been increased up to that limit where the unreacted particles are still gasified completely in the lower part of the BF before negatively impacting permeability and pressure loss of the cohesive zone and upper part of the BF and no carbon losses via the top gas due to PCI do occur.

The adaptation of the blast furnace process to tolerate the highest possible coal injection rate is only feasible within a certain range defined by raw material qualities, burden distribution and given design parameters of the blast furnace (BF) and its ancillary equipment as well as the BF process itself [5].

Consequently, PCI technology has been continuously developed focusing on enhancing the gasification of injected pulverized coal within tuyere and raceway to allow only a minimum of unburnt particles to enter the material bed of the blast furnace. To achieve this target, the necessary preconditions as shown in Figure 2 must be maintained for the injected pulverized coal [4].

A state-of-the-art PCI injection system is based on dense-phase pneumatic conveying of pulverized coal (at grain sizes of 80% < 90 microns) to ensure a low transport gas ingress into the blast furnace. Minimum injection velocities at the lance tip induce good mixing of PC and hot air and longest possible retention time in the raceways for the coal particles to gasify completely.

The most recent step in optimization of pulverized coal injection has been the development of the Reactive PCI-technology. Combined with Oxycoal-Technology, where coal and oxygen are injected

together via coaxial lances, the highest level of coal injection rates into the blast furnace can be achieved using Reactive Oxycoal.

- **max. retention time of injected PC**
- **min. nitrogen ingress into BF**
- **good mixing of injected PC and hot blast**
- **small mean diameter of PC**
- **stable injection process**
- **high oxygen level at injected coal cloud**
- **use of reactive gases**
  => Reactive PCI Technology
  => Reactive Oxycoal Technology

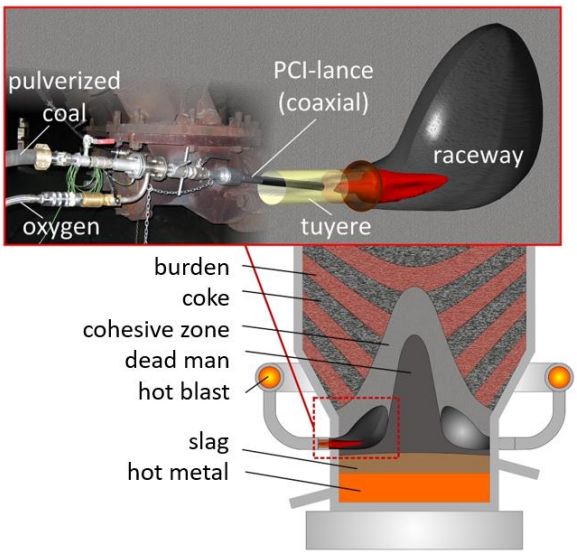

Figure 2. Preconditions for optimum pulverized coal injection [4]

Technology of Reactive PCI and Reactive Oxycoal

The main idea of Reactive PCI and Reactive Oxycoal is to accelerate coal gasification during the flight time of the injected particles within the tuyere and raceway of the BF. A small portion of reactive gas is added to the transport gas into the pulverized coal injection line. These added reactive gases will act as degassed volatiles of the injected coal, thus saving time of the pulverized coal degassing during the injection process and initiating an earlier ignition [2].

The basic flow scheme of a pulverized coal system equipped with Reactive PCI / Reactive Oxycoal technology is shown in figure 3.

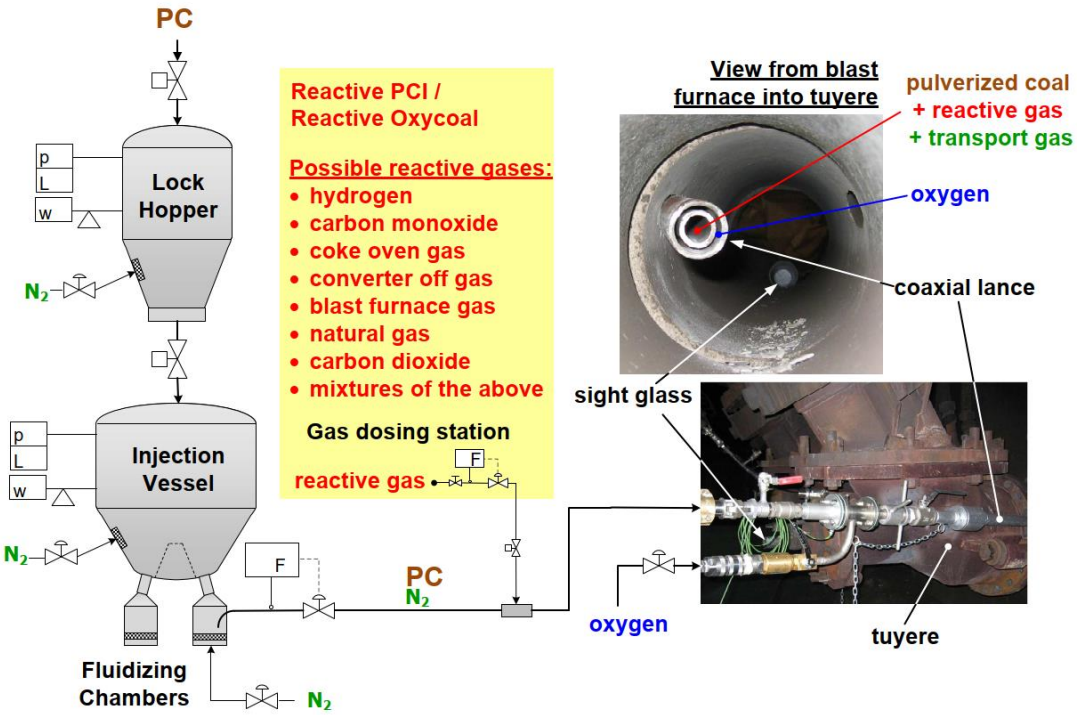

Figure 3. Concept flow scheme of Reactive PCI / Reactive Oxycoal [2]

Pulverized coal is discharged from a pressurized injection vessel into the injection lines and conveyed with the best-possible dense phase technology and minimum transport gas to the blast furnace tuyeres. Downstream of the coal flow regulation valve, the reactive gas is added to the pulverized coal partly replacing nitrogen as transport gas. Different pure gases such as hydrogen or carbon monoxide or gas mixtures like coke oven gas, blast furnace gas or natural gas can be used. Depending on the availability and operation costs of possible reactive gases, an individual solution for each steel work will prove efficient. A gas dosing station will control and distribute the reactive gas flow to all related injection lines and provide stable and safe supply of reactive gas.

Utilizing the advantages of dense phase pneumatic transport, the coal is then injected at a high transport gas loading and low velocities through either a single lance (Reactive PCI) or a coaxial lance with oxygen (Reactive Oxycoal). When leaving the injection lance, the reactive gas immediately ignites and reacts with the oxygen in the hot blast (Reactive PCI) or the oxygen from the coaxial lance (Reactive Oxycoal). The energy released by this reaction will accelerate the further coal gasification reactions within the short flight time of the coal particles through tuyere and raceway. This enables the blast furnace process to increase the pulverized coal injection rate while simultaneously reducing the coke rate according to the replacement ratio in order to improve the profitability of production [2].

The idea and working principle of Reactive PCI and Reactive Oxycoal have been investigated and verified by use of numerical simulations and field trials. To evaluate the impact of the additional reactive gas on the coal gasification in the raceway, first a proven simulation model was used. A specifically designed CFD-raceway model, which has been developed to forecast the effects of the Oxycoal technology in [1], has been adjusted to the operating scenarios of Reactive PCI and Reactive Oxycoal. Simulations have been carried out for different reactive gases and the results were compared to the reference case of standard dense phase PCI. The results clearly indicate an earlier ignition of the injected coal, faster gasification and a better burnout when using reactive gases. Considering coke oven gas (mixed with transport nitrogen component volume shares result to 23,1% H_2, 10,5% CH_4, 6,3% CO, 1,3% CO_2 and 58,8% N_2) a possible increase in pulverized coal injection rate of up to 11,9% for Reactive PCI and up to 26,6% for Reactive Oxycoal can be expected compared to the reference case [2].

Based on the promising simulation results, industrial trials were carried out at one tuyere of blast furnace 1 at thyssenkrupp steel in Duisburg to evaluate the effect of the pulverized coal injection with reactive gases at an operating blast furnace. A mixing gas station was designed and built to create gas mixtures of CO, H_2, CH_4, CO_2 and N_2 similar to common industrial gases such as blast furnace top gas and coke oven gas. The mixed reactive gases were dosed into the injection pipeline via a sinter metal tube and then the mixture of pulverized coal, transport nitrogen and reactive gas was injected via a single lance or a coaxial lance (with Oxycoal) into the blast furnace tuyere. The injection process was observed via the tuyere sight class by either an optical camera combined with a pyrometer or by a thermovision camera. Figure 4 graphically visualizes the effects in tuyere and raceway for the individual cases: standard dense phase PCI, Reactive PCI and Reactive Oxycoal [2].

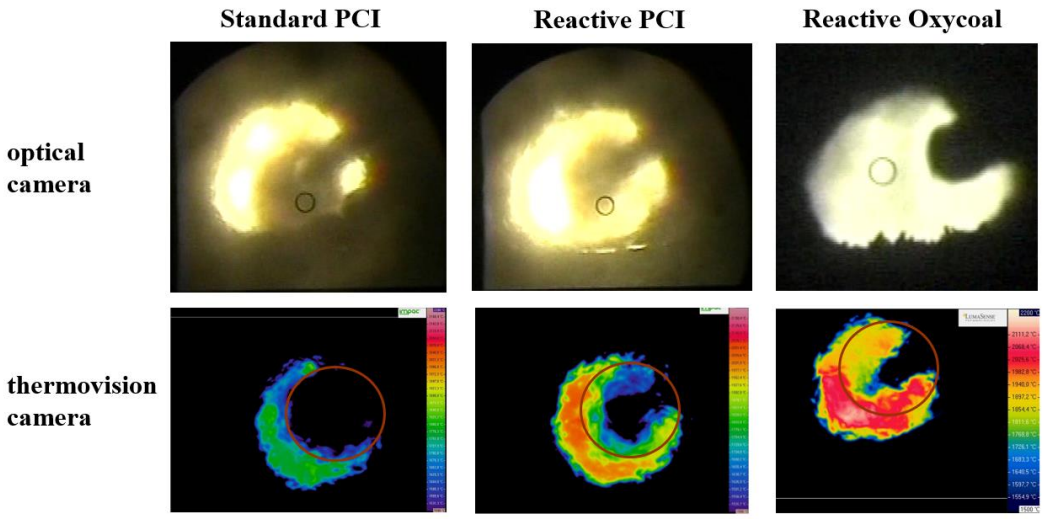

Figure 4. Raceway view of blast furnace: optimized gasification of injected pulverized coal [2]

The successful trials together with the numerical simulations verify the earlier ignition and a faster coal conversion within the raceway when using Reactive PCI instead of standard dense phase PCI or Reactive Oxycoal as an upgrade to standard Oxycoal. This enables the blast furnace process to be operated at increased pulverized coal injection rates associated with corresponding reduced coke rates.

Evaluation of operating cost reduction potential by Reactive PCI and Reactive Oxycoal

Based on the demonstration of the process-related advantages of Reactive PCI / Reactive Oxycoal, the resulting potential of the technology to reduce blast furnace total fuel costs is quantitatively evaluated. The economic analysis considers exemplary a mid-size blast furnace with 28 tuyeres and a daily production rate of 4.960 t_{HM}/d. The heat and mass balances of the BF process have been mathematically modelled based on an in-house BF mass and energy balance model [3] to define the major material and energy streams for the reference case. The blast furnace is operated with standard pulverized coal injection at 181,7 kg/t_{HM} and a corresponding coke rate of 321,7 kg/t_{HM}. The hot blast conditions are given to 1.010 Nm³/t_{HM} of specific hot blast flow with an enriched oxygen content of 23,85 Vol%.

The driving factor for total fuel cost reduction by upgraded injection technology is the price difference between coke and pulverized coal and the achievable boost in injection rate and decrease in coke rate. To validate the economic benefit of the new technologies Reactive PCI and Reactive Oxycoal, first our CFD-raceway model [1] is used to simulate the expected injection rate increase compared to the reference case. Coke oven gas is considered as reactive gas with a flow of 20 Nm³/h per lance (tuyere). The oxygen flow per lance is set to 250 Nm³/h for the Reactive Oxycoal case. The raceway simulation results for these scenarios forecast an injection rate increase of +11,8 % for Reactive PCI and +23,1 % for Reactive Oxycoal compared to standard PCI. The corresponding coke rate reduction is calculated with the replacement ratio coke/coal of 0,85 kg_{Coke}/kg_{PC}.

As a first approximation the cost reduction can be estimated by comparing the fuel costs for the individual consumptions of coke, coal and reactive gas in the three scenarios. The fuel price data presented in Table 1 are based on current information from blast furnace operators.

Table 1. Fuel price data

Fuel	Unit
Coke	119 €/t
Pulverized coal	230 €/t
Coke oven gas	15 €/GJ

The use of oxygen in the Reactive Oxycoal case is not directly impacting the fuel costs, as the oxygen injected through the coaxial lances is only diverted from the hot blast oxygen enrichment. The total oxygen consumption of the blast furnace process remains the same as it is directly linked to the hot metal production rate [3]. The removal of oxygen from the hot blast when using Reactive Oxycoal leads factually to a small reduction of total hot blast flow into the BF.

When applying pulverized coal injection in relation to the all-coke operation of the BF and the subsequent changes by increasing the injection rate and further decreasing the coke rate, the substitution of coke by injected pulverized coal will implicate a higher flow of blast furnace top gas [3]. This additional blast furnace is available for other profitable uses such as electric power generation (credit: 8,6 €/GJ, adjusted for inflation) [5].

This interpretation led to the development of a more comprehensive approach to analyze the cost reduction potential of Reactive PCI and Reactive Oxycoal compared to the standard PCI case. A simplified heat and mass balance model was used to account for the increased output of blast furnace top gas as a function of the injection rate.

With respect to the importance of improving the carbon footprint of blast furnace and coking plant, the potential of mitigating CO_2 emissions by applying the Reactive PCI / Reactive Oxycoal technologies was evaluated. Reduced emissions can further be regarded as economic benefit based on credit per avoided ton of CO_2 (reference value: 55 €/t_{CO2}).

The injection of a reactive gas has a direct influence on the carbon-based emissions of the blast furnace process. Injected reactive gas will additionally act as a reducing agent in the blast furnace process and by itself substitute a certain small amount of coke or PC. Coke oven gas has a hydrogen

content of approx. 55°Vol % and this carbon-neutral hydrogen will replace carbon-related coke (fixed carbon approx. 86 wt%) according to an estimated replacement ratio of 0,19 kg_{Coke}/Nm^3_{H2}. Due to the relatively small amount of reactive gas required to optimize injection, this impact on minimizing scope 1 emissions is rather small but still present.

Mitigated scope 2 emissions are related to the production of blast furnace coke in the coking plant. The coke ovens are generally heated by a mixture of blast furnace top gas and coke oven gas. Both gases are based on fossil fuels and have a significant carbon footprint (reference value for COG: 41,05 t_{CO2}/TJ; for BFG: 263,45 t_{CO2}/TJ). Decreasing the coke rate of the blast furnace by increasing pulverized coal injection rates saves the necessary heating energy of the not produced coke and the required fuel gas consumptions accordingly, thus reducing their contribution to the emissions of the coking plant. In this example the shares in the heating gas of the coke ovens are considered with 60 % BF top gas and 40 % coke oven gas. Considering an energy requirement for coke making to be covered by heating gases of 1,12 MJ/kg_{coke}, the reduced gas consumption can be estimated. The benefit of reducing the total fuel costs is assessed based on the credit for saved CO_2 and further the credit for the saved blast furnace top gas and coke oven gas as both gases are available for other consumers.

The total fuel costs for the three scenarios were calculated using the comprehensive approach described. The costs given for the reference case of standard PCI include the relevant expenditures for coke and pulverized coal minus relevant top gas credits and carbon savings due to injection rate of 181,7 kg/t_{HM} of pulverized coal in comparison to an all-coke operation of the BF.

Injection rates were then increased to 203,1 kg/t_{HM} for Reactive PCI and 223,6 kg/t_{HM} for Reactive Oxycoal, which corresponds to coke rates of 303,5 kg/t_{HM} and 286,0 kg/t_{HM} respectively. Figure 5 illustrates the results of the fuel cost calculation indicating the significant economic impact of the new injection technologies.

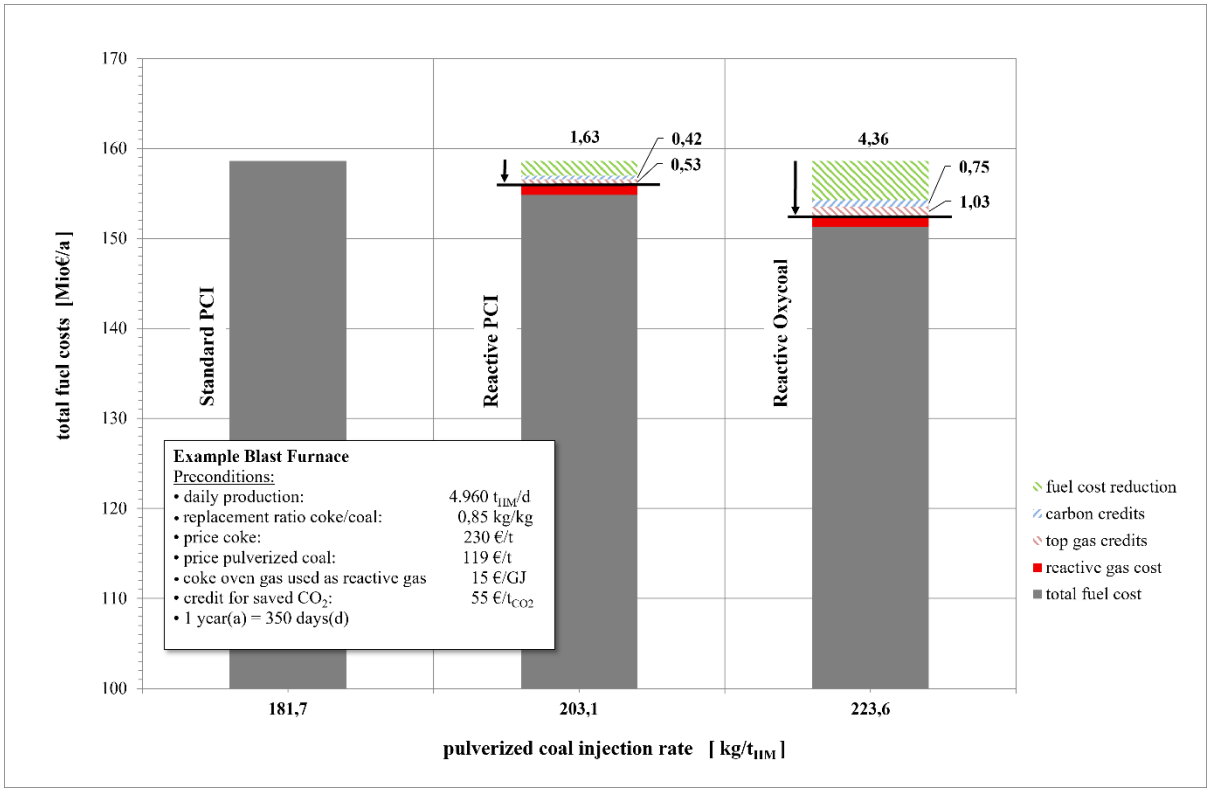

Figure 5. Comprehensive fuel costs compared for standard PCI, Reactive PCI and Reactive Oxycoal

For Reactive PCI an overall total fuel cost reduction of 2,58 Mio€/a compared to the reference case is calculated. The expected benefit for Reactive Oxycoal is even higher, up to 6,14 Mio€/a, demonstrating the potential of further injection rate increase through better gasification using coaxial lances with oxygen.

The individual cost and cost reduction factors are highlighted in figure 5. There is a certain dependency on the price of the selected reactive gas compared to the level of cost reduction. Cheaper blast furnace top gas could also be used, but the expected increase in injection rate is lower compared to coke oven gas [2]. Green hydrogen does have a similar impact on the coal gasification and burnout in tuyere and raceway like coke oven gas but is more expensive (roughly by factor 2).

The consideration of additional credits for blast furnace top gas and saved coke oven heating gas for the cost calculation does reduce the total fuel cost by 0,53 Mio€/a for Reactive PCI and 1,03 Mio€/a for Reactive Oxycoal.

Focusing on the potential of the technologies to contribute to improving the carbon footprint of blast furnace and coking plant, the sum of saved scope 1 and scope 2 emissions is calculated to 7.710 tCO_2 per year for Reactive PCI and 13.629 tCO_2 per year for Reactive Oxycoal in relation to standard PCI operation of the here regarded example blast furnace. The resulting contribution to the total fuel cost reduction by emission credits is calculated to 0,42 Mio€/a for Reactive PCI and 0,75 Mio€/a for Reactive Oxycoal. This relates to a portion of the total reduction of 16,3 % for Reactive PCI and 12,2 % for Reactive Oxycoal.

The major cost reducing factor remains the price difference of injected pulverized coal compared to the substituted expensive coke. The economic analysis of the example blast furnace clearly marks the potential of the Reactive PCI / Reactive Oxycoal technology to further reduce the total fuel costs and thus optimize the efficiency of the blast furnace process. In comparison, the CAPEX costs for the necessary plant technology are relatively low, so that payback periods of 0,9–1,6 years can be expected.

Conclusion

Reactive PCI has been developed by Hatch Küttner to further optimize the pulverized coal injection technology thus achieving highest possible coal injection rates which minimizes the required coke rates and ultimately the blast furnace total fuel costs. Various reactive gases can be added to the pulverized coal injection lines to achieve an earlier ignition and faster coal gasification in the lower part of the blast furnace. The mechanisms and their positive effects on the injection process have been successfully verified using numerical simulations and industrial injection tests on an operating blast furnace.

Before operators invest in new technologies, they need a profitable earnings logic. Therefore, a procedure was developed to forecast the expected impact on the injection process and the potential economic benefits. The CFD raceway model for the numerical simulation of pulverized coal gasification and burnout in the tuyere and raceway of the blast furnace is proven and can be used to reliably predict the extent of the expected optimization of the injection rates. Based on the determined possible increase of the PC injection rate, a calculation model was developed to assess the economic impact on the fuel costs of a blast furnace with standard pulverized coal injection. In addition to the major factor of substitution of expensive coke by cheaper pulverized coal, basic mass and energy balances for coke oven gas, BF top gas and hot blast with related credits as well as scope 1 and scope 2 CO_2 emission savings in the coking plant were considered. The cost optimization potential of Reactive PCI and Reactive Oxycoal has been calculated for an exemplary mid-size blast furnace with coke oven gas as considered reactive gas comparing both scenarios to the reference case of standard dense-phase PCI.

For projected injection rate increases by +11,8 % for Reactive PCI and +23,1 % for Reactive Oxycoal, the results of the economic assessment underline the potential of these technologies to optimize the efficiency of the blast furnace process. Annual savings between 2 - 7 Mio€ are possible for a mid-size blast furnace.

This method for evaluating the potential increase in the pulverized coal injection rate and the resulting process and cost benefits can be adapted with specific cost and operating data for different steel mills and scenarios in order to find the most efficient solution for each individual case. Depending on the local boundary conditions, production capacities and availability of reactive gases, the return on invest (ROI) for the necessary plant modifications can vary. However, ROIs of approx. 0,9-1,6 years are realistic.

The expected availability of affordable green hydrogen in the medium term and potentially further rising prices for CO_2 certificates offer a new opportunity to further improve the cost-optimization potential of this technology alongside reducing the carbon footprint of the blast furnace process. At the current cost of green hydrogen of approx. 0,5 €/Nm^3 this application would not be economically viable.

Literature

[1] Schott, R.; Schumacher, M.: *Modellierung von effizientem Kohlenstaubeinblasen in den Hochofen mittels der Oxycoal-Technik*, stahl und eisen, 134, 29-38, 2014

[2] Schott, R.: *Reactive Pulverized Coal Injection – A quite and simple but very effective idea*, stahl und eisen international, 11, XVI-XXI, 2019

[3] Schott, R.; Malek, C.; Schott, H. K.: *Effizienzsteigerung des Reduktionsmitteleinsatzes im Hochofen zur CO_2-Minderung und Kostenersparnis*, Chemie Ingenieur Technik 84, No. 7, 1076-1084, 2012

[4] Schott, R.: *Optimization strategies for pulverized coal injection into the blast furnace*, stahl und eisen, 136, Nr. 3, 39-47, 2016

[5] Peters, M.; Korthas, B.; Schmöle, P.: *The Past, Present and Future of Pulverized Coal Injection at ThyssenKrupp Steel AG*, Proceedings of 36th McMaster University Symposium on Iron and Steelmaking, 14-29, Hamilton, Ontario, Canada, 2008

Development of a High-Temperature Macro-TGA for Industrial-Scale Calcination and Sintering of Magnesite

R. Aghaei[1,2], B. Weiß[1,2], M. Kiss[1,2], M. Bösenhofer[1], CH. Jordan[1], M. Gruber[3], M. Harasek[1]

reyhane.aghaei@k1-met.com, barbara.weiss@k1-met.com

[1]*Institute of Chemical, Environmental & Bioscience Engineering, Technische Universität Wien, Vienna, Austria*
[2]*K1-MET GmbH, Linz, Austria*
[3]*RHI Magnesite GmbH, Vienna, Austria*

Abstract

Refractory materials such as magnesia (MgO) and doloma (MgO - CaO) play a critical role in high-temperature industrial processes due to their exceptional thermal stability and chemical resistance. Their production relies on controlled calcination and sintering processes, where parameters like temperature, heating rate, and atmosphere directly influence the final material properties. To better understand and optimize these processes, we pursue an integrated approach combining laboratory-scale thermogravimetric analysis (TGA), computational fluid dynamics (CFD) simulations, and the development of a novel high-temperature MacroTGA system. In this manuscript, we present an analysis of the thermal behavior of materials used in the production of refractory materials, based on laboratory-scale thermogravimetric (TG) analyses. Lab-scale TGA and differential scanning calorimetry (DSC) experiments were conducted on various magnesite- and dolomite-based raw material fractions to assess their decomposition behavior and thermal characteristics. The results provide insights into reaction kinetics, mass loss, and enthalpy changes during decomposition, forming a foundation for the development of future MacroTGA experiments. Additionally, we introduce a computational fluid dynamics (CFD) approach for modeling thermal decomposition behavior. The CFD model was developed using a Euler-Euler approach to simulate thermal decomposition in porous media under controlled conditions. The model includes diffusive transport through the porous sample and gas-solid reactions based on Arrhenius-type kinetics. Preliminary results of simulating the lab-scale TGA experiments show the potential of the employed approach and highlight the necessity to determine sample specific reaction kinetics in future work with a novel high-temperature MacroTGA, that is currently in development.

1. Introduction

Refractory materials are essential in high-temperature industrial processes such as metallurgy, cement production, and energy generation due to their ability to withstand extreme thermal and chemical conditions without undergoing significant structural or compositional degradation. These materials, primarily composed of oxides like magnesia (MgO) and calcium oxide (CaO), are critical for lining furnaces, kilns, and reactors where temperatures can exceed 1500°C [1]. Among the most widely used refractory materials are magnesia (MgO) and doloma, which is a composite of magnesium oxide and calcium oxide (MgO - CaO). Their outstanding performance in harsh environments is primarily due to their high melting points, excellent thermal stability, and strong resistance to corrosive agents like iron oxides, alkalis, and lime-rich slags, which are common byproducts in metallurgical processes, especially in steelmaking [2].

Magnesia (MgO), which has a melting point of approximately 2800 °C, is one of the most thermally stable oxide materials used in refractory applications. It is typically derived from the thermal decomposition of magnesite ($MgCO_3$), a naturally occurring mineral. The transformation of magnesite into refractory-grade magnesia involves two key thermal processes: calcination and sintering. During calcination, which typically takes place at temperatures ranging from 600 to 800 °C, magnesite does not melt but decomposes in an endothermic reaction, releasing carbon dioxide (CO_2) and forming reactive, porous magnesium oxide. However, this porous structure lacks the mechanical strength and stability required for refractory applications. Therefore, a subsequent sintering process is employed at much higher temperature [3], [4].

Similarly, dolomite - a sedimentary carbonate rock composed predominantly of $CaMg(CO_3)_2$ - is a key raw material used in the production of doloma-based refractories. When heated in an inert nitrogen atmosphere, dolomite undergoes a single-step decomposition reaction, yielding a mixture of calcium oxide and magnesium oxide (CaO·MgO) along with the release of carbon dioxide. This decomposition begins at around 900 °C, following the breakdown of its carbonate structure. Depending on the atmosphere, dolomite decomposes also in two stages or even three stages. First, $MgCO_3$ decomposes at ~750°C, followed by $CaCO_3$ at ~900°C, yielding a mixture of MgO and CaO. Like magnesite, dolomite must also be subjected to high-temperature sintering - typically between 1600 and 1700 °C - to achieve a dense microstructure with enhanced mechanical properties and thermal stability required for refractory applications [5].

In both magnesia and doloma production, the quality of the final refractory product strongly depends on the temperatures and heating profiles used during calcination and sintering. Calcination temperature, sintering temperature, heating rate, atmosphere, and raw material characteristics directly influence the microstructural evolution, including densification, grain growth, pore morphology, and phase transformation. As demonstrated in recent studies, higher calcination temperatures lead to increased crystallite size and reduced surface area of magnesia, thereby lowering its reactivity and hydration rate [6]. For high-performance refractory applications, such as in steelmaking furnaces exposed to aggressive slags and rapid thermal cycling, the use of dead-burned magnesia with well-developed MgO grains and minimal open porosity is essential to ensure structural stability [7].

Thermogravimetric analysis (TGA) is a powerful technique for studying the decomposition and thermal stability of carbonate minerals. It allows for the precise determination of mass changes due to gas evolution and enables the extraction of kinetic parameters for the decomposition reactions. Conventional lab-scale TGA systems are designed for analyzing small, homogeneous samples (typically in the milligram range). In an industrial rotary kiln, where calcination and sintering processes of raw material happen, the grain size of the raw material is in the range of several cm. For such large samples thermal gradients, heat and mass transport effects, and heterogeneous reactions dominate, that cannot be analyzed with conventional lab-scale TGA systems [8].

To bridge this gap, there is a growing need to develop macro-TGA systems capable of operating at high temperatures and handling sample masses in the range of hundreds of grams to kilograms. Such systems can provide a more realistic approximation of calcination and sintering behavior in industrial setups. However, the design and operation of macro-TGA present significant challenges, including maintaining uniform heating, ensuring accurate mass measurements, and dealing with prolonged reaction durations under high thermal loads. Additional to the big sample size, a macro-TGA to investigate calcination and sintering poses the challenge to be able to reach temperature up to 1800 °C. Such high temperatures require special adaptations for the design of the MacroTGA oven. Commonly applied materials exceed their thermal stability limit when operating the TGA at 1800 °C. The material for the heating elements, the furnace pipe and the crucible must be carefully selected. Achieving and maintaining uniform temperature profiles becomes increasingly difficult at higher temperatures.

In this Manuscript, we give an insight into the thermal behavior of materials used to produce refractory material based on conducted lab-scale TG Analyses. The presented lab-scale experiments give valuable insights into the decomposition of those raw materials, which serve as foundation for the design of future MacroTGA experiments. Furthermore, we present a CFD approach with which the thermal decomposition can be modeled.

Figure 1 shows how the presented work is embedded in the wider scope of pursuing to optimize industrial sintering and calcination processes and make them adaptable to changing process requirements.

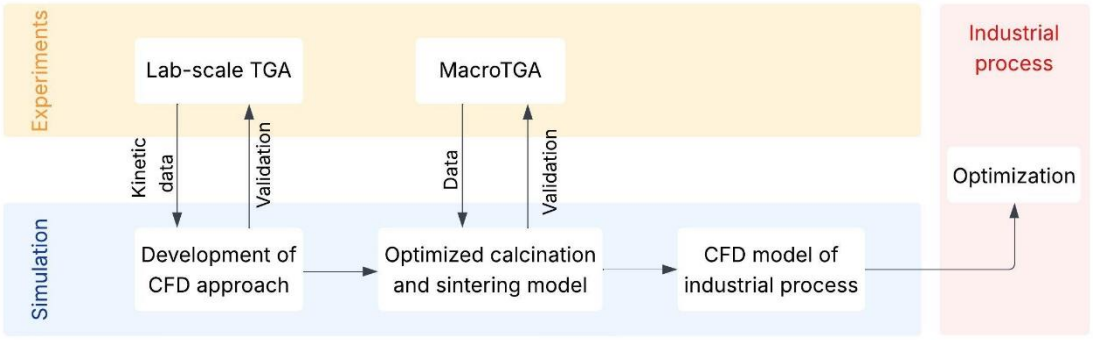

Figure 1: Schematic overview of the integrated approach using experiments and simulations to optimize industrial calcination and sintering process

2. Lab-Scale Thermogravimetric (TGA) Analysis and Results

To assess the thermal behavior and decomposition characteristics of magnesite-based raw materials, lab-scale thermogravimetric analysis (TGA) and differential scanning calorimetry (DSC) tests were conducted. The aim was to monitor mass loss and heat flow behavior under controlled thermal conditions up to a maximum temperature of around 1500 °C. Three different sample types were investigated: Rohstein (sieved to 0.5 - 1 mm), Kauster (the finest dust fraction), and a 50–50 mixture of Rohstein and Kauster. Each sample was tested at a heating rate of 5 K/min under a 50 ml/min air flow, with three repetitions per condition, resulting in a total of nine measurements. The chemical composition of all samples, as determined by XRF and mineralogical analysis via XRD, consists of mainly magnesite ($MgCO_3$) and dolomite ($CaMg(CO_3)_2$), along with minor amounts of periclase (MgO) and calcite ($CaCO_3$). The expected reactions during heat up are the endothermic decomposition of magnesite and dolomite, that can be summarized into two main reactions:

Magnesite Decomposition $MgCO_3 \longrightarrow MgO + CO_2$

Dolomite Decomposition $CaMg(CO_3)_2 \longrightarrow MgO + CaO + 2CO_2$

The TGA curves display the mass loss of each sample as a function of temperature and time, allowing for the identification of decomposition steps such as the release of physically or chemically bound water, carbon dioxide from carbonate decomposition, or volatile impurities. DTG (derivative thermogravimetry) curves - obtained by plotting the rate of mass loss versus temperature highlight the exact temperatures at which the maximum decomposition rates occur. These DTG peaks are particularly useful for pinpointing distinct thermal events and assessing the kinetics of individual decomposition stages [9]. The DSC curves provide complementary insight by recording heat flow into or out of the sample. Endothermic peaks indicate reactions that absorb heat, such as dehydration or decarbonation, whereas exothermic peaks reveal heat-releasing processes like crystallization. By integrating the area under these peaks, the total enthalpy change (ΔH) associated with each thermal event can be calculated. This information is crucial for quantifying the energy involved in the decomposition and transformation processes, which directly influences the material's behavior in high-temperature applications [9].

The following discusses the lab scale TGA results.

Figure **2**a shows the thermogravimetric analysis (TGA) of all analyzed samples.

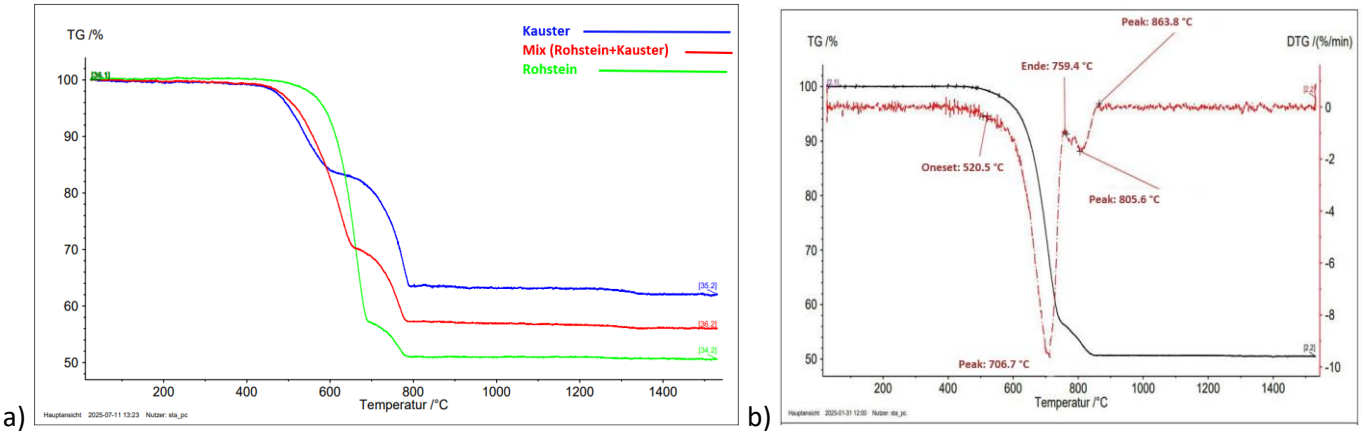

Figure 2: a) TG curves for 5 K/min and all samples b) TG/DTG analysis of the Rohstein

The TGA results illustrate clear decomposition behavior characterized by significant mass loss between approximately 500°C and 800°C, typical for carbonate decomposition. Initially, all samples remain stable up to around 450°C, indicating low moisture content and the absence of early decomposition. The main decomposition occurs in two stages: magnesite decomposes between ~450 - 650°C and dolomite decomposition. Dolomite undergoes a two-step decomposition, initially breaking down into MgO and $CaCO_3$, followed by the decomposition of $CaCO_3$ to CaO at around 700 - 800°C. Quantitatively, the final mass losses are approximately 40% for Kauster, 45% for the 50 - 50 mixture, and 50% for Rohstein, reflecting differences in mineralogical composition and particle size. The 50 - 50 mixture demonstrates intermediate behavior, as expected, confirming that its TGA profile represents a weighted average of its components. Above 800°C, all samples show minimal further mass change, indicating complete decomposition, with only minor additional mass loss likely attributable to slow phase transitions or residual impurities.

Figures 2b show the TGA-DTG and DSC analyses of samples containing magnesite and dolomite during heating. In the TGA-DTG curve, a significant mass loss is observed between 520°C (onset) and 759°C (end), with a DTG peak at 706°C, indicating the decomposition of carbonates with the release of CO_2 and the formation of MgO and CaO. Smaller DTG peaks at 805°C and 863°C may reflect the decomposition of residual carbonate phases or minor phase transitions. The final mass stabilizes around 50%, confirming the completion of decarbonation and indicating the oxide residue after decomposition.

Figure 3 shows the differential scanning calorimetry (DSC) analysis of samples, illustrating their thermal behavior during heating up to 1500°C.

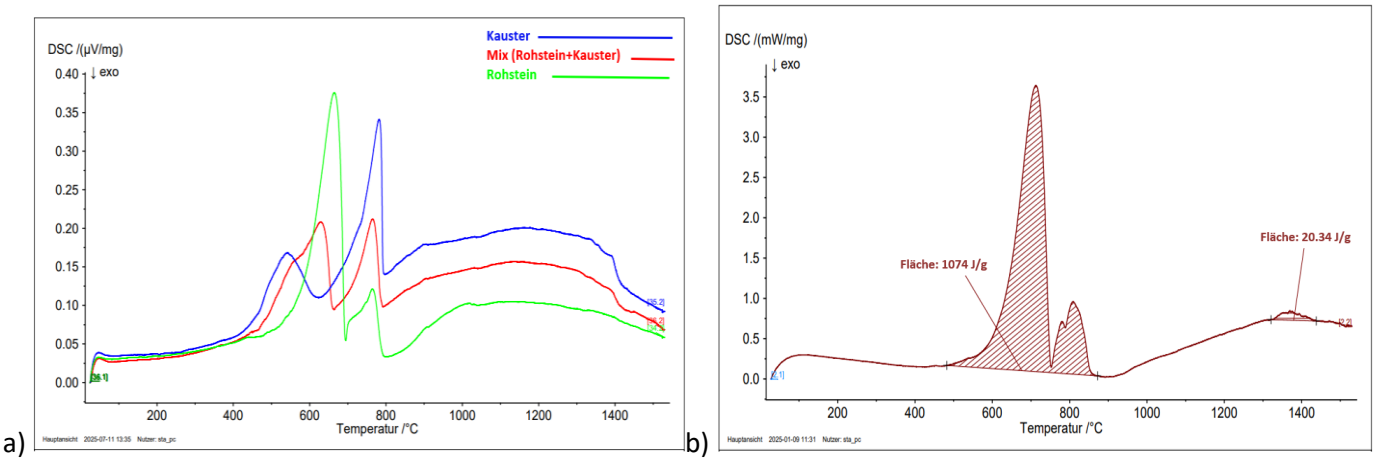

Figure 3: a) DSC curves for 5 K/min and all samples b) DSC analysis of the sample Rohstein

All samples exhibit clear endothermic peaks between approximately 600°C and 800°C, which correspond to the decomposition of magnesite and dolomite, releasing CO_2 and forming MgO and CaO. Kauster and the Mix samples

show broader and less intense peaks in this range, suggesting a higher dolomite content with staggered decomposition, while the Rohstein display sharper and more intense peaks, indicating a higher magnesite content or simpler carbonate composition with faster decomposition kinetics. Above 1200°C, the DSC signals gradually decrease, indicating the completion of major reactions and the progression of sintering and grain growth processes without significant additional decomposition.

By integrating the area under the DSC curves, the enthalpy changes (ΔH) of these reactions can be estimated. Combined with mass loss data from TGA, this allows for a quantitative assessment of reaction efficiency and completeness. The DSC curve complements these observations, showing a large endothermic peak with an enthalpy change of 1074 J/g centered between 500 and 850°C, corresponding to the decomposition of magnesite and dolomite. A smaller endothermic event with an area of 20 J/g near 1400°C suggests possible sintering onset or minor phase transitions within the oxide matrix at high temperatures. Together, these results confirm that the primary decomposition reactions of magnesite and dolomite occur below 800°C, while the stability of the signals beyond this temperature indicates the completion of decomposition, with higher temperatures relevant for sintering and structural rearrangements in the oxide phases, critical for subsequent processing in refractory material applications.

3. CFD Simulation Approach

A multiphase computational fluid dynamics (CFD) model was developed using the open-source simulation environment OpenFOAM® version 10. The simulation is performed using an in-house version of the chtMultiRegionEulerFoam, which allows the coupling of Eulerian fluid regions to multiphase Euler regions. The model treats the sample, the surrounding gas phase, and the oven wall as separate regions. The sample is modeled as a two-phase region, consisting of a solid phase and a gas phase, which are treated as two Eulerian phases. The sample is represented as a porous square with constant dimensions and a specified initial porosity. Within the porous structure, diffusive transport is considered for both species and heat. The effective diffusivity of gas species within the particle is calculated using a pore diffusion model [10]:

$$\mathrm{D}_{eff} = D_{ij}\frac{\varepsilon}{\tau} \tag{1}$$

Where ε is the porosity, τ the tortuosity and D_{ij} the diffusion coefficient. The diffusion coefficient is calculated using the Hayashi-Hishida model [11]. The surrounding gas phase is simulated as a single Eulerian phase and solved using a standard compressible flow solver, i.e. pimpleFoam[12]. The sample region and the surrounding gas region are coupled via the sample surface, which acts as an interface [13]. In the transient simulations, the Eulerian flow is described employing the continuity equation, the momentum equation, the energy equation, and the species equation. Radiation in the gas phase is calculated using the P1 model as implemented in OpenFOAM®.

The thermal decomposition of the solid is simulated using a gas-solid diffusion model. Decomposition reaction rates are commonly described as a function of temperature and a function of the extent of conversion [14]. In the developed model, the temperature dependence is calculated using an Arrhenius approach, leading to following equation for describing the decomposition reactions:

$$\frac{\mathrm{d}\alpha}{\mathrm{d}t} \equiv \beta\frac{\mathrm{d}\alpha}{\mathrm{d}t} = k(T)f(\alpha) = A\exp\left(\frac{-E}{RT}\right)f(\alpha) \tag{2}$$

where A is the pre-exponential factor, E the activation energy, R universal gas constant, T the temperature and α the conversion degree.

In a first step, the kinetic data and $f(\alpha)$ are sourced from literature. Table 1 summarizes the employed kinetic data for the decomposition of magnesite and dolomite.

Table 1: Kinetic data

Reaction	$f(\alpha)$ =	A (1/s)	E (kJ/mol)	Reference
$MgCO_3$ (s) → MgO (s) + CO2 (g)	$3(1-\alpha)^{\frac{2}{3}}$	$4.83*10^6$	161	[15]
$CaMg(CO_3)_2$ (s) → MgO (s) + CaO (s) + 2 CO_2 (g)	1	$2.34*10^6$	175	[16]

The mass loss during decomposition results in an increased porosity of the sample, which relates to a decrease in the sample mass.

In the following we present preliminary results employing the presented approach to a simulation set-up, that replicates a lab-scale TGA experiment for the sample Rohstein. Figure 4 shows the employed mesh and Table 2 summarizes the set boundary conditions to fit the lab-scale experiment.

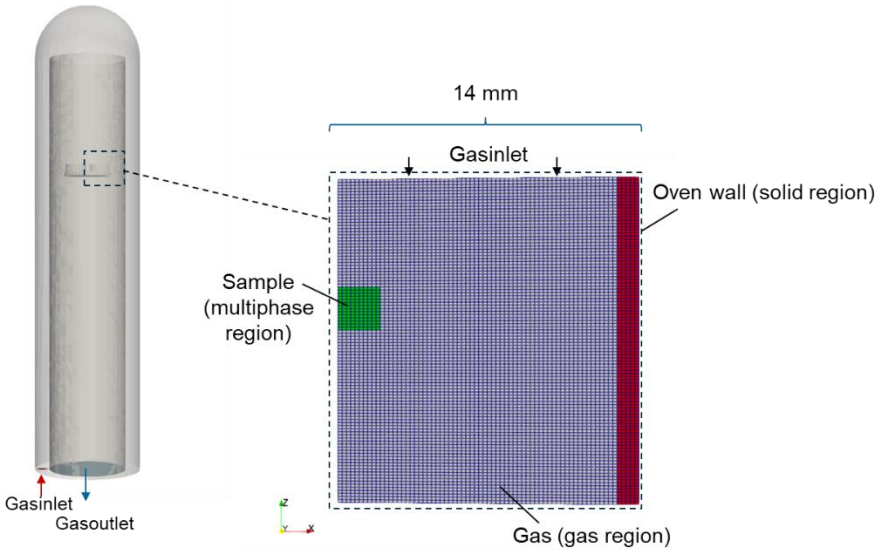

Figure 4: Left: Lab-scale TGA geometry; right: Simulation mesh for multi region simulation

Table 2: Boundary conditions of simulation

Sample type	Rohstein
Dolomite content (kg/kg)	0.133
Magnesite content (kg/kg)	0.867
Heat rate (K/min)	20
Initial sample mass (kg)	$4.6*10^{-5}$
Gas mass flow (kg/s)	$1.4*10^{-8}$

To safe computational time, the lab-scale TGA was simulated as a wedge symmetry. Figure 5 shows the calculated mass loss compared to the measured mass loss from lab-scale TGA experiments along with the corresponding calculated and measured reaction rates for solid decomposition at discrete temperature points between 600 °C and 800 °C. This temperature range was selected because the primary decomposition activity happens in this temperature window. The reaction rates for the solid decomposition from the CFD simulation are the sum of the reaction rates of dolomite and magnesite decomposition.

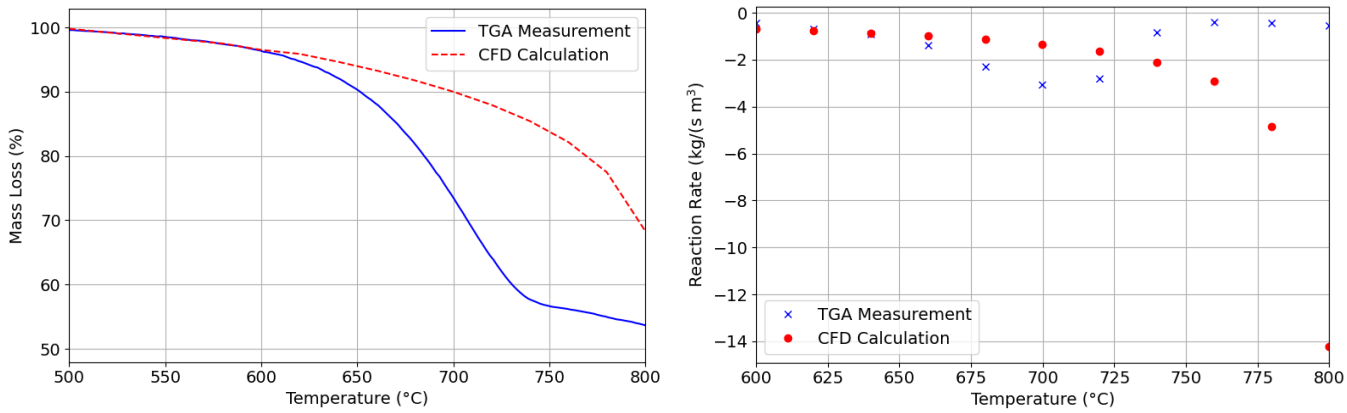

Figure 5: Simulation results; Left: Mass loss over temperature; Right: Reaction rate over temperature

A comparison of simulated and measured mass loss and reaction rates indicates that the simulation accurately captures the decomposition behavior up to approximately 600 - 650 °C. Beyond this temperature range, the simulation predicts peak decomposition at higher temperatures than observed experimentally. These deviations highlight the need for sample-specific reaction kinetics to improve model accuracy. As a first step, reaction kinetics can be derived from laboratory-scale TGA experiments. However, to develop an accurate model for describing industrial sintering and calcination, the MacroTGA setup will play a crucial role in significantly enhancing model development.

4. Conclusion and Outlook

In this work, we presented an integrated experimental and computational approach for analyzing the thermal decomposition behavior of magnesite- and dolomite-based raw materials used in refractory production. Lab-scale thermogravimetric analysis (TGA) combined with differential scanning calorimetry (DSC) provided detailed insights into the decomposition kinetics, thermal behavior, and mass loss characteristics of different raw material fractions. Thermogravimetric analysis (TGA) revealed that the main decomposition of the studied samples occurs between 500°C and 800°C. Final mass losses varied between 40% and 50%, reflecting differences in composition and particle size. The total enthalpy change associated with decomposition was approximately 1074 J/g, further confirming the energy-intensive breakdown of carbonate phases.

Furthermore, a CFD model approach was presented to simulate thermal decomposition under controlled conditions. Initial comparison to lab-scale TGA data demonstrated good agreement in terms of mass loss trends in a lower temperature range of up to 650 °C. For higher temperature it is recommended to enhance the decomposition model by determining sample-specific reaction kinetics directly from lab-scale and later from MacroTGA experiments.

To bridge the gap between lab-scale measurements and industrial processes, a novel high-temperature MacroTGA system is being developed. This system enables realistic thermal analyses of large samples (up to 0.5 kg) under controlled atmospheres at temperatures up to 1800 °C. This MacroTGA will allow us to generate more data on the calcination and sintering behavior under various heating profiles and gas atmospheres. This data can be used to enhance the CFD model of calcination and sintering, that can later be extended to simulate industrial rotary kilns. Such an enhanced model enables the investigation of process modifications such as atmosphere changes, temperature profiles, or material feed characteristics without the need for extensive pilot testing.

References

[1] Serry M.A., El-Kholi M.B., Elmaghraby M.S., Telle R.: Characterization of Egyptian dolomitic magnesite deposits for the refractories industry, Ceramics International, 28, 575–583, 2002.

[2] C. Sadik, O. Moudden, A. El Bouari, and I. E. El Amrani, “Review on the elaboration and characterization of ceramics refractories based on magnesite and dolomite,” Sep. 01, 2016, *Elsevier B.V.* doi: 10.1016/j.jascer.2016.06.006.

[3] Z. Guo, Y. Ma, and M. Rigaud, “Sinterability of macrocrystalline and cryptocrystalline magnesite to refractory magnesia,” *International Journal of Ceramic Engineering and Science*, vol. 2, no. 6, pp. 303–309, Nov. 2020, doi: 10.1002/ces2.10068.

[4] K. V. Fayruzov, I. D. Kashcheev, K. G. Zemlyanoi, and E. F. Chaika, “Investigation of Calcined Magnesite Sintering,” *Refractories and Industrial Ceramics*, vol. 63, no. 2, pp. 226–229, Jul. 2022, doi: 10.1007/s11148-022-00711-y.

[5] C. Wang, X. Zhou, L. Jia, and Y. Tan, “Sintering of limestone in calcination/carbonation cycles,” *Ind Eng Chem Res*, vol. 53, no. 42, pp. 16235–16244, Oct. 2014, doi: 10.1021/ie502069d.

[6] Liu B., Thomas P.S., Ray A.S., Guerbois J.P.: A TG analysis of the effect of calcination conditions on the properties of reactive magnesia, Journal of Thermal Analysis and Calorimetry, 88, 145–149, 2007.

[7] B. Ma and X. Ren, “Effects of key factors on the densification and grain growth behaviour of sintered magnesia from magnesite,” *Ceram Int*, vol. 48, no. 23, pp. 35525–35535, Dec. 2022, doi: 10.1016/j.ceramint.2022.08.159.

[8] L. Sun and Q. Zhang, “The development of a 500 g macro-thermogravimetric analyzer and its typical application in the thermal decomposition of limestone,” *J Therm Anal Calorim*, 2024, doi: 10.1007/s10973-024-13834-w.

[9] C. De Blasio, “Green Energy and Technology.” Available: http://www.springer.com/series/8059

[10] H. Lu, W. Robert, G. Peirce, B. Ripa, and L. L. Baxter, “Comprehensive study of biomass particle combustion,” *Energy and Fuels*, vol. 22, no. 4, pp. 2826–2839, Jul. 2008, doi: 10.1021/ef800006z.

[11] “Numerical Simulation of Pulsed Jet Plume Combustion,” in *Dynamics of Heterogeneous Combustion and Reacting Systems*, American Institute of Aeronautics and Astronautics, 1993, pp. 343–361. doi: 10.2514/5.9781600866258.0343.0361.

[12] H. G. Weller, G. Tabor, H. Jasak, and C. Fureby, “A tensorial approach to computational continuum mechanics using object-oriented techniques,” *Computers in Physics*, vol. 12, no. 6, pp. 620–631, Nov. 1998, doi: 10.1063/1.168744.

[13] Kiss M., Bösenhofer M., Schatzl M., Harasek M.: Species diffusion modeling in porous particles for metallurgical applications, 16th Minisymposium Verfahrenstechnik and 7th Partikelforum, Vienna, Austria, 2020.

[14] S. Vyazovkin, A. K. Burnham, J. M. Criado, L. A. Pérez-Maqueda, C. Popescu, and N. Sbirrazzuoli, “ICTAC Kinetics Committee recommendations for performing kinetic computations on thermal analysis data,” Jun. 10, 2011. doi: 10.1016/j.tca.2011.03.034.

[15] Hurst H.J.: The thermal decomposition of magnesite in nitrogen, Thermochimica Acta, 189, 91–96, 1991.

[16] Samtani M., Dollimore D., Alexander K.S.: Comparison of dolomite decomposition kinetics with related carbonates and the effect of procedural variables on its kinetic parameters, Thermochimica Acta, 392–393, 135–145, 2002.

Tunable Diode Laser Absorption Spectroscopy for CO and NO Emission Analysis during iC_3H_7OH/H_2 Blends Oxidation in Shock Tube and Pre-mixed Flames

G. Wang[1,3], J. Bajrami[2,3], S. Nadiri[1], S. Agarwal[1], R.X. Fernandes[1,3], F. Dinkelacker[2,3], B. Shu[1,3]

*Guanyu.Wang@ptb.de

[1] *Physikalisch-Technische Bundesanstalt (PTB), Braunschweig, Germany*

[2] *Institute of Technical Combustion, Leibniz University Hannover, Germany*

[3] *Cluster of Excellence SE²A –Sustainable and Energy-Efficient Aviation*

Abstract

The advancement of sustainable aviation relies on understanding the combustion characteristics of promising candidates like synthetic e-fuels; accordingly, this work focuses on blends of the e-fuel isopropanol (iC_3H_7OH) and hydrogen (H_2). A new dataset was generated using Tunable Diode Laser Absorption Spectroscopy (TDLAS) across two complementary experimental setups. First, a shock tube was used to measure time-resolved carbon monoxide (CO) concentrations during the ignition of iC_3H_7OH/H_2 mixtures (0-90% H_2) at 1–2 atm and 1250–1850 K. Second, in-flame measurements of CO, nitric oxide (NO), and temperature were performed on a non-swirled burner using a blend of 90% H_2 and 10% isopropanol under lean conditions (equivalence ratios of 0.47–0.61). Results show that while a kinetic model accurately predicts ignition delay times, it consistently overpredicts peak CO concentrations, and the potential kinetic sources for this discrepancy are discussed. Furthermore, in the burner experiments, 20-second recordings of in-flame data at each equivalence ratio were post-processed, with the resulting CO, NO, and temperature distributions plotted as box diagrams to quantify emission trends. Collectively, this work provides a comprehensive dataset that clarifies key chemical kinetic interactions and offers a quantitative basis for the refinement of chemical kinetic models.

1. Introduction

Future aviation concepts should be both CO_2-neutral and near-zero in emissions. One promising solution to achieve this is use of synthetic fuels, known as e-fuels, combined with advanced combustion technologies such as lean premixed prevaporized (LPP) combustion. E-fuels such as isopropanol (iC_3H_7OH) can contribute to CO_2 neutrality when produced from renewable sources, while lean premixed prevaporized (LPP) combustion offers the potential to significantly reduce non-CO_2 emissions, including soot and NO_x [1]. The addition of hydrogen (H_2) to isopropanol blends is a further strategy anticipated to enhance combustion efficiency and reduce carbon-based emissions. To harness the full potential of these fuel blends, a fundamental understanding of their combustion chemistry, flame characteristics, and emission profiles is essential.

High-temperature oxidation and pyrolysis have been extensively investigated in shock tubes for pure isopropanol. For instance, Johnson et al. [2] measured ignition delay times (IDT) at atmospheric pressure, establishing that n-propanol is more reactive than isopropanol at high temperatures (1350-2000 K). Cooper et al. [3] measured ignition delay time data for isopropanol at engine-relevant pressures (10 and 25 atm), along with CO and H_2O species profiles during pyrolysis and oxidation. Their work tested and validated different kinetic models. For ignition delay times, the mechanisms from Saggese et al. [4] showed good agreement with the experimental results, while model performance for species profiles depended on the specific combustion regime. Mertens and Manion [5] used shock tube experiments to provide direct measurements of key reaction kinetics. Their work identified molecular dehydration as the dominant unimolecular pathway and determined site-specific rate constants for H-atom abstraction, providing foundational data for the development of kinetic models for other biofuels.

While these studies provide a robust understanding of pure isopropanol kinetics, the addition of hydrogen introduces new chemical pathways. The interaction between isopropanol and hydrogen has been a key focus of flame studies. Veloo and Egolfopoulos [6] demonstrated that isopropanol flames have inherently lower reactivity and flame speeds compared to their isomers. This is because isopropanol's combustion pathway produces high concentrations of propene, which forms the relatively unreactive allyl radical, thereby retarding the overall reaction rate. This inherent characteristic provides the chemical basis for its moderating effect in more reactive fuel systems. Azatyan et al. [7] has demonstrated that isopropanol acts as an inhibitor to hydrogen combustion. Experiments have shown that small additions of isopropanol to hydrogen-air mixtures reduce the flame speed by terminating reaction chains; active radicals from H_2 combustion are replaced by less reactive radicals derived from isopropanol.

The existing literature provides a strong foundation for isopropanol combustion; a clear gap remains in the quantitative measurement of pollutant species during the oxidation of iC_3H_7OH/H_2 blends. Existing studies have focused primarily on ignition delay or bulk flame effects, without providing the detailed, time-resolved emission profiles. This work addresses this gap by employing Tunable Diode Laser Absorption Spectroscopy (TDLAS) in two complementary experimental configurations. First, time-resolved CO concentration histories are measured in a shock tube (1-2 bar, 1250-1850 K) for lean fuel blends with hydrogen fractions varying from 0% to 90%. Second, spatially resolved in-flame measurements of CO, NO, and temperature are performed on a non-swirl multifuel burner using a blend of 90 vol. % H_2 and 10 vol. % isopropanol. By generating this high-fidelity dataset across temporal species evolution and spatial flame profiles, this study provides a new dataset for validating and refining chemical kinetic models.

2. Experimental Setup and Methodology

Two experimental setups were used in this study. Fig. 1 (left) shows the TDLAS measurement system set up on a high-pressure shock tube, while Fig. 1 (right) shows the TDLAS set up on an unconfined Bunsen flame. Details of the two setups are presented in the section 2.3.

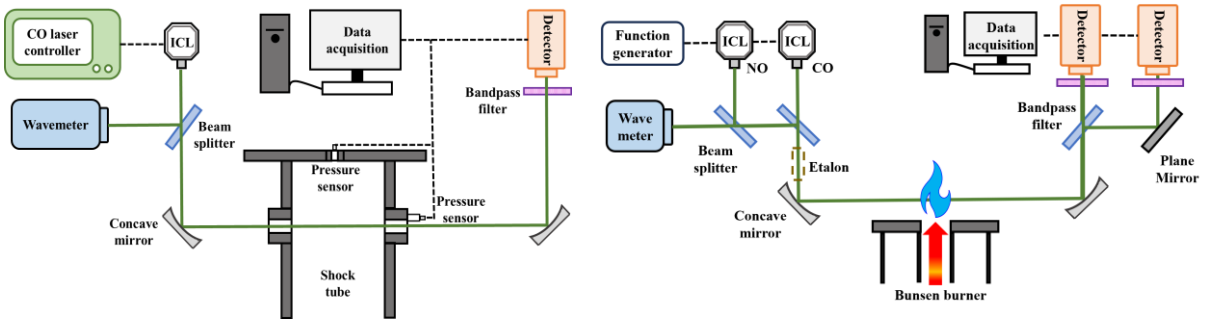

Fig. 1. Schematic of the experimental setups shock tube coupled with TDLAS (left) and non-swirl premixed burner coupled with TDLAS (right).

2.1 Shock tube

The experiments were conducted using a high-pressure shock tube (HPST), consisting of a 3.5 m driver and a 4.5 m, 70 mm inner diameter driven section with an electropolished inner surface. Helium driver gas was used to rupture aluminium diaphragms, initiating the shockwave. Incident shock velocity was calculated from four pressure sensors along the driven section. The reflected shock pressure (P_5) and temperature (T_5) were determined with the one-dimensional shock equation. The uncertainty for the calculated T_5 is estimated to be ±1.8% [8]. Optical access for laser diagnostics was provided by two opposing windows located 29 mm upstream of the endwall.

The reactive gas mixtures, O_2, He, Ar, H_2 and isopropanol were prepared in a 50-L stainless steel mixing vessel. Liquid isopropanol was vaporized prior to being introduced into the vessel to ensure homogeneity. For pure isopropanol mixture, 20% He was added to reduce the vibrational relaxation time [9]. Given the relatively low dilution ratio (90%), the effects of increased pressure and temperature on

the absorption coefficient are taken into consideration. Pressure variations were directly obtained from the measured profile, while temperature changes were obtained from the simulation [10]. Specifically, the measured pressure profiles were used to predict temperatures through chemical mechanisms in a homogeneous reactor, utilizing an in-house Cantera program. Real-time pressure and temperature values for each data point were then used to compute the CO concentration.

Fig. 2 left shows the sidewall pressure profile, CO absorbance, and the corresponding CO mole fraction for the 60% H_2/40% isopropanol mixture (φ = 0.9) under conditions of 1.37 atm and T_5 = 1383 K. The characteristic time at which the CO mole fraction reaches its maximum, referred to as τ (CO max), is defined as the time from shock arrival (time zero) to the point where the CO mole fraction peaks. The maximum relative uncertainty of the CO mole fraction in this study is 10.6% [11]. Time zero corresponds to the abrupt rise in sidewall pressure, marking the arrival of the reflected shock wave, with the pressure (P_5) providing the reference for time zero determination. As Fig. 2 right shows, the ignition delay time (IDT) is defined as the time interval between the arrival of the reflected shock wave and the onset of ignition. The shock arrival is marked by a distinct step rise in the end wall pressure trace. The ignition onset is determined by the first detectable increase in OH* emission, with the ignition time specifically defined as the point where the tangent to the maximum rate of change in the OH* emission signal is extrapolated back to the pre-ignition baseline The uncertainty for the measured IDT is 5.92% [11].

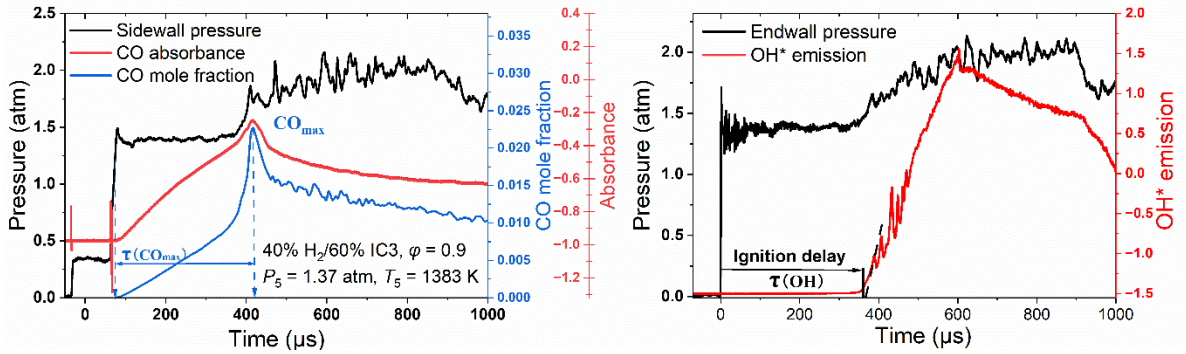

Fig. 2. Introduction of measured time-resolved CO mole fraction (left) and definition of ignition delay time (right)

2.2 Bunsen flame

The multi fuel burner test rig [12] with the modifications described in detail by Zimmermann et al. [13] was used in this study to measure temperature, CO, and NO within a Bunsen flame. The test rig contains a stainless-steel tank, which is pressurized with nitrogen (4.5 bar(g)) to provide the liquid fuel to the vaporizer. A Coriolis meter is utilized to regulate the liquid fuel, which is subsequently converted into a fully vaporized, undiluted fuel vapor in the vaporizer without the incorporation of any additional additives. The temperature of the vaporizer was set to 573 K for all measurements. To prevent condensation the vapor is conveyed to the mixing section via a line that has been preheated to a wall temperature of 423 K. The hydrogen used is adjusted via a mass flow controller. At the start of the mixing section, fuel vapor and hydrogen are introduced radially and mixed with heated combustion air flowing in axially. The mixing of air and fuel is achieved through the utilization of a static mixer, ensuring a homogenous mixture. Downstream of the mixing section the turbulence is mitigated by two 5 mm thick baffle plates, which are used as flow equalizers. Over a quartz glass tube of 500 mm a fully developed flow profile is achieved at the burner head. The internal diameter is constant from the injector unit to the burner head and measures 20 mm. The burner head is cooled by cooling water and made of stainless steel. Around the 20 mm main flame outlet a slotted pilot burner is located that generates a hydrogen diffusion flame to ignite and stabilize the main flame during the starting procedure.

The measurements are started with a combination of pilot and main flame, continuing until the fuel and combustion air flows reach a constant state. Subsequently, the pilot flame is deactivated. Once the burner rim temperature changes by less than 0.5 K/s, the TDLAS measurements are started. Throughout the

duration of the experiment (60 s), the measured flow and temperature values are documented in the background at a sampling rate of 1 Hz.

2.3 TDLAS

TDLAS was implemented in two distinct configurations tailored to different experimental objectives. For CO concentration measurements in a shock tube, a fixed-wavelength scheme was used. In this setup, Laser wavelength was controlled by adjusting the current and temperature through the modular laser diode controller platform (PRO8000, Thorlabs), equipped with the current control module (LDC8002, Thorlabs) and temperature control module (TED8020, Thorlabs). The P(20) [14] absorption line centred at 2059.91cm^{-1} was selected and characterized by a wavelength meter. Fig. 1 (left) illustrates a 2-dimensional view of the TDLAS system integrated with the HPST. The laser passed through the shock tube, and the signal was isolated from thermal emission using a narrow bandpass filter before reaching the detector.

For the burner experiments in this paper, a scanned-wavelength approach was employed to simultaneously measure temperature, CO, and NO in flame region, as depicted in Figure 1 (right). To achieve this, the laser's wavelength was swept using a 201 Hz triangle waveform across two distinct spectral regions: from 2059.2 to 2061.2 cm^{-1} to capture the P(14) and P(20) absorption lines of CO for thermometry, and from 1915.0 to 1916.0 cm^{-1} to probe a selected NO transition. During the scan, the transmitted laser intensities were recorded by a high-speed data acquisition (DAQ) system at a sampling rate of 400 kS/s.

According to Beer Lambert's law, the absorption of effective monochromatic laser radiation can be quantitatively calculated using the equation:

$$a\,(v) = -\,ln\left(\frac{I_t - I_b}{I_0 - I_b}\right) = S(T) \cdot X_{co} \cdot L \cdot p \cdot \varphi\,(v) \tag{1}$$

Here, $a\,(v)$ is the absorbance, I_t and I_0 are transmitted and reference laser signals, respectively, and I_b stands for the offset of the laser signal. $S(T)$ is line strength of CO at temperature T. $\varphi\,(v)$ is the line shape function. The light passes through a path length L, at pressure p containing the mole fraction of CO, denoted as X_{co}. While Equation (1) describes the absorbance at a single frequency, a more robust measurement can be achieved by scanning the laser's frequency across the entire absorption feature. By integrating the absorbance profile $a\,(v)$ over the frequency range of the transition, the dependency on the lineshape function $\varphi\,(v)$ is eliminated, as $\varphi\,(v)\,dv$ is normalized to unity. This yields the integrated absorbance A, which is directly proportional to the total number of absorbing molecules:

$$A = \int \alpha(v)\,dv = S(T) \cdot X_{abs} \cdot L \cdot p \tag{2}$$

For simultaneous temperature determination, the technique is extended to two-line thermometry. This method involves probing two different absorption lines of the same molecule. The lower-state energies of these two lines are significantly different, resulting in a strong and predictable temperature dependent ratio of their line strengths, $S_1(T)/S_2(T)$. By measuring the integrated absorbance for each line (A_1 and A_2), a ratio can be formed where the common terms for mole fraction, path length, and pressure cancel out:

$$R = \frac{A_1}{A_2} = \frac{S_1(T)\cdot p \cdot X_{abs} \cdot L}{S_2(T)\cdot p \cdot X_{abs} \cdot L} = \frac{S_1(T)}{S_2(T)} \tag{3}$$

The theoretical ratio of the line strengths is a known function of temperature, which can be calculated from spectroscopic databases such as HITRAN. By equating the experimentally measured ratio of integrated areas R to the theoretical line strength ratio, the gas temperature T can be determined with high precision. Once the temperature is known, it can be substituted back into Equation (2) for one of the absorption lines. The absolute mole fraction of CO and NO, X_{abs} can then be calculated directly,

provided the path length L and pressure p are known parameters of the experiment. This two-stage process enables the simultaneous, in-situ measurement of both temperature and species concentration.

3. Results and discussions

This section presents the experimental findings from the two distinct setups investigated in this work. First, the results from the shock tube experiments are detailed, focusing on the influence of hydrogen addition on the ignition delay times and CO concentration profiles of isopropanol. These experimental results are compared against predictions from a kinetic model to validate its performance. Following this, the data from the non-swirl premixed burner will be analysed to characterize the effects of hydrogen blending on flame temperature and post-flame CO and NO concentrations.

3.1. Shock tube measurements

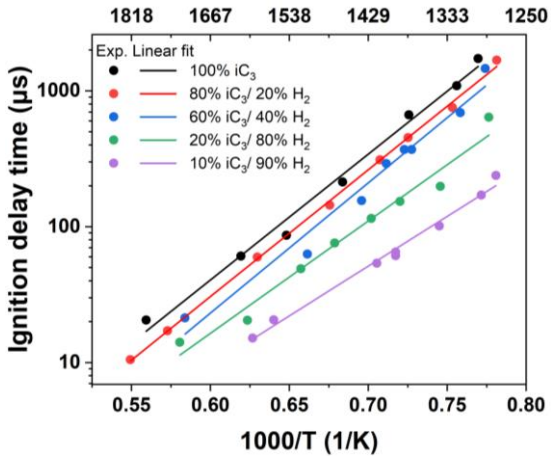

Fig. 3. Comparison of Ignition Delay Times for Isopropanol with 20%, 40%, 80% and 90% H_2 addition

Fig. 3. illustrates the ignition delay times (IDTs) of isopropanol blended with varying concentrations of hydrogen (20%, 40%, 80% and 90%). A clear trend is observed across all fuel blends, as temperature increases, the ignition delay time decreases significantly. Most notably, the addition of hydrogen has a strong promotional effect on IDT. Increasing the hydrogen concentration in the blend drastically reduces the IDT at the measured temperature range. For example, in the common temperature region around 1333 ± 20 K (where 1000/T = 0.75 K^{-1}), increasing the hydrogen content from 0% to 20% noticeably shortens the ignition delay time, from roughly 1100 µs to 750 µs. A further increase to 80% H_2 results in a more than three-fold decrease compared to the 20% blend, down to approximately 200 µs, demonstrating the potent effect of hydrogen in accelerating the overall reactivity of the fuel mixture.

Fig. 4. presents a comparison between the measured (IDTs) for various isopropanol/hydrogen blends (symbols) and model predictions from Saggese et al. (solid lines). The numerical simulations were conducted using an in-house Cantera code (version 3.0.0) [15], modeling the shock tube ignition process with a constant volume, 0-D homogeneous adiabatic reactor. Cantera's '*IdealGasReactor*' model was employed for its robust and efficient solution of the ideal gas energy equation. The model from Saggese et al. demonstrates good agreement with the experimental data across all tested conditions. It successfully captures both the absolute magnitude of the ignition delays and their temperature dependency for the 20%, 40%, and 80% hydrogen blends. This validates the mechanism's performance and indicates its suitability for describing the high-temperature oxidation chemistry of isopropanol/hydrogen fuel mixtures.

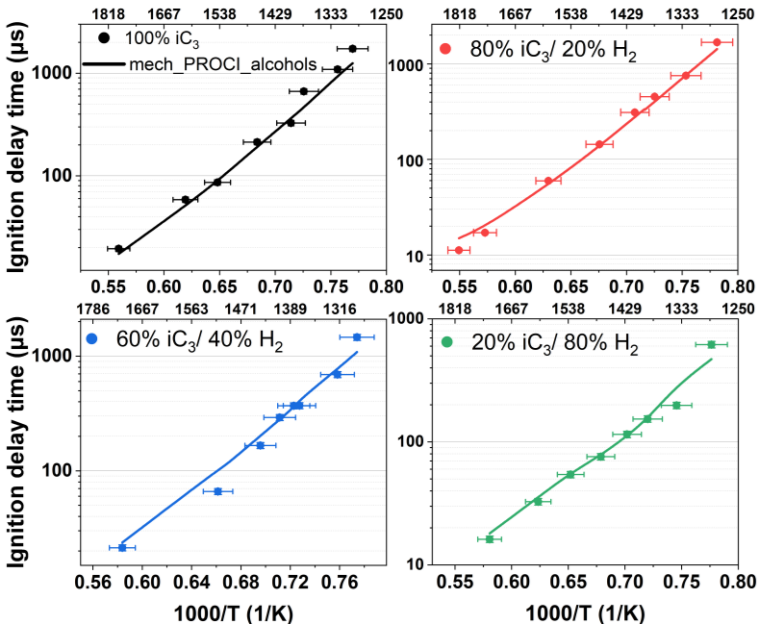

Fig. 4. Comparison of Experimental and simulated IDTs for Isopropanol/Hydrogen blends

Fig. 5. presents a comparison between the measured (solid curves) and simulated (dashed curves) time-histories of CO mole fraction for the oxidation of isopropanol blended with 10% H_2 (left) and 20% H_2 (right) across a range of temperatures. The kinetic model demonstrates good agreement with the experimental data, successfully capturing the dynamic features of CO formation and consumption. Specifically, the timing of the initial CO rise and the τ (CO max) are well-predicted by the simulation for both fuel blends. At lower temperatures ($\sim$1280 K), a notable discrepancy is evident, where the simulation predicts the peak CO timing significantly earlier than observed experimentally. Besides, a consistent discrepancy is observed in the magnitude of the peak CO mole fraction; the simulation consistently overpredicted the CO maximum by a factor of about 1.4 compared to the experimental measurements. Following the peak, both experiment and simulation show a decay in CO concentration, though the model's predictions remain higher. This overprediction likely stems from how the model handles the radical pool interactions. The addition of hydrogen significantly increases the concentration of H and OH radicals. While this accelerates the overall consumption of the fuel, it may also enhance the CO burnout rate (CO + OH $\rightleftharpoons$ CO_2 + H) more effectively than the model predicts, leading to the lower experimental CO levels.

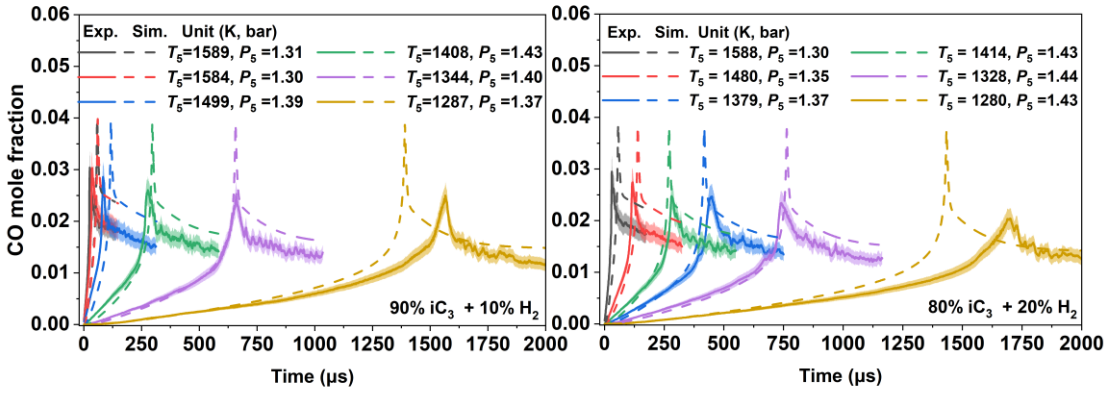

Fig. 5. Comparison of Experimental and simulated CO time history for 90/10 and 80/20 Isopropanol/Hydrogen blends

3.2 Bunsen flame measurements

Fig. 6. left panel shows simulated absorbance spectra for CO and water (H_2O) based on the HITRAN database. A prominent CO absorption feature, consisting of two distinct peaks, was identified at 2059.91 cm^{-1} and 2060.33 cm^{-1}. While water is a major product in combustion and has numerous absorption lines, simulations indicated that a significant H_2O peak is located at 2060.48 cm^{-1}. Based on this analysis,

the CO peak at 2059.91 cm^{-1} was selected for all subsequent measurements. This line offers strong absorbance and is sufficiently separated from the main water peak to minimize cross-interference, ensuring accurate CO quantification. The measured in-flame absorbance of 10% isopropanol and 90% hydrogen blend under varying equivalence ratios, from 0.47 to 0.61 is shown in Fig. 6 (right). A clear trend is observed: as the equivalence ratio decreases, the absorbance of the CO peak at ~2059.9 cm^{-1} diminishes significantly. This observation is driven by the change in the reactant mixture. Reducing the equivalence ratio directly lowers the mole fraction of fuel in the reactant mixture, which means fewer carbon atoms are available to form CO. Therefore, the significant decrease in CO absorbance seen in the data is a direct consequence of this reduced carbon input in leaner flames.

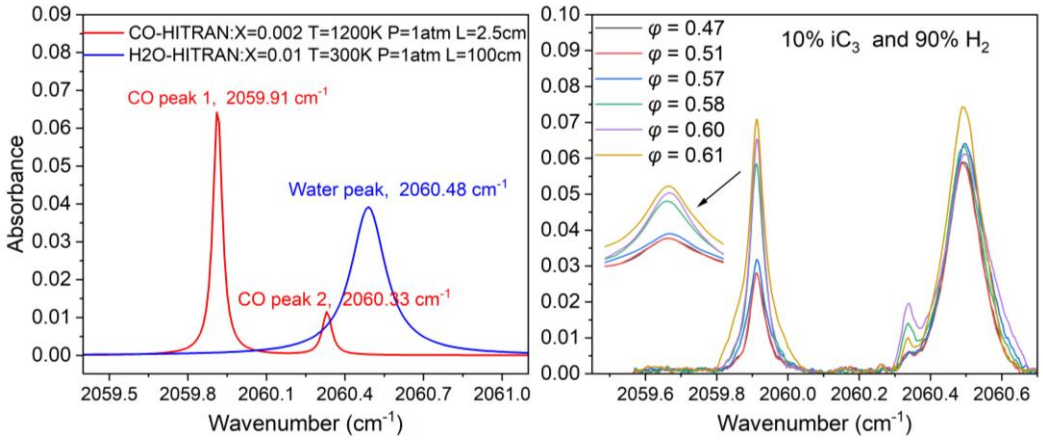

Fig. 6. Simulated absorbance spectra for CO and H_2O based on the HITRAN database (left) and measured in-flame absorbance of 10% isopropanol and 90% hydrogen blends (right)

The raw experimental data consists of the transmitted laser intensity through the flame *It* and a reference intensity *I0* that bypasses the flame to account for laser power fluctuations. A representative measurement is shown in Fig. 7, where the absorption due to CO and H_2O is clearly visible in the transmitted signal. The absorbance spectrum is calculated from these signals using the Beer-Lambert law. To isolate the absorption features from the smoothly varying laser intensity profile, a polynomial baseline is first fitted to the non-absorbing regions of the transmitted signal *It* to reconstruct the initial intensity profile *I0* that would have been observed in the absence of absorption. The resulting experimental absorbance spectrum, as shown in Fig. 6, is then fitted with a multi-peak Voigt profile. This profile is a convolution of Gaussian and Lorentzian functions, which accurately models the combined effects of Doppler and collisional broadening on the spectral lines. A non-linear least-squares algorithm is used to optimize the fit by adjusting the parameters for each peak, including the line center position, amplitude, and the Gaussian and Lorentzian widths. The quality of this procedure is confirmed by the small standard deviation of the fit residuals (7.85×10^{-4}), which shows an good match between the model and the experimental data. The integrated area of each individual Voigt profile is then calculated, providing a robust measure of the column density for both CO and H_2O that is independent of the specific line shape broadening.

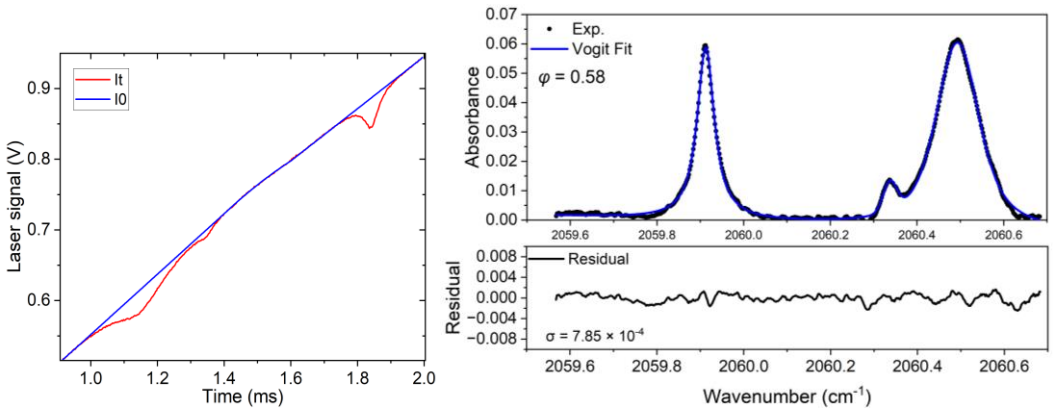

Fig. 7. Transmitted signal *It* and reference intensity *I0* (left). Measured laser signal of CO absorbance and fitted absorption lines (measured at 2 cm height above burner). Bottom—residual of the original intensity signal and the fitted absorption line. (right)

The effective absorption path length L is a critical parameter for converting line-of-sight measurements into mole fraction. It was carefully determined based on the visible flame structure. As illustrated in Fig. 8, the premixed flames in this study exhibit a distinct inner cone of unburned reactants surrounded by an outer mantle of hot combustion products. Since the target species (CO and NO) exist only in the post-flame gas, the central inner cone contributes negligibly to the measured absorption signal. Therefore, the effective path length was calculated from direct flame photographs by subtracting the diameter of the inner unburned cone D_i from the total visible flame diameter D_o, yielding $L = D_o - D_i$ This method provides a robust estimate for the path length through the product zones, and the resulting concentrations represent line-of-sight averaged values across these regions.

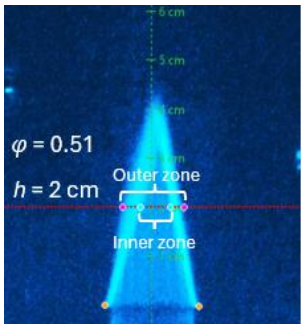

Fig. 8. Typical iC_3H_7OH/H_2 flame structure and schematic of effective path length determination

Fig. 9 presents the measured gas temperatures at different equivalence ratios, with each condition summarized by a box plot derived from 20 seconds of continuous measurement. The data reveals two key trends. First, the median and average flame temperature generally increases with the equivalence ratio, rising from 577 K at φ = 0.47 to 992 K at φ = 0.61. Secondly, the magnitude of temperature fluctuations increases as well. Particularly, as the equivalence ratio increases from 0.57 to 0.61, the boxes and whiskers become significantly larger, indicating increased temperature fluctuations. Based on the collected data, no individual cause for the observed fluctuations can be identified. However, it is estimated that the increase in Reynolds number, and thus in turbulence, as well as the special characteristics of hydrogen, play a role.

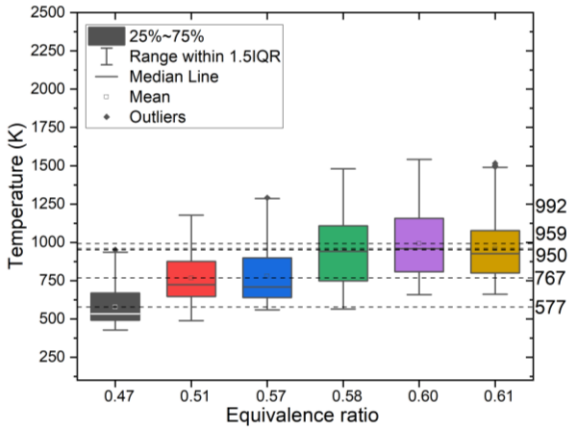

Fig. 9. Measured flame temperature at different equivalence ratios

Figure 10 presents the measured post-flame CO and NO concentrations at different equivalence ratios, with each condition summarized by a box plot derived from 20 seconds of continuous measurement. It is important to note that the gas temperature required for the NO concentration calculation was determined simultaneously using the two-line thermometry from the CO absorption peaks. Both species exhibit a clear increasing trend with the equivalence ratio. The average CO concentration rises from

2418 ppm at φ = 0.47 to 3362 ppm at φ =0.61. Similarly, the average NO concentration increases from 2665 ppm to 4256 ppm across the same range. The growing size of the boxes and whiskers at higher equivalence ratios for both species indicates greater variance in the measurements. This is attributed to the more intense and turbulent flow field generated at these conditions, which introduces noise into the transmitted laser signal and degrades the overall measurement precision. The significant increase in NO concentration is primarily attributed to the thermal NO. This formation pathway is exponentially dependent on temperature. As established previously, the flame temperature rises with the equivalence ratio, leading to a much higher rate of thermal NO production in the high-temperature post-flame region. This explains the sharp increase in measured NO emissions as the flame conditions move towards stoichiometric.

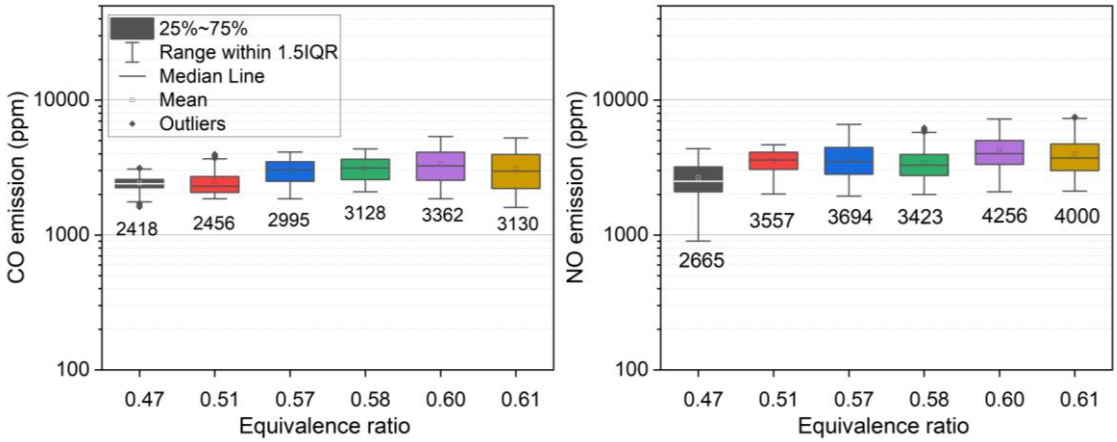

Fig. 10. Measured CO (left) and NO (right) emission at different equivalence ratios

The burner experiments bridge the fundamental kinetic behaviour to the practical goals of LPP combustion. The contrast with fundamental shock tube data provides a clear example. For instance, in shock tube measurements using a 90% H_2 / 10% iC_3H_7OH blend at a near-stoichiometric equivalence ratio of φ = 0.9, the averaged peak CO can be as high as ~7800 ppm. However, in the burner, which is intentionally operated at much leaner and cooler conditions between φ = 0.47 and φ = 0.61 the measured peak CO is significantly lower, at around 3000 ppm. This provides direct quantitative validation of the LPP strategy for emissions control. By operating at leaner conditions, a core principle of LPP, both CO and NO emissions were significantly reduced. Specifically, decreasing the equivalence ratio from the near-flashback limit of φ = 0.61 down to φ = 0.47 resulted in a ~38% reduction in NO and a ~28% reduction in CO, demonstrating the effectiveness of lean operation for minimizing key pollutants.

4. Conclusion

This study investigated the combustion kinetics and emission characteristics of blends of the e-fuel isopropanol and hydrogen using two complementary experimental setups. Key findings from the shock tube experiments show that while the Saggese et al. kinetic model accurately predicts the ignition-accelerating effect of hydrogen addition, it consistently overpredicts peak CO mole fractions. As detailed in the discussion, this discrepancy likely stems from an underestimation of the CO burnout rate ($CO + OH \rightleftharpoons CO_2 + H$) enhanced by the H_2-enriched radical pool. In the non-swirled burner, TDLAS measurements provided quantitative emission trends for CO and NO under lean conditions. The results confirmed that leaner operation reduces emissions but also exposed the trade-off of increased thermal NO production associated with hydrogen's impact on flame temperature.

Collectively, this work provides a comprehensive dataset that clarifies these chemical kinetic interactions and offers a quantitative basis for the refinement of chemical kinetic models for sustainable aviation fuels. Building on these findings, future research should advance on two key fronts. First, the scope of emissions analysis should be broadened to include measurements of unburned hydrocarbons (UHC) and soot precursors, as a comprehensive emissions profile is essential for designing truly clean and efficient LPP systems. Second, further effort is needed to improve signal quality and measurement

precision, particularly under the more turbulent conditions observed at higher equivalence ratios, to provide more accurate validation data from these practically relevant flame regimes.

Acknowledgement
Parts of this research was funded by the Deutsche Forschungsgemeinschaft (DFG, German Research Foundation) under Germany´s Excellence Strategy – EXC 2163/1 – Sustainable and Energy Efficient Aviation – Project-ID 390881007.

Literature

[1] Tacina RR.: *Low NO(x) potential of gas turbine engines*, AIAA 1990.
[2] Johnson MV., Goldsborough SS., Serinyel Z., O'Toole P., Larkin E., O'Malley G., et al.: *A Shock Tube Study of n- and iso-Propanol Ignition*, Energy & Fuels 2009;23:5886–98.
[3] Cooper SP., Grégoire CM., Mohr DJ., Mathieu O., Alturaifi SA., Petersen EL.: *An Experimental Kinetics Study of Isopropanol Pyrolysis and Oxidation behind Reflected Shock Waves*. Energies 2021;14.
[4] Saggese C., Thomas CM., Wagnon SW., Kukkadapu G., Cheng S., Kang D., et al.: *An improved detailed chemical kinetic model for C3-C4 linear and iso-alcohols and their blends with gasoline at engine-relevant conditions*, Proc Combust Inst 2021;38:415–23.
[5] Mertens LA., Manion JA.: *Kinetics of isopropanol decomposition and reaction with H atoms from shock tube experiments and rate constant optimization using the method of uncertainty minimization using polynomial chaos expansions (MUM-PCE)*, Int J Chem Kinet 2021;53:95–126.
[6] Veloo PS., Egolfopoulos FN.: *Studies of n-propanol, iso-propanol, and propane flames,* Combust Flame 2011;158:501–10.
[7] Azatyan VV., Borisov AA., Merzhanov AG., Kalachev VI., Masalova VV., Mailkov AE., et al.: *Inhibition of various hydrogen combustion regimes in air by Propylene and Isopropanol,* Combust Explos Shock Waves 2005;41:1–11.
[8] Zhu D., Agarwal S., Shu B., Fernandes R., Qu Z.: *An ultra-rapid optical gas standard for dynamic processes: Absolute NH3 quantification and uncertainty evaluation,* Measurement 2024;230:114559.
[9] Sen F., Shu B., Kasper T., Herzler J., Welz O., Fikri M., et al.: *Shock-tube and plug-flow reactor study of the oxidation of fuel-rich CH4/O2 mixtures enhanced with additives,* Combust Flame 2016;169:307–20.
[10] Zhu D., Qu Z., Li M., Agarwal S., Fernandes R., Shu B.: *Investigation on the NO formation of ammonia oxidation in a shock tube applying tunable diode laser absorption spectroscopy,* Combust Flame 2022;246:112389.
[11] Li M., Zhu D., Karas H., Agarwal S., Qu Z., Moshammer K., et al.: *NH3/C2H6 and NH3/C2H5OH oxidation in a shock tube: Multi-speciation measurement, uncertainty analysis, and kinetic modeling,* Chem Eng J 2024:155041.
[12] Goldmann A., Dinkelacker F.: *Experimental investigation and modeling of boundary layer flashback for non-swirling premixed hydrogen/ammonia/air flames,*Combust Flame 2021;226:362–79.
[13] Zimmermann P., Bajrami J., Dinkelacker F.: *Validation of a Generic Non-Swirled Multi-Fuel Burner for the Measurement of Flame Stability Limits for Research of Advanced Sustainable Aviation Fuels,* Energies 2023;16:7480,1-17.
[14] Ren W., Farooq A., Davidson DF., Hanson RK.: *CO concentration and temperature sensor for combustion gases using quantum-cascade laser absorption near 4.7 μm,* Appl Phys B 2012;107:849–60.
[15] Goodwin DG., Moffat HK., Schoegl I., Speth RL., Weber BW.: *Cantera: An Object-oriented Software Toolkit for Chemical Kinetics, Thermodynamics, and Transport Processes 2024.*

Entwicklung neuartiger, additiv gefertigter, keramischer Wasserstoffbrenner-Komponenten für innovative Energieeffizienz-Strategien

J. Michel[1*], D. Bernhardt[1], H.-P. Martin[2], K. Schönfeld[2], S. Dahms[3] und M. Beckmann[1]

*jerome.michel@tu-dresden.de

[1] *Professur für Energieverfahrenstechnik, Technische Universität Dresden, George-Bähr-Str. 3b, 01069 Dresden, Deutschland*
[2] *Fraunhofer-Institut für Keramische Technologien und Systeme IKTS, Winterbergstraße 28, 01277 Dresden, Deutschland*
[3] *Günter-Köhler-Institut für Fügetechnik und Werkstoffprüfung GmbH ifw Jena, Ernst-Ruska-Ring 3, 07745 Jena, Deutschland*

Abstract
Die mögliche Substitution von fossilem Erdgas mit (grünem) Wasserstoff als Brenngas in Industriebrennern bringt aufgrund seiner speziellen Verbrennungseigenschaften neue technische und materialwissenschaftliche Herausforderungen mit sich. Durch die höhere Flammentemperatur und -geschwindigkeit brennt die Flamme nicht nur näher und heißer am Brenner, sondern sorgt zusammen mit der hohen Reaktivität von Wasserstoff auch für zusätzliche chemische Belastungen der eingesetzten Materialien. Ziel ist es daher die Effizienz und Einsatzdauer von Wasserstoffbrennern durch die Entwicklung keramischer Komponenten für thermisch und chemisch besonders belastete Bereiche an Industriebrennern zu erhöhen.

Keramikwerkstoffe wie SiC, ZrC, B4C sind in reduzierenden Atmosphären bis zu Temperaturen > 2000 °C chemisch und thermisch stabil. Komposite aus diesen können vorteilhaft an spezifische Prozessanforderungen angepasst werden. Eine optimale Variante soll identifiziert und die Fertigungstechnologie validiert werden. Möglichkeiten zum Diffusionsfügen von keramischen Folien sind bekannt. Dieses Know How wird auf Keramikfolien angepasst und somit die Folienkomponenten additiv aufgebaut.

Aus Sicht der Verbrennungstechnologie werden hochbelastete Brennerkomponenten identifiziert, daraus geeignete Testkörper abgeleitet und diese dann in einer realitätsnahen Verbrennungsatmosphäre experimentell untersucht. Parallel erfolgt die Erstellung eines validierten CFD-Simulationsmodells, welches mit den Erkenntnissen aus den Tests der realen Proben erweitert werden soll und später zugleich Erkenntnisse zur Langzeit-Belastung der Komponenten liefern kann. Die Erhöhung der Betriebszeiten der Komponenten schont Ressourcen und verbessert die Nachhaltigkeit der Brenner gegenüber dem Stand der Technik.

Einleitung

Gasbrenner sind seit vielen Jahrzehnten Bestandteil sehr verschiedener industrieller Anwendungen und zentraler Bestandteil von Thermoprozessanlagen und Industrieöfen. Ziel ist in der Regel die Erzeugung von Heißgasen, die für unterschiedliche Prozesse der Hochtemperaturverfahrenstechnik (500 – 2000 °C Prozesstemperatur) benötigt werden, unter anderem zur Wärmebehandlung von Waren und Produkten, zur Erwärmung von Prozessluft für Trocknungsanlagen, zur Warmwasser- oder Dampferzeugung in Kesselanlagen oder auch zur Nachverbrennung von Luftschadstoffen in thermischen Nachverbrennungsanlagen.

Aktuell werden Industriebrenner vornehmlich mit Erdgas betrieben, wobei auch andere Kohlenwasserstoffe wie Propan, Butan, Ethylen oder auch Kohlenmonoxid als Brenngase eingesetzt werden. Vor dem Hintergrund der Senkung der Treibhausgasemissionen nimmt die Bedeutung alternativer, nichtfossiler Brennstoffe zu. Dazu zählt auch Wasserstoff, der im Bereich der Industriebrenneranwendungen, traditionelle Energieträger substituieren soll.

Während Wasserstoff in industriellen Thermoprozessanlagen historisch vor allem in Spezialfällen genutzt wurde – etwa, als Nebenprodukt in der chemischen Industrie (vgl. Chlor-Alkali-Elektrolyse [1]) – kann unter Voraussetzung einer besseren Verfügbarkeit von einer breiteren, systematischen Integration ausgegangen werden.

Um den veränderten Brenngaseigenschaften von Wasserstoff im Vergleich zu Erdgas und anderen Brenngasen (u.a. höherer massenspezifischer Heizwert, niedriger volumetrischer Heizwert, höhere Flammengeschwindigkeiten, höhere Flammentemperauren), Rechnung zu tragen, sind Anpassungen am Design und im Betrieb von Industriebrennern erforderlich [2]. Ziel ist es, dabei eine hohe Effizienz zu erreichen, die auch durch die Lebensdauer der Industriebrenner bestimmt wird.

Aufgrund der hohen Reaktivität des Wasserstoffs im Vergleich zu Erdgas und der daraus resultierenden höheren Flammengeschwindigkeiten, verlagert sich die Flamme näher an den Brenner. Verbunden mit den höheren Flammentemperaturen erhöht sich der Wärmestrom zum Brenner, was zu höheren Temperaturen von Brennerkomponenten führen kann und eine höhere thermische Belastung des Brenners zur Folge hat.

Gleichzeitig sorgt die hohe Reaktivität des Wasserstoffs und der erhöhte Dampfanteil im Abgas für eine zusätzliche chemische Beanspruchung von Brennerkomponenten als auch Feuerfestausmauerungen [3]. Die sogenannte Wasserstoffoxidation beschleunigt häufig die Korrosionsvorgänge zahlreicher Werkstoffe, was sich auf das gleichzeitige Einwirken hoher Temperaturen zusammen mit Wasserdampf zurückführen lässt. All diese Faktoren führen zu einer erhöhten Materialbeanspruchung, verkürzten Standzeiten und neuen Anforderungen an die Lebensdauer und Wartungszyklen industrieller Brennersysteme.

Vor diesem Hintergrund beschäftigt sich dieser Beitrag mit der Substitution konventioneller, metallischer Brennerkomponenten durch keramische Materialien, speziell additiv gefertigten Keramikfolienverbunden.

Thermisch beanspruchte Brennerkomponenten

Im Kontext von Industriefeuerungen und speziell der eingesetzten Brenner rücken besonders jene Komponenten in den Mittelpunkt der Betrachtung, welche sich unmittelbar an der Reaktionszone oder in deren unmittelbarer Umgebung befinden und damit den höchsten thermischen und chemischen Belastungen ausgesetzt sind. Bei den Betrachtungen wurde sich auf jene Brennersysteme konzentriert, welche auf dem Konvektionsprinzip basieren und deren Wärmetransportmechanismen in besonderem Maße mit den lokalen Strömungsverhältnissen sowie der Flammen und ihrer Eigenschaften verknüpft sind (siehe Abbildung 1) [4].

Als besonders hoch belastete Komponenten gelten dabei insbesondere

- Flammenhalter
- Flammenstabilisatoren
- Mischeinrichtungen
- Leitbleche
- Flamm- und Mischrohre
- Düsen

Die Intensität der Belastung nimmt dabei entlang dieser Aufzählung ab, wobei die Flammenhalter und -stabilisatoren tendenziell am stärksten beansprucht werden, da sie sich in unmittelbarer Nähe der Flamme befinden (Reaktionszone) [4]. Bei den anderen Komponenten führt eine Durch- bzw. Überströmung von unverbranntem Reaktions- und Brenngas zu einem Kühleffekt, welcher zumindest die thermische Belastung senkt.

Die bisher eingesetzten hochtemperaturbeständigen, metallischen Legierungen stoßen vor allem hinsichtlich ihrer thermischen Stabilität bei der Wasserstoffverbrennung an ihre Grenzen. Zudem verursacht die chemische und strukturelle Wechselwirkung von Wasserstoff und Wasserdampf zusätzliche Probleme in Bezug auf Zuverlässigkeit.

		Brennertyp	Beheizung		Brennstoff und Oxidator		Flamme		
Wärmeübertragungs-mechanismus	Kategorie		Methode	Luftzug	Mögliche Brennstofftypen	Oxidator-Temperatur	Flammelänge	Flammenform	Strömungs-geschwindigkeit
Konvektion	Vormischung	Hoch- & Mittelgeschwindigkeits-brenner	direkt	erzwungen	gasförmig/flüssig/ mix	kalt/heiß	kurz - lang	Freistrahl	mittel - hoch
		Lanzen-/Pilot-Brenner	direkt	erzwungen	gasförmig	kalt/heiß	kurz - lang	Freistrahl	mittel - hoch
		Fackeln	direkt	erzwungen	gasförmig	kalt	kurz - lang	Freistrahl	hoch
		Linear/Bandbrenner	direkt	erzwungen	gasförmig	kalt	kurz - lang	Freistrahl	niedrig – mittel
		Drallbrenner	direkt	erzwungen	gasförmig gasförmig/flüssig/ fest/mix	kalt/heiß	kurz - lang	Drallflamme	mittel – hoch
	Diffusion/ Düsenmischung	Hoch- & Mittelgeschwindigkeits-brenner	direkt	erzwungen	gasförmig/flüssig/ mix	kalt/heiß	kurz - lang	Freistrahl	mittel – hoch
		Lanzen-/Pilot-Brenner	direkt	erzwungen	gasförmig	kalt/heiß	kurz - lang	Freistrahl	mittel – hoch
		Monoblock Brenner	direkt	erzwungen	gasförmig/flüssig/ mix	kalt/heiß	kurz - lang	Freistrahl	mittel
		Rekuperatorbrenner	indirekt	erzwungen	gasförmig	-	kurz	Freistrahl	niedrig
		Regenerativbrenner	direkt	erzwungen	gasförmig	-	long	Freistrahl	hoch
Strahlung	Strahlungs-flamme	Flachflammen-Brenner	indirekt	erzwungen	gasförmig	kalt	kurz	Flachflamme	niedrig
	Strahlungs -rohr	Strahlungsrohr-Brenner	indirekt	erzwungen	gasförmig/flüssig	kalt	kurz	Flachflamme	niedrig
	Wärme-strahlung	Infrarot (IR) Brenner	indirekt	erzwungen	gasförmig	kalt	kurz	Oberflächen-verbrennung	niedrig

Abbildung 1. Übersicht verschiedener Brennertypen und ihrer Eigenschaften

Im Bereich der Reaktionszone kommen bereits heute wegen ihrer höheren Temperaturstabilität teilweise keramische Werkstoffe zum Einsatz. Typische Vertreter sind siliziumbasierte Keramiken (z. B. SiC, SiSiC, SiO_2) sowie Aluminiumoxid-basierte Werkstoffe (Al_2O_3, Al_2O_3-ZrO_2), die gute Hochtemperatureigenschaften mit einer gewissen Korrosionsresistenz kombinieren. Trotz ihrer Eignung für hohe thermische Belastungen bestehen noch deutliche Optimierungspotenziale – insbesondere hinsichtlich der erreichbaren Standzeiten sowie fertigungstechnischer Aspekte. Technische Limitationen ergeben sich unter anderem bei minimalen Wandstärken, engen Toleranzen und der geometrischen Flexibilität. Besonders bei dünnwandigen oder komplex geformten Bauteilen führen enge Toleranzanforderungen zu Einschränkungen bei der Realisierung effizienter Brennergeometrien. Darüber hinaus müssen Werkstoffe, die direkt mit dem Verbrennungsprozess in Kontakt stehen, beständig gegenüber den Produkten der Wasserstoffverbrennung sein. Die möglichen Werkstoffe müssen somit höheren Temperaturen und Wasserdampf standhalten und zusätzlich weitgehend unempfindlich gegen Temperaturschocks sein, die beim Starten und Beenden der Gasverbrennung auftreten. Auch wäre eine verbesserte Beständigkeit gegenüber starken Temperaturgradienten wünschenswert, um thermomechanischen Spannungen besser standzuhalten.

Neuartige, additiv gefertigte Keramikfolienverbunde

Eine Übersicht zu potenziellen Keramiktypen für Wasserstoffbrenner ist in Tabelle 1 zu finden.

Tabelle 1. Mögliche Keramiken für thermisch hochbelastete Bauteile [5].

Keramik Material	Schmelztemperatur / °C	Verbrennungsreaktionen
Siliziumkarbid (SiC)	kein Schmelzen > 2400 °C	Oxidation (Wasser, Sauerstoff)
Siliziumnitrid (Si3N4)	Zersetzung > 1900 °C	Oxidation (Wasser, Sauerstoff)
Tonerde Al2O3	2050 °C	Bildung von gasförmigen Spezies
Mullite $3{\cdot}Al_2O_3{\cdot}2{\cdot}SiO_2$	1840 °C	Bildung von gasförmigen Spezies

Kommerziell verfügbare Keramikprodukte wie Si-SiC, Al_2O_3, SiO_2 oder Al_2O_3-ZrO_2 zeigen spezifische Korrosionsreaktionen bei der Wasserstoffverbrennung. Aluminiumoxidkeramiken bleiben

bis zu 1500 °C bei der Verbrennung eines 100 %igen Wasserstoffbrenngases stabil. An Si-SiC Keramiken wurde bereits bei 1250 °C eine erhebliche Korrosion festgestellt [5].

Zur Kombination der Vorteile wie Korrosionsbeständigkeit, thermische und mechanische Stabilität und Vermeidung spezifischer, nachteiliger Eigenschaften wie Thermoschockempfindlichkeit oder Korrosionsempfindlichkeit, sind spezielle Fügetechnologien erforderlich. Über Fügetechniken kann gleichzeitig eine kostengünstigere Herstellung bestimmter Bauteilgeometrien möglich werden, womit eine weitere Hürde für den Einsatz keramischer Komponenten überwunden wird. Das Fügen von Keramiken erfordert von der Fügezone eine ähnliche Temperaturstabilität und Korrosionsbeständigkeit wie vom eingesetzten Keramikwerkstoff.

Unsere Untersuchungen fokussieren sich auf Siliciumcarbidkeramiken ohne freies Silicium, wie er beim Si-SiC vorliegt, um Nachteile bei der Korrosionsstabilität zu vermeiden [6]. Aluminiumoxid (Al_2O_3) in Kombination mit Yttriumoxid (Y_2O_3) ist eine bewährte Flüssigphasen-Sinterphase (LPS), die mit Siliziumkarbid als sogenanntes LPS-SiC kombiniert werden kann. Diese Kombination ermöglicht eine Eigenschaftsanpassung z.B. für die Wärmeleitfähigkeit, die mechanische Festigkeit oder die Wärmeausdehnung. Alle keramischen Komponenten des LPS-SiC besitzen bis zu 1400 °C eine hohe Korrosionsstabilität.

Die Versuche zum Fügen von keramischen Laminaten für den Hochtemperaturbereich über 1200 °C wurden in einem Graphitofen unter Schutzgas oder Vakuum mit einer integrierten Heißpresse durchgeführt. Um eine homogene Flächenpressung über die gesamte Fügefläche zu gewährleisten, ist eine flexible Einleitung der Presskraft erforderlich. Dieses Verfahren erlaubt eine flächenhafte Verbindung im festen Zustand, die auch die Möglichkeit einer additiven Fertigung erlaubt. Dabei können zielgerichtet über eine Schicht auf Schicht-Laminierung (Laminated Object Manufacturing) komplexe Bauteilgeometrien gefertigt werden.

Über die Variationen der Folienschichten (SiC und Sinteradditivgehalten) sowie der technologischen Parameter des Diffusionsfügeprozesses (Fügetemperatur, Fügezeit, Presskraft und Aufheiz- und Abkühlrate) kann die Ausbildung des keramischen Gefüges der LPS-SiC-Verbunde beeinflusst werden.

Tabelle 2: Verbundaufbau (SA – Sinteradditiv) technologische Fügeparameter

Keramische Folien	Name	Fügetemperatur [°C]	Fügezeit [h]	Flächenpressung [MPa]	Atmosphäre
SiC + SA 40	KK10	1200 … 1750	2	1-2	N_2 / Ar
SiC + SA 30	KK11	1200 … 1750	2	1-2	N_2 / Ar
SiC + SA 40 + SiO_2	KK12	1200 … 1750	2	1-2	N_2 / Ar
SiC + SA 30 + SiO_2	KK13	1200 … 1750	2	1-2	N_2 / Ar
SiC + glass	KK14	1200 … 1700	2	1-2	N_2 / Ar

In einem ersten Schritt wurden Sintertests an einzelnen Folien durchgeführt. Der Entbinderungsprozess ist bei etwa 500 °C abgeschlossen, bevor der Füge- und Sinterprozess beginnt. Dabei wurden Sintertemperaturen von 1200 °C bis 1700 °C unter Inertatmosphäre betrachtet, wobei Fügezeit und Flächenpressung konstant gehalten wurden (siehe Tabelle 2).

Die fügetechnische Verfahrensqualifizierung zeigte, dass keramische Folien mit Sinteradditiven Sintertemperaturen über 1500 °C benötigen, um thermisch stabil, rissfrei und spannungsarm zu sein. Diese wiesen auch einen typischen keramischen hellen Klang auf. Die zusätzliche Modifikation der keramischen Folien mit Glasphase oder SiO_2 beeinflusste das Schrumpfungs- und Sinterverhalten in Abhängigkeit der Füge- bzw. Sintertemperaturen.

Zusätzlich wurden Fügeversuche analysiert, die sich auf ein additives Fertigungskonzept mit schichtweisem Aufbau konzentriert. Ziel war es, die Temperatur- und Thermoschockbeständigkeit durch die Kombination verschiedener Laminat-Variationen mit Glasphasenanteilen zu erhöhen. Die homogene Sinteranbindung an den Folienübergängen wurden im Temperaturbereich zwischen 1500 °C und 1700 °C nachgewiesen. Die eingebrachte Glasphase und die Schmelzbereiche im keramischen Gefüge der Folien KK12 und KK14 sind deutlich erkennbar (siehe Abbildung 2).

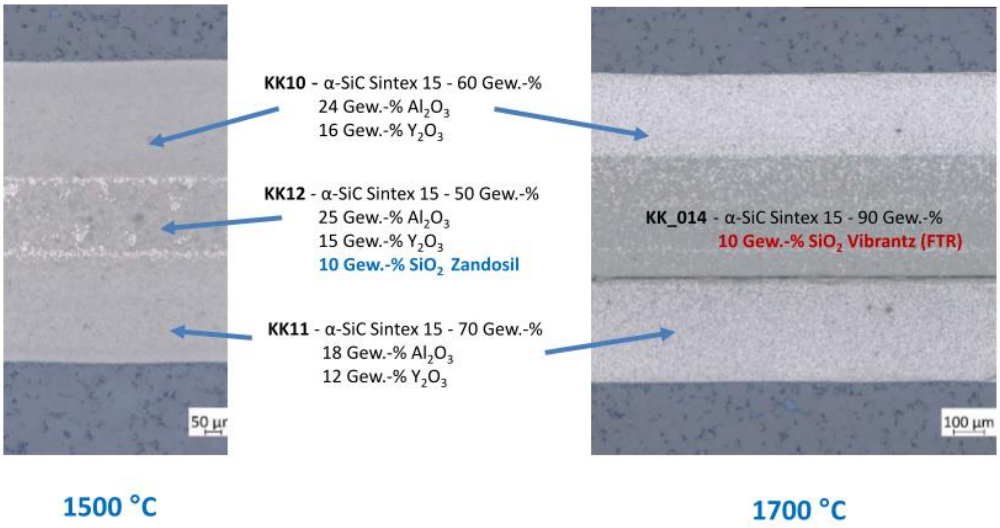

Abbildung 2. Lichtmikroskopische Aufnahme von Folienlaminaten mit SiO2-haltiger Glasphase nach dem Fügeprozess bei 1500 °C (links), 1700 °C (rechts)

Detaillierte Analysen wurden mit der Rasterelektronenmikroskopie durchgeführt (siehe Abbildung 3). Die Kombination der Folienvarianten zeigte ein weitgehend defektfreies Folienlaminat mit einer Schrumpfung von 5 % im Durchmesser sowie einer offenen Porosität von etwa 28 %. Silicatphasen waren im gesamten Laminatverbund nachweisbar.

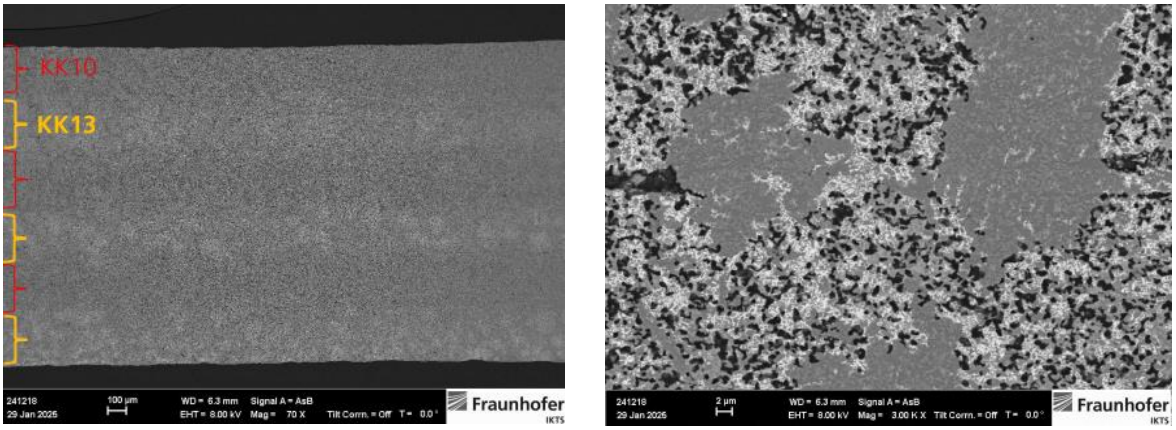

Abbildung 3: SiC-Folien mit Sinterhilfsmittel und Glasphase im Wechsel (Fügetemperatur 1600 °C, Flächenpressung 1 MPa in Stickstoff)

Neben dem additiven Aufbau wurden fügetechnische Ansätze für Hochtemperaturanwendungen verfolgt, um monolithische Nichtoxidkeramikkomponenten hochtemperaturstabil, korrosionsbeständig und spannungsarm miteinander zu verbinden. Mögliche technische Anwendungen sind hierbei Verschlussstrategien für Hochtemperaturwerkstoffe bzw. Bauteilkomponenten zu entwickeln.

Materialtests unter praxisnahen Bedingungen

Zur Analyse der thermischen und chemischen Belastbarkeit keramischer Werkstoffe unter realitätsnahen Einsatzbedingungen wurde ein Versuchsstand im Technikumsmaßstab konzipiert (siehe Abbildung 4). Dieser bildet die zentralen Merkmale eines industriellen Systems aus Industriebrenner und Feuerungsraum nach und soll reproduzierbare, und kontrollierte Materialtests unter realistischen Betriebsbedingungen sowohl für reine Erdgas- als auch für reine Wasserstoffverbrennung ermöglichen.

Die Brennkammer verfügt über einen zylindrischen Feuerungsraum mit einem Durchmesser von 400 mm und einer Länge von ca. 1000mm (von Brennersitz bis Übergang Mischzone). Die Ausmauerung besteht aus drei Lagen Feuerleichtsteinen mit einer dahinterliegenden, mehrschichtigen Wärmedämmung. Auf der Abgasseite erfolgt eine kontrollierte Abkühlung mittels schräger, radialer Quenschlufteindüsung, um das Abgas auf maximal 300 °C abzukühlen und so die thermischen Grenzwerte der Abgasanlage nicht zu überschreiten.

Als Brenner kommt ein Hochgeschwindigkeits-Gasbrenner der Firma IBS Industrie-Brenner-Systeme GmbH zum Einsatz, welcher sowohl für den Betrieb mit 100 % Erdgas, als auch mit 100 % Wasserstoff geeignet ist.

Zur Durchführung der Materialtests sind sechs Messebenen im Abstand von 115 mm vorgesehen. Diese bestehen aus gegenüberliegenden Bohrungen/Zugängen: auf der einen Seite mit einem Schauglas aus Borosilikatglas zur Beobachtung der Proben/Flammenüberwachung, auf der anderen Seite mit einem Schleusenzugang zur Einführung von Messinstrumenten (bspw. Gas- und Temperaturmessung) und Proben(-halter).

Die maximal zulässige Wandtemperatur beträgt 1500 °C, was dem Grenzwert der Feuerleichtsteine (unter Einhaltung des Sicherheitsfaktors) entspricht. Die Temperaturüberwachung erfolgt mittels Thermoelementen, die sowohl in die Ausmauerung als auch ins Abgas eingebracht sind.

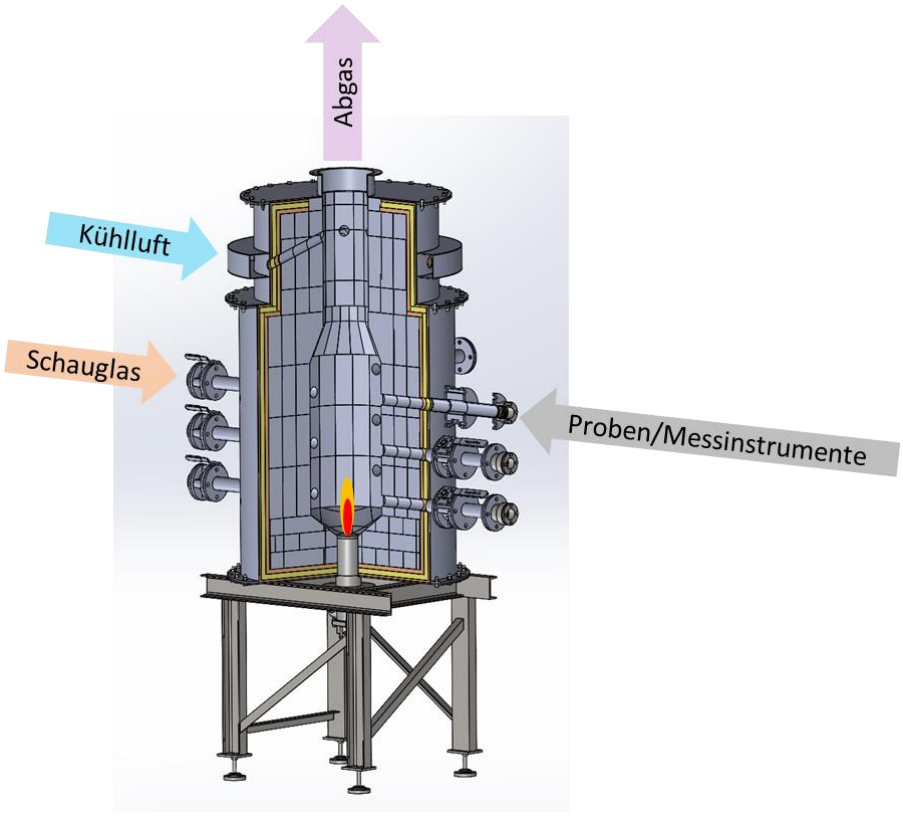

Abbildung 4. Schematische CAD-Konstruktion des geplantes Brenner-Brennkammer-System

Ziel ist die Untersuchung verschiedener keramischer Probenkörper im Feuerungsraum unter praxisnahen Bedingungen – sowohl aus etablierten Hochtemperaturwerkstoffen als auch aus den neuartigen, keramischen Folienverbunden. Im Fokus stehen dabei insbesondere die Temperaturwechselbeständigkeit, chemische Stabilität sowie der strukturelle Zustand nach definierten Testzyklen. Die Versuche erfolgen unter definierten Bedingungen sowohl im Erdgas- als auch im Wasserstoffbetrieb, um Unterschiede in den Materialbeanspruchungen systematisch erfassen zu können.

Ausgehend von typischen, thermisch beanspruchten Brennerkomponenten (s. Abschnitt Thermisch beanspruchte Brennerkomponenten), wurden geeignete Probenkörper abgeleitet. Aufgrund fertigungstechnischer Randbedingungen wurde sich zunächst auf runde, ebene Scheiben mit einem Durchmesser von ca. 30mm und einer Dicke von ≥ 2mm konzentriert. Die Proben sollen mithilfe eines

eigens entwickelten Hochtemperatur-Probenhalters (voraussichtliche Konstruktion und Probenkörper siehe Abbildung 5) in die Brennkammer eingebracht werden. Dieser besteht aus einem gekühlten Führungsrohr, zwei Aufnahmen aus hochtemperaturbeständigem Stahl und zwei Al2O3-Keramikstäben.

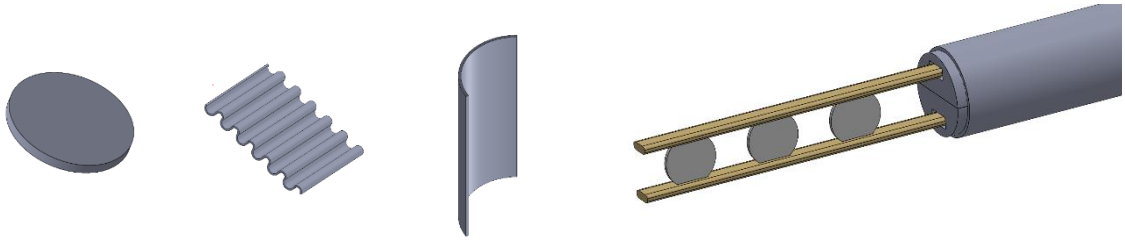

Abbildung 5. Abgeleitete Probenkörper und Hochtemperatur-Probenhalter mit ausgewählten Proben

Um die Probenkörper den komponentenspezifischen Betriebsbedingungen (Temperatur, Gasatmosphäre) auszusetzen, ist eine Charakterisierung des Verbrennungsverhaltens im Erdgas- und Wasserstoffbetrieb erforderlich. Dazu werden axiale und radiale Messungen in der Brennkammer bei verschiedenen Luftüberschusszahlen und thermischen Leistungen durchgeführt. Die Messergebnisse dienen auch der Validierung eines CFD-Modells, welches im nächsten Abschnitt genauer beschrieben ist.

CFD-Simulation des Versuchsstandes

Zur Abbildung der typischen Betriebsbedingungen in der Brennkammer kommt ein numerisches Strömungsmodell zum Einsatz. Ziel ist die detaillierte Analyse der Temperaturverteilung, Strömungsbedingungen und Spezieskonzentration im Feuerungsraum, die Ermittlung der Temperaturbelastung keramischer Bauteile und die Ermittlung geeigneter radialer Positionen der Proben für die durchzuführenden Messungen. Außerdem wurde das entwickelte Modell zur Vorauslegung des Versuchsstandes hinsichtlich Temperaturbelastung von Armaturen und Anbauten genutzt.

Das Simulationsmodell basiert auf einer gekoppelten Multi-Physics-Berechnung mit Ansys Fluent 2024 R2 unter Berücksichtigung von Turbulenz, Verbrennung und Strahlung sowie konvektivem und konduktivem Wärmeübergang in der Ausmauerung/Wärmedämmung/Stahlhülle und den Brennerkomponenten. Die vereinfachte Geometrie wurde in ein Rechennetz mit insgesamt 8,8 mio. Zellen überführt (siehe Abbildung 6), wovon 5,6 mio Zellen den Fluidbereich beschreiben. Im Bereich der Verbrennungszone sowie am Rand (5 Boundary Layers) wurde eine gezielte Zellverfeinerung vorgenommen, um trotz RANS-Ansatz eine hinreichend genaue Abbildung der Flammenstruktur zu gewährleisten.

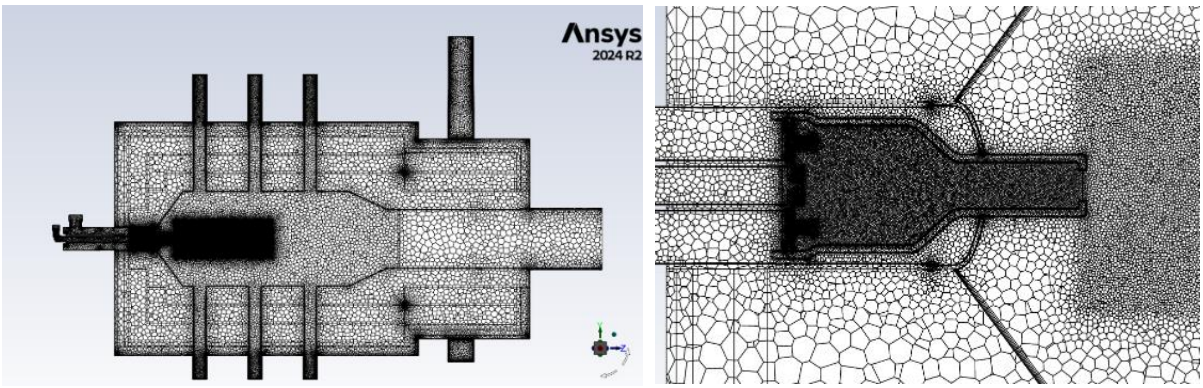

Abbildung 6. Gesamtes Rechennetz und Detailansicht der Netzverfeinerung im Bereich der Reaktionszone

Die wichtigsten Modellparameter und Einstellungen sind in Tabelle 1 zusammengefasst. Diese orientieren sich am Stand der Technik für die Simulation komplexer, realitätsnaher Geometrien [8]. Zur Voreinschätzung und Kontrolle der Ergebnisse sowie zur Auslegung des Versuchsstands wurde zudem ein stationäres Energiebilanz-Modell mittels Process-Excel erstellt.

Tabelle 3. Simulationseinstellungen.

	Modell	Einstellungen
Turbulenz	Standard k-ε-Modell	Default Parameter
Verbrennung	Partially Premixed Combustion Modell	Steady Diffusion Flamelet
Reaktionsmechanismen	GRI-Mech 3.0	53 Spezies, 325 Reaktionen
Strahlung	Discrete Ordinate (DO)	4 x 4 Richtungen; 3 x 3 Pixel, WSGGM-Modell (domain-based)
Wärmedurchgang	Loosely Coupled Conjugate Heat Transfer	Intervall: 10-15 Iterationen
Inlet/Outlet	Mass-Flow-Inlets (Brennstoff/Oxidator/ Quensche) Pressure Outlet (Abgas)	Oxidator/Quensche Luft – Volumenanteile: O2: 0,21; N2: 0,79 Brennstoff H2: 100% H2 Brennstoff Erdgas – Volumenanteile: CH4: 0,929; C2H6: 0,02; C3H8: 0,01 N2: 0,031; CO2: 0,01

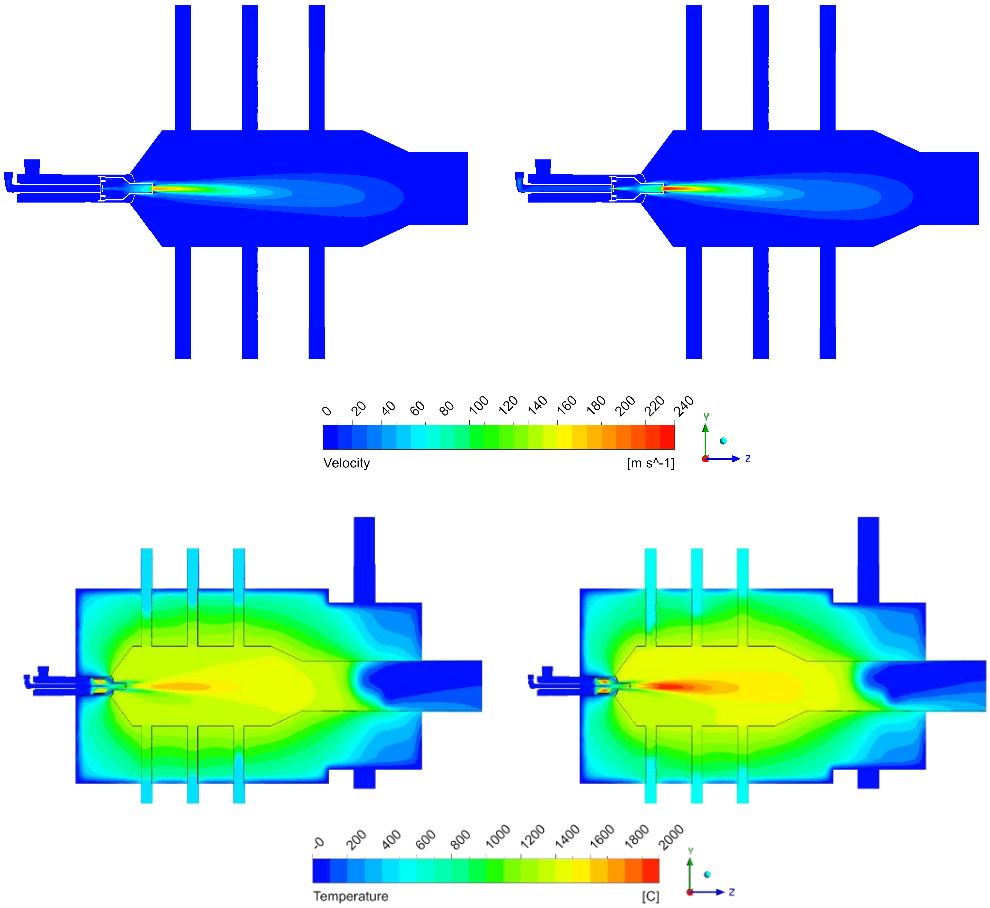

Abbildung 7. Temperatur- (oben) und Geschwindigkeitsverteilung (unten) im Fall von Erdgas (links) und Wasserstoff (rechts) bei 50kWs Leistung und einem Restsauerstoff von 4 Vol.-% (trocken)

Basierend auf den genannten Simulationseinstellungen wurden Berechnungen für Erdgas- und Wasserstoffverbrennung bei 50kW Brennerleistung durchgeführt. Zur Vergleichbarkeit der Ergebnisse, wurde der Luftüberschuss so eingestellt, dass sich laut Verbrennungsbilanz ein Restsauerstoffgehalt von 4% im trockenen Abgas ergibt. Dies entspricht einer real typischen Einstellung in Thermoprozessanlagen. Damit ergibt sich ein λ (Luftzahl) von 1,21 bei Erdgas und 1,18 bei Wasserstoff. Die entsprechende Temperatur- und Geschwindigkeitsverteilung eines Schnitts durch das komplette Modell ist in Abbildung 7 dargestellt. Im Vergleich mit Erdgas ist zu erkennen, dass im Fall von Wasserstoff deutlich höhere Strömungsgeschwindigkeiten im Bereich der Flammenzone erreicht werden, insbesondere nach Austritt aus der keramischen Vorbrennkammer. Diese höheren Geschwindigkeiten sind im Wesentlichen auf die geringere Dichte sowie die stärkere thermische Expansion der Verbrennungsgase aufgrund der höheren Flammentemperatur zurückzuführen. Auch hinsichtlich der Temperaturverteilung ergeben sich im gesamten Feuerungsraum und insbesondere in der Flammenzone deutlich höhere Temperaturen. Diese resultieren zum einen aus der höheren Reaktivität von Wasserstoff, die zusammen mit der geringeren Anzahl an Zwischenspezies zu einer schnelleren Umsetzung des Brennstoffs führt.

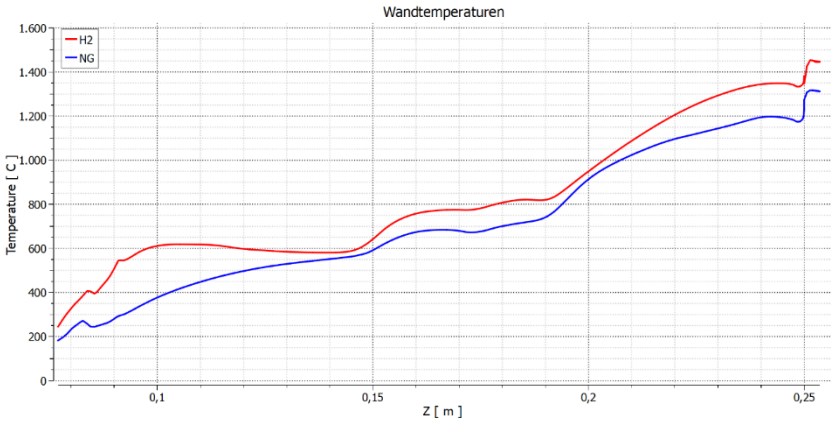

Abbildung 8. Temperaturverlauf entlang der Innenwand der keramischen Vor-Brennkammer im Fall von Erdgas (NG) und Wasserstoff (H2)

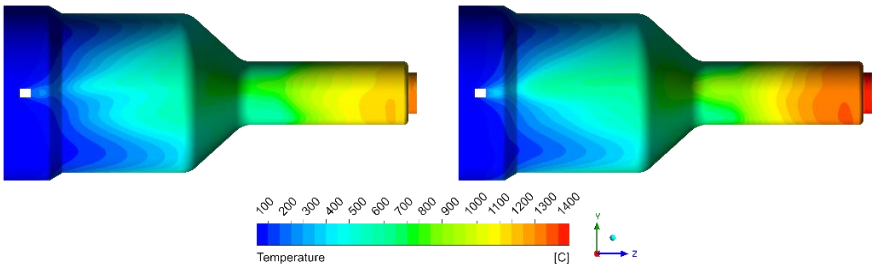

Abbildung 9. Temperaturverlauf entlang der Innenwand der keramischen Vor-Brennkammer (links) im Fall von Erdgas (links) und Wasserstoff (rechts)

Des Weiteren wurde der Temperaturverlauf entlang der Innenwand der keramischen Vor-Brennkammer im Inneren des Industriebrenners untersucht. Abbildung 8 zeigt den Temperaturverlauf entlang der unteren Kante, des in Abbildung 9 gezeigten Schnittes. Es stellt sich heraus, dass die Temperaturbelastung im Fall von Wasserstoff über die komplette Länge deutlich höher liegt (bis zu 200K) als bei Erdgas. Es liegen Wandtemperaturmaxima von 1335 °C bei Erdgas und 1485 °C bei Wasserstoff vor. Auch wenn die Temperaturverläufe geometrisch ähnlich erscheinen, ist beim Wasserstoff ein früherer, recht starker Anstieg der Temperatur zu erkennen, welcher beim Erdgas ausbleibt. Da kurz vor der Vorbrennkammer die Mischzone des Brenners liegt, wird angenommen, dass der Start der Verbrennung aufgrund der beschleunigten Reaktionskinetik der Wasserstoff-Verbrennung näher an die Mischzone rückt. Dies spiegelt sich auch in den Temperaturverläufen der Kontour-Plots in Abbildung 9 wider. Auch wenn eine Validierung des Modells durch Messungen aussteht, bestätigen die Ergebnisse die Hypothese, dass Brennerkomponenten bei Wasserstoff-Verbrennungen deutlich höheren, thermischen Belastungen ausgesetzt sind, als es das bei Erdgas der Fall ist.

Zusammenfassung und Ausblick

Für den zuverlässigen und wirtschaftlichen Betrieb von Wasserstoffbrennern werden neue Materialkonzepte benötigt, die den erhöhten thermischen und chemischen Belastungen im Vergleich zu Erdgas standhalten. Die erhöhte Temperaturbelastung konnte durch Simulationsstudien nachgewiesen werden. Weiterhin wurden hochbelastete Komponenten identifiziert, welche von den vielversprechend erscheinenden, neuartigen keramischen Folienverbunden profitieren könnten. Zur Charakterisierung dieser Materialien wurde eine Methodik für die experimentelle Untersuchung neuer keramischer Verbundwerkstoffe vorgestellt.

Erste Ergebnisse zeigen vielversprechende Ansätze für keramische Folienverbunde: Für bestimmte Zusammensetzungen konnte eine ausreichende Verdichtung sowie eine stoffschlüssige Verbindung den keramischen Lagen erzielt werden. Die Kombination stabiler Siliciumcarbid-Schichten mit temperaturabhängig viskosen Zwischenschichten eröffnet die Möglichkeit, thermisch induzierte Spannungen bei Temperaturwechseln zu kompensieren. Auf diese Weise können Rissbildungen reduziert bzw. kleinere Risse durch Selbstheilungseffekte im Abkühlvorgang geschlossen werden.

In zukünftigen Versuchsreihen sollen verschiedene Betriebszustände und die Auswirkung dieser auf eine Reihe von Werkstoffproben und deren Thermoschockbeständigkeit untersucht werden. Dabei werden sowohl konventionelle Materialien (hochtemperaturbeständige Stähle, Al2O3, SiC) als auch neuartigen Materialien (keramische Folienverbunde, Al2O3-CMC) bezüglich ihrer Beständigkeit verglichen und anschließend materialwissenschaftlich untersucht.

Durch Messungen am realen Versuchsstand soll das Simulationsmodell validiert werden und ggf. verschiedene Modelle gegeneinander verglichen werden. Außerdem ist es geplant, die Proben in das Modell zu integrieren und so deren reale Belastung in der Brennkammer abzuschätzen.

Die dargestellten Untersuchungen befinden sich derzeit in der Durchführung. Das entwickelte Konzept wird in weiterführenden Experimenten und numerischen Simulationen systematisch überprüft und validiert.

Danksagung

Die hier vorgestellten Ergebnisse sind Bestandteil des IGF-Leittechnologieprojekts KerKoWas. Die Forschungsvorhaben (01IF00072 E; 01IF00073 E) werden im Rahmen des Programms zur Förderung der industriellen Gemeinschaftsforschung (72 LBR/1 and 73 LBR/1) durch das Bundesministerium für Wirtschaft und Klimschutz (BMWK) über den Projektträger DLR-PT aufgrund eines Beschlusses des Deutschen Bundestages gefördert.

Literaturverzeichnis

[1] Bernhardt D., Wilhelm R., Götze J., Beckmann M.: Auswirkungen der Substitution von Erdgas durch Wasserstoff in Industriefeuerungen – Experimentelle Untersuchungen und CFD-Simulationen an Pilotbrennern, 55. Kraftwerkstechnisches Kolloquium, Dresden, 2023.

[2] Wilhelm R.: H2-ready! – Erfahrungen und Anwendungsbeispiele aus der Feuerungstechnik, in: Beckmann M. (Hrsg.): Wasserstoff 2022 – Hydrogen, SAXONIA Standortentwicklungs- und -verwaltungsgesellschaft mbH, Freiberg, 2022.

[3] Forschungsgemeinschaft Industrieofenbau e.V.: Innovative Werkstoffkonzepte für den Einsatz in Wasserstoff und dessen Verbrennungsprodukten – Feuerfestmaterialien, Stähle, Keramiken für Thermoprozessanlagen, IGF-Schlussbericht, IGF-Vorhaben Nr. 33 LBG

[4] Baukal C.E.: Industrial Burners Handbook (1st ed.), CRC Press, ISBN: 978-0-8493-1285-6, 2004.

[5] Gas- und Wärme-Institut Essen e.V., Forschungsgemeinschaft Feuerfest e. V.: Auswirkungen der Zumischung erneuerbarer Energien im Erdgasnetz auf thermoprozesstechnische Anlagen in der keramischen Industrie. IGF-Schlussbericht, IGF-Vorhaben Nr. 18684 N

[6] X. Hou, E. Wang, B. Li, J. Chen, K.-C. Chou, Corrosion behavior of porous silicon nitride ceramics in different atmospheres, Ceram. Int. 43, 4344-4352, 2017.

[7] Kislinger C., Daurer G., Schwarz S., Demuth M., Gaber C., Hochenauer C.: CFD study of hydrogen combustion effects on the heat-up characteristics of steel samples using a low-swirl burner: A comparative analysis with methane, Applied Thermal Engineering, 261, 2025.

Bedeutung von sekundären Gasphasenreaktionen bei der Pyrolyse von PMMA: Experimente und Modellierung

S. Pielsticker[1*], K. Gfall[1,2] und R. Kneer[1]

*pielsticker@wsa.rwth-aachen.de

[1] *Lehrstuhl für Wärme- und Stoffübertragung (WSA), RWTH Aachen University, Augustinerbach 6, 52056 Aachen, Deutschland*
[2] *Leibniz-Institut für Polymerforschung Dresden, Hohe Straße 6, 01069 Dresden, Deutschland*

Abstract
Die wachsende Menge an Kunststoffabfällen erfordert die verstärkte Suche nach effektiven Recyclingstrategien. Polymethylmethacrylat (PMMA), ein weit verbreiteter thermoplastischer Kunststoff, stellt aufgrund seiner Langlebigkeit eine Herausforderung für das Abfallmanagement dar. Das chemische Recycling mittels Pyrolyse bietet einen vielversprechenden Ansatz zur Umwandlung von PMMA-Abfällen in wertvolle Ressourcen sowie zur Förderung einer Kreislaufwirtschaft. Bei der Pyrolyse erfolgt eine thermische Zersetzung in einer inerten Atmosphäre, wobei das Monomer Methylmethacrylat (MMA) und andere nutzbare Verbindungen entstehen. Das Zusammenspiel von primärer Depolymerisation des PMMA (Feststoffphase) und sekundärer Zersetzung in Monomerbruchstücke (Gasphase) hat starken Einfluss auf die Selektivität der Endprodukte bzw. den Wirkungsgrad des Recyclingprozesses. Neben der Partikel- und Gastemperatur spielt dabei insbesondere die jeweilige Verweilzeit eine entscheidende Rolle. In dieser Studie wird das Produktspektrum bei der PMMA-Pyrolyse in einem Wirbelschichtreaktor mit Hilfe eines Fourier-Transform-Infrarotspektrometers bestimmt. Um die Rolle der sekundären Pyrolyse näher zu untersuchen, werden zusätzlich Experimente mit reinem gasförmigem MMA durchgeführt, um primäre und sekundäre Reaktionspfade zu differenzieren.

Einleitung

Das wachsende Problem der Kunststoffabfälle hat das weltweite Streben nach wirksamen Recyclingstrategien verstärkt. Polymethylmethacrylat (PMMA), ein weit verbreiteter Thermoplast, der für seine Transparenz und Witterungsbeständigkeit bekannt ist, stellt aufgrund seiner Langlebigkeit und weit verbreiteten Verwendung eine Herausforderung für die Abfallwirtschaft dar. Das chemische Recycling durch Pyrolyse ist ein vielversprechender Weg, um PMMA-Abfälle im Sinne einer Kreislaufwirtschaft in wertvolle Ressourcen zurückzuwandeln [1]. Die Pyrolyse von PMMA umfasst die thermische Zersetzung in einer inerten Atmosphäre, wobei das Monomer Methylmethacrylat (MMA) und andere wertvolle Verbindungen entstehen. Die Effizienz des Prozesses hängt vom Verständnis der Reaktionskinetik der thermischen Zersetzung ab. Faktoren wie Temperatur, Aufheizgeschwindigkeit, Molekulargewicht und Katalysatoren oder Verunreinigungen beeinflussen die Depolymerisations- und Abbauwege. Ein üblicher Ansatz ist die Annahme, dass während der primären Pyrolyse die PMMA-Polymerketten zu MMA-Monomeren gespalten, die dann anschließend in der Gasphase weiter zu kleineren Abbauprodukten zersetzt werden. Das Verständnis der Wechselwirkung zwischen primären und sekundären Reaktionen ist entscheidend für die Optimierung der Pyrolyse, insbesondere wenn die Verweilzeiten von Partikeln und Gasen separat gesteuert werden können [2]. Um die Rolle der sekundären Pyrolyse und die relevanten Mechanismen zu klären, werden Experimente mit reagierenden festen PMMA-Partikeln und reinem gasförmigen MMA durchgeführt. Sowohl für den primären Abbau des Feststoffs als auch für die anschließenden Zersetzungsreaktionen in der Gasphase werden verschiedene Modellansätze untersucht, um den notwendigen Detaillierungsgrad der Modellierung zu evaluieren.

Experimentelle Untersuchung

Für die experimentelle Untersuchung wird ein Wirbelschichtreaktor in zwei leicht unterschiedlichen Modifikationen verwendet. In beiden Konfigurationen wird die Reaktionstemperatur ($T_B = 623$–1073 K) über einen elektrisch beheizten Ofen eingestellt, in dem der Reaktor platziert ist. Das Bett aus Al_2O_3-Partikeln ($d_P = 100$–180 µm) wird mit einem N_2-Strom fluidisiert.

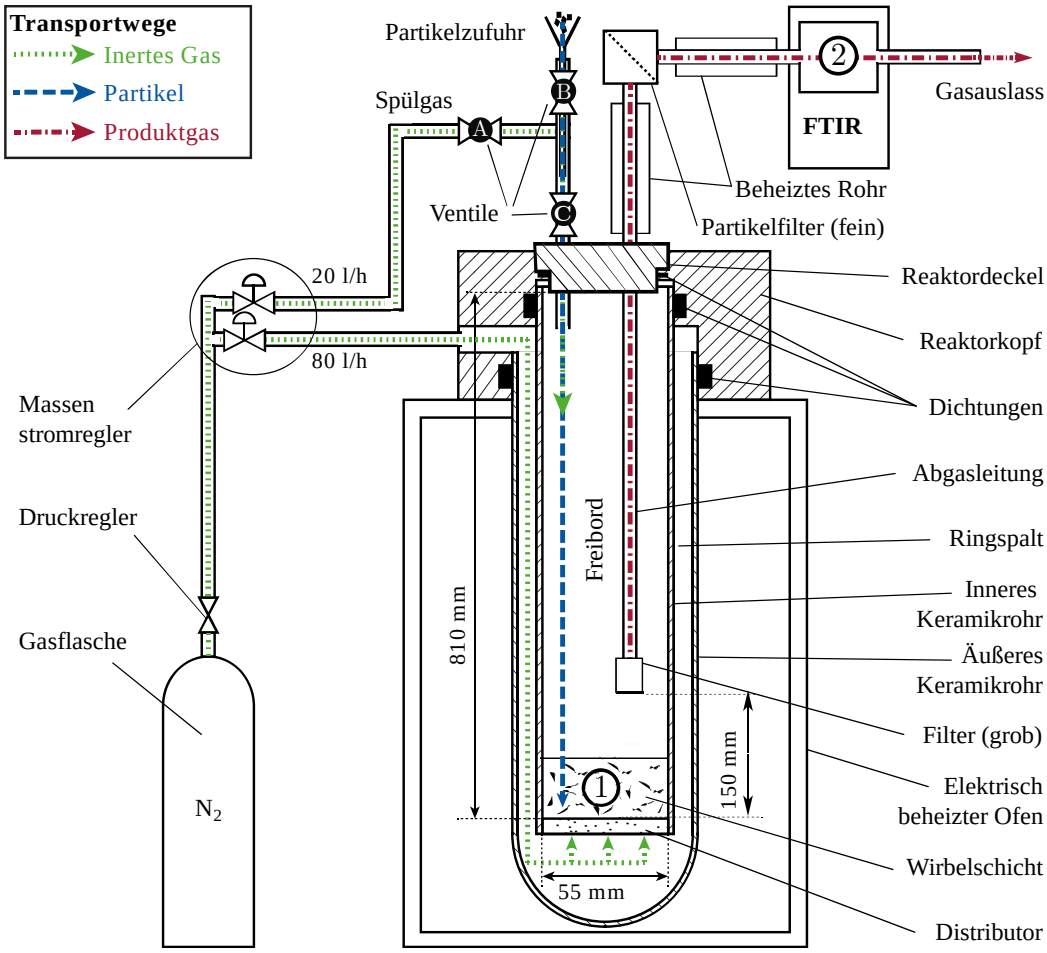

Abbildung 1. Wirbelschichtreaktor für die experimentelle Untersuchung der Pyrolyse von PMMA-Partikeln [3].

Um die pyrolytische Zersetzung der festen PMMA-Partikel zu untersuchen, werden diskontinuierlich Brennstoffproben ($m_{PMMA} = 15$ mg, $d_P = 600$–800 µm) über ein Schleusensystem und einen Spülgasstrom in das Bett eingebracht, wie in Abbildung 1 dargestellt. Das PMMA-Probenmaterial besteht aus recyceltem PLEXIGLAS® der Firma Röhm. Das ursprüngliche Material wurde durch radikalische Polymerisation mit einer molaren Masse von $M = 400.000$ g mol^{-1} synthetisiert. Als recyceltes Material wird jedoch aufgrund des Alterungsprozesses eine niedrigere molare Masse erwartet. Während die Partikel bis zur vollständigen Zersetzung im Reaktor verbleiben, vermischen sich die gasförmigen Reaktionsprodukte, das Fluidisierungsgas und das Spülgas miteinander und verlassen die Reaktionszone über ein beheiztes Abgasrohr. Beim verwendeten Fluidisierungsvolumenstrom von 80 l/h beträgt die Verweilzeit der Gase in der heißen Reaktionszone etwa 6 bis 8 s.

Bei der MMA-Pyrolyse wird ein leicht modifizierter Reaktor verwendet. Der Spülgasstrom wird zunächst durch ein temperiertes Bad aus flüssigem MMA geleitet, bevor er auf eine bestimmte Temperatur abgekühlt wird, um einen mit MMA gesättigten Gasstrom zu erzeugen. Der Prozess ist ähnlich wie beim Kalibrierungsprozess, der in der Studie von Pielsticker et al. [4] beschrieben wird. Anschließend wird der Gasstrom durch ein kleines Keramikrohr zum Boden des Reaktors geleitet und vermischt sich mit dem Bett. Durch eine Veränderung des Volumenstroms zwischen 50 und 150 l/h wird die mittlere

Verweilzeit des Gases je nach Temperatur zwischen 3,0 und 9,1 s (773 K) bzw. 2,4 und 7,2 s (973 K) variiert.

Modellierung

Die mathematische Modellierung des Pyrolyseprozess von PMMA im Wirbelschichtreaktor untergliedert sich in drei Teilmodelle: ein Partikelmodell für Massen- und Energiebilanz zur Berechnung der Partikeltemperatur, ein reaktionskinetisches Modell zur Bestimmung der freigesetzten Produkte aus dem Partikel und ein Gasphasenmodell zur Beschreibung sekundärer Zersetzungsreaktionen und dem Gastransport von der Reaktionszone in der Wirbelschicht zum FTIR-Analysator.

Die Energiebilanz dient dazu, die zeitabhängige homogene Partikeltemperatur $T_\mathrm{P}(t)$ zu bestimmen. Wie in Gfall et al. [3] gezeigt, ist die Annahme einer homogenen Partikeltemperatur gerechtfertigt, da die intrapartikulären Transportwiderstände kleiner ausfallen als der externe Widerstand zwischen Partikel und Bett. Die zugehörige Energiebilanz in Gleichung (1) für einen repräsentativen Einzelpartikel berücksichtigt bei der Partikelerwärmung einen konvektiven Wärmeübergang, Wärmeübertragung durch Strahlung sowie eine Energiesenke durch die endotherme Depolymerisationsreaktion und die Verdampfung des MMA im Partikel:

$$m_\mathrm{P} \cdot c_\mathrm{P} \cdot \frac{\mathrm{d}T_\mathrm{P}}{\mathrm{d}t} = \alpha \cdot S_\mathrm{P} \cdot (T_\mathrm{G} - T_\mathrm{P}) + \dot{Q}_\mathrm{Str} + \frac{\mathrm{d}m_\mathrm{P}}{\mathrm{d}t} \cdot \left(\Delta h_\mathrm{Depol} + \Delta h_\mathrm{V}\right) \tag{1}$$

Sowohl für den konvektiven Wärmeübergangskoeffizienten α als auch für den Strahlungswärmestrom $\dot{Q}_\mathrm{Str}$ werden je nach Partikelposition unterschiedliche Modellierungsansätze genutzt um den veränderlichen Randbedingungen während des Dosierprozesses und der Reaktion im Wirbelbett gerecht zu werden. Eine detaillierte Beschreibung aller berücksichtigten Gleichungen für die Partikelbewegung und die Wärmeübertragung ist in der Arbeit von Pielsticker et al. [5] zu finden. Benötigte Stoffdaten (z. B. Wärmekapazität c_P, Dichte ρ_P) und Enthalpien ($\Delta h_\mathrm{Depol}, \Delta h_\mathrm{V}$) für den PMMA-Partikel sind aus der Arbeit von Pielsticker et al. [4] entnommen. Die Massenbilanz in Gleichung (2) beschreibt den zeitabhängen Massenverlust eines Partikels und ist hier direkt für das genutzte Einschrittreaktionsmodell formuliert:

$$\frac{\mathrm{d}m_\mathrm{P}}{\mathrm{d}t} = m_{\mathrm{P},0} \cdot r_\mathrm{PMMA}(T_\mathrm{P}) \cdot \left(1 - \frac{m_\mathrm{P}}{m_{\mathrm{P},0}}\right) \tag{2}$$

Die aktuelle Partikelmasse m_P kann aus der anfänglichen Partikelmasse $m_{\mathrm{P},0}$ abgeleitet werden. Zusätzlich erfolgt eine Skalierung mit einer fiktiven Partikelanzahl, um die Masse der aufgegebenen Probe zu erzielen. Die charakteristische Reaktionsrate $r_\mathrm{PMMA}(T_\mathrm{P})$ ist dabei direkt an die Partikeltemperatur gekoppelt und kann somit auch Effekte durch limitierten Wärmetransport beschreiben. Sie folgt der gegebenen Reaktionskinetik aus Abbildung 3.

Die Produkte des primären Pyrolysemodells in der Partikelphase dienen als Quellterme im Gasphasenmodell. Je nach aktueller Partikelposition wird der Quellterm in einem anderen Gasphasenelement appliziert. Die verschiedenen Gasphasenelemente („Freibord über der Wirbelschicht“, „Wirbelschicht“, „Abgasleitung“, „Filter“ und „FTIR-Gaszelle“) repräsentieren die unterschiedlichen Zonen des Reaktorsystems und berücksichtigen durch unterschiedliche Volumina und Temperaturen das Transport- und Reaktionsverhalten entlang der Gastransportstrecke vom Wirbelbett zum FTIR-Analysator. Die Gasphasenreaktion erfolgt vereinfachend ebenfalls mittels eines Einschrittreaktionsmodells mit Arrhenius-Ansatz (analog der bisher betrachten Teezersetzung [5]) mit der bestimmten MMA-Zersetzungskinetik aus Gleichung (4).

Die Modellimplementierung ist objektorientiert in MATLAB realisiert, sodass eine einfache Austauschbarkeit einzelner Modellkomponenten (z. B. Wärmeübertragungsmodell, primäres Reaktionsmodell oder Gasphasenreaktionsmodell) erfolgen kann [6].

Ergebnisse

Im folgenden Abschnitt werden die Ergebnisse der durchgeführten Versuche und korrespondierenden Modellierungen vorgestellt. Zunächst erfolgt eine Betrachtung der Experimente mit reinem MMA, wo

lediglich die Zersetzung in der Gasphase untersucht wird. Die gewonnen Ergebnisse dienen als wichtige Eingangsgröße in das gekoppelte Pyrolysemodell, wo primäre Zersetzungsreaktionen im Partikel und sekundäre Gasphasenreaktionen simultan betrachtet werden können. Dies erlaubt eine tiefgreifende Analyse der zugrundeliegenden Reaktionspfade während der PMMA-Pyrolyse, bei der primäre und sekundäre Reaktionen mit dem vorliegenden Reaktoraufbau nicht getrennt voneinander untersucht werden können.

Abbildung 2 zeigt die Ausbeuten von MMA ($C_5H_8O_2$) und leichten gasförmigen Zersetzungsprodukten bei unterschiedlichen Reaktortemperaturen T und drei verschiedenen Volumenströmen $\dot{V}$ (50, 100 und 150 l/h). Unter der Annahme eines idealen Strömungsrohres resultieren daraus die angegebenen mittleren Gasverweilzeiten zwischen 2,4 und 9,1 s. Im Niedertemperaturbereich bis 823 K sind die hauptsächlich zu beobachtende Reaktionsprodukte CO_2, Methanol (CH_3OH) und Formaldehyd (CH_2O). Erstes und Letztes resultieren als Produkte der beiden Hauptspaltungsreaktionen, wie von Zeng et al. [2] und Forman et al. [7] beschrieben. Die Bildung von Methanol lässt sich über die Spaltung der CO-Bindung, die Bildung von OCH_3-Radikalen und einer Wasserstoffaddition erklären. Insbesondere im Temperaturbereich zwischen 873 und 943 K werden signifikante Mengen CH_2O gebildet, bevor ab höheren Temperaturen vor allem reine Kohlenwasserstoffe (CH_4, C_2H_4, C_3H_6 und C_6H_6) und CO gebildet werden.

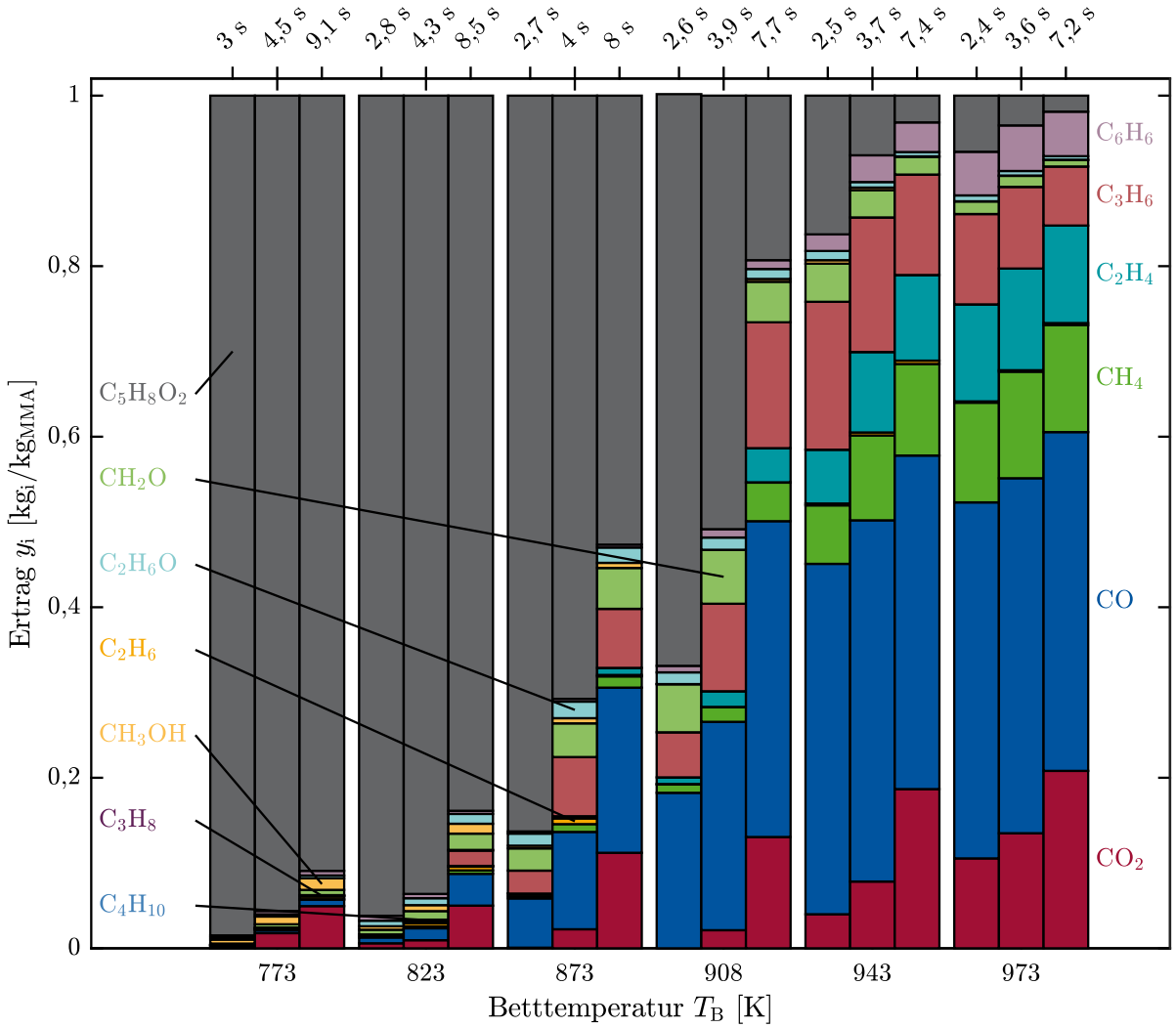

Abbildung 2. Zersetzungsprodukte von MMA bei der Pyrolyse in N_2 für verschiedene Reaktortemperaturen und Gasvolumenströme

Durch Variation des Volumenstroms können verschiedene Gasverweilzeiten unter heißen Bedingungen untersucht werden. Für den untersuchten Temperaturbereich ist zwischen 873 und 943 K die stärkste Abhängigkeit von der untersuchten Verweilzeit zu beobachten. Für geringere Temperaturen liegt die

Zersetzung von MMA in Leichtgasprodukte selbst bei der größten Verweilzeit unter 20 %, während höhere Temperaturen bei den untersuchten Verweilzeiten zu Zersetzung von mehr als 80 % führen. Für Temperaturen außerhalb des gezeigten Temperaturbereichs ist die Zersetzung entweder nicht signifikant oder es findet ein nahezu vollständiger Umsatz statt. Beide Bedingungen lassen daher keine Rückschlüsse auf die Zersetzungskinetik zu.

Unter der Annahme einer idealen Pfropfenströmung im Reaktor und einer globalen Einschritt-Zersetzungsreaktion kann die charakteristische Zersetzungsrate r_{MMA} des MMA in Leichtgaskomponenten mittels Gleichung 3 beschrieben werden

$$r_{\mathrm{MMA}} = \ln(1 - y_{\mathrm{LG}}) \cdot \frac{\dot{V}}{V} \tag{3}$$

wobei y_{LG} die summierte Ausbeute an leichten Gasen und V das Reaktorvolumen zwischen Bett und Reaktorausgang ist. Obwohl es für die Modellierung der Gasphasenreaktion bei der MMA-Zersetzung auch detailliertere Mechanismen gibt (z.B. Yang et al. [8]), wird hier zunächst auf eine detailliertere Modellierung verzichtet, um die Kopplung mit dem primären PMMA-Partikelreaktionsmodell und dem Reaktormodell zu gewährleisten. Die vorhandenen Messdaten bieten sich aber auch für eine tiefergehende Modellierung der vorliegenden Gasphasenchemie an.

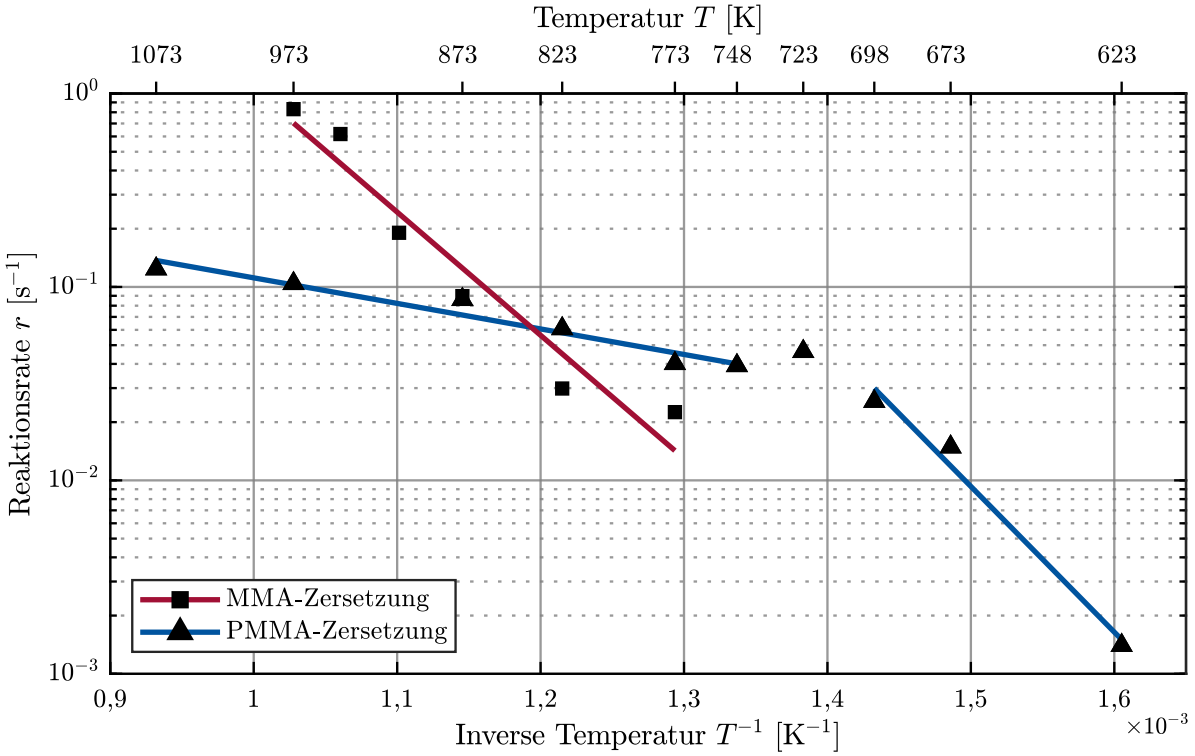

Abbildung 3. Arrhenius-Diagramm für die Einschritt-Zersetzungskinetik von MMA im Vergleich zur primären Zersetzungskinetik von PMMA mit kinetisch kontrolliertem und Wärmetransport limitiertem Reaktionsregime [3].

Abbildung 3 zeigt die ermittelten Reaktionsraten in einem Arrhenius-Diagramm. Der lineare Zusammenhang zeigt, dass die MMA-Zersetzungsrate über einen Arrhenius-Ansatz

$$r_{\mathrm{MMA}} = A_{\mathrm{MMA}} \cdot \exp\left(-\frac{E_{\mathrm{a}}}{R \cdot T}\right) \tag{4}$$

modelliert werden kann. Über eine Minimierung der Fehlerquadrate werden die kinetischen Parameter Aktivierungsenergie $E_{\mathrm{a}} = 99{,}1$ kJ/mol und präexponentieller Faktor $A_{\mathrm{MMA}} = 1{,}02 \cdot 10^5$ s^{-1} bestimmt.

Zusätzlich ist auch die primäre Zersetzungskinetik von PMMA in Abbildung 3 gezeigt, die in der Studie von Gfall et al. [3] mit dem gleichen Reaktorsystem bestimmt wurde. Hierbei sind zwei unterschiedliche Reaktionsregime – gekennzeichnet durch unterschiedliche Steigungen – zu beobachten. Für den reaktionskinetisch limitierten Bereich für Temperaturen $T < 700$ K sind für das globale Einschrittmodell die intrinsischen Parameter $E_a = 144$ kJ/mol und $A_{PMMA} = 1{,}85 \cdot 10^9$ s^{-1} bestimmt. Für höhere Temperaturen wird die Reaktion durch einen unzureichenden Wärmetransport von der Wirbelschicht zum PMMA-Partikel limitiert. Dieser Effekt kann über eine scheinbare Reaktionskinetik mit den Parametern $E_a = 25{,}3$ kJ/mol und $A_{PMMA} = 2{,}33$ s^{-1} beschrieben werden.

Um das Zusammenspiel von primärer Zersetzung des festen PMMA während der Pyrolyse und die sekundäre Gasphasenzersetzung von MMA zu analysieren, werden experimentelle Ergebnisse der PMMA-Pyrolyse aus dem Wirbelschichtreaktor mit unterschiedlichen Modellierungsansätzen in Abbildung 4 verglichen.

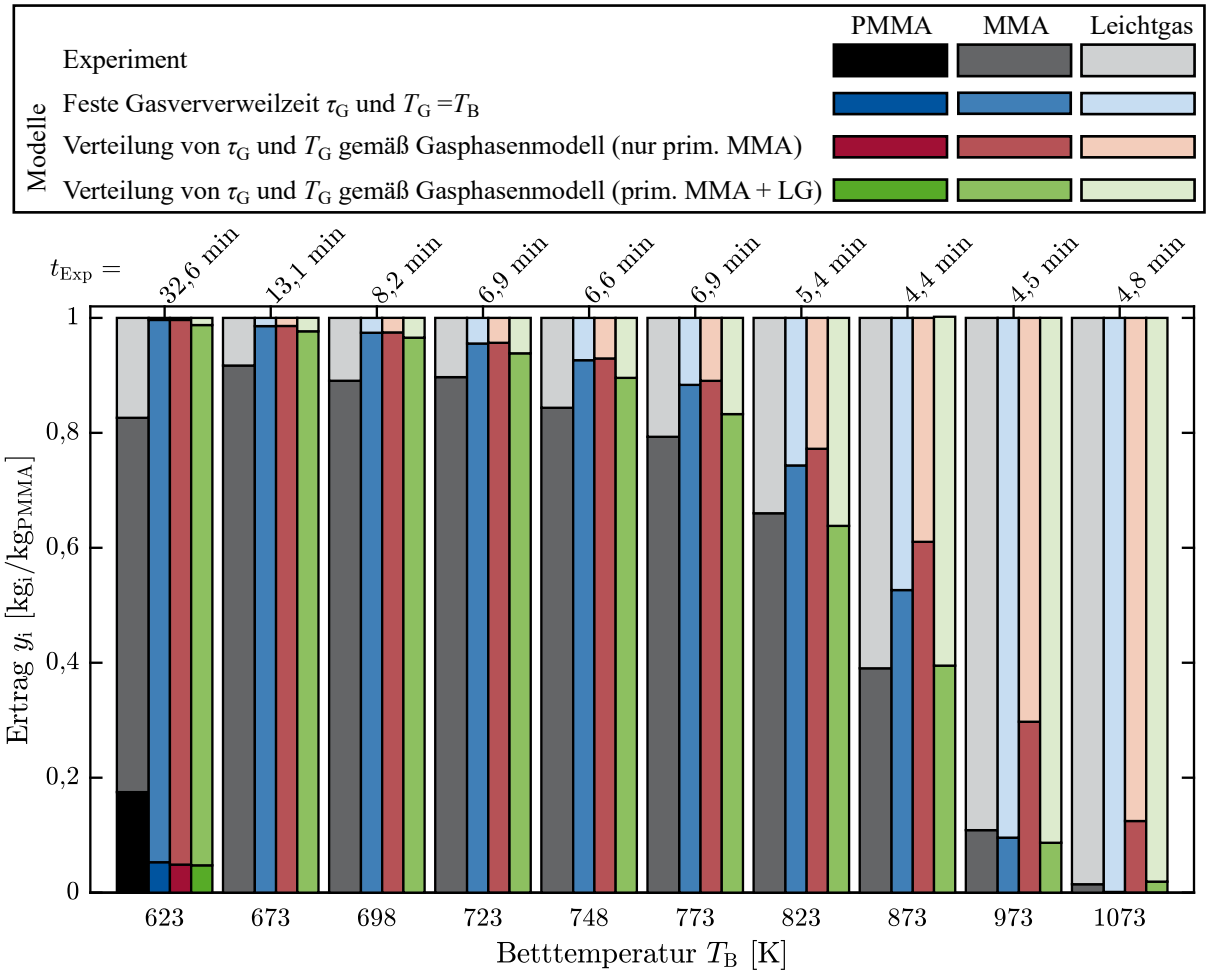

Abbildung 4. Experimentell bestimmte Erträge vom PMMA, MMA und Leichtgasen im Vergleich zu Vorhersagen verschiedener Modelle bei unterschiedlichen Reaktortemperaturen

Im ersten Modellansatz wird ein vereinfachtes Gasphasenmodell betrachtet. Die Zersetzung des MMA findet dort ausschließlich innerhalb der Wirbelschicht statt, wobei die Gastemperatur T_G der Betttemperatur T_B entspricht und die Gasverweilzeit mit $\tau_G = \frac{V_B}{\dot{V}}$ aus dem Volumen des Betts und dem Volumenstrom (korrigiert auf die Betttemperatur) berechnet wird. Insgesamt kann mit diesem Ansatz der Trend der Verteilung von Leichtgas und MMA gut vorhergesagt werden. Allerdings wird der experimentell nachgewiesene MMA-Anteil für die meisten untersuchten Reaktortemperaturen überschätzt.

Mit dem zweiten Modellansatz soll untersucht werden, ob das in der primären Pyrolyse gebildete MMA nicht nur im Bett zersetzt wird, sondern z.B. auch im Freibord oberhalb der Wirbelschicht oder im Abgasrohr. Hierzu wird das aus mehreren Elementen gekoppelte Gasphasenmodell genutzt, um so das Temperaturprofil des Reaktors und die jeweilige Verweilzeitverteilung abbilden zu können. Die

Ergebnisse zeigen, dass gegenüber des vorherigen Modellansatzes die vorhergesagten MMA-Anteile ansteigen. Dies resultiert daraus, dass ein Teil des im Bett freigesetztes MMA die Reaktionszone über das Abgasrohr verlässt. Dadurch liegt eine deutlich geringere Verweilzeit des Gases gegenüber dem ersten Fall vor. Durch die vergleichsweise hohe Gasgeschwindigkeit im Abgasrohr und die damit verbundene kurze Verweilzeit, ist die Zersetzung im Abgasrohr vernachlässigbar (ca. 1–2 %). Die im Freibord während des Dosiervorgangs freigesetzten MMA-Anteile, die eine deutlich größere Verweilzeit besitzen und somit fast vollständig zersetzt werden, sind auf die Gesamtmasse gesehen für die untersuchte Partikelgröße nicht relevant. Ein Gasaustausch von der Wirbelschicht in das Freibord entgegen dem Spülgasstrom ist in der aktuellen Modellierung nicht möglich.

Die beiden bisherigen Modellansätze beruhen darauf, dass Leichtgas nur als finales Produkt der rein sequentiell ablaufenden Zersetzungsreaktionen entsteht. Das bedeutet, in der primären Pyrolyse im Partikel wird ausschließlich PMMA zu MMA umgesetzt, das dann in der Gasphase weiter zu Leichtgas zerfällt. Im dritten Modellansatz ist zusätzlich eine Leichtgasbildung während der primären Pyrolysereaktion implementiert. Vereinfachend wird angenommen, dass diese Reaktion die gleiche Aktivierungsenergie, aber einen um den Faktor 100 reduzierten präexponentiellen Faktor als die Bildungsreaktion von MMA besitzt. Die Annahme einer ähnlichen Aktivierungsenergie resultiert daraus, dass jede Kettenspaltungsreaktion mit dem Abspalten eines Nebenprodukts einhergeht. Mit dem gewählten Ansatz kann der Anteil an verbliebenem MMA deutlich besser vorhergesagt werden als mit den anderen beiden Modellansätzen. Lediglich im niedrigen Temperaturbereich wird der nachgewiesene MMA-Anteil weiterhin überschätzt. Das stark steigende Verhältnis von Leichtgas zu MMA für eine Reaktortemperatur von 673 K deutet darauf hin, dass die direkte Leichtgasbildung für geringere Temperaturen vermutlich im Verhältnis zur MMA-Bildung schneller abläuft. Dadurch würde auch hier die Vorhersagegenauigkeit verbessert werden, wenn die Reaktionskinetik der primären Leichtgasbildung von der MMA-Bildung entkoppelt wird.

Neben den integral freigesetzten Erträgen soll die Modellvorhersagegenauigkeit auch anhand der beobachteten Freisetzungsraten beurteilt werden. In Abbildung 5 sind die in der FTIR-Gaszelle beobachteten Freisetzungsraten jenen aus dem Gasphasenmodell extrahierten Raten gegenübergestellt. Da hierfür das detaillierte Gasphasentransportmodell erforderlich ist, sind Ergebnisse aus dem ersten Modellansatz mit der Annahme einer festen Gasverweilzeit nicht gezeigt. Es zeigt sich, dass bei niedrigen Temperaturen ($T_B = 673$ K) die beiden anderen Modellansätze die Rate leicht unterschätzen. Dies bestätigt die Theorie aus den integralen Messdaten, dass bei niedrigen Temperaturen die Bedeutung der direkten Leichtgasbildung steigt. Bei hohen Temperaturen hingegen führt der Modellansatz mit primärer Gasbildung zu einer Überschätzung der Rate, während der Ansatz ohne primäre Gasbildung zu einer Unterschätzung führt. Höchstwahrscheinlich wird mit der getroffenen Annahme, dass die Aktivierungsenergie der primären Leichtgasbildung identisch mit der MMA-Bildung ist, die Reaktionsrate für die hohen Temperaturen überschätzt.

Zusammenfassung

Die vorgestellte Arbeit untersucht die Pyrolyse von PMMA (Polymethylmethacrylat) in einem Wirbelschichtreaktor, um ein besseres Verständnis der primären (Partikel) und sekundären (Gasphase) Zersetzungsreaktionen zu gewinnen. Durch ein zweistufiges experimentelles Konzept – einerseits mit festem PMMA, andererseits mit gasförmigem MMA (Methylmethacrylat) – werden sowohl die Depolymerisation im Partikel als auch die nachfolgende Zersetzung in der Gasphase separat charakterisiert. Die Experimente mit MMA haben gezeigt, dass Temperatur und Verweilzeit als wichtigste Einflussgrößen das Verhältnis von nicht reagiertem MMA zu leichten Zersetzungsprodukten (z. B. CO, CO_2, Methanol oder Kohlenwasserstoffe) bestimmt. Aus der Summe aller gemessenen Leichtgasprodukte konnte der Zersetzungsgrad des MMA und mit der Annahme eines Pfropfenstromreaktors eine Reaktionskinetik für ein globales Einschrittreaktionsmodell abgeleitet werden.

Um das Pyrolyseverhalten von PMMA im Wirbelschichtreaktor mathematisch zu beschreiben, sind verschiedene Modellierungsansätze untersucht worden. Zum einen wird ein reines Sequenzmodell betrachtet, in dem primär im Partikel ausschließlich MMA gebildet wird, das dann danach in der Gasphase weiter abgebaut wird, und zum anderen ein Modell, das bereits während der primären Pyrolyse im Partikel auch leichte Gasprodukte annimmt.

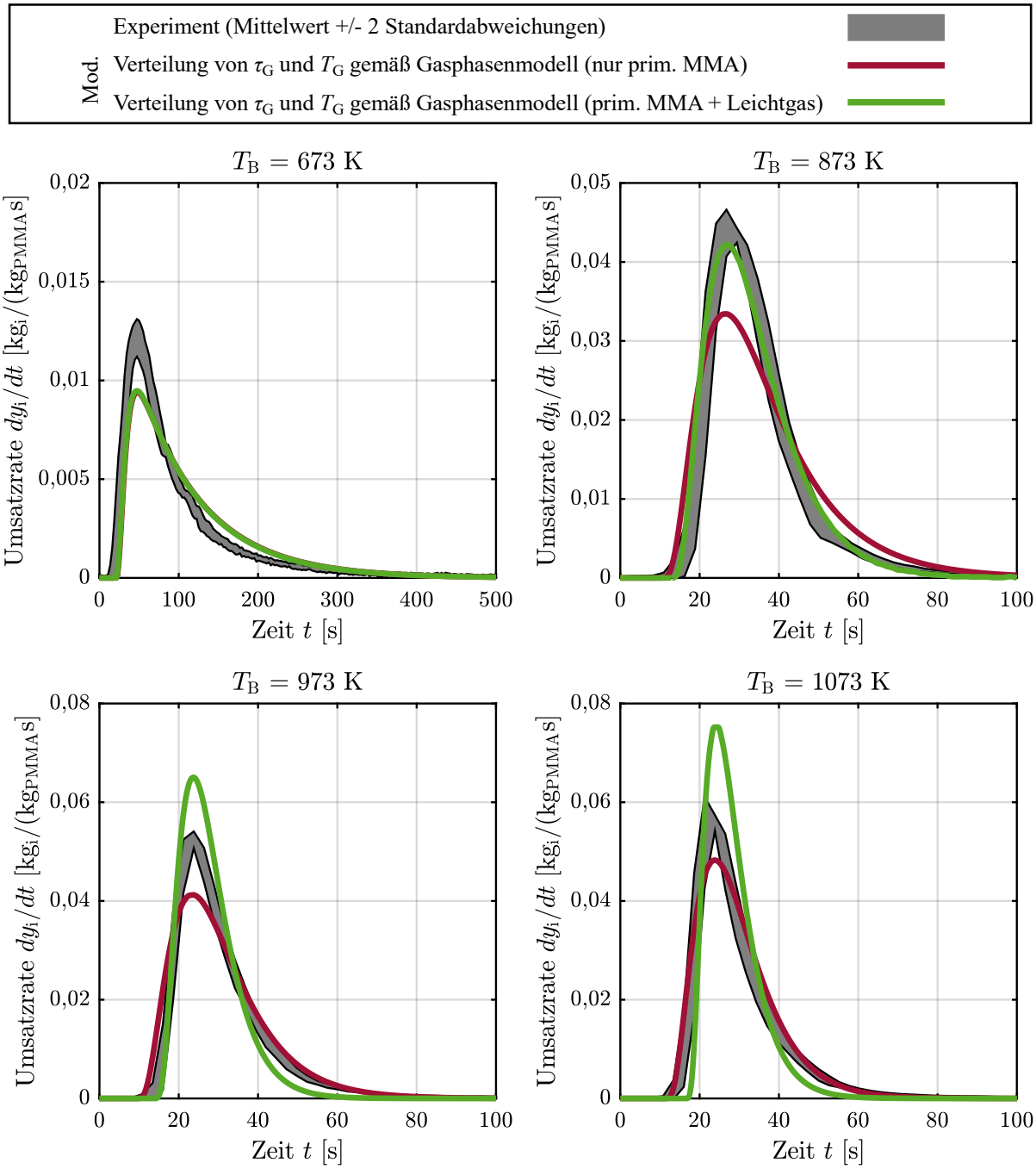

Abbildung 5. Experimentell beobachtete Umsatzraten in der FTIR-Gaszelle im Vergleich zu Modellvorhersagen bei unterschiedlichen Reaktortemperaturen

Die Gegenüberstellung der Modellrechnungen mit gemessenen Ausbeuten und Freisetzungsraten zeigt, dass beide Reaktionspfade – direkte Leichtgasbildung und sequenzielle Bildung über MMA – relevante Beiträge liefern. Besonders bei niedrigen Temperaturen unterschätzen alle Modellvarianten die Freisetzungsrate, was darauf hinweist, dass hier die direkte Leichtgasbildung stärker ist als angenommen. Bei hohen Temperaturen führt dagegen die Annahme identischer Aktivierungsenergien für die Bildung von MMA und direkten Leichtgasen zu einer Überschätzung der Freisetzungsrate.

Insgesamt bestätigen die Ergebnisse, dass neben Wärmetransportphänomenen und sekundärer Gasphasenzersetzung auch die unmittelbare Bildung leichter Gasprodukte im Partikel eine zentrale Rolle spielt. Die Studie unterstreicht somit die Bedeutung einer differenzierten Modellierung von Reaktionspfaden und Transportmechanismen, um das thermische Recycling von PMMA durch Pyrolyse gezielt optimieren zu können.

Literatur

[1] Kikuchi Y., Hirao M., Ookubo T., Sasaki A.: *Design of recycling system for poly(methyl methacrylate) (PMMA). Part 1: Recycling scenario analysis*, International Journal of Life Cycle Assessment,19(1),120–129, 2014.

[2] Zeng W. R., Li S. F., Chow W. K.: *Review on chemical reactions of burning poly(methyl methacrylate) PMMA*, Journal of Fire Sciences, 20(5),401–433, 2002.

[3] Gfall K., Kneer R., Pielsticker S.: *Determination of PMMA pyrolysis kinetics and the role of heat transfer limitations*, 13th Mediterranean Combustion Symposium, Korfu, Griechenland, 2025.

[4] Pielsticker S., Hendricks K., Knevels C., Lehnertz M. S., Palkovits R., Kneer R.: *Experimental determination of quantitative yields from polymethyl methacrylate (PMMA) flash pyrolysis in a fluidized bed reactor via online FTIR gas analysis*, Fuel, 392, 134827, 2025.

[5] Pielsticker S., Ontyd C., Kreitzberg T., Hatzfeld O., Schiemann M., Scherer V. et al.: *Adaptation of the chemical percolation devolatilization model for low temperature pyrolysis in a fluidized bed reactor*, Combustion Science & Technlogy,94(2), 417–434, 2022.

[6] Pielsticker S.: *Experimentelle Untersuchung und reaktionskinetische Modellierung der Pyrolyse biogener Feststoffe*, Dissertation, RWTH Aachen University, 2022.

[7] Forman R. L., Mackinnon H. M. , Ritchie P. D.: *Studies in pyrolysis. Part XXV. Acrylic, methacrylic, and crotonic acid, and some derivatives: Novel decarbonylation of αβ-unsaturated carboxylic acids*. Journal of the Chemical Society C, 2013–2016, 1968.

[8] Yang B., Westbrook C. K., Cool T. A., Hansen N., Kohse-Höinghaus K.: *Photoionization mass spectrometry and modeling study of premixed flames of three unsaturated $C_5H_8O_2$ esters*, Proceedings of the Combustion Institute, 34(1),443–451, 2013.

Modelling chemistry integration via deep neural networks in turbulent non-premixed methane flames

Weitao Liu*, Andreas Kronenburg and Thorsten Zirwes

*weitao.liu@irst.uni-stuttgart.de

[1]*Institute for Reactive Flows (IRST), University of Stuttgart, Pfaffenwaldring 31, 70569 Stuttgart, Germany*

Abstract

Solving finite-rate chemistry via direct integration yields accurate predictions without assumptions on time scales but is computationally expensive, representing a major bottleneck in high-fidelity combustion simulations. Deep neural networks (DNNs) offer a promising alternative by directly modelling integrated chemical source terms. In our previous work, we proposed a randomisation and unrolling training framework, through which the trained DNNs accurately captured multiple combustion regimes in a two-dimensional direct numerical simulation (DNS) of a transient counterflow laminar flame. In this work, we extend the evaluation of the same training strategy to two turbulent non-premixed methane–air flames exhibiting distinct turbulence–chemistry interactions. Additionally, we analyze the computational performance of the DNNs on both CPU and GPU architectures in parallel simulations.

Introduction

Detailed chemical mechanisms are essential for high-fidelity simulations of reactive flows, as they enable accurate representation of chemically fast and slow species across a wide range of conditions. Direct integration (DI) of finite-rate chemistry avoids assumptions about chemical time scales, making accurate predictions of species and radicals evolution, and is used in direct numerical simulations (DNS) and probability density function (PDF) methods. However, the high stiffness of chemical kinetics requires restrictive time stepping in time integration algorithms, resulting in a significant efficiency bottleneck thus, in most cases, the use of DI becomes unaffordable, especially for detailed chemical mechanisms in turbulent flame simulations.

Artificial neural networks (ANNs) are well-suited for approximating highly non-linear and stiff correlations in an efficient manner which is associated with their numerous non-linear activation units and inherently parallel architectures. These properties make ANNs a promising alternative to DI of finite-rate chemistry in reacting flow simulations. Nearly 30 years ago, Christo et al. [1, 2] pioneered the use of a multilayer perceptron (MLP) with two hidden layers in PDF simulations of turbulent flames. Their results showed good agreement with DI solutions, highlighting the potential of ANNs for chemistry integration under combustion conditions. Blasco et al. [3] later modelled chemistry integration using two MLPs with one and two hidden layers for a simplified methane mechanism and achieved satisfactory predictions. However, these early studies were limited to global reaction mechanisms involving no more than five reaction steps, constrained by the computational resources and machine learning capabilities of the time. As the complexity of chemical kinetics increases, shallow networks struggle with the growing nonlinearity and dimensionality.

To address this, Blasco et al. [4] introduced a self-organizing map (SOM) to partition the chemical state space into multiple subdomains, applying individual networks to each. This approach was successfully applied to partially stirred reactor simulations with a 9-species methane mechanism and was subsequently extended to more detailed mechanisms, including 16-species [5] and 32-species [6] methane systems. An et al. [7] compared three different SOM configurations for a skeletal kerosene mechanism (41 species, 132 reactions) in Reynolds-averaged Navier-Stokes (RANS) simulations of a rocket-based combined cycle engine. Their results suggested that prediction accuracy depends on the SOM architecture and the number of subdomains used. Furthermore, Readshaw et al. [8] noted that subdomains of similarity identified by SOM during training may not match the thermochemical distribution encountered

in posteriori simulations, potentially limiting SOM generalizability. As an alternative to composition splitting, Ding et al. [9] proposed the multiple multilayer perceptron (MMLP) approach, in which the evolution of each species is modelled by a set of MLPs. This strategy yielded accurate predictions in both laminar and turbulent methane flames with the use of GRI 1.2 mechanism. Ding et al. [10] further improved the MMLP framework by utilizing different ANNs based on input magnitudes rather than output characteristics. This significantly improved the prediction accuracy for nitrogen-related species in both laminar and turbulent flames simulated with the GRI 3.0 mechanism. This study also demonstrated that a careful design of the MMLP configuration prior to training is crucial, especially when dealing with detailed chemical mechanisms. Besides, implementing multiple MLPs in simulations introduces additional complexity and could increase computational overhead.

Another apporach to tackle the high non-linearity of detailed mechanisms is to adopt deep neural networks (DNNs). Zhang et al. [11] proposed a multi-scale sampling approach and employed a three-hidden-layer MLP for H_2 flames with six active species. The predictions by the network showed good agreement with ODE solutions. Xu et al. [12] extended this by training a four-hidden-layer MLP on the detailed GRI 3.0 mechanism. This network reasonably predicted ignition delay times and flame speeds in 0D auto-ignition and 2D premixed flame scenarios, though predictions of detailed temperature and species profiles were not included. Notably, Xu et al. [12] reported a slight flame front shift in the network's predictions for a spherical flame compared to the ODE solutions, likely due to error accumulation over the simulation time. Wang et al. [13] employed DNN for a skeletal dimethyl ether (DME) mechanism (39 species, 175 reactions) in a one-dimensional premixed flame and two-dimensional forced ignition of a mixing layer flame. DNN predictions were observed to gradually deviate from the combustion manifolds as errors accumulated in posteriori simulations, leading to unphysical thermochemical states. By enforcing elemental mass conservation via post-processing of predictions, the performance of the DNNs in terms of stability and accuracy was significantly improved. While post-processing predictions can enhance ANN performance, it may also introduce artificial errors, since mass conservation is only one constraint of thermochemical state manifolds [14], and applying different weights to species can result in different outcomes. Our recent work proposed a hybrid randomisation/unrolling training strategy to suppress error accumulation [15]. An increase in unrolling steps can efficiently enhance DNN performance without increasing computational costs in posteriori simulations. DNNs with more than five unrolling steps can accurately capture multiple combustion regimes, including ignition, propagation and extinction, in a two-dimensional transient counterflow laminar flame using the GRI 3.0 mechanism.

This study is an extension of our previous work [15] and investigates the generalizability and effectiveness of the hybrid randomisation/unrolling training approach in turbulent flame configurations. The DNN is trained by randomized states based on laminar methane-air flames using the DMR19 mechanism (19 reactive species, 84 reactions). Its performance is systematically evaluated in two three-dimensional simulations of turbulent non-premixed methane–air flames with different Damköhler numbers exhibiting significant variations in local extinction. In addition, the computational efficiency of the approach is assessed on both CPU and GPU architectures in parallel simulations.

Methodology

Randomized dataset generation

A hybrid manifold/random dataset generation approach is employed in this work. The core idea is to use thermochemical states sampled from laminar flame simulations as manifold references, while a randomisation algorithm introduces perturbations to species concentrations. This procedure extends the dataset boundaries and smooths the internal distribution. It is worth noting that only the randomized dataset is used during training. Regarding the simple canonical flame simulations for dataset generation, two two-dimensional counterflow methane-air flames under atmospheric conditions are considered: a transient flame at a strain rate of $10\,\mathrm{s}^{-1}$ and a steady-state solution at a strain rate of $50\,\mathrm{s}^{-1}$. In both cases, the separation distance between fuel and oxidizer nozzles is set to 20 mm. The fuel stream consists of pure methane while the oxidizer stream comprises air (23% O_2 and 77% N_2 by mass fraction) at an inlet temperature of $T_0 = 650\,\mathrm{K}$. In the transient flame simulation, the fuel and oxidizer streams are initially non-reacting and pre-mixed, with steady-state velocity and species fields provided as initial conditions.

Ignition is triggered by a 0.9 mm $\times$ 1.0 mm hot spot at 1950 K, located on the centerline from the fuel nozzle. Following ignition, the flame propagates away from the centerline and gradually transitions into a non-premixed mode. The transient flame simulation in total runs for 20 ms and provides reference (i.e., manifold) thermochemical states spanning multiple combustion regimes. The inclusion of the steady-state flamelet solution at a strain rate of 50 s^{-1} accounts for states that occur under enhanced mixing conditions. The randomisation algorithm developed in this work builds upon the approach by Ding et al. [9]. Since not all thermochemical states are chemically active, only those sampled from laminar flame simulations that lie within the flammability limits are considered. This corresponds to temperature and mixture fraction ranges of $T \in [700,\ 3000]$ K and $f \in [0.01,\ 0.36]$, respectively. The randomisation step then adds random variations in sensible enthalpy and species mass fractions to manifold states via

$$h' = h + \frac{c}{a}(h_{\max} - h_{\min}), \tag{1}$$

and

$$Y_i' = Y_i^{(1+\frac{c}{b})}, \tag{2}$$

where h and Y_i represent the sensible enthalpy and the i^{th} species mass fraction of the sampled manifold state, respectively. The subscripts "$\max$" and "$\min$" refer to the maximum and minimum values in the sampled states, respectively. c is a uniformly distributed random number ranging from -1 to 1. a and b are constant coefficients controlling the extent of randomisation, set to 8 and 5, respectively by default [15]. In this work, a and b values are changed to $a = 6$ and $b = 4$, respectively to enlarge the randomisation variation. The mass fractions are normalized to ensure that their sum equals unity, and the corresponding temperature is computed from the randomized enthalpy and mass fractions. Each generated random state passes through an acceptance/rejection process, where its chemical reactivity is evaluated based on its mixture fraction and temperature. In this evaluation, the ranges are slightly expanded to $T \in [650, 3000]$ K and $f \in [0.00, 0.39]$. Additionally, the elemental ratios of C/H and O/N for each random state are examined, with a tolerance of 2% deviation from its reference state.

Deep neural networks (DNNs)

A six-hidden-layer MLP is employed to model the the average rate of change in thermochemical states due to chemical reactions over a computational fluid dynamics (CFD) time step. The CFD time interval is set to $\Delta t_{\mathrm{CFD}} = 1\,\mu$s, which is consistent with [9,13,15]. We employ Box-Cox Transformation (BCT), denoted by $\mathcal{F}_{BCT}$, which is applied to species mass fractions to enhance species/radicals in low concentrations. Z-Score normalization, denoted by $\mathcal{N}_z$, is used for the normalization of the training dataset, ensuring a mean of 0 and a standard deviation of 1. This improves convergence and numerical stability. For open systems, pressure can be assumed approximately constant during the combustion process. Therefore, we limit our analysis to atmospheric pressure condition thus pressure is not included in the DNN's inputs. The processed thermochemical state used as input to the neural network at time t_0 is denoted as $\hat{\phi}_{DNN}(t_0) = \mathcal{N}_z[T(t_0), \mathcal{F}_{BCT}(\mathbf{Y}(t_0))]$. The corresponding label computed as

$$\begin{aligned}\Omega^{\mathcal{P}}(T(t_0), \mathbf{Y}(t_0), \Delta t_{\mathrm{CFD}}) = \\ \mathcal{N}_z\left[\frac{T(t_0+\Delta t_{\mathrm{CFD}}) - T(t_0)}{\Delta t_{\mathrm{CFD}}}, \frac{\mathcal{F}_{BCT}\left(\mathbf{Y}(t_0+\Delta t_{\mathrm{CFD}})\right) - \mathcal{F}_{BCT}\left(\mathbf{Y}(t_0)\right)}{\Delta t_{\mathrm{CFD}}}\right],\end{aligned} \tag{3}$$

where the superscript $\mathcal{P}$ in $\Omega^{\mathcal{P}}(T(t_0), \mathbf{Y}(t_0))$ suggests the processing of averaged chemical source terms including BCT and Z-Score normalization. The goal of training is to find the parameters $\hat{\theta}$ that minimize the following expression,

$$\hat{\theta} = \underset{\theta}{\operatorname{argmin}} \left[\mathcal{L}\left(\overline{\mathcal{S}}(\widehat{\phi}_{DNN}|\theta), \Omega^{\mathcal{P}}(T, \mathbf{Y}, \Delta t_{\mathrm{CFD}})\right)\right], \tag{4}$$

where $\mathcal{L}$ refers to the loss function and the mean absolute error is employed in this work, which has shown reliable performance in previous relevant studies [13, 15, 16]. $\overline{\mathcal{S}}(\widehat{\phi}_{DNN}|\theta)$ denotes the DNN's prediction of averaged chemical source terms, parameterized by the network's coefficients θ, over the time

interval Δt_{CFD}. The ground truth values of temperature and species mass fractions after integration are solved via the SEULEX ODE solver with absolute and relative tolerances of 1×10^{-10} and 1×10^{-6}, respectively. Each neuron in the hidden layers employs a self-gated activation function (i.e., Swish function) to introduce non-linearity. Previous studies have shown the effectiveness of the Swish function in modelling chemistry integration for hydrogen, methane and ethylene 0D auto-ignition premixed flames [16]. The network is optimized using the Adam optimizer, an extension of stochastic gradient descent (i.e., SGD). Our previous study demonstrated that a randomisation/unrolling training strategy can effectively suppress error accumulation over time, particularly for species with long chemical time scales. In this work, we adopt ten unrolling steps for training the neural network, as this configuration has shown excellent performance in a transient counterflow laminar methane-air flame across multiple combustion regimes. More details can be found in [15].

Three-dimensional turbulent non-premixed methane-air flames

Two direct numerical simulations (DNS) of temporally evolving planar methane-air jet flames at atmospheric pressure are conducted, referred to as Case A and Case B. The configuration features a central fuel jet surrounded by two opposing oxidizer streams, as illustrated in Fig. 1. The velocity field is based on the setup of Hawkes et al. [17] (Case L), with a prescribed turbulence intensity of 5%. The two cases differ in their Reynolds (Re) and Damköhler (Da) numbers, which are varied by adjusting the characteristic velocity, defined as the velocity difference $\Delta U = U_{\mathrm{jet}} - U_{\mathrm{ox}}$, while keeping the jet width H constant. As a result, the flow time scale $t_f = H/\Delta U$ is also modified. The characteristic velocity is set to $45.85\,\mathrm{m/s}$ in Case A and $22.93\,\mathrm{m/s}$ in Case B. In both cases, the central jet width is $H = 2.88\,\mathrm{mm}$, and the computational domain dimensions are $L_x \times L_y \times L_z = 12H \times 14H \times 8H$. The corresponding cold-jet Reynolds numbers for Case A and Case B are $\mathrm{Re_A} = 1162$ and $\mathrm{Re_B} = 581$, respectively. Using an assumption of a constant chemical time scales leads to $\mathrm{Da_A} = 0.5 \cdot \mathrm{Da_B}$.

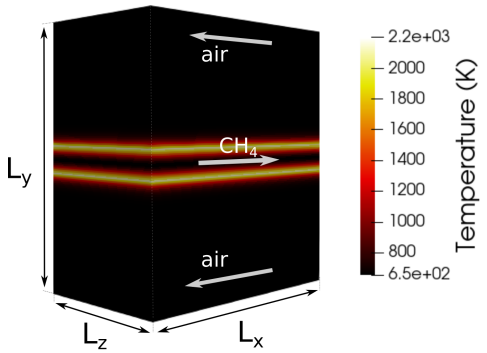

Figure 1. Initial temperature field of the three-dimensional planar turbulent non-premixed methane-air flame.

The initial mixture fraction field, Z, is prescribed according to Eq. (5) as suggested in [18]. Periodic velocity and reacting scalar boundary conditions are applied at the streamwise and spanwise boundaries, while zero-gradient boundaries exist at the cross-stream boundary. For the pressure, a zero gradient condition is applied at the streamwise boundaries and a fixed value atmospheric condition exists at the spanwise and cross-stream boundaries. The computational domain is discretized by $N_x \times N_y \times N_z = 144 \times 168 \times 96 \approx 2.4$ million grid cells. Note that the focus of this work is to compare DNN and ODE results in the context of turbulence, rather than to perform fully resolved DNS. Therefore, the number of grid cells is not required to resolve all turbulent scales, but is sufficient to capture the main turbulence–chemistry interaction features.

$$Z(y) = \frac{\tanh(\frac{y+w}{c}) - \tanh(\frac{y-w}{c})}{\tanh(\frac{w}{c}) - \tanh(-\frac{w}{c})}. \tag{5}$$

Here, w is the fuel slab width parameter and c determines the slope of the profile. In this work, w is set to 0.576 mm (i.e., $w = 0.2H$) and c is tuned such that the scalar dissipation rate at the stoichiometric

mixture fraction matches that of a steady-state flamelet solution under a global strain rate of $\alpha = 400$ s^{-1}. The initial temperature and species mass fraction fields are also initialized from a laminar flamelet solution at the same strain rate. The simulations are run for 80 characteristic jet time scales in both cases. All simulations are performed at atmospheric conditions using a fully compressible Navier-Stokes solver developed within the OpenFOAM framework and LibTorch 2.5.1, assuming a unity Lewis number.

Results and discussion

Figure 2a compares the temperature values of the training dataset (blue points) with those of the thermochemical states sampled from the turbulent flame Case A (orange points), plotted in mixture fraction space. It is worth noting that Case A involves significant partially extinction due to turbulent mixing, which will be presented and discussed in the next paragraph. None of the thermochemical states from the turbulent flame are included in the training dataset. Instead, the training dataset is constructed by randomizing thermochemical states derived from two abstract laminar flames. The distribution of temperature in mixture fraction space, which serves as an indicator of the composition space, in the training dataset covers the corresponding distribution in the turbulent flame. Meanwhile, the dataset retains key combustion features, including chemical equilibrium, partial extinction and pure mixing (i.e., $T = 650\,\mathrm{K}$). These indicate that the training data is consistent with combustion physics and is not limited to thermochemical states in laminar flames. Figure 2b further compares the loss evolution for the training, validation, and turbulent datasets. All three exhibit similar behavior, with losses decreasing rapidly over the first 3000 epochs and stabilizing thereafter. Quantitatively, the training and validation losses are nearly identical, while the loss on the turbulent dataset is lower due to narrower distribution in the composition space compared to the training dataset (see Fig. 2a). These results suggest that the training process is well-converged, shows no signs of overfitting, and further supports that thermochemical states from the turbulent flame can be effectively represented by randomized states based on laminar flames.

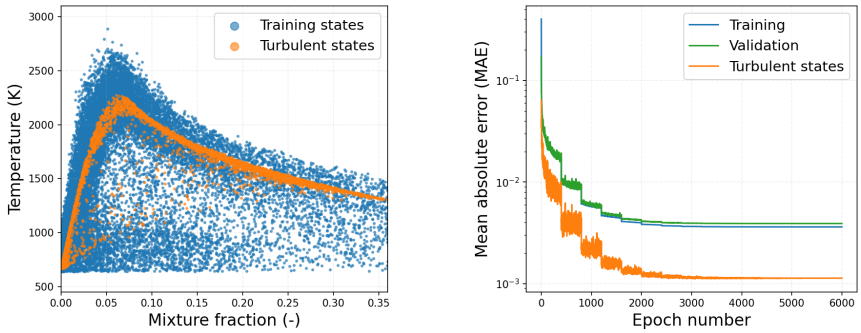

(a) **(b)**

Figure 2. Comparison of (a) temperature values between training dataset (blue points) and thermochemical states appearing in the turbulent flame (orange points, Case A) as a function of mixture fraction, and (b) loss evolution across training (blue), validation (green), and turbulent (orange) datasets during training.

Figure 3 presents 2D slices of instantaneous flame temperature fields at five time instances from $20t_{jet}$ (left) to $80t_{jet}$ (right) for DNS-ODE simulations of two turbulent non-premixed methane–air flames: Case A (3a) and Case B (3b). These flame evolution exhibits distinctly different turbulence–chemistry interactions. In Case A, the development of strong shear leads to high dissipation rates, resulting in local extinction during early stages ($t \leq 40t_{jet}$). As turbulence decays over time, re-ignition occurs, accompanied by thermal expansion of the mixtures. This flame thus spans multiple combustion regimes. In contrast, Case B does not experience extinction. Its flame structure remains close to laminar, featuring continuous fronts with minimal wrinkling, due to the lower turbulence intensity. This configuration challenges the network to accurately and consistently capture near-zero chemical source terms under near-equilibrium conditions over time steps.

Figure 4 compares mass-weighted conditional mean (blue) and root-mean-square (rms, orange) temperature profiles in mixture-fraction space between DNS-ODE (circles) and DNS-DNN (lines) at $t = 20t_{jet}$ (left), $t = 40t_{jet}$ (middle) and $t = 80t_{jet}$ (right) for Case A (4a) and Case B (4b). Instantaneous

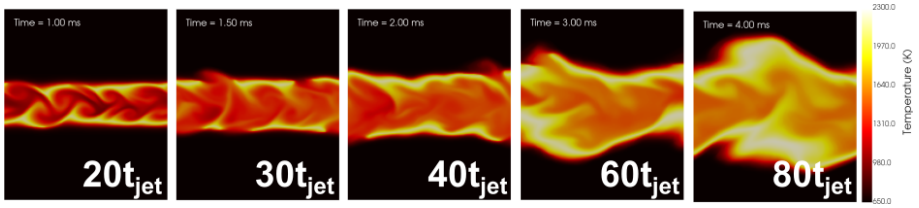

(a) Case A

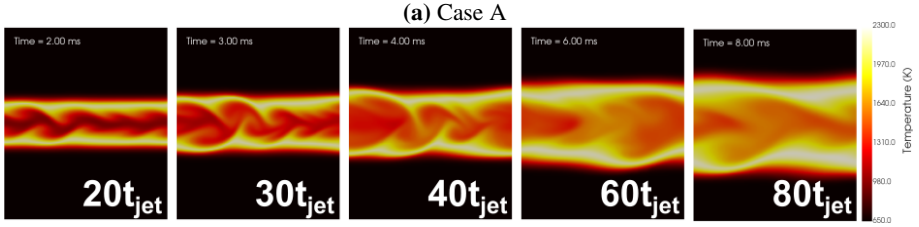

(b) Case B

Figure 3. Instantaneous flame temperature fields at five time instances ranging from $20t_{jet}$ (left) to $80t_{jet}$ (right) for Case A (top) and Case B (bottom). Note that t_{jet} corresponds to 50 µs in Case A and 100 µs in Case B.

temperature distributions (gray points) illustrate flame structures. Note that only DNS-ODE points are shown for clarity due to their near-identical distribution with DNS-DNN. In Case A, the maximum mean temperature is about 2000 K at $t = 20t_{jet}$, decreases to 1800 K at $t = 40t_{jet}$ due to partial extinction, and recovers to 2100 K during re-ignition as turbulence decays. Case B remains close to the equilibrium line, with a maximum mean temperature of approximately 2200 K. In both cases, DNS-DNN predictions agree closely with DNS-ODE results for both conditional mean and rms values, confirming the DNN's capability to capture turbulence–chemistry interactions even when trained on a randomized dataset derived from laminar states. The scatter points highlight substantial variability in the composition space between the two cases, particularly in Case A. Despite being trained on a fixed state distribution, the DNN accurately resolves the evolution of the flame throughout the simulations.

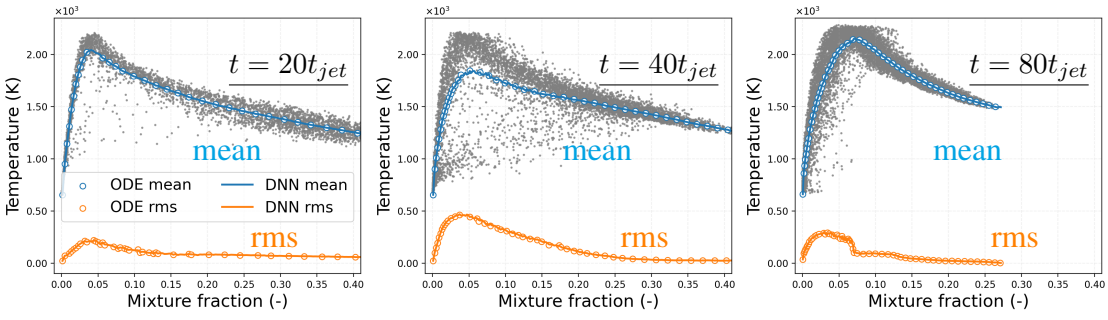

(a) Case A

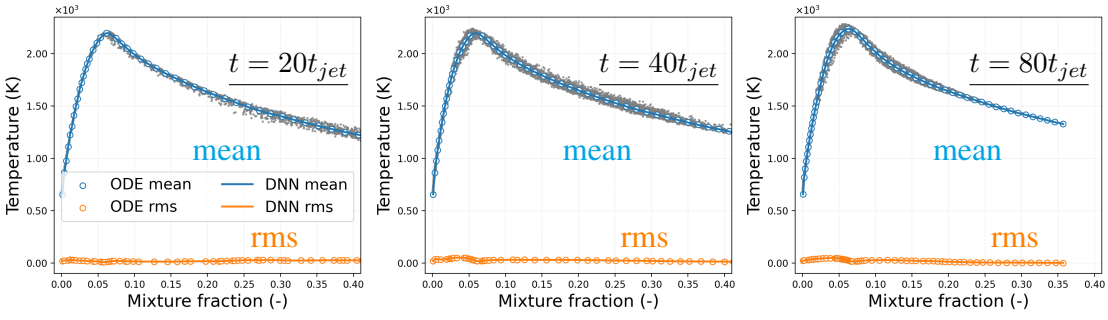

(b) Case B

Figure 4. Comparison of mass-weighted conditional means (blue) and root-mean-square (rms, orange) temperature profiles in mixture fraction space between DNS–ODE solutions (circles) and DNS–DNN predictions (lines) at $t = 20t_{jet}$ (left), $t = 40t_{jet}$ (middle), and $t = 80t_{jet}$ (right) for Case A (top) and Case B (bottom). Note that the instantaneous temperature values at each time instance are also included (gray scatter points).

Figures 5 and 6 further compare the the conditional mean and rms values of species mass fractions for 20 species ranging from C_0 to C_2 in mixture fraction space between DNS-ODE solutions (circles) and DNS-DNN predictions (lines) for turbulent flame Case A at $t = 40\,t_{jet}$ (i.e., partially extinction) and for flame Case B at $t = 80\,t_{jet}$ (i.e., near-equilibrium), respectively. In Case A, species mass fractions exhibit strong fluctuations in mixture fraction space, as indicated by the instantaneous values (gray points) and rms values. Correlations with mixture fraction are generally weak due to rapid turbulence-induced mixing, particularly for radicals, which are highly sensitive to variations in flame structure. In Case B, although the flame temperature and major species closely follow the equilibrium line, species such as H_2, CH_3, and C_2H_2 still show scattering, reflecting the complexity of combustion chemistry under turbulent conditions. In both cases, the DNN accurately predicts the conditional mean and rms of all species mass fractions, with no discernible differences from the ODE solutions. These results demonstrate that a single DNN can effectively capture multiple combustion regimes in turbulent flames while resolving intrinsic species correlations dictated by chemical kinetics.

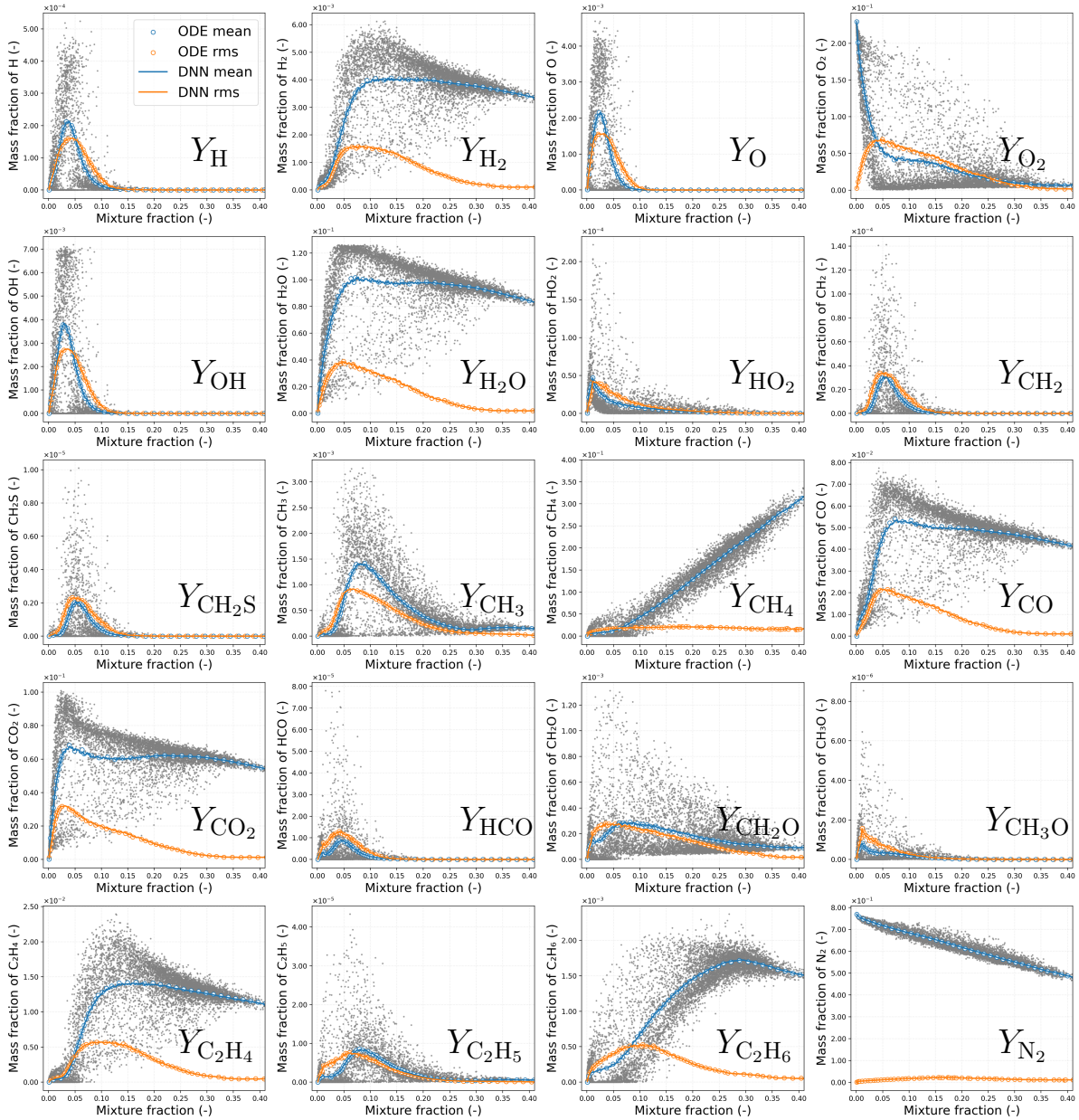

Figure 5. Comparison of mass-weighted conditional mean (blue) and root-mean-square (rms, orange) mass fractions of all 20 species in the DRM19 mechanism between DNS-ODE solutions (circles) and DNS-DNN predictions (lines) for the turbulent flame Case A at $t = 40t_{jet}$. Note that the instantaneous temperature values at each time are also included (gray scatter points).

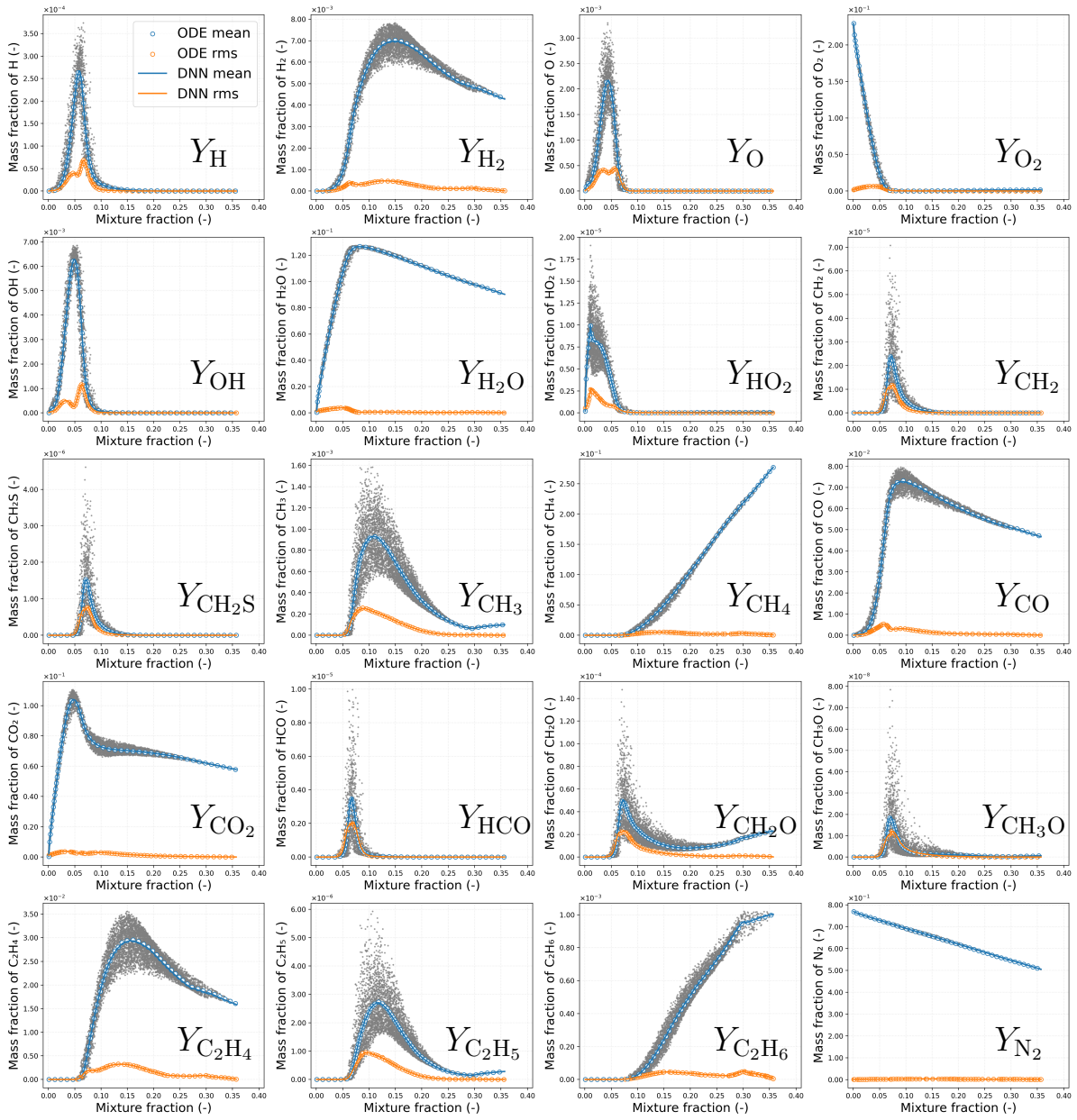

Figure 6. Comparison of mass-weighted conditional mean (blue) and root-mean-square (rms, orange) mass fractions of all 20 species in the DRM19 mechanism between DNS-ODE solutions (circles) and DNS-DNN predictions (lines) for the turbulent flame Case B at $t = 80t_{jet}$. Note that the instantaneous temperature values at each time are also included (gray scatter points).

The computational performance of the DNN is evaluated in a parallel simulation using 64 CPU cores, with a batch size of 4096 for inference, as this setting yields good performance on both CPU and GPU [15]. The computational time is averaged over 100 time steps, starting from $t = 40\,t_{\mathrm{jet}}$, in turbulent flame Case A. Figure 7a compares the chemistry integration time for the SEULEX ODE solver (blue), the DNN on CPU (orange, AMD EPYC 7513) and the DNN on GPU (green, NVIDIA A100). The DNN on CPU achieves a speed-up of roughly one order of magnitude over the SEULEX solver, while GPU inference increases the acceleration to more than a factor of 80. It is worth noting that, in [15], the DNN on GPU achieved an acceleration of about 1000 compared to the SEULEX solver, which is associated with the use of the more detailed GRI 3.0 chemical mechanism and the computational cost of conventional ODE solvers scales with the size and stiffness of the chemical system. Therefore, the performance gain from the DNN approach is more pronounced for more detailed mechanisms. As shown in Fig. 7b, when using an ODE solver, solving chemistry integration takes around 60% of the total computational time and this precentage drops to 14% and 2% when using DNN on CPU and GPU,

respectively. With the use of DNN, especially on GPU, chemistry integration of detailed mechanisms is not the computational bottleneck anymore. Moreover, when using the DNN, the computing algorithm consists of three phases: (1) collecting the thermochemical states into a matrix, (2) feeding the matrix to the DNN and computing the DNN's predictions, and (3) updating the chemical source terms. Note that, if the DNN inference (i.e., Phase2) is executed on a GPU, data transfer between the CPU and GPU is required. Figure 7c compares the computational cost of each phase of DNN inference on the CPU and GPU. The results indicate that network inference is the dominant bottleneck on both platforms, although the GPU executes it much more efficiently. The data transfer between CPU and GPU introduces additional overhead, but it remains small compared with the inference cost.

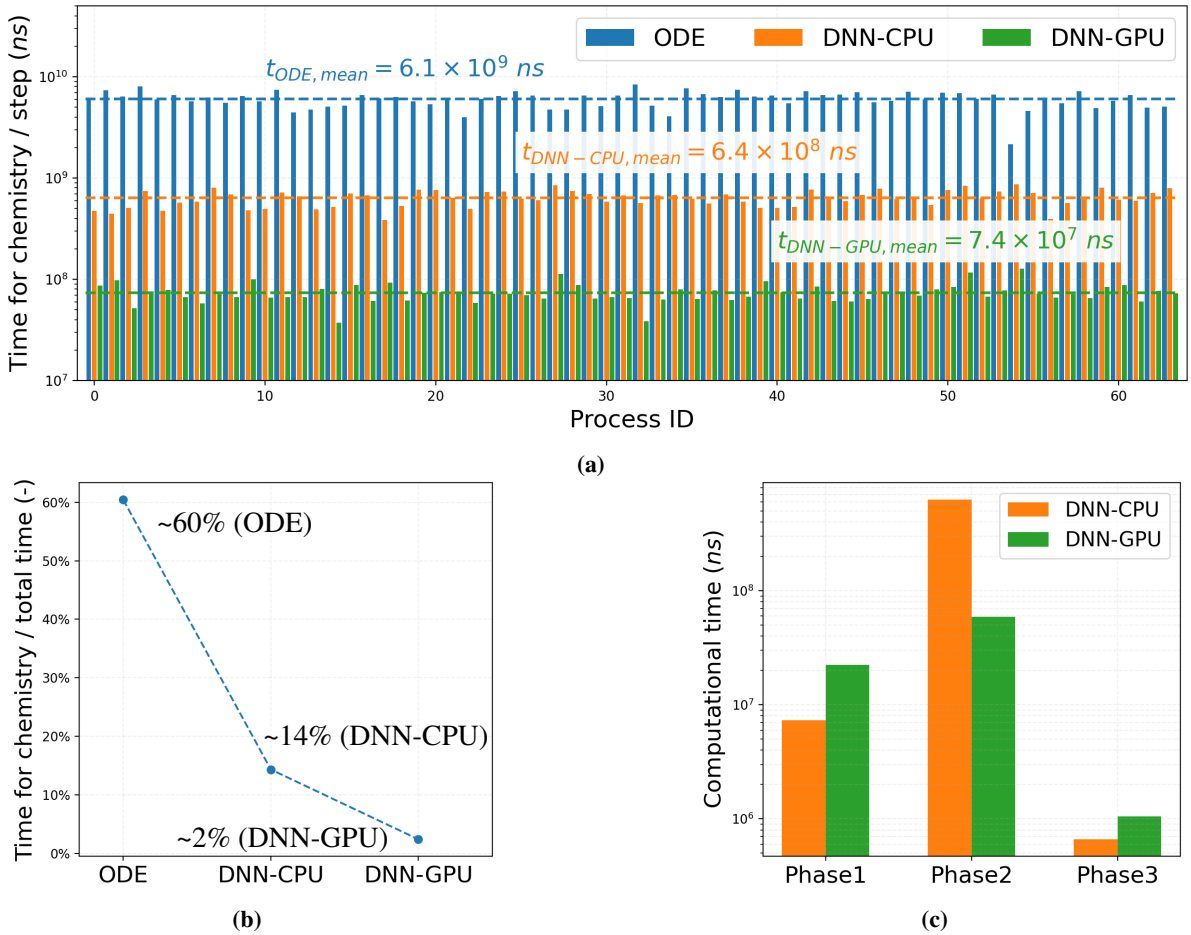

Figure 7. Comparison of (a) computational time per time step for chemistry integration using the SEULEX ODE solver (blue), the DNN on CPU (orange) and the DNN on an NVIDIA A100 GPU (green) in a parallel simulation of turbulent flame Case A with 64 CPU cores; (b) the corresponding percentage of total runtime spent on chemistry integration; and (c) the computational time of (1) generating a matrix of thermochemical states (i.e., Phase1), (2) performing DNN inference (i.e., Phase2) and (3) updating integrated chemical source terms (i.e., Phase3), for chemistry integration using DNN both CPU and GPU architectures.

Conclusions

This work investigates the performance of a DNN for the DRM19 chemical mechanism (19 reactive species, 84 reactions) in two turbulent non-premixed methane–air flames exhibiting distinct turbulence-chemistry interactions. Flame Case A undergoes partially extinction and re-ignition, while the flame Case B approaches equilibrium conditions without much fluctuations of temperature and major species. A randomisation and unrolling training strategy is employed, with the training dataset built upon two laminar flames and subsequent randomisation, and the DNN is trained using a 10-step unrolling approach. The results show that the randomized thermochemical states based on laminar flames are consistent with combustion physics and can well cover the thermochemical states in the turbulent flames. Predictions of the DNS-DNN have an excellent agreement with DNS-ODE solutions in both turbulent flames for

temperature and all species mass fractions. The results demonstrate the generalisation capability of the unrolling strategy and reveal that a single DNN can effectively capture turbulence-chemistry interactions across multiple combustion regimes. Finally, the computational performance of the DNN is analysed against the implicit SEULEX ODE solver. Using the DNN on the CPU and GPU results in approximately $10\times$ and $80\times$ acceleration, respectively. The percentage of total runtime spent on chemistry integration decreases from 60% with the SEULEX solver to 14% with the DNN on the CPU and 2% with the DNN on the GPU. Consequently, chemistry integration is no longer a computational bottleneck. An even higher acceleration is expected when employing a more detailed chemical mechanism.

Acknowledgements

The authors acknowledge the financial support from the Chinese Scholarship Council (CSC, No. 202108340023).

References

[1] Christo F. C., Masri A. R., Nebot E. M., Combustion and Flame 106 (4) (1996) 406–427.
[2] Christo F. C., Masri A. R., Nebot E. M., Pope S. B., Symposium (International) on Combustion 26 (1) (1996) 43–48.
[3] Blasco J. A., Fueyo N., Dopazo C., Ballester J., Combustion and Flame 113 (1) (1998) 38–52.
[4] Blasco J., Fueyo N., Dopazo C., Chen J.-Y., Combustion Theory and Modelling 4 (1) (2000) 61–76.
[5] Franke L. L. C., Chatzopoulos A. K., Rigopoulos S., Combustion and Flame 185 (2017) 245–260.
[6] An J., Qin F., Zhang J., Ren Z., Fundamental Research 2 (4) (2022) 595–603.
[7] An J., He G., Luo K., Qin F., Liu B., International Journal of Hydrogen Energy 45 (53) (2020) 29594–29605.
[8] Readshaw T., Ding T., Rigopoulos S., Jones W. P., Physics of Fluids 33 (3) (2021) 035154.
[9] Ding T., Readshaw T., Rigopoulos S., Jones W. P., Combustion and Flame 231 (2021) 111493.
[10] Ding T., Jones W. P., Rigopoulos S., Combustion and Flame 277 (2025) 114130.
[11] Zhang T., Yi Y., Xu Y., Chen Z. X., Zhang Y., E W., Xu Z.-Q. J., Combustion and Flame 245 (2022) 112319.
[12] Xu Z.-Q. J., Yao J., Yi Y., Hang L., E W., Zhang Y., Zhang T. (2024). arXiv:2401.01220.
[13] Wang T., Yi Y., Yao J., Xu Z.-Q. J., Zhang T., Chen Z., Combustion and Flame 275 (2025) 114105.
[14] Maas U., Pope S. B., Combustion and Flame 88 (3) (1992) 239–264.
[15] Liu W., Kronenburg A., Zirwes T., in: 13th Mediterranean Combustion Symposium, Corfu, Greece, 2025.
[16] Chen X., Mehl C., Faney T., Di Meglio F., Energy & Fuels 37 (18) (2023) 14222–14239.
[17] Hawkes E. R., Sankaran R., Sutherland J. C., Chen J. H., Proceedings of the Combustion Institute 31 (1) (2007) 1633–1640.
[18] Scialabba G., Davidovic M., Attili A., Pitsch H., Combustion and Flame 275 (2025) 114093.

Nanoparticle Deposition in Iron Powder Combustion – Effects of Thermophoresis on Deposition Efficiencies

N. Hartmann[1*], A. Kronenburg[1], T. Zirwes[1], D. Märker[2], T. D. Luu[2] and O. T. Stein[2]

*nils.hartmann@irst.uni-stuttgart.de

[1]*Institute for Reactive Flows - University of Stuttgart, Pfaffenwaldring 31, 70569 Stuttgart, Germany*

[2]*Engler-Bunte-Institute Chair for Simulation of Reacting Thermo-Fluid Systems - Karlsruhe Institute of Technology, Engler-Bunte-Ring 7, 76131 Karlsruhe, Germany*

Abstract

Combustion of iron is carbon free and provides high temperature heat, which makes it an attractive fuel for a renewable energy cycle. The formation of nanoparticles as by-products and their subsequent slip from exhaust gases give, however, rise to concerns regarding cycle efficiency and sustainability. Nanoparticle slip is mitigated by fuel particles that act as spherical collectors. Due to strong changes in temperature during iron combustion, the thermophoretic force is expected to substantially affect the nanoparticle collection. In this study, a model for the nanoparticle collection efficiency is derived analytically that expresses thermophoretic nanoparticle removal as a function of Reynolds number and the normalized temperature difference. Its validity is assessed by two independent numerical implementations, a purely Eulerian and an Euler-Lagrangian, that confirm the model's accuracy for large temperature differences but also indicates its limitations at small effects of thermophoresis as here, diffusion induced by concentration gradients dominates.

Introduction

Combustion of iron microparticles constitutes an integral part of a carbon-free energy cycle that will be needed to achieve our current climate goals [1–3]. One issue related to iron microparticle combustion is the formation and slip of nanoparticles [4–11] that results in emissions with unknown health risks [12] and reduces the recyclability of the iron fuel. Nanoparticle slip may be mitigated by reduced nanoparticle formation or improved nanoparticle collection. While nanoparticle formation has been investigated numerically [13–16], the latter has received little attention and will therefore be covered within this work. Experiments suggest that nanoparticles can be captured by utilizing the fuel microparticles as a collector [7, 9–11] but the mechanisms that favor nanoparticle collection on the microparticles are not yet sufficiently quantified. Particle collection on spherical collectors is investigated in the context of e.g. atmospheric science or groundwater filtration [17–22], where mechanisms like Brownian diffusion, inertial impaction and interception are evaluated. This knowledge can be transferred, to some extent, to iron microparticle combustion, however, unique characteristics like strong Stefan flow [23] and temperature gradients [15, 16] require special attention. The main mechanisms for nanoparticle collection in iron combustion are diffusion, inertial impaction, Stefan flow and thermophoresis. The first three mechanisms were subject of our previous work [24] and correlations for the prediction of a collision efficiency were derived. Thermophoresis was omitted but is expected to be a major driver of particle motion to/from the fuel particle's surface and notably affect nanoparticle collection [25]. Thermophoresis is caused by temperature gradients and induces nanoparticle movement towards low temperatures [18]. In case of iron microparticle combustion, these low temperatures change in space and time [14–16]. Cold fuel particles are injected into the combustion chamber containing hot gas, which results in a thermophoretic force pointing towards the microparticle surface and enhances the collection of nanoparticles. Upon heat-up, the microparticles react heterogeneously with the oxygen in the gas and release heat. Consequently, the microparticle temperature rises above the gas temperature, which changes the direction of

the thermophoretic force. To evaluate the effects of thermophoresis on the collection of nanoparticles, we first derive an analytic solution for the collection efficiency based on the works of Waldmann and Schmitt [26]. Then, two different numerical frameworks for the nanoparticles, an Eulerian and a Lagrangian, are used to assess the validity of and improve on the analytical solution. For the Eulerian framework, nanoparticles are assumed to be point particles that can be described by a continuum approach, i.e. a convection-diffusion equation. The Lagrangian framework considers nanoparticles as discrete entities, the individual pathlines of which are governed by the forces acting on them – the Langevin equation. In this paper we perform a comparison between all three methods, analytical evaluation, Eulerian and Lagrangian framework, to evaluate consequences of thermophoresis on nanoparticle collection in iron microparticle combustion.

Analytical evaluation of the thermophoretic collection efficiency

The collection efficiency is defined as the nanoparticle mass flow at the surface of the microparticle, J_s, normalized by the nanoparticle mass flow rate within the swept volume of the microparticle [27]

$$\eta = \frac{J_s}{n_\infty u_\infty \pi R_{mp}^2}, \tag{1}$$

where the microparticle radius, the gas stream velocity far upstream of the microparticle, i.e. at the inlet, and the nanoparticle number density at the inlet are denoted by R_{mp}, u_∞ and n_∞, respectively. The nanoparticle mass flow at the surface of the microparticle is governed by various mechanisms, e.g., Brownian diffusion, inertial impaction or thermophoresis that may interact. Under certain conditions one mechanism can dominate and be studied independently of the other mechanisms, which is referred to as a limiting case. For the limiting case of thermophoretic collection, the nanoparticle flow towards the microparticle surface is given by

$$J_s = u_{tp} n_\infty 4\pi R_{mp}^2. \tag{2}$$

For small nanoparticles, i.e. large Knudsen numbers Kn $\gg 1$, Waldmann and Schmitt [26] derived an equation for the thermophoretic velocity as

$$u_{tp} = -0.55 \frac{\nu_g}{T_g} \nabla T_g, \tag{3}$$

where ν_g and T_g are the kinematic viscosity and temperature of the gas. The temperature gradient at the microparticle surface, $\nabla T_g|_s$, can be evaluated based on the Nusselt number,

$$\alpha(T_\infty - T_{mp}) = -\lambda \nabla T_g|_s \rightarrow \nabla T_g|_s = -\frac{\mathrm{Nu}_\infty}{2R_{mp}}(T_\infty - T_{mp}), \tag{4}$$

which is given by the correlation of Ranz and Marshall [28] as $\mathrm{Nu}_\infty = 2 + 0.6 \mathrm{Re}_\infty^{1/2}\, \mathrm{Pr}^{1/3}$. The definitions of the Nusselt, Reynolds and Prandtl numbers are given by

$$\mathrm{Nu}_\infty = \frac{2k_g R_{mp}}{\lambda_g},$$
$$\mathrm{Re}_\infty = \frac{2u_\infty R_{mp}}{\nu_g},$$
$$\mathrm{Pr} = \frac{\nu_g}{\alpha_g},$$

where λ_g, k_g and α_g are heat conductivity, heat transfer coefficient and thermal diffusivity in the gas. For low Reynolds numbers, i.e. $\mathrm{Nu}_\infty \approx 2$, combination of Eqs. (1)-(4) yields the analytical correlation for the limiting case of thermophoretic collection as

$$\eta_{tp} = 0.55 \frac{4\nu_g}{u_\infty R_{mp}} \frac{(T_\infty - T_{mp})}{T_\infty} \approx 4\mathrm{Re}_\infty^{-1}\Theta, \tag{5}$$

where

$$\Theta = \frac{(T_\infty - T_{mp})}{T_\infty},$$

is the normalized temperature difference.

Eulerian Framework

Governing Equations

The gas flow around the microparticle is governed by the steady-state continuity, momentum and energy equations

$$\nabla \cdot (\rho_g \vec{u}_g) = 0, \tag{6}$$

$$\nabla \cdot (\rho_g \vec{u}_g \vec{u}_g) = \nabla \cdot (\mu_g \nabla \vec{u}_g) - \nabla p, \tag{7}$$

$$\nabla \cdot (\rho_g h \vec{u}_g) = \nabla \cdot (\lambda_g \nabla T_g), \tag{8}$$

where the latter neglects viscous heating. The variable gas density, ρ_g, is evaluated from the ideal gas law. Variables $\vec{u}_g$, μ_g and p denote the velocity, dynamic viscosity of the gas and pressure, respectively. Nanoparticles are treated as point particles that do not affect the governing equations of the gas (Eqs. (6)-(8)), which is applicable for low nanoparticle number densities [18] that are to be expected in iron microparticle combustion [15]. Therefore, their motion can be represented by passive scalar transport of the nanoparticle number density, i.e.

$$\nabla \cdot (\rho_g \vec{u}_{tot} n_{np}) = \nabla \cdot (\rho_g D_{np} \nabla n_{np}), \tag{9}$$

where $\vec{u}_{tot} = \vec{u}_g + \vec{u}_{tp}$, and $\vec{u}_{tp}$ is calculated from the temperature field according to the analytic solution of Waldmann and Schmitt (Eq. (3)) [26]. The nanoparticle diffusivity is governed by the Stokes-Einstein correlation

$$D_{np} = \frac{k_B T_g C^{slip}}{6\pi \mu_g (d_{np}/2)}, \tag{10}$$

with Boltzmann constant k_B, nanoparticle diameter d_{np} and Cunningham correction factor C^{slip} that is calculated according to Corson et al. [29]. The collection efficiency, Eq. (1), can be computed directly, as all boundary layers resulting from Eqs. (7), (8) and (9), namely hydrodynamic, thermal and nanoparticle, are resolved. Similar to the analytic evaluation, the collection efficiency is obtained from the nanoparticle flow at the surface of the microparticle. However, as the Eulerian framework resolves the hydrodynamic, temperature and nanoparticle boundary layers (Eq. (6)-(9)), the nanoparticle flow at the surface can be computed directly as $J_s = -\rho_{g,s} D_{np,s} \nabla n|_s A_{mp} + \vec{u}_{tot,s} n_s A_{mp}$, where A_{mp} is the surface area of the microparticle and the subscript s indicates surface values. Assuming a perfect sink, i.e. $n_s = 0$ according to the Smoluchowski-Levich approximation [30, 31], the convective part is zero. Then, the collection efficiency is given by

$$\eta = \frac{\int -\rho_{g,s} D_{np,s} \nabla n|_s \, \mathrm{d}A_{mp}}{\rho_\infty n_\infty u_\infty \pi R_{mp}^2}, \tag{11}$$

where integration over the microparticle surface is performed to account for nonuniform surface values. Thermophoresis is implicitly included in Eq. (11), as it affects the nanoparticle gradient at the surface $\nabla n|_s$. For positive normalized temperature differences, $\Theta > 0$, nanoparticles are transported towards the microparticle surface (Eq. (9)), which results in larger nanoparticle gradients $\nabla n|_s$. For $\Theta < 0$, we can observe the opposite effect and the collection efficiency is reduced.

Numerical Setup

The computational domain is a 2D wedge geometry as the flow is laminar. The microparticle is placed at the origin. The domain extensions are based on the microparticle radius and extend $15R_{mp}$ upstream, downstream and in cross-stream direction each, to ensure that the hydrodynamic, temperature and nanoparticle boundary layer are not affected by the boundaries. Fixed value boundary conditions are imposed at the inlet for the gas velocity, gas temperature and nanoparticle number density, i.e. u_∞, T_∞ and n_∞. At the microparticle surface, $\vec{u}_g$ is set to zero (no-slip), and $\vec{u}_{tp}$ is determined by the temperature field, where a fixed value for the microparticle surface temperature, T_{mp}, is set. The nanoparticle number density at the microparticle surface, n_s, is set to zero according to the Smoluchowski-Levich approximation [30, 31] of a perfect sink. Figure 1 depicts an example temperature field and the corresponding nanoparticle streamlines resulting from $\vec{u}_{tot}$. As the thermophoretic velocity points towards

the microparticle, the nanoparticle streamlines terminate on its surface. Consequently, the nanoparticle number density drops from n_∞ to zero in a thin boundary layer that must be fully resolved. To ensure this, a total of approximately $85\,000$ cells with strong grading at the microparticle surface are used, which results in a cell size of $\Delta < 1 \times 10^{-3} R_{mp}$ at the surface.

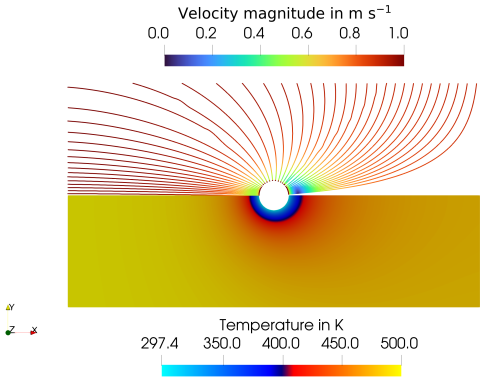

Figure 1. Streamlines of $\vec{u}_{tot}$ that result from superposition of the thermophoretic and gas velocity (top half) and the corresponding temperature field (bottom half).

Lagrangian Framework

Governing Equations

In the Lagrangian framework, nanoparticles are discrete entities and their individual pathlines are calculated by the Langevin equation,

$$m \frac{\mathrm{d}\vec{u}_{np}}{\mathrm{d}t} = \vec{F}_d + \vec{F}_{tp} + \vec{F}_b. \tag{12}$$

In contrast to the continuum description of the Eulerian framework, Eq. (9)), nanoparticle drag is considered as

$$\vec{F}_d = -f\vec{u}_{rel} = \frac{6\pi\mu_g(d_{np}/2)}{C^{slip}}\vec{u}_{rel}, \tag{13}$$

where a spherical shape is assumed, i.e. the friction coefficient f is governed by Stokes' law, and the relative velocity between the nanoparticle and the gas is given by $\vec{u}_{rel} = \vec{u}_{np} - \vec{u}_g$. The thermophoretic force acting on the nanoparticles is given by

$$\vec{F}_{tp} = -f\vec{u}_{tp}, \tag{14}$$

where the thermophoretic velocity is evaluated according to the analytic solution of Waldmann and Schmitt (Eq. (3)) [26]. The Brownian force,

$$\vec{F}_b = \sqrt{\frac{2fk_BT_g}{\Delta t}}\vec{G}, \tag{15}$$

is stochastic and contains a vector, $\vec{G}$, the spatial components of which are sampled from a Gaussian distribution with zero mean and unity variance. The variable Δt is the numerical time step that is also used for integration of the Langevin equation (12). The flow and temperature field for Eqs. (13), (15) and (14) come from a separate simulation using the Eulerian framework. Since the Lagrangian framework uses discrete nanoparticles, the definition of the collection efficiency is adapted from Eq. (1) to give

$$\eta = \frac{N_{np}\,\text{collected}}{n_\infty \times \text{swept volume}}, \tag{16}$$

with N_{np} being the number of nanoparticles.

Numerical Setup

The nanoparticles move randomly in 3D-space according to Eq. (12). Therefore, symmetry conditions cannot be invoked and a full 3D setup is needed. Similar to the Eulerian framework, the microparticle is placed at the origin. The domain is rectangular, where all boundaries are at a distance of $15R_{mp}$ from the origin. Figure 2 depicts the general setup for the Lagrangian framework. The bulk flow in combination with the thermophoretic force transports the nanoparticles towards the microparticle, as indicated by the streamlines resulting from $\vec{u}_{tot}$. The Brownian force leads to a random motion of the nanoparticles that diverges from these streamlines. Since the nanoparticle size is small compared to the microparticle, $(d_{np}/2)/R_{mp} << 1$, collection by interception can be neglected [18] and their collection does not contribute to a notable growth of the microparticle diameter and thus the collector's surface. Neither do the nanoparticles affect each other or the gas flow, as conditions are dilute. At the inlet a constant nanoparticle flux is imposed, where the drag force, (Eq. (13)), is zero initially. The nanoparticles are monosized and their distribution is random but statistically uniform. For the remaining boundaries, outflow conditions are used. The integration time step is set to $\Delta t = 1 \times 10^{-7}$ s, which is smaller than the nanoparticle relaxation time, $\Delta t < \tau^{relax} = \rho_{np} d_{np}^2 C^{slip}/(18\mu_g)$ [18], for all simulations. However, the combination of a full 3D domain with small cell sizes results in computationally expensive simulations. We therefore restrict our investigation here to rather small normalized temperature differences Θ. A total of approximately 11×10^6 cells is used with strong grading at the microparticle surface, which results in cell sizes of approximately $\Delta \approx 0.035 R_{mp}$ at the microparticle surface.

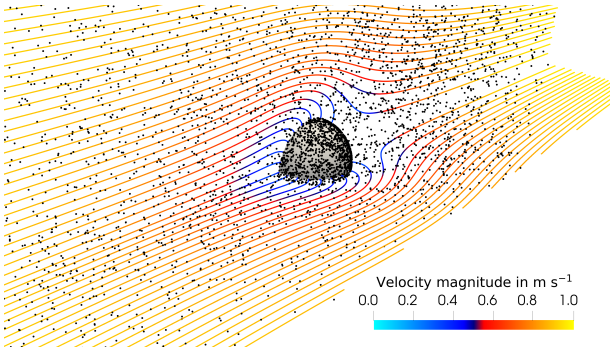

Figure 2. Visualization of the Lagrangian setup. For clarity, the nanoparticle number density and size is adjusted. The Streamlines result from $\vec{u}_{tot}$, i.e. superposition of the thermophoretic and gas velocity, and indicate the nanoparticle flow from front left to rear right.

Results and discussion

Table 1 gives a summary of the process conditions that are typical for iron combustion. It includes the range for the expected Reynolds numbers and additionally the temperature difference $\Delta T = T_\infty - T_{mp}$ with the corresponding range of Θ that is investigated here. Negative values of ΔT are chosen such that the collection efficiency is reduced to approximately zero.

Table 1. Parameter range representing typical process conditions in iron microparticle combustion. The Reynolds number and the normalized temperature difference indicate the range that the variations of the parameters covers.

Variable	Value	Reference
R_{mp}	$5.67 - 80\,\mu\mathrm{m}$	[8–11]
d_{np}	$20 - 200\,\mathrm{nm}$	[4, 9, 14]
T_{mp}	$1500 - 2700\,\mathrm{K}$	[11, 13, 14, 16, 32, 33]
u_∞	$< 1.25\,\mathrm{m\,s^{-1}}$	[8]
Re_∞	< 0.83	
ΔT	-5 - $200\,\mathrm{K}$	
Θ	5×10^{-3} - 0.4	

The analytic solution for the thermophoretic collection efficiency is a function of Reynolds number

and normalized temperature only, $\eta_{tp} = f(\mathrm{Re}_\infty, \Theta)$ (Eq. (5)). Detailed investigations on heat transfer by Thijs et al. [32] show, that the approximation of $\mathrm{Nu}_\infty \approx 2$ is accurate for most process conditions in iron combustion. For $\Theta = 0$, the analytic correlation predicts a collection efficiency of zero and for negative normalized temperature differences, $\Theta < 0$, the collection efficiency becomes negative which is certainly unphysical. This is, however, a consequence of the (purely theoretical) limiting case of thermophoretic collection that does not consider other collection mechanisms. In case of the Eulerian framework, the collection efficiency converges against the solution for the limiting case of collection by diffusion [24,27,31] in the absence of thermophoresis. For negative values of the normalized temperature difference, thermophoresis reduces the diffusive nanoparticle collection (which is therefore referred to as the 'thermophoretically reduced collection regime'). Negative values of the normalized temperature difference result from hot microparticle temperatures due to heat release during combustion of the fuel. For positive values of normalized temperature difference the thermophoretic force points towards the microparticle increasing the collection efficiency, which is referred to as the thermophoretically enhanced collection regime.

Thermophoretically enhanced collection regime

Figure 3 compares results from the Eulerian simulations with the analytic correlation for various Reynolds numbers and positive normalized temperatures, i.e. a thermophoretic force that drives particles towards the microparticle surface and enhances the collection efficiency. The Eulerian framework shows a deviation from the linear dependence predicted by the analytical model for small values of Θ, corresponding to $\Delta T < 5\,\mathrm{K}$. This is due to the contribution of ordinary diffusion to the collection efficiency, which was evaluated in our previous work [24]. The value for the limiting case of collection by diffusion is a function of the Péclet number [24, 27, 31], $Pe_\infty = 2u_\infty R_{mp}/D_{np}$, and indicated by the dashed lines in Fig. 3 that refer to isothermal conditions, i.e. $\Theta = 0$. As the analytical correlation represents a limiting case for thermophoretic collection only, it cannot capture the interaction of multiple collection mechanisms such as diffusion overlapping with thermophoresis. However, the Eulerian framework suggests that thermophoresis is the dominating collection mechanism for temperature differences with $\Delta T > 5\,\mathrm{K}$. This is especially apparent from the cases of similar Reynolds numbers but different Péclet numbers (light green with $\mathrm{Pe}_\infty = 2199$ and orange with $\mathrm{Pe}_\infty = 47470$ symbols in Fig. 3). For $\Theta < 2 \times 10^{-3}$ the collection efficiencies converge towards the limiting case of collection by diffusion (dashed lines) governed by their different Péclet numbers [24, 27, 31], but for larger values of Θ, both cases converge towards a similar collection efficiency that depends only on Reynolds number and normalized temperature difference, as predicted by the analytical correlation. Therefore, when multiple collection mechanisms are relevant, the collection efficiency becomes a function of additional dimensionless numbers, such as the Péclet number in case of diffusive nanoparticle collection. The deviations between the analytical correlation and the Eulerian framework are generally small for the case of dominant thermophoresis.

Thermophoretically reduced collection regime

Figure 4 depicts the results of the Lagrangian framework for a representative case of $\mathrm{Re}_\infty = 0.0422$. The Eulerian solution and the analytical correlation are added for comparison. Generally, the Lagrangian simulations give similar results to the Eulerian simulations, which is expected, if the definition of the Brownian force is consistent with the definition of the nanoparticle diffusion coefficient. The deviations for small values of the normalized temperature difference, $\Theta \approx 0$, indicate that the collection efficiency is dependent on collection by diffusion. This is especially important when the thermophoretic force points away from the microparticle surface, $\Theta < 0$. Then, the nanoparticle boundary layer becomes thicker and collection by diffusion is mitigated, which reduces the collection efficiency to approximately zero for $\Delta T = -5\,\mathrm{K}$ (i.e., $\Theta = 1.67 \times 10^{-3}$).

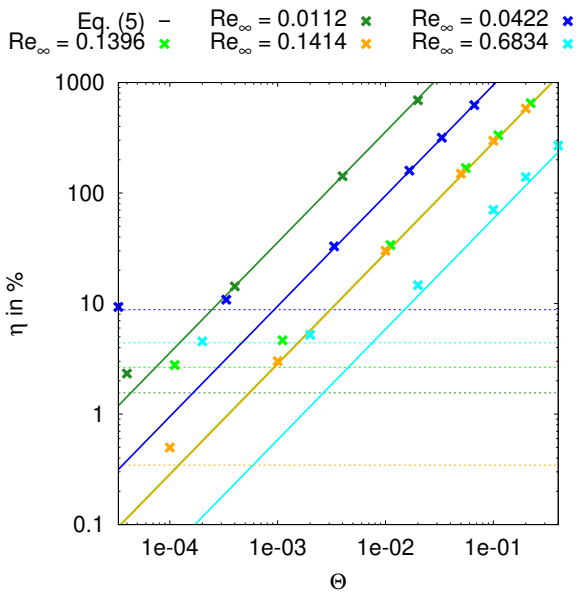

Figure 3. Eulerian nanoparticle framework in comparison to the analytical correlation (Eq. (5)). The dashed lines indicate the limit given by Brownian diffusion [24] for $\Theta = 0$ (isothermal) [24].

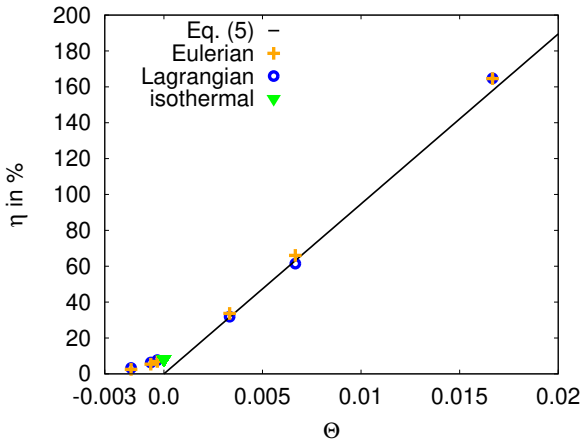

Figure 4. Results of the Lagrangian nanoparticle framework in comparison to the Eulerian nanoparticle framework and the analytical correlation (Eq. (5)). The isothermal result is taken from our previous work [24].

Conclusions

An analytical correlation for the limiting case of thermophoretic nanoparticle collection was derived based on the thermophoretic velocity evaluated by Waldmann and Schmitt [26]. It is shown, that the thermophoretic collection efficiency is a function of Reynolds number and the normalized temperature difference. Two different numerical frameworks for the nanoparticles, an Eulerian and a Lagrangian, are used to assess these functional dependencies. For dominant thermophoresis, the analytical correlation and both numerical frameworks converge against the same value. When thermophoresis is not dominant, the numerical simulations converge against the solution of the limiting case of collection by diffusion [24], as they can resolve the interaction of multiple collection mechanisms. The analytical correlation is only applicable for the case of dominant thermophoresis, i.e. large temperature differences between the microparticle and the surrounding gas. These conditions are to be expected in iron microparticle combustion, however they are usually accompanied by strong Stefan flows [16, 23, 32, 33]. Therefore, the functional dependencies identified here for the limiting case of thermophoretic collection must be combined with previous findings, where Stefan flow and diffusion was considered [24], to give a complete description of nanoparticle collection in iron combustion.

Acknowledgements

Funding: This work was supported by the Friedrich and Elisabeth Boysen-Stiftung, project BOY-195. O.T. Stein gratefully acknowledges the financial support by the Helmholtz Association of German Research Centres (HGF), within the research field Energy, program Materials and Technologies for the Energy Transition (MTET).

References

[1] Bergthorson J., Goroshin S., Soo M., Julien P., Palecka J., Frost D., Jarvis D., Applied Energy 160 (2015) 368–382.
[2] Bergthorson J. M., Progress in Energy and Combustion Science 68 (2018) 169–196.
[3] Debiagi P., Rocha R., Scholtissek A., Janicka J., Hasse C., Renewable and Sustainable Energy Reviews 165 (2022) 112579.
[4] Wiinikka H., Vikström T., Wennebro J., Toth P., Sepman A., Energy & Fuels 32 (9) (2018) 9982–9989.
[5] Fedoryk M., Stelzner B., Harth S., Trimis D., Applications in Energy and Combustion Science 13 (2023) 100111.
[6] Tóth P., Ögren Y., Sepman A., Gren P., Wiinikka H., Powder Technology 373 (2020) 210–219.
[7] Panahi A., Chang D., Schiemann M., Fujinawa A., Mi X., Bergthorson J. M., Levendis Y. A., Applications in Energy and Combustion Science 13 (2023) 100097.
[8] Li T., Heck F., Reinauer F., Böhm B., Dreizler A., Combustion and Flame 245 (2022) 112357.
[9] Buchheiser S., Deutschmann M. P., Rhein F., Allmang A., Fedoryk M., Stelzner B., Harth S., Trimis D., Nirschl H., Materials 16 (5).
[10] Ning D., Shoshin Y., van Stiphout M., van Oijen J., Finotello G., de Goey P., Combustion and Flame 236 (2022) 111801.
[11] Li S., Huang J., Weng W., Qian Y., Lu X., Aldén M., Li Z., Combustion and Flame 241 (2022) 112099.
[12] Wen D., Energy Environ. Sci. 3 (2010) 591–600.
[13] Ning D., Shoshin Y., van Oijen J. A., Finotello G., de Goey L., Combustion and Flame 244 (2022) 112296.
[14] Thijs L., van Gool C., Ramaekers W., van Oijen J., de Goey L., Proceedings of the Combustion Institute 39 (3) (2023) 3551–3559.
[15] Nguyen B.-D., Scholtissek A., Li T., Ning D., Stein O. T., Dreizler A., Hasse C., Chemical Engineering Journal 507 (2025) 160039.
[16] Mich J., da Silva A. K., Ning D., Li T., Raabe D., Böhm B., Dreizler A., Hasse C., Scholtissek A., Proceedings of the Combustion Institute 40 (1) (2024) 105538.
[17] Langmuir I., Journal of the Atmospheric Sciences 5 (1948) 175–192.
[18] Friedlander S., Topics in chemical engineering, Oxford University Press, 2000.
[19] Yao K.-M., Habibian M. T., O'Melia C. R., Environmental Science & Technology 5 (11) (1971) 1105–1112.
[20] Tufenkji N., Elimelech M., Environmental Science & Technology 38 (2) (2004) 529–536.
[21] Nelson K. E., Ginn T. R., Water Resources Research 47 (5).
[22] Messina F., Marchisio D. L., Sethi R., Journal of Colloid and Interface Science 446 (2015) 185–193.
[23] Vance F. H., Scholtissek A., Nicolai H., Hasse C., Combustion and Flame 265 (2024) 113199.
[24] Hartmann N., Kronenburg A., Zirwes T., Märker D., Luu T. D., Stein O. T., Fuel (accepted 2025).
[25] Gallier S., Braconnier A., Godfroy F., Halter F., Chauveau C., Combustion and Flame 228 (2021) 142–153.
[26] Waldmann L., Schmitt K., Academic Press Inc. (London) Ltd., 1966.
[27] Friedlander S. K., AIChE Journal 3 (1) (1957) 43–48.
[28] Ranz W. E., Marshall R. W., Chem. Eng. Prog. 48 (1952) 141–146, 173–180.
[29] Corson J., Mulholland G. W., Zachariah M. R., Aerosol Science and Technology 51 (6) (2017) 766–777.

[30] Smoluchowski M., Zeitschrift fuer physikalische Chemie 92 (1917) 129 – 168.
[31] Levich V., Prentice-Hall international series in the physical and chemical engineering sciences, Prentice-Hall, 1962.
[32] Thijs L. C., van Gool C. E. A. G., Ramaekers W. J. S., Kuerten J. G. M., van Oijen J. A., de Goey L. P. H., Combustion Science and Technology 196 (4) (2024) 572–588.
[33] Nguyen B.-D., Braig D., Scholtissek A., Ning D., Li T., Dreizler A., Hasse C., Fuel 371 (2024) 131866.

Development of a Surrogate-Based Optimization Framework for Hydrogen Burner Design

L. Juris[1*], S. Nerzak[2], J. Willkomm[1], G. Melo[1], M. Gauding[2], H. Pitsch[2], J. H. Schleifenbaum[1]

*luca.juris@dap.rwth-aachen.de

[1] *Chair for Digital Additive Production (DAP), RWTH Aachen University, Campus-Boulevard 73, 52074 Aachen, Germany*

[2] *Institute for Combustion Technology, RWTH Aachen University, Templergraben 64, 52056 Aachen, Germany*

Abstract

Hydrogen's specific combustion properties, such as high consumption speeds, wide flammability limits, and low ignition energy, pose significant challenges for burner design: conventional manual iterations are time-consuming, enable limited insight into the multi-dimensional design space, and risk missing global optimal configurations. A full-factorial exploration, on the other hand, becomes expensive under realistic computational budgets. To overcome these limitations, a simulation driven, surrogate-based optimization framework that couples parametric CAD generation, steady-state Reynolds-Averaged Navier-Stokes (RANS) CFD simulations and an Efficient Global Optimization (EGO) algorithm is introduced. By constructing a Gaussian-Process surrogate and iteratively refining it via Expected Improvement, the framework systematically navigates a four-dimensional burner design space. With this methodology, an improved configuration that achieves a 52 % reduction in mixture inhomogeneity relative to the dataset mean can be identified. Crucially, only 72 high-fidelity simulations were required—a computational saving of 87.5 % compared to a full-factorial approach—demonstrating both the efficiency and effectiveness of the proposed framework for automated hydrogen burner design.

Introduction

Hydrogen is a key enabler for the decarbonisation of energy-intensive sectors and forms a central pillar of the EU's Green Deal and REPowerEU plan, which targets 20 million tonnes of renewable hydrogen by 2030 [1, 2]. One example for decarbonization is the thermochemical energy conversion process by replacing conventional hydrocarbon fuels like methane with hydrogen. Compared to methane, hydrogen exhibits higher laminar flame speeds, broader flammability limits, and lower ignition energy, increasing the risk of flashback and complicating flame stabilization in premixed systems [3, 4]. In addition, the potential for thermal NO_X formation is greater with hydrogen, as the adiabatic flame temperature is approx. 200° C ($\Phi = 1$) higher than with methane [5, 6]. To minimize NO_X formation, modern burner designs rely on lean premixed or partially premixed operation. These configurations have two limitations. First, these conditions are sensitive to thermo-diffusive flame instabilities and therefore exhibit significantly increased reaction rates and super-adiabatic temperatures. Second, in technical applications, highly homogeneous mixing over a short mixing length has to be ensured to minimize the risk of flashback [7, 8]. Modern burner concepts need to be optimized to enable the combustion of hydrogen safely and with low emissions. Different approaches for diffusion and premixed burners have been proposed and special low- NO_X concepts such as micro mixing burners are currently being developed such as in [9]. With the micro mixing concept, the fuel is injected through many small openings to produce a large number of small localized flames. This keeps the local temperature lower and the residence time of the hot combustion products short, which reduces NO_X formation and flashback risk, as the flame front cannot spread into the fuel opening [10]. Similar concepts are pursued by tangentially arranged fuel injectors, which generate a slight swirl. The flames become smaller and the residence time of the hot gas is reduced, thereby lowering NO_X emissions as the swirl increases [11]. The introduced concepts offer potential solutions for safe and efficient hydrogen burners but require complex geometries that are difficult to manufacture with conventional manufacturing processes like milling or casting.

Additive manufacturing (AM), particularly Powder Bed Fusion using a Laser Beam of Metals (PBF-LB/M), enables the layer-wise fabrication of complex internal features without the constraints of conventional tooling or assembly [12]. This design freedom allows for the integration of flow-guiding structures and distributed injection systems directly into the burner geometry. However, PBF-LB/M also imposes limitations such as surface roughness, anisotropic material properties, and geometric deviations—especially in thin-walled or overhanging regions [13]. These effects must be considered early in the design process to ensure manufacturability and consistent performance.

The combination of hydrogen-specific burner requirements and the capability of AM necessitates a novel, simulation-based design approach that integrates combustion dynamics, flow behavior, and manufacturing constraints into a unified optimization process.

This process has to be able to cover the complex, multi-objective challenge due to the interplay of application-specific operating conditions, high-dimensional parameter spaces, and non-linear trade-offs that the design of hydrogen burners presents. Traditional, sequential design and optimization approaches are ill-suited to this context, as they rely heavily on manual iteration and fail to systematically identify high-performance geometries [14]. To address these limitations, automated design frameworks have emerged that integrate parametric modelling, simulation, and optimization algorithms. These frameworks enable efficient and reproducible exploration of the design space, particularly when using inverse design strategies such as generative design [15]. While such methods have been applied in the broader field of hydrogen technologies only a few have been used in burner design [16]. State-of-the-art optimization techniques include gradient-based algorithms, evolutionary strategies, and surrogate-based optimization (SBO). The latter being particularly effective in scenarios involving computationally expensive simulations [17, 18]. Surrogate models, such as Gaussian Processes (GP), approximate the simulation input–output relationships, allowing rapid exploration of a parameterized design space without full CFD simulations for each variant [19]. In early design stages, this mapping uncovers key variables, interactions, and performance trends that isolated case studies or single-point optimizations might miss [20]. Efficient Global Optimization (EGO) pairs a GP surrogate with the Expected Improvement Function (EIF) to iteratively refine designs, balancing exploration and exploitation and converging to global optima with few evaluations in costly, high-dimensional settings [21].

This study aims to develop an additively manufacturable, partially premixed crossflow jet burner for hydrogen combustion, targeting improved mixing quality, thereby ensuring low NO_x emissions. To this end, an automated simulation-driven design approach is pursued, combining parametric geometry generation, cold-flow CFD simulations, and surrogate-based optimization. The proposed framework enables efficient exploration of the design space to identify high-performance burner configurations that fulfil functional and manufacturing constraints.

Methods

This study presents a design automation framework that is specifically tailored for the optimization of hydrogen burner geometries. Figure 1 illustrates the overall architecture of the optimization framework, which establishes an automated loop between the open-source software tools Dakota, Salome, meshing, and OpenFOAM [22, 23, 24]. Dakota generates design parameters, which are converted into parametric geometries in Salome, meshed, and then evaluated via CFD in OpenFOAM. The simulation results are returned to Dakota to inform further sampling and optimization. Each step is described in detail in the following sections.

To reduce computational cost and develop a generalizable design methodology, the framework is applied to a simplified burner configuration based on a jet-in-crossflow setup. This includes multiple fuel inlets injecting transversely into a main oxidizer stream within a confined duct, capturing key mixing mechanisms while avoiding the complexity of full burner assemblies. By isolating a single mixing region from combustion and micro-mixing effects, the setup enables focused analysis of how geometry influences mixture homogeneity at reduced computational cost. The simplified configuration allows for the systematic modulation of several parameters, including the fuel inlet angle α, inlet height h, and inlet diameter d, as well as the quantity of inlets $N_{\mathrm{fuel\_inlets}}$. This parametric flexibility forms the basis for generating a comprehensive dataset used in training and validating the surrogate model.

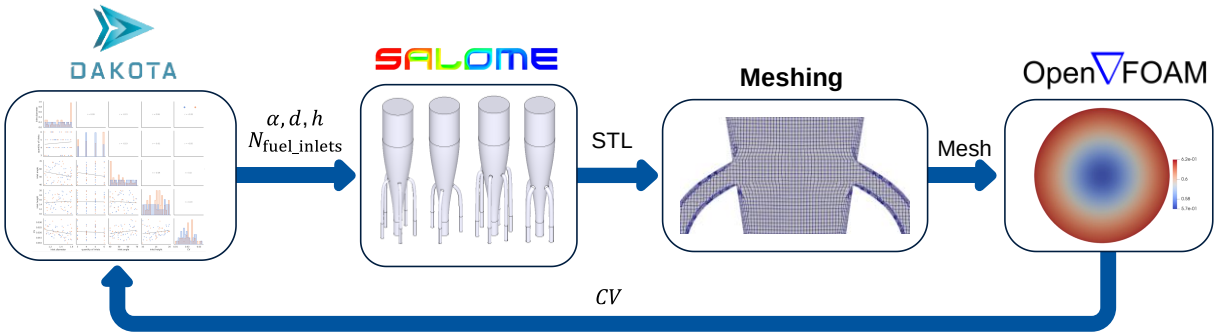

Figure 1. Framework architecture.

Parametric CAD model

The parametric model is built in Salome, which is an open-source tool that supports both graphical and script-based CAD modelling and offers a Python interface for automating geometry generation and variation. In this study, geometric parameters with a significant influence on the mixing behavior are selected. These parameters are systematically varied to populate the design space. In Figure 2, one representative geometry is shown, illustrating the definition and variation of the considered parameters. A parametric Python script automates geometry generation and modification based on parameter sets which are created in Dakota.

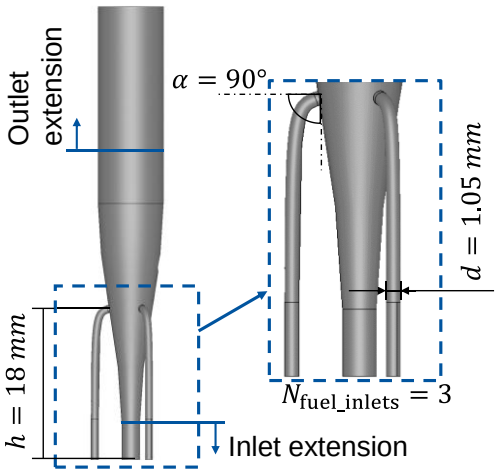

Figure 2. Parametric Salome model.

To improve the numerical stability of the simulation, the geometry generated in Salome includes extensions at both the inlet and outlet. The inlet section is extended by 5 mm to allow the velocity profile to develop before entering the mixing region. Similarly, the outlet is extended by 15 mm to reduce backflow effects and dampen transient behavior, thereby enhancing the robustness of the simulation results.

CFD Simulation

OpenFOAM is an open-source CFD toolbox with modular architecture used for simulating fluid flow and heat and mass transfer. In the presented framework, OpenFOAM is used to simulate the steady-state flow using the RANS equations in combination with the k-ε turbulence model in reactingFoam. The unityLewisFourier scalar transport model is used the which is the standard in the reactingFoam solver. This configuration models a non-reacting hydrogen–air mixing process with a global Reynolds number of 7000 and an equivalence ratio of $\Phi = 0.6$. While the total mass flow rate and equivalence ratio remain constant across all simulations, geometry-dependent variations in the fuel inlet configuration lead to case-specific inlet velocities, turbulence intensities, and k–ε values, which are computed to automate the simulation setup. Table 1 lists all additional boundary and initial conditions that remain constant during the simulations.

Table 1. Simulation setup.

	oxidizer	fuel	boundary condition
inlet	$U_{\text{air}} = 122\ \frac{m}{s}$	$U_{\text{air}} = \text{calculated}$	U = fixed value
	$\rho_{\text{air}} = 1.2\ \frac{kg}{m^3}$	$\rho_{\text{H}_2} = 0.084\ \frac{kg}{m^3}$	
	$Q_{\text{air}} = 6.0367 * 10^{-4}\ \frac{m^3}{s}$	$Q_{\text{H}_2} = 1.5217 * 10^{-4}\ \frac{m^3}{s}$	p = zero gradient
	$T_{\text{air}} = 298\ K$	$T_{\text{H}_2} = 298\ K$	
outlet	-	-	U = zero gradient
			p = total pressure

A consistent mesh is maintained with a 0.14 mm base cell and a 1.2 expansion ratio to balance resolution and cost. Boundary layers are resolved conservatively: the oxidizer uses five layers at a 55 % growth ratio, while the tight, curved fuel inlets use three layers at 30 %, avoiding cell distortion. These settings strike a compromise between physical accuracy and geometric feasibility and are kept constant because manual mesh tuning is not possible in the automated optimization workflow.

The CFD simulations are conducted using the reactingFoam solver in OpenFOAM, which handles compressible, turbulent, reacting flows. A local Euler time integration scheme improves the resolution of unsteady effects in the mixing region compared to a steady state scheme, and an adjustable timestep adapts dynamically to local Courant numbers, enhancing transient accuracy without compromising stability. As the study focuses solely on mixing behavior, the combustion model is deactivated. Each simulation runs for 4000 outer iterations, based on preliminary tests showing that residuals stabilize sufficiently within this range for reliable evaluation. Each CFD simulation, including preprocessing (geometry preparation, meshing) and postprocessing (data extraction, objective function evaluation), requires approximately 60 minutes of wall-clock time on the high-performance computing (HPC) cluster CLAIX-2023 at RWTH Aachen University using one node with 48 processor cores.

Design space exploration and SBO

Dakota is an open-source tool for optimization and design-space exploration. In this framework, it coordinates the workflow by linking geometry generation in Salome with CFD simulations in OpenFOAM and automating the evaluation of design variants.

For the design optimization phase, this study uses the Efficient Global Optimization (EGO) method implemented in Dakota. EGO was selected due to its suitability for simulation-driven workflows with high computational cost, as it enables targeted refinement of the surrogate model while requiring relatively few CFD evaluations. This makes it effective for exploring complex, high-dimensional design spaces under limited computational resources.

For initial design space exploration, the Latin Hypercube Sampling (LHS) method is used. LHS is a stratified sampling technique that ensures a uniform, space-filling distribution of sample points across the parameter space, as compared to simple random sampling [20]. This sample size is chosen based on the Dakota framework's recommendation of selecting between $2x$ and $10x$ samples, where x is the number of design variables, depending on the problem's complexity and nonlinearity [23]. For this study the initial sample size consists of $10x$ samples resulting in 40 initial CFD simulations. In Table 2 the limits for the design variables are shown, which were chosen based on a combination of geometric constraints, manufacturing limitations, and numerical stability considerations.

Table 2. Limits of design variables.

	Inlet angle α [°]	Inlet height h [mm]	Inlet diameter d [mm]	Quantity of inlets $N_{\text{fuel\_inlets}}$
Upper limit	40	10	1.1	3
Lower limit	70	20	1.6	6

The inlet angle is limited to 40–70°: angles below 40° cannot be modelled robustly in Salome across all heights, while angles above 70° cause inconsistent surface patch assignments due to randomized face numbering. The inlet height range of 10–20 mm is chosen to avoid regions of high oxidizer velocities, which occur for h < 10 mm and lead to solver instabilities, and to respect the physical space available in the burner assembly, since h > 20 mm would interfere with adjacent flow paths. The inlet diameter is constrained to 1.1–1.6 mm to prevent manufacturing issues in PBF-LB/M, because diameters < 1.1 mm require extensive post-processing and to maintain sufficient fuel inlet momentum, since diameters > 1.6 mm in combination with many inlets produce excessively low velocities. Finally, the number of fuel inlets is varied from 3 to 6: fewer than three cause asymmetry, while more than six cannot be physically arranged in the diverging duct. Because Dakota's EGO algorithm only handles continuous variables, the quantity of inlets is treated continuous during sampling and rounded to the nearest integer before geometry generation in Salome, preserving automation and ensuring valid discrete configurations.

The objective function is defined based on the spatial distribution of the equivalence ratio (Φ) at the outlet plane (excluding the outlet extension) with the goal to minimize the variation of Φ, which is defined as the ratio of the actual to the stoichiometric fuel–oxidizer ratio:

$$\Phi = \frac{(\dot{m}_{fuel}/\dot{m}_{oxidizer})_{actual}}{(\dot{m}_{fuel}/\dot{m}_{oxidizer})_{stoich}} \tag{1}$$

Values of $\Phi < 1$ correspond to fuel-lean conditions and $\Phi > 1$ to fuel-rich conditions. To reduce numerical fluctuations in the steady-state RANS results, hydrogen and oxidizer mass fractions are averaged over the final outer iterations. Sampling is performed cell-wise on an outlet plane (excluding the outlet extension), and local Φ values are calculated for each cell based on the averages of hydrogen massfraction. To quantify the overall mixture homogeneity, the coefficient of variation (CV) is computed across all outlet surface cells. The CV is defined as the ratio of the standard deviation to the mean of the equivalence ratio:

$$CV = \frac{\sigma_\phi}{\bar{\Phi}}, \tag{2}$$

where $\bar{\Phi}$ is the mean equivalence ratio and σ_ϕ its standard deviation over the outlet plane. A low CV indicates a more homogeneous mixture and thus represents an improved mixing performance. This scalar value serves as the final objective function in the optimization process. CV is chosen because it provides a dimensionless, statistically robust indicator that captures both the magnitude and consistency of local deviations. Alternatively, other metrics such as the variance of the equivalence ratio could replace CV or be incorporated as an additional objective function to further enhance the optimization process.

The accuracy of the surrogate model is assessed both during and after the optimization process. Within the EGO algorithm, surrogate predictions are iteratively validated by selecting new sample points based on the EIF. At each iteration, the design variables set with the highest expected improvement are evaluated using a CFD simulation, and the resulting value is used to update the GP model. This process ensures a continuous refinement of the surrogate model in promising regions of the design space.

The initial sampling was followed by 32 additional simulations during the EGO-based optimization phase, where each newly proposed design was evaluated based on its expected improvement. To assess the predictive accuracy of the surrogate model, the mean absolute percentage error (MAPE) is used in a Leave-One-Out (LOO) cross-validation scheme. For each of the data points, a GP surrogate is trained on the remaining samples, and the excluded point is used for testing. This is repeated for all samples, and the average relative error is computed. MAPE is particularly suitable here, as the objective function takes on small values. Unlike error metrics such as the mean square error (MSE) or R^2, which are sensitive to scale and outliers, MAPE is scale-independent and more robust for low-magnitude targets and varying output scales. The MAPE is calculated according to Eq. 3 where y_i denotes the true objective values, $\hat{y}_i$ the surrogate predictions and N the total number of samples [25]:

$$MAPE = \frac{1}{N}\sum_{i=1}^{N}\left|\frac{y_i - \hat{y}_i}{y_i}\right| \times 100 \quad (3)$$

Results

This section presents the results of the surrogate-based optimization process, including the sampling behavior, surrogate model performance, and the evaluation of the optimal design configuration.

The evaluation of the sample distribution and optimization outcomes shows distinct trends in mixing performance. Figure 3 shows the scatterplot matrix, highlighting scatterplots for each pair of design variables on the off-diagonal elements, histograms of individual variable distributions on the diagonal, and includes Pearson correlation coefficients to quantify the strength and direction of relationships between parameters, providing a comprehensive overview of parameter interactions and sampling behavior.

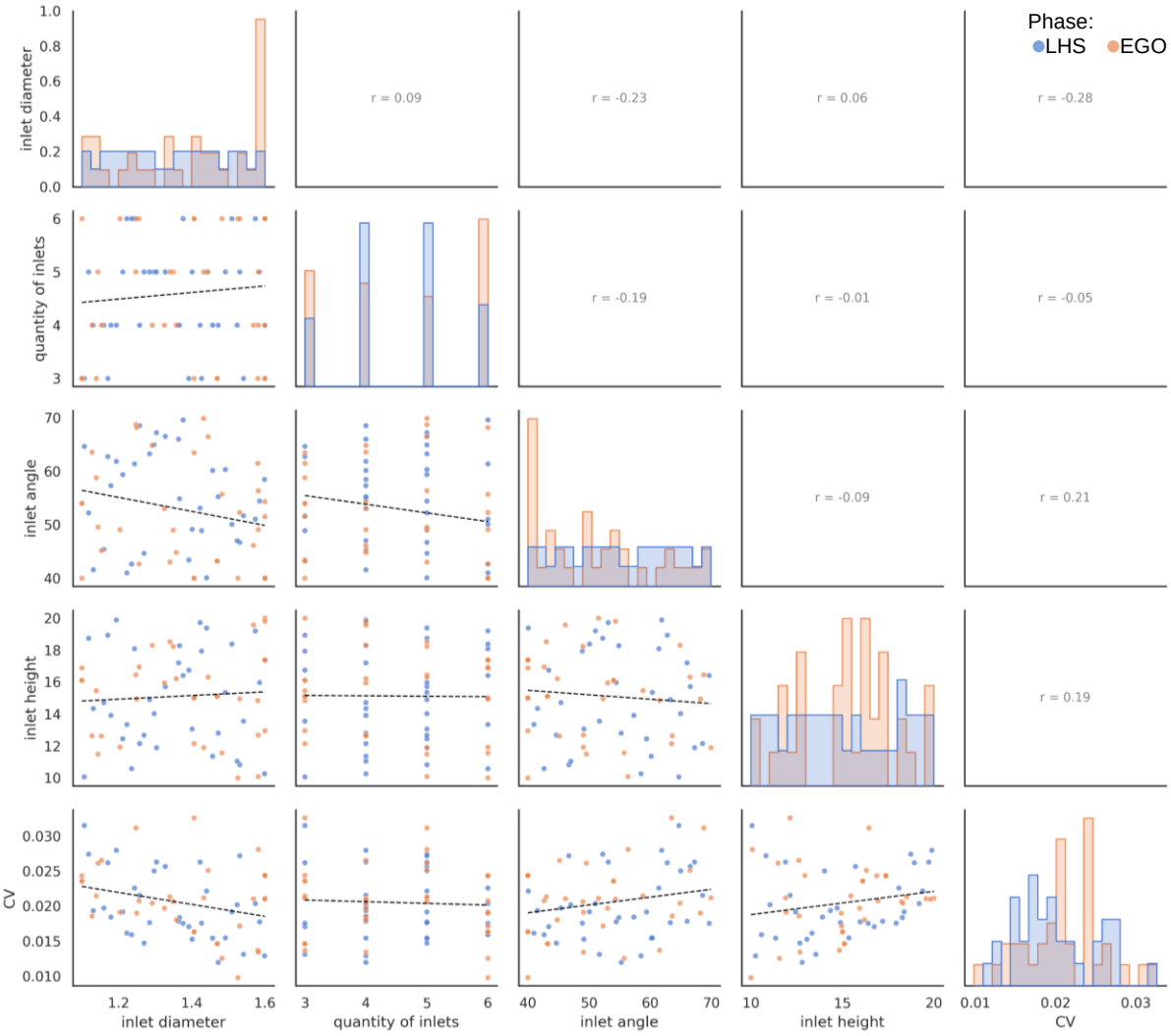

Figure 3. Scatterplot matrix of LHS and EGO samples.

The initial LHS samples, represented by blue points, ensure uniform coverage across diameter and inlet angle, whereas the inlet height exhibits underrepresentation within the range of 16 to 18 mm. Because the number of inlets was sampled continuously and then rounded to integers, the LHS stage produces an uneven distribution of inlet counts which are clustered at 4 and 5 inlets. The EGO phase, denoted by orange points, incorporates an increase in samples with a higher quantity of inlets and larger diameters, which is also indicated by the Pearson correlation (r = -0.28). Notably, EGO adds more points at 1 and 6 inlets to probe underexplored discrete regions. Additionally, EGO favors smaller angles within the range of 40° to 50°, aligning with the observed weak positive correlation (r = 0.21). For the inlet height, supplementary samples are introduced at 12 mm and within the previously underrepresented 16 to 18

mm range to optimize the design space comprehensively. The increase in the quantity of inlets, shows a low linear correlation of r = -0.05.

The prediction accuracy of the surrogate model starts at a mean average percentage error of 19,86% with 40 initial LHS samples and stabilizes at 16,76% after a total of 32 EGO samples are added. This indicates a gradual improvement in the model's reliability for predicting the coefficient of variation (CV) as the EGO phase refined the design space.

The optimization process identifies a design with the following parameters as the best-performing configuration: inlet diameter = 1.53 mm, number of inlets = 6, inlet angle = 40.0°, and inlet height = 10.0 mm. This design achieves a CV value of 0.0098, which is 52.2% smaller than the mean CV of the overall dataset with a value of 0.0205, indicating an improved mixing homogeneity. This parameter set and its corresponding CV value are not a prediction from the surrogate model. It was selected by the EGO algorithm during the optimization process due to its highest expected improvement in that iteration and was subsequently validated through a CFD simulation. Table 3 compares this optimized design with a configuration whose CV value is close to the dataset mean. The mean CV design exhibits a smaller diameter, fewer inlets, larger angles, and higher inlet heights aligning with the observed Pearson correlations.

Table 3. Parameter sets of optimal and mean CV.

	Inlet angle α [°]	Inlet height h [mm]	Inlet diameter d [mm]	Quantity of inlets $N_{\text{fuel\_inlets}}$	CV
Optimal design	40	10	1.53	6	0.0098
Design with mean CV	65	18.3	1.29	4	0.0204

Figure 4 shows a contour plot of the equivalence ratio at the outlet plane of the burner of both designs. The optimized design exhibits a uniform distribution with small local gradients or wall accumulations, whereas the comparison case shows steep gradients of equivalence ratio and in general higher values at the wall. The equivalence ratio in the optimized configuration is bounded between 0.5854 and 0.6073, indicating a higher mixture homogeneity compared to the mean CV value case.

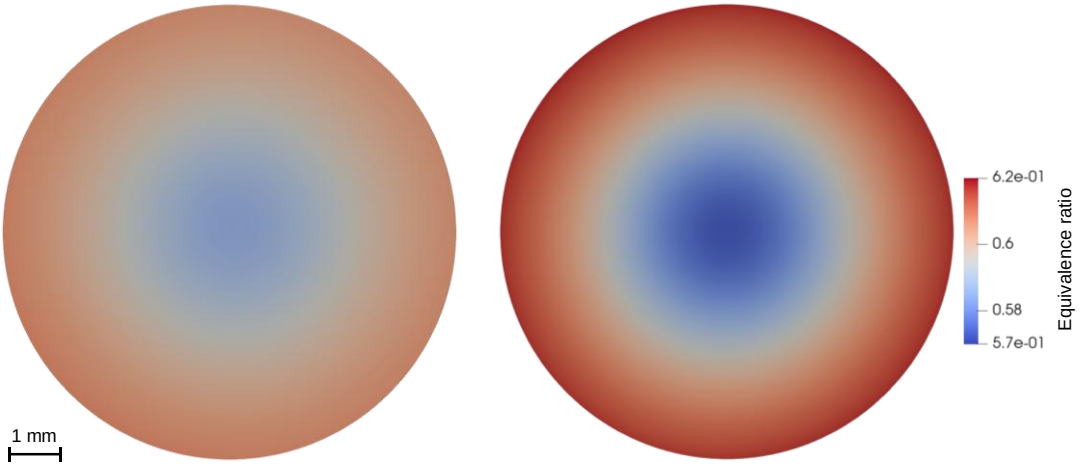

Figure 4. Equivalence ratio at the outlet of optimized (left) and mean CV design (right).

Figure 5 compares the radial profiles of equivalence ratio from the center (radius = 0 mm) to the wall (radius = 4.5 mm) for the optimized design (dashed line) and a mean CV reference design (solid line). These graphs highlight the differences in gradient behavior: in the optimized design, the gradient is shallower throughout the cross-section compared to the mean CV design. In the mean CV case the gradient increases in the near-wall region compared to the optimized case where the gradient decreases near the wall.

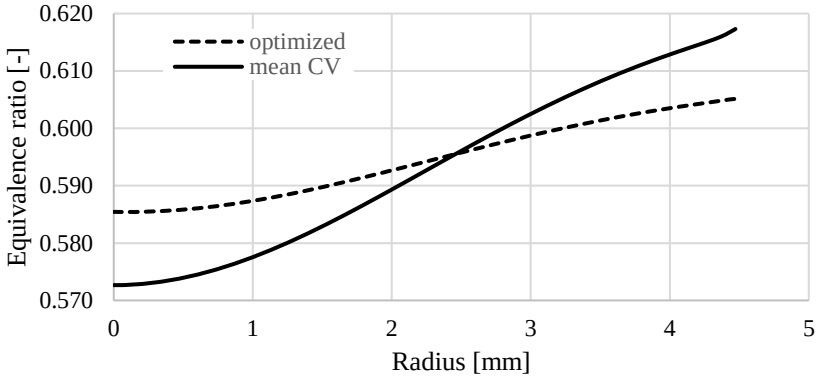

Figure 5. Plot of Equivalence ratio at the outlet of optimized and mean CV design.

In contrast to the surrogate-based approach employed in this study, a full-factorial design of experiments with equivalent variable limits would require 576 simulations to cover the design space. This results from discretising the inlet diameter into six steps of 0.1 mm, the number of inlets from 3 to 6 in integer increments, the inlet angle in 10° steps from 40° to 70°, and the inlet height in 2 mm steps between 10 mm and 20 mm. Such a grid ensures full parameter coverage but relies on relatively coarse resolution for certain variables, potentially overlooking local sensitivities. The surrogate-based optimization, in contrast, reduced the number of required simulations to 72, enabling a more efficient and adaptive exploration of the design space. The SBO framework reduces the computational effort by an estimated 87.5 %, while still enabling the identification of high-performance design candidates.

Discussion

The results demonstrate that the surrogate-based optimization framework can effectively identify burner geometries with improved mixing homogeneity. The optimized configuration exhibits a uniform, low-gradient profile of equivalence ratio across the outlet plane, in contrast to the high-gradient zones observed in the mean CV reference design. This uniform mixing mitigates two critical combustion risks: first, it prevents a lean core with a locally hydrogen-rich boundary layer, which promotes high equivalence-ratio values at the walls and increases flashback risk; second, it reduces localized hot spots caused by uneven equivalence-ratio distributions, thereby decreasing thermal NO_X formation. By achieving a tight equivalence-ratio band with small radial gradients, the optimized design reduces both hazards.

The sampling behavior of the EGO algorithm further underscores its capability to balance exploration and exploitation. Early iterations introduce points in underrepresented inlet-height regions and across a broad range of diameters and inlet counts, reflecting an exploratory phase to map the global design space. Subsequent clustering of samples at larger diameters, higher inlet numbers, and lower angles shows the exploitation of regions predicted by the EIF to yield the improvements in mixing performance. The leading-order effects driving improved mixing performance are primarily associated with larger inlet diameters (Pearson correlation r = -0.28) and smaller inlet angles (r = 0.21), which reduce CV values, while smaller inlet heights (r = 0.19) also contribute by providing a longer mixing length that allows more time for homogenization. In combination with the higher quantity of inlets, despite the low Pearson correlation, lower inlet velocities for hydrogen produce more homogeneous mixtures.

Despite these successes, the framework is subject to several constraints. All key metrics are derived from temporally averaged RANS data, which can obscure localized or transient peaks in equivalence ratio that are critical for flashback initiation and hot-spot-driven NO_x formation and fail to capture time-dependent mixing that could significantly influence performance in practice. Moreover, the fact that the optimal solution lies at the lower limits of inlet angle (40°) and inlet height (10 mm) and at the upper limits of inlet diameter (1.53 mm) and number of inlets (6) suggests that further improvements may exist beyond the chosen parameter ranges. Although the EGO algorithm is designed to efficiently search for global optima, a guarantee for global optimum cannot be provided due to the probabilistic nature of the surrogate model, limited sample budget, and model inaccuracies. While the MAPE of 16.76% indicates a high percentage error, the absolute error remains small given the low CV values. Additionally, the

limited number of EGO samples may not yet fully cover all regions of the design space, potentially missing other high-performing configurations. Finally, the high MAPE and low Pearson correlation observed for the quantity of inlets indicate nonlinear interactions, that the current GP surrogate, particularly given its continuous treatment of a discrete variable, may not fully resolve.

Conclusion and Outlook

This work establishes a surrogate-based optimization framework that effectively integrates parametric geometry generation, steady-state RANS CFD simulations, and an EGO algorithm to systematically explore and optimize hydrogen burner configurations for enhanced mixing homogeneity. While the identified optimal design demonstrates promising performance, achieving a coefficient of variation of 0.0098 (a 52.2 % improvement over the dataset mean), the primary contribution lies in the development of the methodology itself, as the optimized result remains subject to uncertainties inherent to the simulation and modeling assumptions. By automating the exploration of a four-dimensional design space, the framework reduces the required number of high-fidelity simulations from 576 in a full-factorial grid to 72, corresponding to an 87.5 % decrease in computational expense. The optimal design achieves a coefficient of variation of 0.0098, a 52.2 % improvement over the dataset mean, while respecting additive-manufacturing constraints and avoiding problematic overhangs or narrow channels.

Beyond demonstrating substantial gains in mixing performance, the sampling of the EGO algorithm revealed systematic tendencies: early exploration addressed sparsely sampled inlet heights and diameters, whereas later exploitation concentrated on large diameters, high inlet counts, and low angles. This behavior not only demonstrates the EIF balance between exploration and exploitation but also highlights key sensitivity trends, which is information that would remain unexplored in purely manual or grid-based approaches. The surrogate's MAPE reduction from 19.9 % to 16.8 % further indicates that iterative refinement effectively increases predictive accuracy in regions of interest, despite the continuous approximation of discrete variables.

In future work, the framework may be extended and strengthened through several approaches. First, reactive CFD simulations that capture local equivalence-ratio peaks which indicate flashback risks can be incorporated. Second, further investigation into alternative optimization algorithms, as the EGO algorithm does not guarantee a global optimum necessitating exploration of other methods. Third, experimental validation of the optimized geometries manufactured in PBF-LB/M will quantify real-world performance and inform any necessary modifications to the surrogate model or objective definition. Third, expanding or refining the design limits (e.g., angles < 40°, heights < 10 mm, diameters > 1.6 mm, and higher inlet counts) may reveal further improvements, provided manufacturing feasibility is ensured and mesh stability is maintained. To better resolve discrete and strongly nonlinear interactions, the surrogate strategy can be enhanced through mixed-integer GP or multi-fidelity modeling that accommodates integer variables natively. Finally, extending the framework to multi-objective optimization (e.g., balancing mixing homogeneity, NO_x formation, pressure loss, and flashback margins) will support the holistic design of hydrogen burners tailored to industrial applications.

By pursuing these developments, the proposed methodology can evolve into a comprehensive toolchain for the rapid, reliable, and manufacturability-aware design of next-generation hydrogen combustion systems.

Acknowledgement

This work has been funded by the Deutsche Forschungsgemeinschaft, Germany (DFG, German Research Foundation) under the IGNITER project within the DFG-SPP 2419 HyCAM (project number: 523874889). Computations were performed with computing resources granted by RWTH Aachen University under project rwth1837.

Literatur

[1] Europäische Kommission: *Umsetzung des europäischen Grünen Deals:* Auf dem Weg zu einem klimaneutralen Europa bis 2050, Brüssel, 2021.

[2] Europäische Kommission: *Mitteilung der Kommission an das Europäische Parlament, den Europäischen Rat, den Rat, den Europäischen Wirtschafts- und Sozialausschuss und den Ausschuss der Regionen:* REPowerEU-Plan, Brüssel, 2022.

[3] Aniello A., Poinsot T., Selle L. und Schuller T.: *Hydrogen substitution of natural-gas in premixed burners and implications for blow-off and flashback limits* International Journal of Hydrogen Energy, 47, S. 33067–33081, 2022.
[4] Fruzza F., Lamioni R., Tognotti L. und Galletti C.: *Flashback of H2-enriched premixed flames in perforated burners: Numerical prediction of critical velocity* International Journal of Hydrogen Energy, 48, S. 31790–31801, 2023.
[5] Law C. K., Makino A. und Lu T. F.: *On the off-stoichiometric peaking of adiabatic flame temperature* Combustion and Flame, 145, S. 808–819, 2006.
[6] Choudhuri A. R. und Gollahalli, SR: *Characteristics of hydrogen–hydrocarbon composite fuel turbulent jet flames* International Journal of Hydrogen Energy, 28, S. 445–454, 2003.
[7] Zhang L., Wu C., Zhang J., Zhang B. und Sui C.: *Numerical Simulation of the Combustion Characteristics in a Flue Gas Internal Recirculation Burner* ACS omega, 7, S. 42264–42271, 2022.
[8] Pignatelli F.: *Impact of pilot flame and hydrogen enrichment on turbulent methane/hydrogen/air swirling premixed flames in a model gas turbine combustor* Experimental Thermal and Fluid Science, 152, S. 111124, 2024.
[9] Singh G., Schreiner B. D. J., Sun X. und Sethi V.: *A review of hydrogen micromix combustion technologies for gas turbine applications* International Journal of Hydrogen Energy, 127, S. 295–310, 2025.
[10] York W. D., Ziminsky W. S. und Yilmaz E.: *Development and testing of a low NOx hydrogen combustion system for heavy-duty gas turbines* Journal of Engineering for Gas Turbines and Power, 135, S. 22001, 2013.
[11] Kim Y., Kwon H. und Lee M. J.: *Mitigating NOx Emissions in Hydrogen-Fueled Industrial Burners Through Residence Time Control* Case Studies in Thermal Engineering, S. 106523, 2025.
[12] Andreas Gebhardt, Julia Kessler und Laura Thurn, *3D Printing - Understanding Additive Manufacturing*. Hanser Publishers, Munich, ISBN: 978-1-56990-702-3, 2019.
[13] *DIN EN ISO/ASTM 52911-1:2020-05: Additive manufacturing – Design – Part 1: Laser-based powder bed fusion of metals (ISO/ASTM52911-1:2019)*, 52911-1, DIN Deutsches Institut für Normung e. V., Berlin, Mai. 2020.
[14] Reumschüssel J. M., Saldern J. G. R. von, Ćosić B. und Paschereit C. O.: *Data-driven optimization of a gas turbine combustor: A Bayesian approach addressing NO x emissions, lean extinction limits, and thermoacoustic stability* Data-Centric Engineering, 5, 2024.
[15] Willkomm J., Weller V., Bredow A. von, Putz C. und Schleifenbaum J. H.: *Design Automation: Term Definition and Methodical Analysis for Software Selection* RTe Journal, 2025.
[16] Angelo, C., Carla, D., Mariangela, L., Giuseppe, S., & Domenico, L.: *Knowledge Based Engineering for Hydrogen Gas Turbines and Burners Design: A review*, 2022.
[17] Serani A., Scholcz T. P. und Vanzi V.: *A Scoping Review on Simulation-Based Design Optimization in Marine Engineering: Trends, Best Practices, and Gaps* Archives of computational methods in engineering : state of the art reviews, 31, S. 4709–4737, 2024.
[18] Liu X.: *Surrogate-assisted global and distributed local collaborative optimization algorithm for expensive constrained optimization problems* Scientific reports, 15, S. 1728, 2025.
[19] Gauger N. R. *et al., Advances in Evolutionary and Deterministic Methods for Design, Optimization and Control in Engineering and Sciences*. Springer International Publishing; Imprint: Springer, Cham, ISBN: 9783319899886, 2019.
[20] Jiang P., *Surrogate Model-Based Engineering Design and Optimization*. Springer Singapore Pte. Limited, Singapore, ISBN: 9789811507311, 2020.
[21] Jones D. R., Schonlau M. und Welch W. J.: *Efficient Global Optimization of Expensive Black-Box Functions* Journal ofGlobal Optimization, S. 455–492, 1998.
[22] CEA, EDF, Open Cascade, *SALOME PLATFORM*, 9.13, opensource, Rocky 9.6, https://www.salome-platform.org/
[23] Sandia National Laboratories, *Dakota*, 6.22, opensource, Rocky 9.6, https://dakota.sandia.gov/
[24] OpenCFD Ltd, *OpenFOAM*, v2312, opensource, Rocky 9.6, https://www.openfoam.com/
[25] Kim S. und Kim H.: *A new metric of absolute percentage error for intermittent demand forecasts* International Journal of Forecasting, 32, S. 669–679, 2016.

Population Balance Simulations of the Mixing Zone of Double Nozzle Flame Spray Pyrolysis (DFSP) Processes

A. Pandey[1*], T. Tabeling[2,3], A. Kronenburg[1] and U.Fritsching[2,3]

*anjul.pandey@irst.uni-stuttgart.de

[1]*Institut für Reaktive Strömungen, Universität Stuttgart, Pfaffenwaldring 31, 70569 Stuttgart, Deutschland*
[2]*Leibniz-Institut für Werkstofforientierte Technologien - IWT, Badgasteiner Str. 3, 28359 Bremen, Deutschland*
[3]*Particles and Process Engineering, Universität Bremen, Bibliothekstraße 1, 28359 Bremen, Deutschland*

Abstract

Effective mixing of multicomponent materials is crucial for numerous industrial applications, particularly in pharmaceutical and cosmetic product development. Heteroagglomeration - the process of combining dissimilar particles - enables the creation of advanced functional materials with tailored properties. This study investigates particle formation dynamics in a Double Flame Spray Pyrolysis (DFSP) reactor using a population balance equation (PBE) framework that simultaneously tracks agglomerate size and composition evolution through a Brownian collision kernel. We examine two distinct nozzle configurations ($\alpha = 20^\circ$ and $\alpha = 30^\circ$) to evaluate their mixing efficiency and particle formation characteristics. Our results reveal significant geometric effects: the 30° configuration induces rapid heteroagglomeration near the nozzle exit with decreasing interaction intensity downstream, while the 20° configuration demonstrates more gradual but sustained agglomeration over extended regions. Compositional analysis shows that the the 30° nozzle produces agglomerates with superior mixing homogeneity compared to the 20° configuration.

Introduction

Targeted precise mixing of particulate materials is a fundamental challenge with far-reaching implications across multiple industries, including pharmaceuticals (e.g., drug formulation and powder blending), food processing (e.g., homogenization of additives and flavorants), construction (e.g., cement and composite materials), and cosmetics (e.g., pigment dispersion in sunscreens and makeup). The functional performance of these materials is governed by their micro-structural organization, particularly the spatial distribution of dissimilar particles and the formation of hetero-contacts-interfacial interactions between chemically or physically distinct particles. These hetero-contacts critically influence bulk properties such as mechanical strength, catalytic activity, optical characteristics, and dissolution behavior. Consequently, achieving a controlled and homogeneous mixture is not merely a processing objective but an imperative for successful material design, necessitating advanced synthesis techniques capable of fine-tuning inter-particle interactions at the nanoscale.

Flame Spray Pyrolysis (FSP) has emerged as a leading technique among nanoparticle synthesis methods, with the capabilities to generate nanostructured materials of high purity while maintaining scalability for large-scale production. In a typical FSP process, a precursor solution is first atomized into small droplets which is then introduced into a high temperature zone. These droplets vaporize and decompose to form nanoparticles and these nanoparticles undergo sintering, surface growth and agglomeration [1]. In the recent years, Double Flame Spray Pyrolysis (DFSP) has been developed as an advanced variant, wherein two separate precursor streams, are combusted in tandem or intersecting flames, enabling the synthesis of bi-component or hybrid nanoparticle agglomerates, as shown in Fig. (1). The key advantage of DFSP over conventional FSP lies in its flexibility to control the important flame parameters such as temperature and concentration fields, which affect particle formation, and it provides good control of particle mixing at the nano-level in multi-component systems [2]. In the DFSP setup, different streams from both the nozzles interact with each other in the mixing zone which serves

as a dominant site for the hetero-agglomeration. The extent of mixing of both streams can be controlled either by changing the distance between the nozzles or by changing the nozzle angle [3].

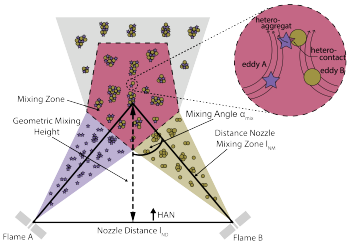

Figure 1. Schematic of DFSP setup.

Nanoparticle agglomeration is typically studied using the population balance equations (PBE), which provides a statistical framework for tracking the evolution of particle/agglomerate size distribution. The collision kernel is a key factor in describing the agglomeration process, as it represents the rate at which particles/agglomerates interact. The collision kernel takes different forms based on the surrounding environments and the agglomerate characteristics. Based on the size of agglomerates, the dynamics of agglomeration is governed either by Brownian motion or turbulence.

Despite several advances, full-scale simulation of DFSP reactors remains computationally intractable due to the multi-scale and multi-physics nature of the problem, which involves turbulent combustion, and particle dynamics across all scales. In this study, we adopt a sequential computational approach, first conducting CFD simulations of the DFSP configuration to obtain flow field data (including velocity, temperature, and viscosity fields), which subsequently serve as inputs for independent PBE simulations focusing on the mixing zone. We examine two different nozzle angle configurations with $\alpha = 20°$ and $30°$. Due to the current unavailability of turbulent collision kernel models for binary particle systems, we employ a Brownian kernel formulation for two-component systems [4,5] to model the agglomeration process.

Theory

Flow Simulations

The numerical simulations of the flame spray process use a coupled Euler-Lagrange approach. In this framework, the gas phase is treated as a compressible Newtonian fluid using an Eulerian formulation, while the dispersed droplets are tracked individually through Lagrangian particle methods. The gas-phase dynamics are governed by the conservation laws for mass, momentum, and energy. The continuity equation tracks density changes due to fluid motion and mass transfer from evaporating droplets. The momentum balance incorporates pressure effects, viscous forces, gravity, and interactions with the dispersed phase. The energy equation considers both thermal and kinetic energy, including heat conduction and energy exchange from droplet-phase processes such as heat transfer and combustion. The system is closed thermodynamically using the ideal gas law, with temperature-dependent properties for specific heat and viscosity. For brevity, the full forms of these standard governing equations are omitted, as they are well-documented in fundamental fluid dynamics literature.

The Lagrangian droplet model to track parcel trajectories, temperature and mass loss are also well documented and can be found in the literature [6]. For turbulent closure, the k-ω SST model was selected due to its robustness in the confined nozzle region and its ability to accurately predict downstream flow structures [7–9].

The agglomerate size distribution

In CFD simulations, explicitly resolving particle nucleation, growth and agglomeration is computationally intractable due to the high number concentrations in aerosol reactors (often exceeding 10^{15} particles / cm^3 [10]). Instead, the particle size distribution is typically modelled using a population balance equation (PBE), where the number density function $n(\psi, x, t)$, which is dependent on particle/agglomerate properties, spatial coordinates, x, and time, t, is solved via moment-based methods (e.g.,

QMOM, DQMOM) or sectional methods (e.g., discrete bins). The general form of the PBE incorporates key physical mechanisms governing the particle dynamics [11]

$$\frac{\partial n(\psi,x,t)}{\partial t}+\nabla\cdot(\boldsymbol{u}n(\psi,x,t))-\nabla\cdot(D_{eff}\nabla n(\psi,x,t))+\frac{\partial\dot{\psi}_i n(\psi,x,t)}{\partial\psi_i}=\dot{S}_{nucl}+\dot{S}_{aggl}+\dot{S}_{frag}. \quad (1)$$

Here, the second, third and fourth terms on the left hand side of Eq. (1) are the convection, diffusion and surface growth terms, respectively. The right hand side of the Eq. (1) describes the mechanisms of particle formation, growth and breakage with $\dot{S}_{nucl}$ and $\dot{S}_{frag}$ accounting for nucleation and fragmentation, and

$$\dot{S}_{aggl}=\frac{1}{2}\int_0^{\psi}\beta(\psi-\psi',\psi')n(\psi-\psi')n(\psi')d\psi'-n(\psi,x,t)\int_0^{\infty}\beta(\psi,\psi')n(\psi')d\psi' \quad (2)$$

is the agglomeration term with the first term on the RHS accounting for the formation of new agglomerates and the second term accounting for the loss of agglomerates. Here, we only consider the agglomeration while ignoring the formation and breakage. Thus Eq. (1) simplifies to

$$\frac{\partial n(\psi,x,t)}{\partial t}+\nabla\cdot(\boldsymbol{u}n(\psi,x,t))-\nabla\cdot(D_{eff}\nabla n(\psi,x,t))=\dot{S}_{aggr}. \quad (3)$$

The cumulative property vector, $\psi=(m,v,N_P,R_g,...)^T$ may include the mass, m, volume, v, number of particles, N_P or the gyration radius, R_g. For the closure of collision kernel, we employ the Brownian kernel derived in our previous work [5]. While a turbulent kernel would theoretically be more appropriate for this system, we justify our approach based by the demonstrated insensitivity of the dynamics of small agglomerates to the specific kernel formulation, as Brownian and turbulent kernels yield nearly identical results for sub-micron particles [12]. For the characterization of agglomerates composed of two distinct components, we have used the number of primary particles, N_P, and the number fraction, N_F, to characterize the agglomerates. The number fraction is defined as

$$N_F=\frac{N_{P,large}}{N_{P,large}+N_{P,small}} \quad (4)$$

with $N_{P,large}$ and $N_{P,small}$ being the number of large and small primary particle within the agglomerate. This is consistent with our previous methodology [5]. Utilizing these parameters and maintaining a constant size ratio, $\gamma=d_{P,large}/d_{P,small}$, with d_P being the diameter of primary particles, we obtain a bi-variate size distribution $n(N_P,N_F;x;t)$ which evolves in space and time.

The parameter β in Eq. (2) represents the collision kernel, a function that governs the agglomeration dynamics of particles/agglomerates within the system. The collision kernel is quantified as the number of collisions between two particles/agglomerates per unit time per unit number concentration, which is affected by both, the structural characteristics of agglomerates and the surrounding conditions. In this work, we use our previously derived Brownian kernel for two-component systems to close the agglomeration term. The complete derivation of our collision kernel model can be found in [4, 5] which was adapted from earlier work by Gopalakrishnan et al. [13].

Numerical Setup

Flow simulations

The numerical model was developed within the OpenFOAM v2112 framework, adopting an Euler-Lagrange approach to simulate dual-flame spray pyrolysis (DFSP) as two intersecting spray flames. Here, the gas phase is handled in an Eulerian framework, solving the continuity, momentum, and energy equations, while liquid droplets are injected and tracked individually via a Lagrangian method. As the nanoparticles are not expected to affect the flow field, the initial simulations do not include particle generation.

Turbulence-chemistry interactions are captured using the eddy dissipation concept (EDC), which links turbulent mixing directly to reaction rates, and the chemical source terms are integrated with an implicit Euler scheme to ensure stability. The combustion of xylene, which was chosen as fuel, is described by a detailed 36-step reaction mechanism comprising 24 species [14].

The boundary conditions for the patches are chosen in a way that the dispersion gas, supporting flame and co-flow are described via a mass flow rate. The outlet has been described as a pure outlet, with gas only allowed to exit the simulation. The other patches are set as ambient air, allowing entrainment air to enter the simulation domain.

To track mixing, each nozzle's dispersion gas is doped with a unique inert tracer at a concentration of 0.01 % by volume mixed into a 99.99 % oxygen stream. Both tracers share the oxygen's thermophysical properties but remain chemically inert, allowing clear delineation of the two jets. The local mixing is then assessed by a mixing index that is based on the local tracer concentrations c_A and c_B and given by

$$\theta_{mix} = \frac{c_A \cdot c_B}{c_A + c_B}. \tag{5}$$

Based on the local mixing a global mixing quality is then determined and computed as

$$\text{Mixing Quality} = \frac{\int \theta_{mix}}{\int_{x_{min}}^{x_{max}} c_A + \int_{x_{min}}^{x_{max}} c_B}. \tag{6}$$

The computational grid was generated using snappyHexMesh, producing a 3D spatially resolved mesh that fully captures the DFSP setup. The final grid consists of 22,651,162 hexahedral cells. The fuel droplets are injected at a rate of 3 mL/min and dispersed with pure O_2 (5 L/min), resulting in a constant pressure drop of 1.5 bar. For ignition, a pre-combusted pilot flame (composed of CH_4 at 1.5 L/min and O_2 at 3.2 L/min) is introduced. The pilot flame composition is approximately 10% O_2, 30% CO_2, and 60% H_2O, with an initial temperature of 3500 K-slightly above the adiabatic flame temperature of methane. Upon interaction with the dispersion gas, the temperature stabilizes at 2500 K, as illustrated in Fig. (2e) and (2f). A co-flow of pure N_2 (30 L/min) is also included to stabilize the flame.

For the geometric setup as presented in Fig. (1), two mixing angles have been selected with $\alpha = 20°$ and $\alpha = 30°$. The nozzle distance, l_{ND} is constant at 150 mm.

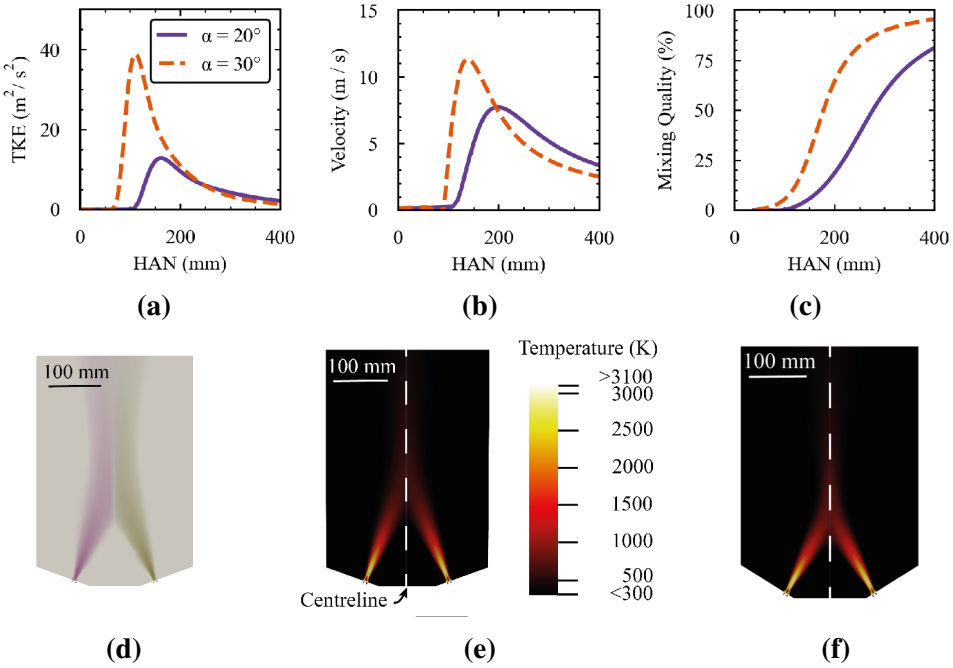

Figure 2. Results from CFD simulations.

Shown in Fig. (2) is the analysis of the CFD results on the centreline and as a contour plot. Figures

(2a) through (2c) illustrate quantitative trends along the centreline, which serves as a representative axis for the mixing zone of the interacting flame jets. Figure (2d) shows the tracer gas concentrations in a plot, showing the nozzle and mixing zone part of the domain. Figures (2e) and (2f) provide temperature contours of the overall flow field, offering visual insight into the temperature distribution. The centreline from which the line plots are derived is also added to the temperature contour plots. The data is presented over height above the nozzle (HAN).

In Fig. (2a), the turbulent kinetic energy (TKE) is displayed. The TKE begins to show noticeable increases at a height of approximately 100 mm for 20° and 70 mm for 30°, this height signifies the point where the two flame jets first make contact. This interaction point effectively marks the initiation of the turbulent mixing region. As the flame jets continue to interact more fully, the TKE reaches its maximum value of around 13 m^2 / s^2 at a height of 160 mm for 20° and around 39 m^2 / s^2 at 110 mm for 30°. This peak is a direct result of the enhanced turbulence generated by the complete collision of the opposing jets. Shortly after this TKE peak, the velocity, which is shown in Fig. (2b), also reaches its maximum, with a value of around 8 m/s at 200 mm for 20° and 12 m/s at 140 mm for 30°.

In Fig (2c), the global mixing quality profiles are analyzed. The mixing quality, which reflects how effectively the two flame jets combine in the gas phase, increases very slowly at first. This gradual rise indicates minimal mixing during the initial phase. The 20° and 30° configurations exhibit distinctly different mixing behaviors. The 30° case shows a rapid increase in mixing quality after a slow start, while the 20° configuration remains comparatively modest. Overall, the 30° configuration achieves a higher level of mixing quality in a shorter period, demonstrating more intense and efficient mixing.

Figure (2d) shows a contour plot of the tracer gases within a section of the domain. The concentrations are visualized using a logarithmic scale on the color bar. By tracking the gas concentration throughout the domain, it is possible to estimate gas mixing using the mixing quality metric. The inlet location for the PBE domain was deliberately chosen such that the streams remain mostly separated, allowing for the independent introduction of the two particle streams. For graphical reasons, the overlay of tracer gas concentrations is not visible in the contour plot; however, the mixing quality metric still effectively captures the overall mixing behavior.

Finally, Figs. (2e) and (2f) display the temperature contour plot of the intersecting flame configurations. The temperature field ranges from 300 K to 3100 K, effectively capturing the full extent of the thermal profile within the domain. Here the temperature evolution from the nozzle into the single flame and then further downstream into the mixing zone gets described. Showing for both configurations short intense flame which decays downstream, before combining at around 700 K for 20° and around 900K for 30° in the mixing zone.

PBE simulations

We solve the population balance equation (Eq. (3)) in a two-dimensional domain representing the mixing zone of the DFSP setup, where two particle-laden streams interact. The computational domain is discretized using a structured 100×200 mesh, ensuring sufficient resolution to capture spatial gradients in particle and agglomerate concentrations. For spatial discretization, an upwind scheme is applied to the convective term for numerical stability, while central differencing is used for the diffusion terms to maintain accuracy. Time integration is handled by a fourth-order Runge-Kutta (RK4) method, balancing computational efficiency with numerical precision. The underlying flow field, including velocity, temperature, and turbulent viscosity-is obtained from steady-state RANS simulations and treated as a frozen input for the PBE simulations.

The effective diffusivity D_{eff} combines molecular and turbulent contributions, expressed as $D_{eff} = D_{molecular} + D_{turbulent}$. Consistent with the modeling approach of Neto et al. [15], we assume an initial particle number density of 10^{17} particles/m^3 at the mixing zone inlet for both flame streams. For both nozzle configurations ($\alpha = 20°$ and $30°$), we further assume that all particles enter the mixing zone as discrete primary particles, with no pre-existing agglomerates. The size of the particles entering the mixing zone is taken from Table 1 of [3] for their respective angle configurations. The agglomeration process is resolved in a two-dimensional property space using the fixed-pivot method [16], applied to the mixing zone illustrated in Fig. (3). The property space is discretized into a 20×20 structured grid, with

each axis representing the number of primary particles from components 1 and 2 within an agglomerate. A geometric progression with a growth factor of 1.3 ensures finer resolution for small particles while accommodating larger agglomerates.

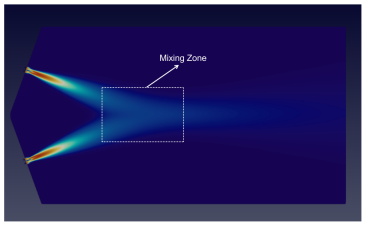

Figure 3. Mixing Zone in the DFSP setup.

The velocity, temperature, and turbulent diffusivity fields are extracted from the precomputed CFD results and implemented via lookup tables. The simulation time step is determined based on the most restrictive criterion among the CFL condition, diffusion stability, and agglomeration kinetics. Continuous flow conditions are enforced by injecting particles at the inlet and removing them at outflow boundaries. All results are analyzed after three flow-through times to ensure statistical reliability and convergence.

Results and discussion

Spatial distribution of agglomerates

The temporal evolution of particle number concentrations is presented in Figure (4a). Here, we distinguish agglomerates that are composed of one component only (pure) and of the two components (mixed). The system reaches steady state after approximately 0.1 ms. As shown, the configuration with $\alpha = 30°$ yields a significantly higher number of mixed agglomerates compared to $\alpha = 20°$. This difference occurs because a larger angle facilitates more direct interaction between particle streams, enhancing agglomeration across different components and leading to a higher concentration of mixed agglomerates near the interaction zone. In contrast, the $\alpha = 20°$ configuration exhibits a more gradual interaction, leading to slower but sustained mixing of different streams over time. Although the $\alpha = 30°$ case initially produces a greater number of mixed agglomerates, the difference between the two configurations diminishes at later times due to the prolonged agglomeration process in the $\alpha = 20°$ case. Figure (4b) compares the percentage of mixed agglomerates between the two configurations. The results show that the $\alpha = 30°$ configuration produces twice as many mixed agglomerates as the $\alpha = 20°$ configuration.

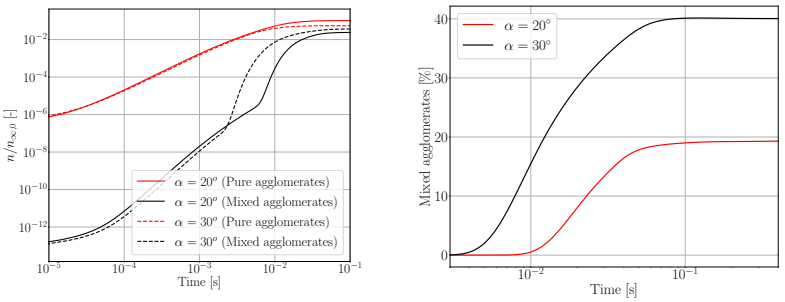

(a) Pure and mixed agglomerates. **(b)** Mixed agglomerates (in %)

Figure 4. Temporal evolution of number concentration of pure and mixed agglomerates. The number concentration is normalized with its initial value.

Figure (5) presents the normalized number concentration profiles at steady state for different nozzle configurations. The total number concentration profiles for both configurations ($\alpha = 20°$ and $\alpha = 30°$) are shown in Figures (5a)-(5b). The $\alpha = 30°$ configuration exhibits a more pronounced and localized

interaction zone between particle streams, whereas the $\alpha = 20°$ case displays a broader, more smeared interaction region. Additionally, Figures (5c)-(5d) highlight the zones where agglomeration between different components occurs. Notably, the $\alpha = 30°$ configuration produces a significantly larger number of mixed agglomerates, as evidenced by the higher concentration magnitudes in these regions.

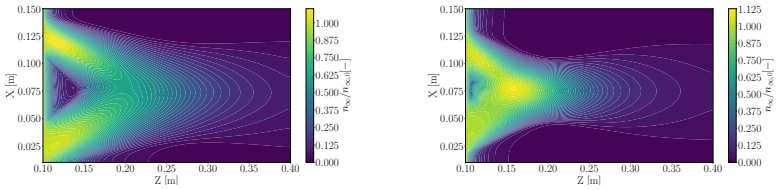

(a) n_∞ for $\alpha = 20°$. **(b)** n_∞ for $\alpha = 30°$.

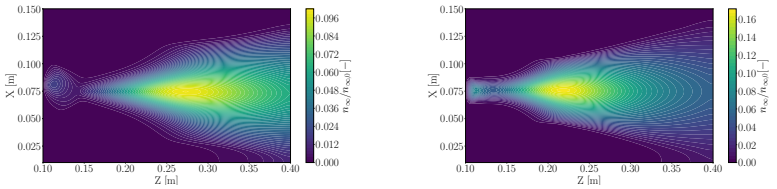

(c) $n_{\infty,mixed}$ for $\alpha = 20°$. **(d)** $n_{\infty,mixed}$ for $\alpha = 30°$.

Figure 5. Spatial contour of number concentration.

Figure (6) displays axial profiles of the overall number concentration at various downstream locations. At Z = 0.25 Z_{max}, the configuration with $\alpha = 20°$ exhibits two distinct maxima on either side with a central dip, indicating limited interaction between the two streams. In contrast, the $\alpha = 30°$ case shows only a single maximum, suggesting an earlier merging of the streams. Further downstream, the peaks for the $\alpha = 20°$ configuration gradually diminish, reflecting a slow but progressive interaction between the streams. Meanwhile, the $\alpha = 30°$ case demonstrates an almost complete merging of the streams at an earlier stage, accompanied by an decrease in number concentration-implying greater agglomerate formation as the flow develops.

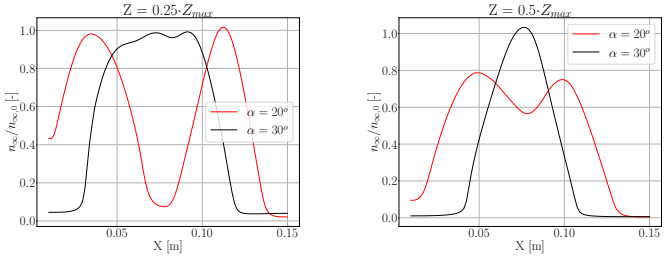

(a) **(b)**

(c) **(d)**

Figure 6. Number concentration plots at different axial locations.

Agglomerate size distribution

To analyze the agglomerate size distribution, the number concentration from PBE simulations is represented on a 2D histogram, where agglomerates are categorized based on their primary particles, N_P and composition, N_F. These histograms are generated at various axial locations along the flow direction to track evolutionary trends. To enhance clarity in tracking distribution changes, the number concentrations in each CFD cell are normalized relative to the corresponding cell values at Z = 0.05 Z_{max}.

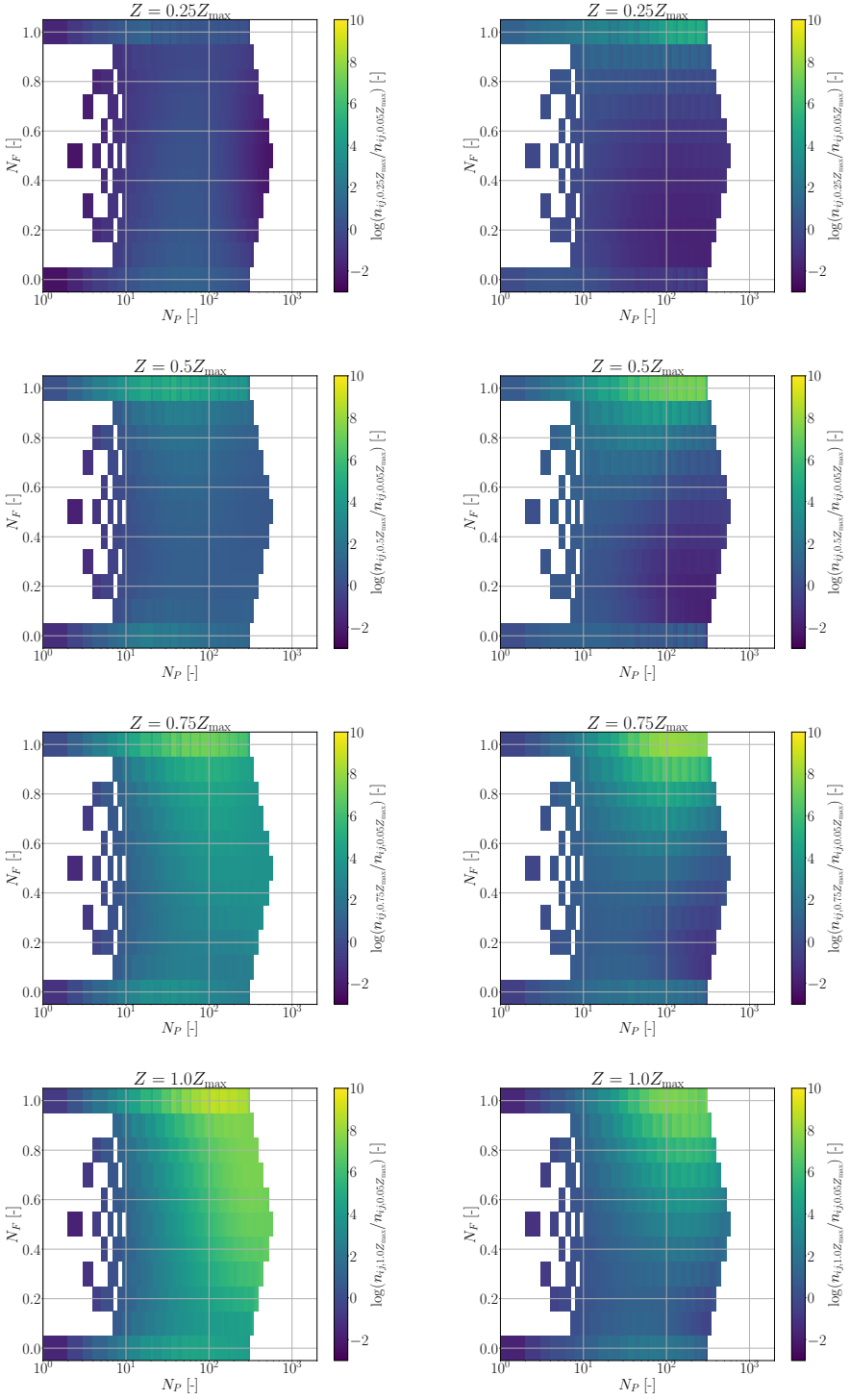

Figure 7. 2D histograms from PBE simulations for $\alpha = 20°$ (left) and 30° (right) configurations.

Rather than displaying data for all computational cells, the histograms consolidate results from four centerline cells, providing a focused view of the agglomeration dynamics. Areas with lighter shading correspond to increase in number concentration corresponding to base and darker areas represent decrease in number concentration.

At the lowest height, Z = 0.25 Z_{max}, the $\alpha = 20°$ configuration exhibits an increase in particle number concentration. This occurs because, compared to the $\alpha = 30°$ case, the interaction between the two particle streams takes place further downstream. In contrast, the $\alpha = 30°$ configuration shows a larger region with minimal agglomeration near the inlet. This difference arises because the steeper angle causes earlier stream interactions, leading to significant agglomeration at lower heights. Further downstream, both configurations display a lighter region where agglomerates with large N_P and $N_F \approx 0.4 - 0.5$ form, suggesting the agglomeration of smaller clusters into larger structures. However, the $\alpha = 20°$ case exhibits a more extensive lighter region, indicating slow but sustained agglomeration along the flow direction. In contrast, the $\alpha = 30°$ configuration shows fewer lighter zones, implying limited agglomeration events downstream.

To further analyze the agglomerate size distribution, Fig. (8) presents vertical slices of the histograms, illustrating the composition distribution conditioned on the number of primary particles. At Z = 0.25 Z_{max}, the configuration with $\alpha = 30°$ exhibits a relatively narrow distribution, whereas the $\alpha = 20°$ case displays a broader spread. This wider distribution suggests increased agglomeration between pure agglomerates of different components or those with extreme number fractions (either very low or very high). This trend persists further downstream, where the $\alpha = 20°$ configuration continues to show a more varied composition distribution. In contrast, the $\alpha = 30°$ case features a higher number of agglomerates with uniformly distributed particles by Z = 0.5 Z_{max}, beyond which the distribution remains largely constant. Meanwhile, the $\alpha = 20°$ configuration exhibits a slight downstream increase in agglomerate count meanwhile depleting the pure agglomerates composed of distinct components.

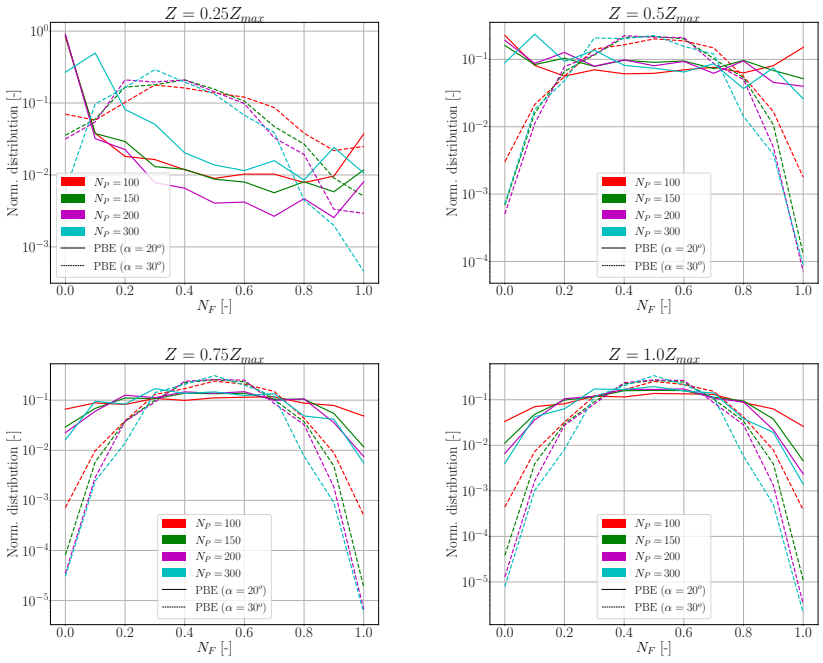

Figure 8. Agglomerate size distribution conditioned on number of particles at different axial locations.

Conclusions

We performed coupled CFD and population balance equation (PBE) simulations to analyze particle dynamics in a DFSP setup, comparing two nozzle configurations with angles of $\alpha = 20°$ and $30°$. The CFD simulations provided resolved flow-field data-including velocity, temperature, and turbulent diffusivity profiles-which served as inputs for the bi-variate PBE model. Initial conditions assumed a

particle number density of 10^{17} particles/m^3 at the mixing zone inlet, with agglomeration neglected upstream due to the absence of experimental agglomerate size distribution data.

The PBE results revealed distinct agglomeration behaviors between the two configurations. For $\alpha = 20^\circ$, hetero-agglomeration occurred over a broader but less intense region, yielding a higher total number of agglomerates with a wider compositional distribution. In contrast, the $\alpha = 30^\circ$ case exhibited a more localized and pronounced agglomeration zone, producing fewer agglomerates with a narrower compositional range. This suggests that the 30° configuration promotes more homogeneous mixing of primary particles, whereas the 20° configuration leads to a more varied but less uniform agglomerate composition. These findings highlight the significant influence of nozzle geometry on particle agglomeration dynamics and mixture homogeneity.

Acknowledgements

We acknowledge the financial support by DFG (project number 462463789 and grant number FR 912/47-1, both within the priority program SPP 2289 'HeteroAggregates'). Anjul Pandey would like to thank the state of Baden-Württemberg through bwHPC. Tobias Tabeling would like to thank the NHR@ZIB for computing time on the Lise cluster, with the account hbi00064.

References

[1] Zhu Y., Choi S. H., Fan X., Shin J., Ma Z., Zachariah M. R., Choi J. W., Wang C., Advanced Energy Materials 7 (7) (2017) 1601578.

[2] Strobel R., Mädler L., Piacentini M., Maciejewski M., Baiker A., Pratsinis S. E., Chemistry of Materials 18 (10) (2006) 2532–2537.

[3] Stahl J., Mahr C., Gerken B., Pokhrel S., Rosenauer A., Mädler L., Powder Technology 448 (2024) 120305.

[4] Pandey A., Karsch M., Kronenburg A., Proceedings of the Combustion Institute 40 (1-4) (2024) 105706.

[5] Pandey A., Kronenburg A., Journal of Aerosol Science 183 (2025) 106480.

[6] Crowe C., Sommerfeld M., Tsuji Y., et al., Ž1998.

[7] Menter F. R., AIAA journal 32 (8) (1994) 1598–1605.

[8] Adibi O., Farhanieh B., Afshin H., International Journal of Heat and Technology 35 (4) (2017) 959–968.

[9] Kmecova M., Sikula O., Krajcik M., in: IOP Conference Series: Materials Science and Engineering, Vol. 471, IOP Publishing, 2019, p. 062045.

[10] Neuber G., Kronenburg A., Stein O. T., Garcia C. E., Williams B. A., Beyrau F., Cleary M. J., Flow, Turbulence and Combustion 106 (4) (2021) 1167–1194.

[11] Friedlander S. K., et al., Vol. 198, Oxford university press New York, 2000.

[12] Karsch M., Kronenburg A., Journal of Aerosol Science 186 (2025) 106552.

[13] Gopalakrishnan R., Hogan Jr C. J., Aerosol Science and Technology 45 (12) (2011) 1499–1509.

[14] Nanjaiah M., Roderigo K., Janbazi H., Peukert S., Eigemann J., Kempf A., Wlokas I., Energy & Fuels 37 (23) (2023) 19188–19195.

[15] Neto P. B., Meierhofer F., Meier H. F., Fritsching U., Noriler D., Powder Technology 370 (2020) 116–128.

[16] Vale H. M., McKenna T. F., Industrial & engineering chemistry research 44 (20) (2005) 7885–7891.

Sensitivity analysis of a wall-bounded turbulent jet flow with adjoint-based data assimilated RANS models

X. Song[1*], K. Hildebrandt[1], S. Knechtel[1], A. Jaeschke[2], C.O. Paschereit[2], K. Oberleithner[1], and T.L. Kaiser[1]

*xiuyang.song@campus.tu-berlin.de

[1] *Laboratory for Flow Instabilities and Dynamics, Technische Universität Berlin, Müller-Breslau-Str. 8, 10623, Berlin, Germany*

[2] *Institute of Fluid Dynamics and Technical Acoustics, Technische Universität Berlin, Müller-Breslau-Str. 8, 10623, Berlin, Germany*

Abstract

The design of hydrogen-fuelled combustors demands models that are both accurate and suitable for optimization based on linear methods. While Large Eddy Simulation (LES) can provide high-fidelity flow information, the turbulence closure issues after linearization make it impractical for optimization purposes, whereas conventional Reynolds-Averaged Navier–Stokes (RANS) models often lack sufficient accuracy for such applications. Adjoint-based data assimilation (DA) has emerged as a promising strategy to improve the predictive capabilities of RANS models by incorporating high-fidelity data. However, most existing research has neglected the impact of DA on model linearity and sensitivity analysis. In this work, we assess three DA strategies: (i) DA of **frozen eddy viscosity**, where a spatially varying eddy viscosity field is optimized directly to represent the temporal-mean effects of turbulence; (ii) DA of the **model constant C_μ**, which is an empirical constant in the expression of eddy viscosity in k-ε model and globally tuned; (iii) DA of a **corrective eddy viscosity**, which retains the standard turbulence model but adds an optimized corrective viscosity term. These strategies are applied to RANS simulations of a wall-bounded turbulent jet flow, with LES serving as the reference. The strategies are evaluated not only by their ability to reconstruct mean flow fields but also by sensitivity analysis to variations in the inlet velocity profiles. Our results show that all three approaches improve the mean flow prediction, with the frozen eddy viscosity approach yielding the most significant improvement. However, in reproducing the sensitivity fields, the frozen-eddy-viscosity approach performs the worst — even worse than the baseline RANS — likely due to its limited model adaptability. These findings underscore the importance of evaluating DA strategies within a sensitivity analysis framework, especially for applications involving optimization and inverse design. Future efforts should aim to balance accuracy on both mean fields and sensitivities to enable robust, DA-enhanced turbulence modelling for hydrogen combustion applications.

1 Introduction

Hydrogen is widely recognized as a promising energy carrier in the pursuit of carbon-free combustion technologies [1]. However, its high chemical reactivity give rise to significant challenges for combustion system design. This is because hydrogen flames can become unstable in commonly used hydrocarbon-based combustor configurations [2]. For example, flashback and thermo-acoustic instabilities can be triggered when burning syngas with a high hydrogen ratio [3]. As a result, the development of hydrogen-fuelled combustors requires a fundamental redesign that accounts for its physical and chemical characteristics. To support this effort, adjoint-based sensitivity analysis can serve as a powerful and computationally efficient approach to evaluate the influence of design parameters on system performance. By providing gradient information with respect to a wide range of parameters, this method is particularly valuable in optimization, control, and uncertainty quantification tasks[4,5].

The effectiveness of adjoint-based sensitivity analysis relies on its governing models, which should be both accurate and linearizable. Large Eddy Simulation (LES), which captures complex turbulence dynamics and detailed flame structures, provides high-fidelity predictions but leads to significant turbulence closure issues after linearization [6],[7]. In contrast, Reynolds-Averaged Navier–Stokes

(RANS) models offer the required linearizability but often suffer from significant modelling errors in turbulent reacting flows. To combine the advantages of both approaches, data assimilation (DA) techniques have been increasingly adopted to improve RANS models by integrating information from LES or experimental data [8–10].

While previous studies in this area have demonstrated notable improvements in mean flow predictions, limited attention has been paid to linear analyses , which are essential for obtaining accurate sensitivity information in adjoint-based optimization and inverse design. The data-assimilated models can perform poorly when subjected to linear analyses due to their overfitting to nonlinear mean fields [10]. In such cases, the modified model may no longer exhibit consistent linear responses, thereby reducing the effectiveness of adjoint-based tools in the design process. Hence, it becomes crucial to evaluate DA strategies not solely based on their ability to recover accurate mean flows, but also on their compatibility with linear analysis and adjoint optimization frameworks [11].

In this study, three different data assimilation strategies are applied to RANS models used to simulate a wall-bounded turbulent jet flow. With LES computations conducted as the reference truth, the fidelity of each strategy in capturing both mean velocity fields and sensitivity fields is accessed. Our findings highlight the importance of incorporating linear analysis metrics into the evaluation of data assimilation methods, paving the way toward robust and reliable model corrective techniques for hydrogen combustor design.

The structure of the paper is summarized in the following. A brief description of the case setup including LES settings is presented in the first section. The theory of adjoint-based data assimilation of RANS models is introduced in the next section. Three data assimilation strategies are presented in the following. In the results section, both mean velocity fields and sensitivity fields are compared with each other, and the performances of the DA strategies are evaluated.

2 LES setup: wall-bounded turbulent jet flow

The CFD domain is constructed based on the experimental setup for a wall-bounded hydrogen jet burner as shown in Figure 1(a). Key sizes of the test rig are as follows: the diameter of injection tube is $D_{\mathrm{tube}} = 20$ mm, that of the combustion chamber $D_{\mathrm{comb}} = 105$ mm, while the length of the combustion chamber $L_{\mathrm{comb}} = 295$ mm. The combustor and a part of the injection tube are modelled in the simulation. The length of the modelled injection tube is $L_{\mathrm{tube}} = 60$ mm.

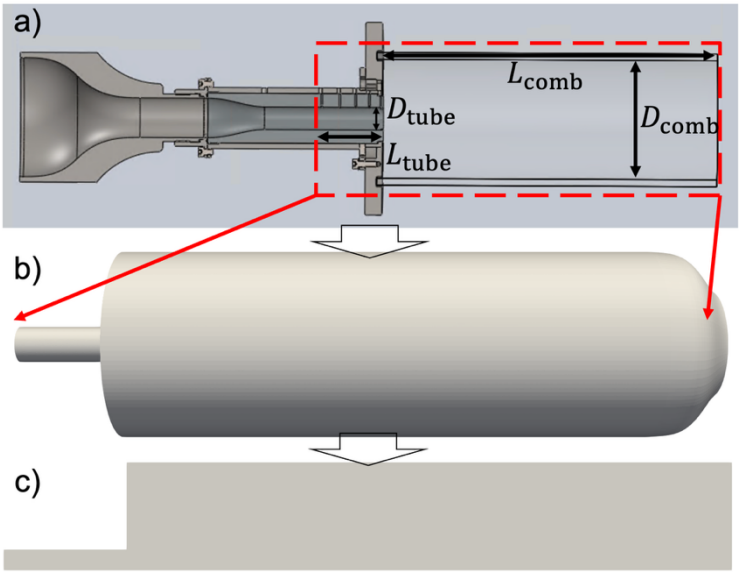

Figure 1. Sketches of the domain: a) experimental rig, b) 3-D domain, c) 2-D axisymmetric domain

Figure 1(b) shows the 3D CFD domain, in which a contraction section is added at the downstream end of the combustor to prevent backflow and enhance the robustness of the simulation. The 3D CFD domain shown in Figure 1(b) is used for LES simulations, while a 2-D axisymmetric domain is created for RANS simulation, as shown in Figure 1(c).

CFD computations and sensitivity analyses are conducted on a baseline case based on a cold-flow experiment. LES simulations are performed using the open-source CFD solver OpenFOAM [12]. The subgrid-scale (SGS) model employed is the Smagorinsky model. A second order accurate backward scheme is used for time stepping. Spatial discretization schemes for convective fluxes and diffusion terms are all based on the Gauss linear method, which is unbounded and has second-order accuracy.

An air flow at a bulk velocity of 6.2 m/s enters at the inlet, corresponding to a Reynolds number of Re=8572 based on the tube diameter. The mean velocity profile at the inlet surface is obtained from experimental measurement and fitted to the following expression:

$$u(r) = \dot{V}\left(\frac{n+2}{n}\frac{1}{\pi R^2}\right)\left(1-\left(\frac{r}{R}\right)^n\right). \quad (1)$$

Here, the volume flow rate $\dot{V} = 0.00196\ \mathrm{m}^3/\mathrm{s}$, the fitting exponent $n = 3.9$, the radius of the injection tube $R = 0.01$ m, and r is the radial coordinate. For simplification, the turbulence at the inlet is assumed to be homogenous, with a uniform turbulence intensity of 8.13% based on experimental measurements. The walls of the combustor and the injection tube are treated as no-slip, and the outlet is modeled as a fixed-pressure boundary.

The turbulentDigitalFilterInlet boundary condition [13] in OpenFOAM is used to generate turbulent-like inflow conditions, with input parameters based on the measured mean velocity profile and turbulence intensity. After simulation in the 3D domain, the results are averaged in time- and azimuthal direction and then interpolated onto the 2D axisymmetric domain, as shown in Figure 2.

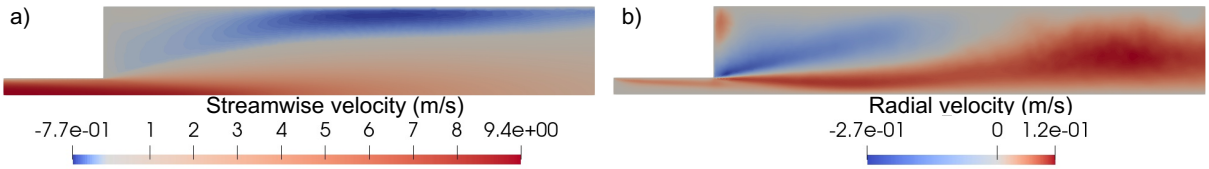

Figure 2. Time- and azimuthally averaged velocity fields of LES which are interpolated onto the 2D axisymmetric domain: a) Streamwise velocity, b) radial velocity.

3 Adjoint-based data assimilation of RANS models

One goal of the work is to calibrate the RANS models to a specific operating point with LES results as reference. An adjoint-based data assimilation framework is developed for RANS simulations to achieve this. The framework is implemented within the finite element library FEniCSx [14]. The incompressible RANS equations with the standard $k-\varepsilon$ model[15] are implemented as follows:

$$\nabla \cdot \boldsymbol{u} = 0. \quad (2)$$

$$(\boldsymbol{u}\cdot\nabla)\boldsymbol{u} + \frac{1}{\rho}\nabla p - \nabla\cdot\nu_{Eff}[\nabla\boldsymbol{u} + (\nabla\boldsymbol{u})^T] + \frac{2}{3}\nabla k = 0. \quad (3)$$

$$\boldsymbol{u}\cdot\nabla k - \nabla\cdot(\nu_k\nabla k) - P_k + \varepsilon = 0. \quad (4)$$

$$\boldsymbol{u}\cdot\nabla\varepsilon - \nabla\cdot(\nu_\varepsilon\nabla\varepsilon) - C_{1\varepsilon}\frac{\varepsilon}{k}P_k + C_{2\varepsilon}\frac{\varepsilon^2}{k} = 0. \quad (5)$$

Here, $\boldsymbol{u}, p, k, \varepsilon$ are mean values of the velocity vector, pressure, turbulent kinetic energy and its dissipation rate, respectively. The effective viscosity is $\nu_{Eff} = \nu + \nu_t$, where the eddy viscosity is calculated as:

$$\nu_t = C_\mu\frac{k^2}{\varepsilon}. \quad (6)$$

In Eq. (3), $\nu_k = \nu + \frac{\nu_t}{\sigma_k}$, and $P_k = \nu_t[\nabla\boldsymbol{u} + (\nabla\boldsymbol{u})^T]:(\nabla\boldsymbol{u})$; in Eq. (4), $\nu_\varepsilon = \nu + \frac{\nu_t}{\sigma_\varepsilon}$. The constants are: $C_\mu = 0.09, \sigma_k = 1.00, \sigma_\varepsilon = 1.30, C_{1\varepsilon} = 1.44, C_{2\varepsilon} = 1.92$.

The adjoint-based data assimilation is applied to optimize the RANS models, with the goal to reproduce the temporal mean velocity fields obtained by LES at the given operation point. Here, the adjoint method will provide the gradient of the cost function, i.e. the agreement between RANS and LES results, with respect to parameters inside the RANS models. The general procedure is discussed in the following.

The flow equations (2–5) are written compactly as:

$$\mathcal{N}(\boldsymbol{q}, \boldsymbol{\Pi}) = 0. \quad (7)$$

where $\boldsymbol{q} = [\boldsymbol{u}, p, k, \varepsilon]$ are the state quantities of the flow, $\boldsymbol{\Pi}$ is the set of tuneable parameters, e.g. eddy viscosity. The cost function to be minimized is defined as:

$$\mathcal{J} = \int_\Omega j(\boldsymbol{q}, \boldsymbol{\Pi}) d\Omega. \tag{8}$$

Where $j(\boldsymbol{q}, \boldsymbol{\Pi})$ can be any integrable expression, Ω is the integration domain. The cost function in the present work is defined as the domain-integrated squared difference between the RANS velocity field and time-averaged LES velocity:

$$\mathcal{J} = \int_\Omega |\overline{\boldsymbol{u}_{\mathrm{LES}}} - \boldsymbol{u}_{\mathrm{RANS}}|^2 \, d\Omega. \tag{9}$$

The gradient of $\mathcal{J}$ with respect to $\boldsymbol{\Pi}$, $\frac{d\mathcal{J}}{d\boldsymbol{\Pi}}$ can be written as:

$$\frac{d\mathcal{J}}{d\boldsymbol{\Pi}} = \int_\Omega \left(\frac{\partial j}{\partial \boldsymbol{q}} \frac{d\boldsymbol{q}}{d\boldsymbol{\Pi}} + \frac{\partial j}{\partial \boldsymbol{\Pi}} \right) d\Omega \, . \tag{10}$$

To avoid the numerically expensive computation of the sensitivity $\frac{d\boldsymbol{q}}{d\boldsymbol{\Pi}}$ by exploring the entire parameter space, a similar derivation of the governing equation $\mathcal{N}$ can be done:

$$\frac{d\mathcal{N}}{d\boldsymbol{\Pi}} = \frac{\partial \mathcal{N}}{\partial \boldsymbol{q}} \frac{d\boldsymbol{q}}{d\boldsymbol{\Pi}} + \frac{\partial \mathcal{N}}{\partial \boldsymbol{\Pi}} = 0. \tag{11}$$

The sensitivity can be obtained by:

$$\frac{d\boldsymbol{q}}{d\boldsymbol{\Pi}} = -\left(\frac{\partial \mathcal{N}}{\partial \boldsymbol{q}} \right)^{-1} \frac{\partial \mathcal{N}}{\partial \boldsymbol{\Pi}}. \tag{12}$$

Then the gradient can be expressed as:

$$\frac{d\mathcal{J}}{d\boldsymbol{\Pi}} = \int_\Omega \left(-\frac{\partial j}{\partial \boldsymbol{q}} \left(\frac{\partial \mathcal{N}}{\partial \boldsymbol{q}} \right)^{-1} \frac{\partial \mathcal{N}}{\partial \boldsymbol{\Pi}} + \frac{\partial j}{\partial \boldsymbol{\Pi}} \right) d\Omega. \tag{13}$$

To avoid the inverse term $\left(\frac{\partial \mathcal{N}}{\partial \boldsymbol{q}} \right)^{-1}$, a vector $\boldsymbol{q}^\dagger$is introduced to replace $\frac{\partial j}{\partial \boldsymbol{q}} \left(\frac{\partial \mathcal{N}}{\partial \boldsymbol{q}} \right)^{-1}$. A new equation describing the relationship is introduced as well:

$$\left(\frac{\partial \mathcal{N}}{\partial \boldsymbol{q}} \right)^H \boldsymbol{q}^\dagger = \left(\frac{\partial j}{\partial \boldsymbol{q}} \right)^H. \tag{14}$$

This formulation is called "adjoint equation". The superscript *H* represents the Hermitian transpose. The gradient is finally assembled as:

$$\frac{d\mathcal{J}}{d\boldsymbol{\Pi}} = \int_\Omega \left(-q^\dagger \frac{\partial \mathcal{N}}{\partial \Pi} + \frac{\partial j}{\partial \Pi} \right) d\Omega. \tag{15}$$

The optimization loop for $\boldsymbol{\Pi}$ based on the gradient $\left(\frac{d\mathcal{J}}{d\boldsymbol{\Pi}} \right)$ is as follows:

1. Solve the RANS equations (2-5) to get $\boldsymbol{q}$ for a given $\boldsymbol{\Pi}$;
2. Solve the adjoint equation (3) to obtain $\boldsymbol{q}^\dagger$. Partial derivatives are automatically and symbolically computed through the Unified Form Language [16], e.g. for the Jacobian of the RANS equations $\frac{\partial \mathcal{N}}{\partial \boldsymbol{q}}$ and cost functional $\frac{\partial j}{\partial \boldsymbol{q}}$.
3. Assemble the gradient $\frac{d\mathcal{J}}{d\boldsymbol{\Pi}}$ with equation (15).
4. Based on the gradient, a L-BFGS-B optimizer [17,18] is applied to evaluate the change in $\boldsymbol{\Pi}$. Then, if the termination criterion is not met, the loop is continued starting with step 1.

4 Parameter optimization strategies

Three different DA strategies are compared and discussed in the present study:

1. DA ν_t: Optimization of the frozen eddy viscosity
   Only Equations (2) and (3) are solved, with ν_t initialized with k and ε. It is then treated as the parameter to optimize. A penalization term is added to smooth the result:
   $$\mathcal{J}_{\mathrm{Penaty}} = \int_\Omega \alpha |\nabla \nu_t|^2 d\Omega. \tag{16}$$
2. DA C_μ: Optimization of the constant C_μ
   Equations (2–5) are solved, and the constant C_μ in equation (6) is directly optimized from an initial value of 0.09. No penalty term is used in this strategy.
3. DA ν_{corr}: Optimization of corrective eddy viscosity
   Equations (2–5) are solved. An additional corrective term ν_{corr} is added in the definition of ν_{Eff} in equation (3), which becomes $\nu_{\mathrm{Eff}} = \nu + \nu_t + \nu_{\mathrm{corr}}$. The initial value of ν_{corr} is zero everywhere. A penalization term similar to (16) is applied by replacing ν_t to ν_{corr}.

5 Results

5.1 Mean velocity fields

To evaluate the different DA strategies, the most direct approach is to compare the mean velocity fields with LES reference data. This comparison is also reflected in the cost function, as the goal is to minimize the discrepancy between LES and RANS velocity fields. Figure 3 presents contour plots of the LES and baseline (non-DA) RANS velocity fields, overlaid with streamlines. Three key differences can be observed: (1) the size and location of the primary recirculation bubble, (2) the presence of a secondary (small) recirculation bubble, and (3) the radial velocity near the inlet.

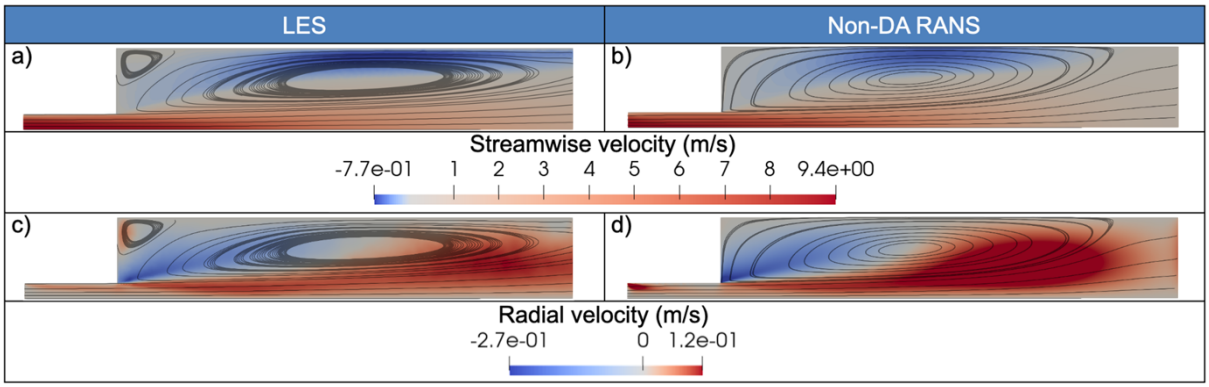

Figure 3. Contours of velocity fields, overlaid with streamlines: a) Streamline velocity of LES, b) streamline velocity of non-DA RANS, c) radial velocity of LES, d) radial velocity of non-DA RANS.

Figure 4 shows the velocity fields for RANS simulations with various DA strategies applied. The most notable improvement is seen in the DA ν_t case. Here, the primary recirculation bubble is significantly larger than in the RANS baseline and in better agreement with the LES results. Additionally, the magnitude of the radial velocity is reduced compared to the non-DA case, both downstream of the inlet and downstream of the cross-section jump. Although this strategy still fails to capture the small upstream recirculation bubble, it outperforms the other DA strategies, which show improvement only in the size and location of the primary recirculation bubble. Figure 5 presents line plots of streamwise velocities for all cases and demonstrates that the frozen eddy viscosity DA results align best with the LES profile.

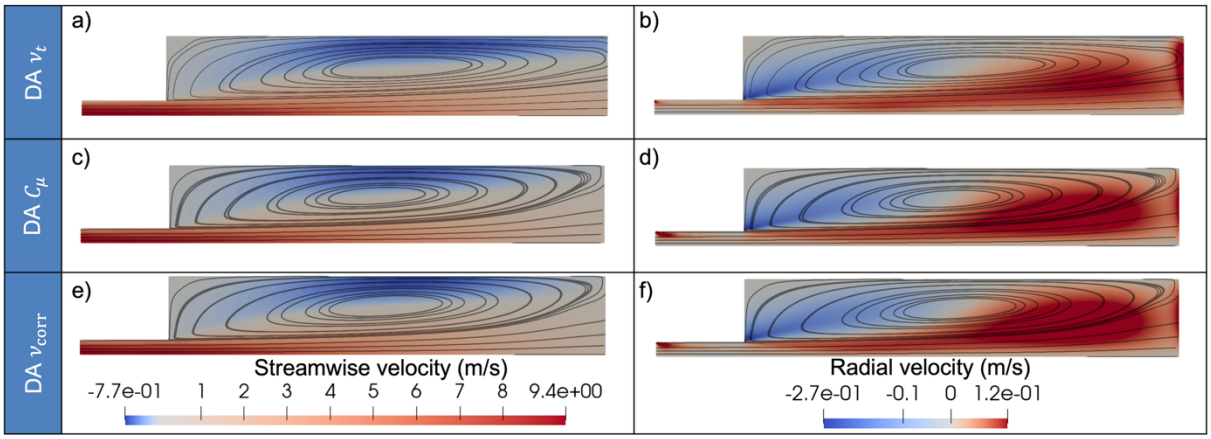

Figure 4. Contours of velocity fields, overlaid with streamlines. a) Streamline velocity of DA ν_t case, b) radial velocity of DA ν_t case, c) Streamline velocity of DA C_μ case, d) radial velocity of DA C_μ case, e) Streamline velocity of DA ν_{corr} case, d) radial velocity of DA ν_{corr} case.

Table 1. Change of cost functions of different DA strategies.

DA method	Initial value	Optimized value	Ratio of decrease
DA ν_t	4.4×10^{-5}	3.7×10^{-6}	91.6%
DA C_μ	4.4×10^{-5}	2.6×10^{-5}	39.8%
DA ν_{corr}	4.4×10^{-5}	2.9×10^{-5}	33.8%

To quantify the effectiveness of each DA strategy, the reduction in cost function is displayed in Table 1. The cost function for the DA ν_t case is reduced by more than an order of magnitude, while the other methods achieve approximately 39.8 % (DA C_μ) and 33.8 % (DA ν_{corr}). The significant improvement of the frozen eddy viscosity approach is likely due to two factors: (1) the reduced number of equations solved in the frozen eddy viscosity case, which makes the solver more robust, and (2) the greater flexibility of modifying the eddy viscosity field without being constrained by the specific form of the turbulence model.

5.2 Sensitivity analysis

Here, we determine the capability of (DA-improved) RANS set-ups to predict the sensitivity of the kinetic energy of the temporal mean state with respect to the exponent n in the inlet velocity profile (Eq. 1). That is, we evaluate ∂J/∂n, where n controls the radial shape of the inflow velocity, and J is the kinetic energy. The sensitivity obtained using finite-difference calculations based on LES results is regarded as the reference for comparison.

Before evaluating the DA results regarding its impact on the sensitivity, it is instructive to first compare the baseline LES and RANS sensitivity fields. As shown in Figure 5, the non-DA RANS results qualitatively capture the shape of the LES sensitivity patterns, however, they differ in magnitude. Within the pipe, the sensitivity is positive near the wall and negative along the axis. In the combustor section, a strong region of positive sensitivity appears. This behavior can be explained by the fact that an increase in n results in a thinner shear layer within the pipe, which enhances the velocity gradient near the wall and reduces the centerline velocity. Downstream of the sudden expansion, where the free shear layer begins to develop, a thinner shear layer promotes a longer potential core, thereby increasing the kinetic energy in that region. The RANS model, however, predicts a shorter sensitivity pattern in the pipe and significantly higher sensitivity downstream, likely due to its tendency to overpredict near-wall shear stress, which results in an even thinner shear layer both inside the pipe and at the nozzle exit.

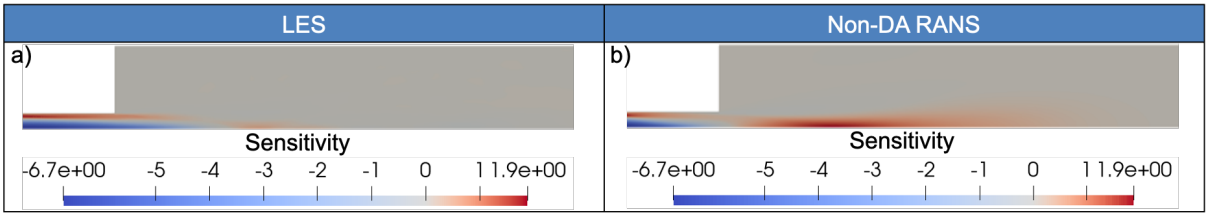

Figure 5. Contours of sensitivity fields of kinetic energy of a) LES case, b) non-DA RANS case.

The performance of DA strategies in sensitivity analysis differs significantly from their performance in reproducing mean velocity fields. As shown in Figure 6, DA ν_{corr} or DA C_μ shows little difference between the baseline RANS. However, the DA ν_t case performs better in the pipe region but fails at downstream region, where it does not capture the expected positive sensitivity region. This is confirmed by the line plots in Figure 7, which highlights the same trends observed in the contours. Such an opposite sensitivity implies that the optimizer would adjust the parameter in the wrong direction, leading to a failure of the optimization.

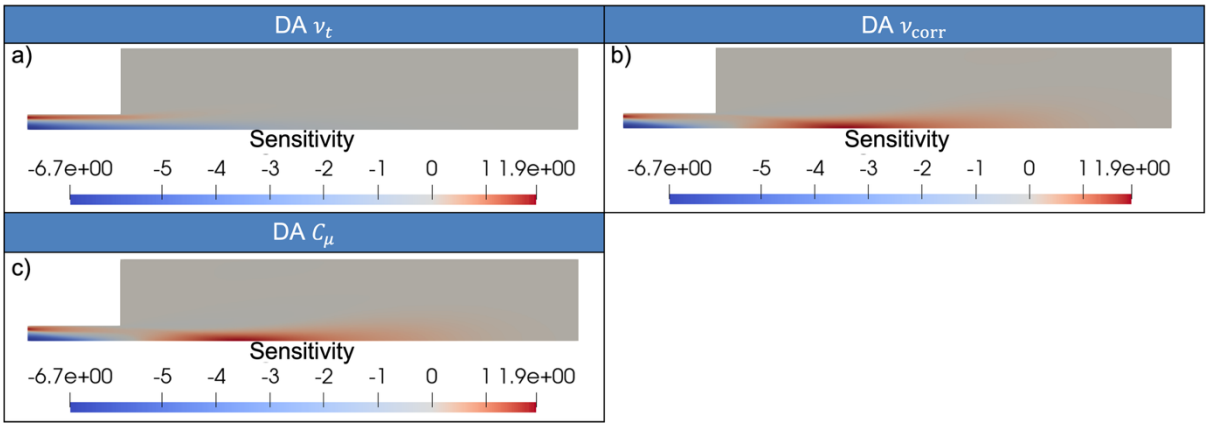

Figure 6. Contours of sensitivity fields of kinetic energy of a) DA ν_t, b) DA ν_{corr}, c) DA C_μ case.

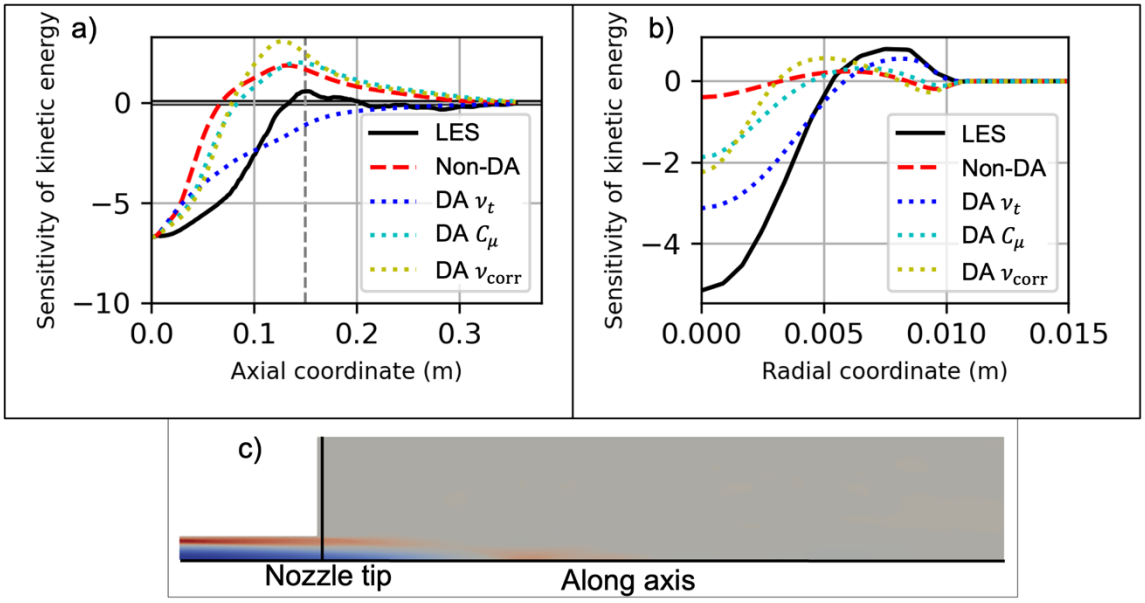

Figure 7. Line plots of the sensitivity of kinetic energy vs. a) axial coordinates along axis b) radial coordinates at nozzle tip. The positions of line plots are marked in c).

Further insights are provided by examining the sensitivity of eddy dissipation E, defined as:

$$\mathrm{E} = \nu_t(\nabla \boldsymbol{u} + (\nabla \boldsymbol{u})^T) : (\nabla \boldsymbol{u} + (\nabla \boldsymbol{u})^T). \tag{17}$$

Its sensitivity $\frac{d\mathrm{E}}{dn}$ for both the non-DA and DA ν_t cases is shown in Figure 8. The two cases exhibit distinct behaviors. In the pipe region, the frozen eddy viscosity case shows a consistently positive sensitivity near the wall, whereas in the non-DA RANS case, it quickly turns negative after a short distance downstream. This suggests that the frozen eddy viscosity approach mitigates the problem of overestimating shear stress in the near-wall region of $k-\varepsilon$ model, thereby improving performance in the pipe. However, this strategy doesn't capture the positive sensitivity further downstream like the baseline case. One possible explanation is that by freezing the eddy viscosity field, the model loses flexibility in adapting to changes in the inlet velocity profile. As a result, it cannot correctly reflect the shifting turbulence structures caused by velocity field variations, leading to the failure in sensitivity prediction in the downstream region.

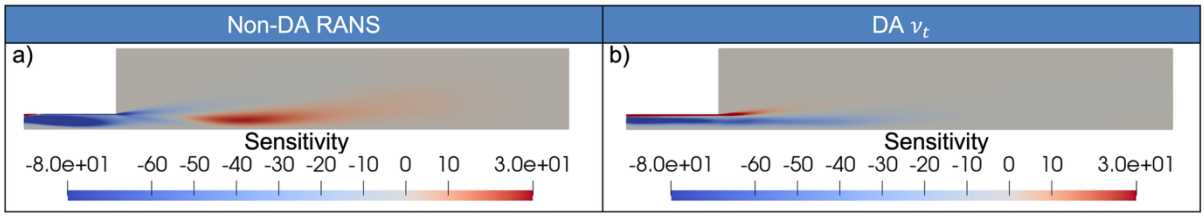

Figure 8. Contours of sensitivity fields of eddy dissipation of a) non-DA RANS, b) DA ν_t case.

6 Conclusion

In this study, RANS models with three different data assimilation strategies: optimization of frozen eddy viscosity ν_t, global constant C_μ in $k-\varepsilon$ model, and a corrective eddy viscosity ν_{corr}, are investigated in a wall-bounded jet flow configuration. Their performance is evaluated by comparing with LES results, focusing on both the accuracy of the reconstructed mean flow fields and the effectiveness in sensitivity analysis. While the frozen eddy viscosity method achieved the most significant improvement in capturing mean velocity profiles, particularly in recovering the size and location of the primary recirculation zone, it failed to reproduce accurate sensitivity fields in the flow region downstream of the cross-section jump. This limitation is attributed to the fixed eddy viscosity field and lack of turbulence-transport models. Consequently, this model cannot adapt to changes in the velocity field and thus fails to represent the evolving turbulence structures necessary for accurate sensitivity prediction.

These results underscore the need for a more comprehensive evaluation framework when applying data assimilation, especially in applications that depend on adjoint-based sensitivity information, such as inverse design and optimization. Looking forward, alternative DA strategies such as modifying source terms or additional turbulence model coefficients should be explored. However, it is essential to ensure that the turbulence modeling framework remains consistent and physically motivated. As demonstrated by the frozen eddy viscosity case, ignoring the dynamic nature of turbulence can hinder the model's ability to capture both mean flow behaviour and sensitivity responses.

Acknowledgment

This work is funded by the Deutsche Forschungsgemeinschaft (DFG, German Research Foundation) – 523881008.

Reference

[1] Sazali N.: *Emerging technologies by hydrogen: A review,* Int J Hydrog Energy, 45, 18753–71, 2020.

[2] de Vries H., Levinsky HB.: *Flashback, burning velocities and hydrogen admixture: Domestic appliance approval, gas regulation and appliance development,* Appl Energy 259, 114116, 2020.

[3] García-Armingol T., Ballester J.: *Operational issues in premixed combustion of hydrogen-enriched and syngas fuels,* Int J Hydrog Energy, 40, 1229–43, 2015.

[4] Chieregatti B.G., Brasil Lima J.S., Hayashi M.T., Volpe E.V.: *Optimization loop based on adjoint sensitivity analysis for flows through porous media with adsorption,* Int J Numer Methods Eng, 123, 729–54, 2022.

[5] Braman K., Oliver T.A., Raman V.: *Adjoint-based sensitivity analysis of flames,* Combust Theory Model, 19, 29–56, 2015.

[6] Kaiser T.L., Varillon G., Polifke W., Zhang F., Zirwes T., Bockhorn H., et al: *Modelling the response of a turbulent jet flame to acoustic forcing in a linearized framework using an active flame approach,* Combust Flame, 253, 112778 2023.

[7] Arias-Ramírez W., Oberoi N., Larsson J.: *Multifidelity Approach to Sensitivity Estimation in Large-Eddy Simulation,* AIAA J, 61, 3485–95, 2023.

[8] Brenner O., Piroozmand P., Jenny P.: *Efficient assimilation of sparse data into RANS-based turbulent flow simulations using a discrete adjoint method,* J Comput Phys, 471, 111667, 2022.

[9] Mons V., Marquet O.: *Linear and nonlinear sensor placement strategies for mean-flow reconstruction via data assimilation,* J Fluid Mech, 923, A1, 2021.

[10] Wu J., Xiao H., Sun R., Wang Q.: *Reynolds-averaged Navier–Stokes equations with explicit data-driven Reynolds stress closure can be ill-conditioned,* J Fluid Mech, 869, 553–86, 2019.
[11] Mons V., Vervynck A., Marquet O.: *Data assimilation and linear analysis with turbulence modelling: application to airfoil stall flows with PIV measurements,* Theor Comput Fluid Dyn, 38, 403-29, 2024.
[12] Weller H.G., Tabor G., Jasak H., Fureby C.: *A tensorial approach to computational continuum mechanics using object-oriented techniques,* Comput Phys, 12, 620-31, 1998.
[13] Klein M., Sadiki A., Janicka J.: *A digital filter based generation of inflow data for spatially developing direct numerical or large eddy simulations.* J Comput Phys, 186, 652–65, 2003.
[14] Baratta I.A., Dean J.P., Dokken J.S., Habera M., Hale J.S., Richardson C.N., et al: *DOLFINx: The next generation FEniCS problem solving environment*, 2023.
[15] Launder B.E., Spalding D.B.: *The numerical computation of turbulent flows*, Comput Methods Appl Mech Eng, 3, 269-89, 1974.
[16] Alnæs M.S., Logg A., Ølgaard K.B., Rognes M.E., Wells G.N.: *Unified form language: A domain-specific language for weak formulations of partial differential equations,* ACM Trans Math Softw, 40, 2014.
[17] Morales J.L., Nocedal J.: *Remark on "algorithm 778: L-BFGS-B: Fortran subroutines for large-scale bound constrained optimization."*, ACM Trans Math Softw, 38, 2011.
[18] Byrd R.H., Lu P., Nocedal J., Zhu C.: *A Limited Memory Algorithm for Bound Constrained Optimization,* SIAM J Sci Comput, 16,1190–208, 1995.

Visualisierung von OH* an ausgewählten Industriebrennern mit einem wassergekühltem UV-Endoskop

K. Mannel[1*], S. Bialek[2] und B. Stranzinger[2]

*kmannel@lavision.de

[1] *LaVision GmbH, Anna-Vandenhoeck-Ring 19, 37081 Goettingen, Deutschland*

[2] *VDEh-Betriebsforschungsinstitut GmbH, Sohnstraße 69, 40237 Düsseldorf, Deutschland*

Kurzfassung

Die optische Vermessung von Flammen ist ein wichtiges Werkzeug, um die Veränderung der Flammen-Geometrie aufgrund geänderter Brenngas-Zusammensetzung zu charakterisieren. Die im Rahmen der Dekarbonisierung zunehmende Beimischung von z.B. Wasserstoff (oder Derivaten wie Ammoniak) führt aufgrund der unterschiedlichen Eigenschaften und Kinetik zu einem geänderten Flammenbild gegenüber einer reinen Erdgas-Flamme. Gerade wasserstoffreiche Flammen sind aber in der heißen Ofenumgebung optisch nur schwer zu erkennen. Daher wird hierfür häufig die Chemilumineszenz des OH^* Radikals genutzt (308 nm Emissionswellenlänge). Gewöhnliche bildgebende Systeme sind für diese UV-Wellenlänge nicht empfindlich, daher wird hier auf bildverstärkte Kameras zurückgegriffen. Zusätzlich muss aber auch die gesamte, der Kamera vorgeschaltete Optik für diese UV-Wellenlänge transparent sein. Bei industriellen Öfen mit mehreren MW Anschlussleistung sind die optischen Zugänge aber in der Regel nicht trivial: Öffnungen im Brenner, z.B. für die Flammenüberwachung, sind ungeeignet, um einen ungehinderten optischen Zugang zur Brennerflamme zu gewähren.

In den vorliegenden drei Anwendungsfällen wurde daher erstmalig ein wassergekühltes, UV-geeignetes Endoskop mit ca. 40° Bildwinkel eingesetzt, um auch bei schwierigen Brenner-Geometrien ein verlässliches Bild der Brennerflamme zu erhalten. Zur Visualisierung ist dem Endoskop ein bildverstärkendes Kamerasystem nachgeschaltet. Dessen hohe zeitliche Auflösung in Kombination mit extrem kurzen Belichtungszeiten ermöglicht es, Fluktuationen der Flamme zu erfassen und statistisch auszuwerten. Die Wasserkühlung und Spülung der Endoskop-Spitze mit Druckluft machen das Endoskop einsetzbar bis 2000°C

Am Technikum der VDEh-Betriebsforschungsinstitut GmbH wurde in drei Projekten der Einfluss von Wasserstoffbeimischung bis zu 100 % an bestehenden Erdgasbrennern untersucht. Ein 50 kW Brenner für den Einsatz an einem Tunnelofen, ein 80 kW Brenner für den Einsatz an einer Haubenglühe und ein 350 kW Flachflammenbrenner für den Einsatz an einem Wiedererwärmungsofen. In Kombination mit traversierenden Heißgasmessungen und CFD-Simulationen konnte die Eignung der Brenner und die Auswirkungen auf den Prozess beim Wechsel von Erdgas zu Wasserstoff detailliert untersucht werden. Das Kamerasystem sowie ausgewählte Ergebnisse der Forschungsprojekte werden vorgestellt.

Einleitung

Im Rahmen der Defossilisierung werden aktuell verschiedene Technologien untersucht, um die energiebedingten CO_2-Emissionen an z.B. erdgasbetriebene Thermoprozessanlagen zu vermeiden. Die nationale Wasserstoffstrategie vom 10. Juni 2020 identifizierte Wasserstoff als potenziellen Energieträger zur Substitution von Erdgas. Wasserstoff ermöglicht eine erhebliche Senkung der CO_2-Emissionen und kann z.T. mit vorhandener Infrastruktur und Anlagen eingesetzt werden. Trotz ähnlichem Wobbe-Index weisen Erdgas und Wasserstoff jedoch z.T. erhebliche Unterschiede in den verbrennungstechnischen Eigenschaften auf (s. Tabelle 1). Der Wechsel des Brennstoffs von Erdgas zu Wasserstoff führt zu einer Erhöhung der adiabaten Flammentemperatur um etwa 200 K (s. Abbildung 1). Zudem steigt die Austrittsgeschwindigkeit der Verbrennungsgase auf etwa das Dreieinhalbfache, während die laminare Flammengeschwindigkeit um den Faktor acht zunimmt. Die abweichende

Geschwindigkeitsverteilung, die Flammentemperatur und die laminare Flammengeschwindigkeit lassen vermuten, dass die Flammenform und ggf. die Stabilität der Flamme beim Brenngaswechsel beeinflusst werden. Durch die deutlich weiteren Explosionsgrenzen des Wasserstoffs können zudem Zündung und Verlöschen der Flamme beeinflusst werden. Die Ausbildung der Flamme hat einen erheblichen Einfluss auf den Prozess und auf die Sicherheit der Anwendung. Durch mutmaßlich kürzere und heißere Flammen wird die thermische Belastung am Brennerkopf und der Ausmauerung bzw. dem Brennerstein deutlich erhöht. Zudem können Hotspots auf dem Produkt auftreten, die zu einer deutlich verminderten Produktqualität führen.

Tabelle 1. Verbrennungstechnische Eigenschaften im Vergleich.

Brenngaseigenschaften	**H_2**	**CH_4**	**Erdgas H**	**NH_3**
Heizwert in MJ/m³	10,78	35,84	37,21	14,05
Wobbe-Index in MJ/m³	40,89	48,18	47,83	18,6
Mindestluftbedarf m^3_{BL}/m^3_{BG}	2,38	9,52	9,85	3,58
Zündtemperatur in° C	530	645	640	650
untere Explosionsgrenze in Vol.-%	4	4,4	4,3	15
obere Explosionsgrenze in Vol.-%	77	16,5	16,3	34
laminare Flammengeschwindigkeit in cm/s	346	43	43	7

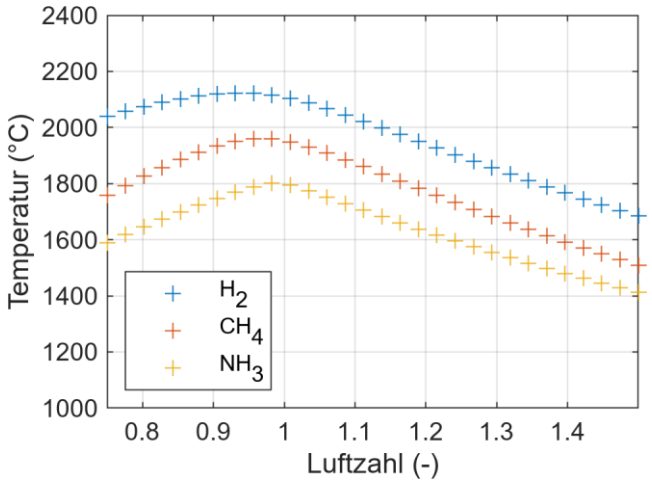

Abbildung 1. Adiabate Flammentemperatur von CH_4, H_2 und NH_3 aufgetragen über die Luftzahl

UV-Kamerasystem mit wassergekühlter Optik

Das von der Firma LaVision für diese Anwendung konzipierte und gelieferte System trägt den besonderen Anforderungen speziell in thermischer Hinsicht Rechnung. Es handelt sich dabei um ein modulares System, bestehend aus einer CMOS-Kamera (Imager M-lite 2M-160), einem modularen Bildverstärker (IRO-X P43, S20, 2:1) und ein wassergekühltes UV-Endoskop mit 1200 mm Länge und 38 mm Durchmesser. Dieses bildgebende System ist an einen Messrechner mit Aufnahme- und Auswerte-Software und Trigger-Elektronik (PTU-X) angeschlossen.

Vergleichbare Systeme sind in der Verbrennungs-Forschung relativ häufig anzutreffen und werden seit vielen Jahren in Laboren zur Visualisierung von OH* eingesetzt. Das wassergekühlte Endoskop ermöglicht jedoch erst den Einsatz an Brennern in industriellem Maßstab.

Um der hohen thermischen Belastung gerade an der Spitze des Endoskops gerecht zu werden, wird das Endoskop mit einem Kühlwasser-Durchfluss von ca. 15 l/min betrieben. Zusätzlich sorgt eine Luft-Düse

am vorderen Ende dafür, dass die vorderste Linse möglichst frei von Verbrennungs-Rückständen bleibt und zusätzlich von Wärmeeinwirkung geschützt wird. Hier soll eine Luft- bzw. Stickstoff-Flussrate von 10 bis 20 m^3/Stunde eingestellt werden. Um das System vor einer möglichen thermischen Überlastung - beispielsweise durch den Ausfall des Kühlwassers - zu schützen, ist eine akustische Warneinrichtung in die Versorgungs-Einheit (Abbildung 2) des Endoskops integriert. Hierbei wird sowohl die Menge als auch die Temperatur des Kühlwasser-Rücklaufs überwacht. Mit diesen Vorsorge-Maßnahmen soll das Endoskop einer Spitzentemperatur von bis zu 2000 °C standhalten. In den hier dokumentierten Versuchen lag die Temperatur nur bei ca. 1200°C, es waren im Langzeitbetrieb keine Auffälligkeiten am Endoskop zu beobachten.

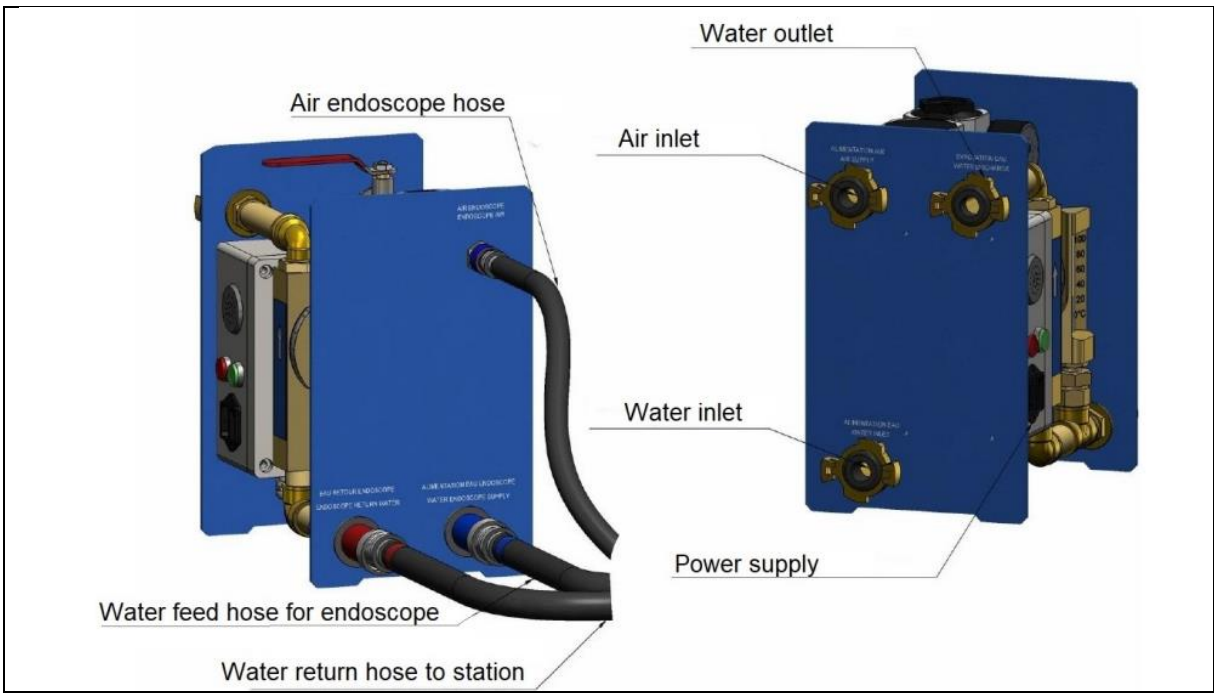

Abbildung 2. Wasser- und Druckluft-Versorgungs-Einheit

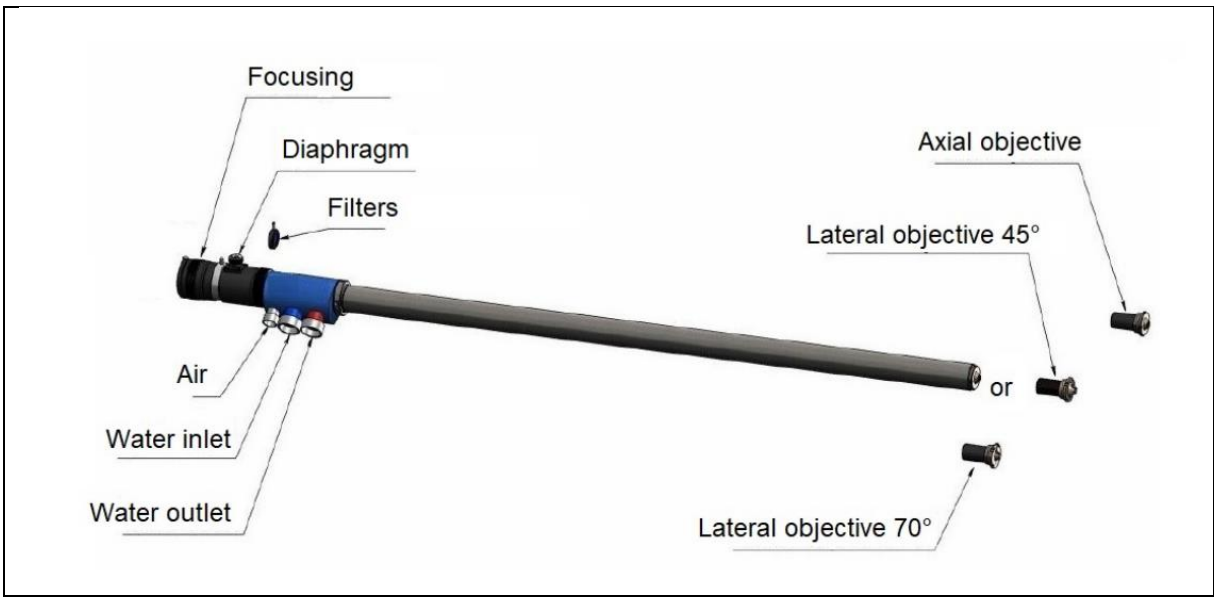

Abbildung 3. Hochtemperatur-Endoskop

Rückwärtig wird das Endoskop an eine UV-sensitive Kamera oder einen modularen Bildverstärker mit nachgeschalteter VIS-Kamera angeschlossen. Durch das Gewicht des Endoskops von ca. 7 kg musste eine spezielle Halterung vorgesehen werden. Im Gegensatz zu anderen Endoskopen benötigt dieses UV-Endoskop kein reguläres Kamera-Objektiv, um das Bild auf den Sensor zu fokussieren. Dies bedeutet auch, dass keine regulären OH* Filter (üblicherweise mit M52 Gewinde für Objektive) eingesetzt werden können. Im hinteren Teil des Endoskops befindet sich daher eine eigene Filter-Halterung. Die „Trennstelle“ des Endoskops von der Kamera ist dabei so, dass auch bei abmontiertem Endoskop der OH* Filter immer an der Kamera belassen werden kann. Dies stellt einen gewissen Sicherheits-Aspekt gegen ungewollte Überbelichtung des Bildverstärkers dar. Durch starke Licht-Einstrahlung auf die ungeschützte Photokathode kann ansonsten der Bildverstärker auch im ausgeschalteten bzw. nicht-getriggerten Zustand beschädigt werden.
Um die OH* Emission im ultravioletten Spektralbereich (ca. 308 nm) sichtbar zu machen, wird ein 1-stufiger modularer Bildverstärker eingesetzt. Dieser wandelt die einfallenden UV-Photonen zunächst in Elektronen um. Diese werden in einer Multi-Channel-Plate (MCP) elektronisch durch Mehrfach-Kollision mit den geladenen Wänden der Kanäle verstärkt (Abbildung 4 links), bevor sie auf einen Phosphorschirm treffen und dort wieder in sichtbares (grünes) Licht umgewandelt werden.

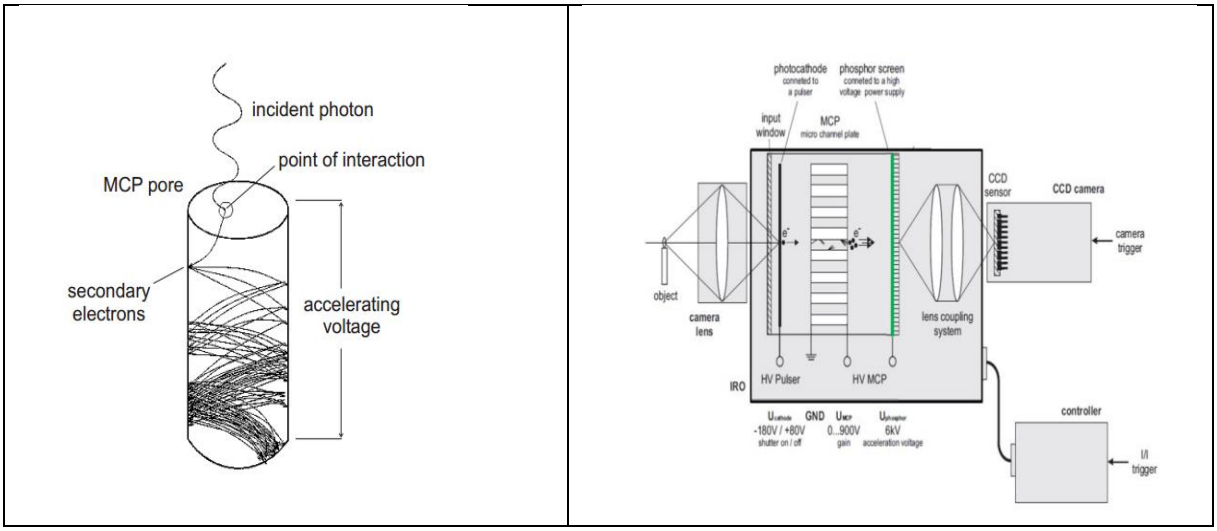

Abbildung 4. Prinzip der Elektronen-Vervielfachung im Bildverstärker und schematischer Aufbau

Die Gate-Dauer dieses Prozesses sowie der Verstärkungsgrad (Gain) können dabei unabhängig voneinander eingestellt werden. Bei maximalem Gain ist es möglich, einzelne Photonen sichtbar zu machen. In der Praxis wählt man beim Gain einen Kompromiss zwischen Signal-Helligkeit und optischem Rauschen, welches bei hohen Werten auftritt. Die Belichtungsdauer und Intensität der Bild-Helligkeit wird gänzlich über den Bildverstärker eingestellt. Die nachgeschaltete CMOS-Kamera hat nur die die Aufgabe, das grünliche Leuchten des Phosphorschirms abzubilden. Die Belichtungszeit der Kamera wird dabei vom System so nachgeführt, dass sie der Gate-Zeit des Bildverstärkers folgt und keinesfalls kürzer als diese ist.
Die Bildrate der Kamera liegt bei voller Auflösung und 12 Bit Dynamik bei 130 Bildern/s. Der Bildverstärker kann dieser Bildrate ohne Probleme folgen.
Bei Messungen mit regulären UV-Objektiven an offenen Flammen im Labor-Maßstab genügen in der Regel moderate Einstellungen des Bildverstärker-Gains (50-70%) sowie Gate-Dauern im Bereich einiger µs, um ein ausreichendes Signal bei einem Einzelbild zu generieren. Dies hängt natürlich in Maßen auch von der OH* Konzentration an der jeweiligen Stelle der Flamme ab.
Die numerische Apertur des Endoskops (F-Zahl) war im Vorfeld nicht bekannt, daher wurden bei LaVision vergleichende Messungen mit einem bekannten UV-Objektiv an einem McKenna Brenner durchgeführt. Im Rahmen der Messung konnte dem Endoskop eine F-Zahl von ca. 55 zugeordnet werden. Dies bedeutet, dass bei ansonsten vergleichbaren Aufnahme-Parametern mit dem Endoskop

deutlich länger belichtet werden muss, um eine gleiche Bild-Helligkeit wie bei einem konventionellen Objektiv-System zu erhalten. Gegenüber Flammen-Bildern mit einem normalen UV-Objektiv mit Blendenzahl 2.8 waren die Helligkeiten beim Endoskop um einen Faktor von 100 – 200 reduziert, je nach Gain-Einstellung des Bildverstärkers.
Diese reduzierte Lichtmenge kann über eine Verlängerung der Belichtungsdauer um einen vergleichbaren Faktor kompensiert werden. Dabei ist jedoch zu beachten, dass dann unter Umständen aufgrund der einsetzenden Bewegungsunschärfe kein scharfes Bild einer flackernden Flamme mehr möglich ist. Ob und inwieweit dieser Effekt auftritt, hängt natürlich von der Dynamik der Flamme ab. Tendenziell sind leichte Unschärfen bei diffusen Objekten wie OH* Konzentrationen eher zu verschmerzen als bei anderen optischen Messtechniken wie z.B. Particle Image Velocimetry.
Andere Möglichkeiten zur Erhöhung der Bildhelligkeit sind das kameraseitige Binning, d.h. Zusammenfassen von mehreren Pixeln der CMOS-Kamera (z.B. 2x2 oder 4x4) oder eine Erhöhung des Gains. Die erste Methode reduziert prinzipiell die optische Auflösung des Systems, die zweite Methode erzeugt ein höheres Bildrauschen. Das Binning ist von daher unkritisch und zu bevorzugen, da die effektive Auflösung des Bildverstärkers ohnehin geringer als die der nachgeschalteten CMOS-Kamera ist.
Die aufgenommen Bilder können auch bei maximaler Bildrate direkt auf die Festplatte des angeschlossenen Rechners projektbezogen abgespeichert und mit der DaVis-Software weiterverarbeitet werden. Typische Operationen sind hier der Abzug von Hintergrund-Bildern sowie die Erstellung von Mittelwert- und RMS- Bildern und ggf. weitere statistische oder Schwellwert-Operationen. Zur Visualisierung stehen zahlreiche Falschfarben-Paletten zur Verfügung.
Eine quantitative OH* Messung ist mit dieser Art von System jedoch nicht möglich. Jedwede Änderung der Aufnahme-Parameter (Gain, Belichtungsdauer, Öffnung der Iris-Blende im Endoskop) hat unmittelbare und kaum korrigierbare Einflüsse auf die Helligkeit der aufgenommenen OH* Emission. Daher ist darauf zu achten, dass die Aufnahme-Parameter innerhalb einer Mess-Serie nicht verändert werden. Quantitative Messungen bedingen eine schmalbandige, abstimmbare Laser-Anregung des OH Radikals, was ein deutlich komplexeres System benötigen würde (OH-LIF). Derartige Systeme haben durchaus ihre Berechtigung im Labor, sind jedoch nur schwierig an Brennern im industriellen Umfeld einzusetzen.

Anwendungsfall Ziegel-Tunnelofen
Im Projekt H_2-Ziegel wurde die Eignung von H_2 als Brenngas an einer erdgasbefeuerten Tunnelofenanlage der Ziegelindustrie untersucht [1][2]. Der Bestandsbrenner zeigte bereits nach geringer Beimischung von H_2 im Erdgas erhebliche Korrosionsschäden. Der Bestandbrenners wurde am Technikum und mittels Simulationsrechnungen (CFD) untersucht. Darauf aufbauend wurde ein neuer Zweistoffbrenner entwickelt, der eine gute Performance für beide Brennstoffe zeigte.
Die Bestandsbrenner wurden mit Erdgas und Beimischungen von Koksofengas mit einem H_2-Anteil im Mischgas von 0 / 10 / 20 Vol.-% untersucht. In den in Abbildung 5 dargestellten Fotos erkennt man den Brennermund bei Brennernennlast und einer Ofenraumtemperatur von 1.200 °C. Das Foto oben links zeigt den Zustand bei Verbrennung von reinem Erdgas, das Foto oben rechts den Zustand bei 20 Vol.-% H_2 im Erdgas mit weißglühendem Brennerrohr. Der hohe Umsatz im Brennerrohr erzeugt eine hohe Temperatur und führt zu einer Überhitzung des Materials und damit zur Zerstörung. Die entsprechenden UV-Aufnahmen bestätigen, dass bei reinem Erdgasbetrieb noch ein Umsatz nach Brenneraustritt stattfindet (unten links), bei 20 Vol.-% H_2 hingegen ist der Umsatz nahezu vollständig im Brennerrohr erfolgt (unten rechts). Die Untersuchungen mit dem Bestandsbrenner wurden auf 20 Vol.-% H_2 im Brenngas begrenzt, da der Brennermund bereits stark korrodierte.

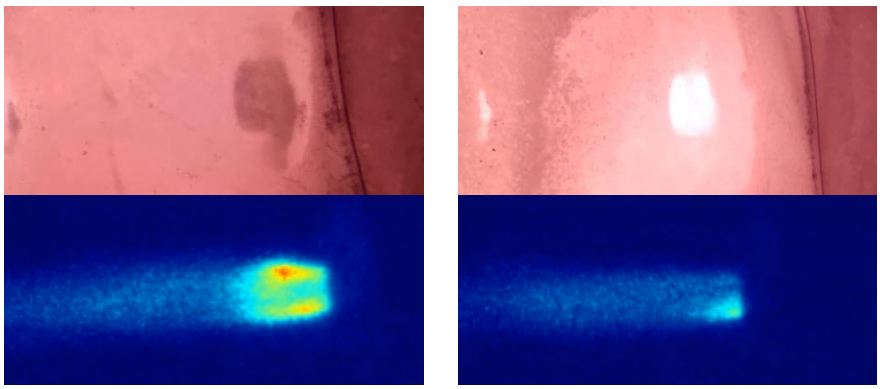

Abbildung 5. Fotos des Brennermunds im sichtbaren (oben) und UV-Bereich (unten), jeweils mit reinem Erdgas (links) und 20 % Wasserstoff (rechts) am Bestandsbrenner

Im Rahmen des Forschungsvorhabens wurde ein neuer Dual-Fuel-Brenner entwickelt und unter vergleichbaren Randbedingungen untersucht. In Abbildung 6 sind die UV-Aufnahmen des neu entwickelten Brenners beim Betrieb mit Erdgas (links) und mit reinem Wasserstoff (rechts) dargestellt. Der Brenner zeigt eine schmale, stabile Flamme, die hinreichend in den Brennraum hineinragt, Zündung und Flammenüberwachung mittels UV-Sonde waren stabil, die NO_x-Emissionen lagen innerhalb der Grenzwerte der TA Luft.

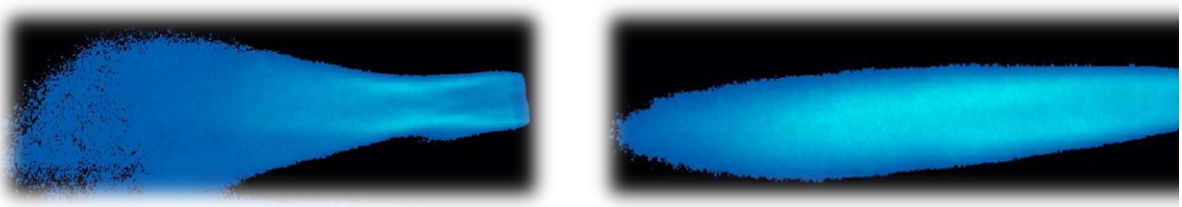

Abbildung 6. UV-Aufnahmen des Brennermunds mit reinem Erdgas (links) und mit reinem Wasserstoff (rechts) am Dual-Fuel-Brenner

Anwendungsfall Haubenofen

Das Verbundvorhaben H_2-DisTherPro [3][4] befasst sich mit der Dekarbonisierung der Stahlindustrie am Beispiel eines Haubenofens. Die Erwärmung erfolgt indirekt, indem mehrere Brenner tangential in einen Ringspalt zwischen Heizhaube und Schutzhaube feuern (s. Abbildung 7). Eine Herausforderung bei der Umstellung auf „grünen“ Wasserstoff ist die Form und Lage der Flamme, um lokale Überhitzung und damit Schäden der Schutzhaube zu vermeiden. In Brennerversuchen wurden ausgewählte Erdgas-Wasserstoffgemische unter konstanter Last und Luftzahl untersucht. In Abbildung 8 sind die zeitlich gemittelten UV-Aufnahmen der Reaktionszone dargestellt. Mit zunehmendem Wasserstoffgehalt wird die Flamme schlanker und die Flammenlänge ändert sich nur geringfügig. Durch Messungen und die UV-Aufnahmen konnte bestätigt werden, dass der Bestandsbrenner prinzipiell für den Einsatz beliebiger Erdgas-Wasserstoff-Gemische geeignet ist.

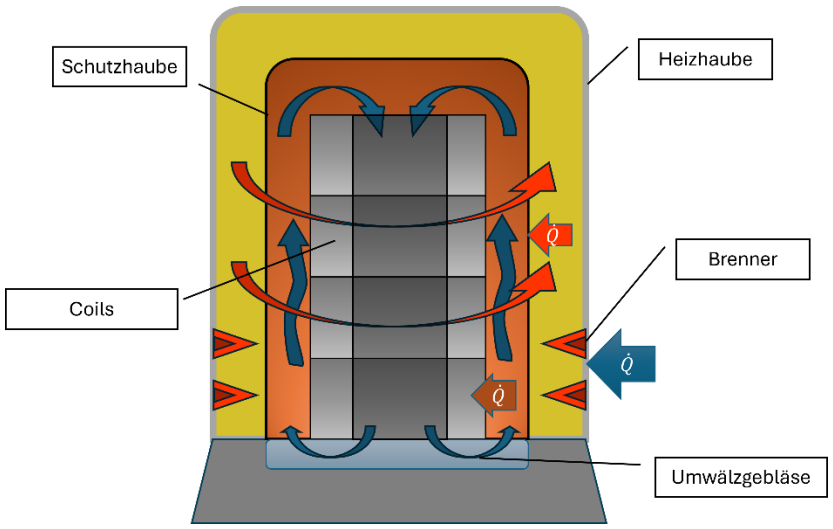

Abbildung 7. Schematische Darstellung des Haubenglühverfahrens

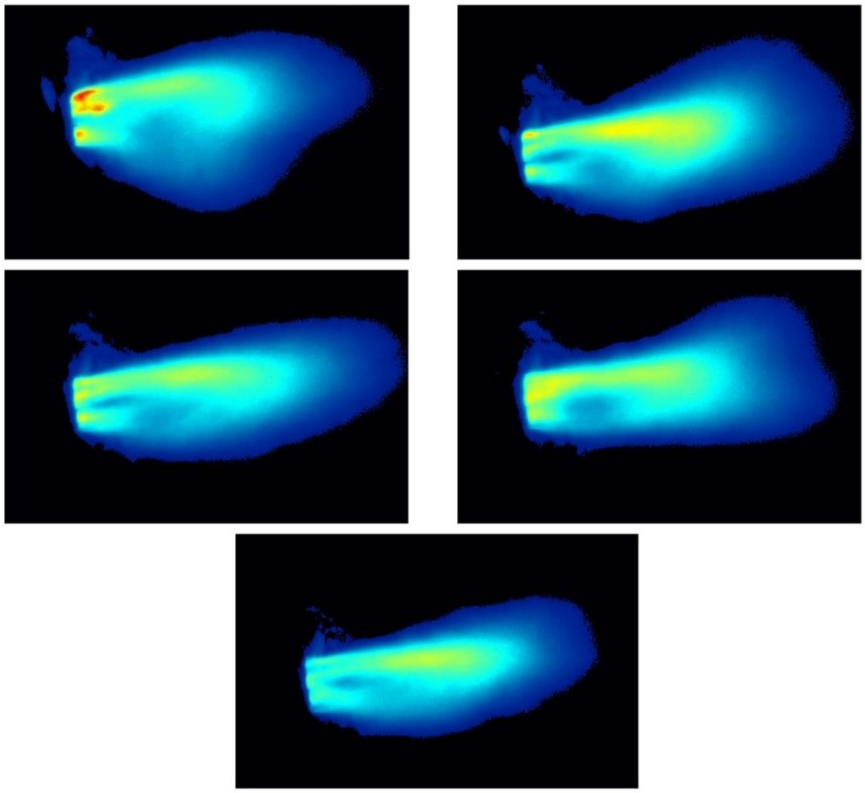

Abbildung 8. UV-Aufnahmen des Brennermunds im Betrieb mit reinem Erdgas (o.l.), 20 Vol.-% H_2 (o.r.), 40 Vol.-% H_2 (m.l.), 60 Vol.-% H_2 (m.r.) und mit reinem Wasserstoff (unten)

Zur Beurteilung der Auswirkungen auf den Prozess wurden CFD-Simulationen durchgeführt, die zunächst mit den Brennerversuchen validiert wurden und dann auf den Haubenofen übertragen wurden. Eine Herausforderung bei der Validierung waren transiente Effekte der Flamme, die messtechnisch schwierig zu erfassen sind. Durch die UV-Aufnahmen konnten diese Effekte erfasst und zur Validierung genutzt werden. Die CFD-Simulationen des Wärmeübergangs und der Temperaturverteilung wurden anschließend zur Modellerstellung und Implementierung eines digitalen Zwillings eingesetzt, wodurch eine dynamische Regelung des Prozesses ermöglicht wird.

Anwendungsfall Wiedererwärmungsofen mit Flachflammenbrenner

Das Verbundvorhaben H_2-HotRoll untersucht den Einsatz von Wasserstoff an kontinuierlichen Wiedererwärmungsöfen der Stahlindustrie. Hierbei werden die Auswirkungen auf den Prozess als auch

auf das Material bzw. die Produktqualität unter dem Einfluss verschiedener Erdgas-Wasserstoff-Gemische analysiert. In den Wiedererwärmungsöfen der Stahlindustrie werden häufig sogenannte Flachflammenbrenner eingesetzt, um zum einen eine gleichmäßige Erwärmung der Ofenwände zu erreichen und zum anderen den direkten Kontakt der Flamme mit dem Material zu vermeiden.
Zur Überprüfung der Eignung der aktuell eingesetzten 350 kW Flachflammenbrenner wurden Untersuchungen mit ausgewählten Wasserstoff-Erdgas-Gemischen an der Versuchsanlage des BFI durchgeführt. Eine besondere Herausforderung stellt hierbei die vollständige messtechnische Erfassung der Reaktionszone dar. Typischerweise zeigen Flachflammenbrenner eine symmetrische Verteilung von Temperatur und Gaszusammensetzung in Wandnähe. Der vorliegende Brenner nutzt jedoch gestufte Verbrennung, wobei ein Teil des Brenngases über sekundäre Düsen der bereits verdrallten Strömung zugeführt wird. Hierdurch ergibt sich eine untypische Verteilung der Gaszusammensetzung und Temperatur am Brennerstein, die durch traversierende Messungen nicht abbildbar ist.
Ein wesentliches Werkzeug bei der Charakterisierung der Flammstruktur ist hier das wassergekühlte UV-Kamerasystem. Durch ein Schauloch in der Ofenwand wurde das wassergekühlte Endoskop in den Ofen eingeführt, um den Bereich des Brennersteins zu filmen. In Abbildung 9 sind für ausgewählte Gasgemische bei gleicher Leistung und Luftzahl die zeitlich gemittelten UV-Aufnahmen dargestellt. Während bei der reinen Erdgasverbrennung der Hauptumsatz in der Mitte des Brennersteins stattfindet, finden sich mit steigendem Wasserstoffanteil stärker ausgeprägte Ausläufer. Position und Struktur weisen jedoch untereinander eine hohe Ähnlichkeit auf. Aus den UV-Aufnahmen lässt sich keine Verkürzung der Flamme ableiten. Die Ergebnisse lassen eher darauf schließen, dass die Reaktionszone mit steigendem H_2-Anteil aus dem Brennerstein getragen wird. Aus den Videoaufnahmen ist zudem zu erkennen, dass die Flammenstruktur mit steigendem H_2-Anteil geringere Fluktuationen aufweist.
In Kombination mit den traversierenden Messungen zur Bestimmung von Temperatur und Heißgaszusammensetzung konnten hier ebenfalls CFD-Simulationen validiert werden, die zur Simulation des vollständigen Ofens eingesetzt werden. Hierdurch können die Wärmeübergange sowie die Heißgaszusammensetzung an Material und Bauteilen unter Berücksichtigung verschiedener Gasgemische analysiert werden.

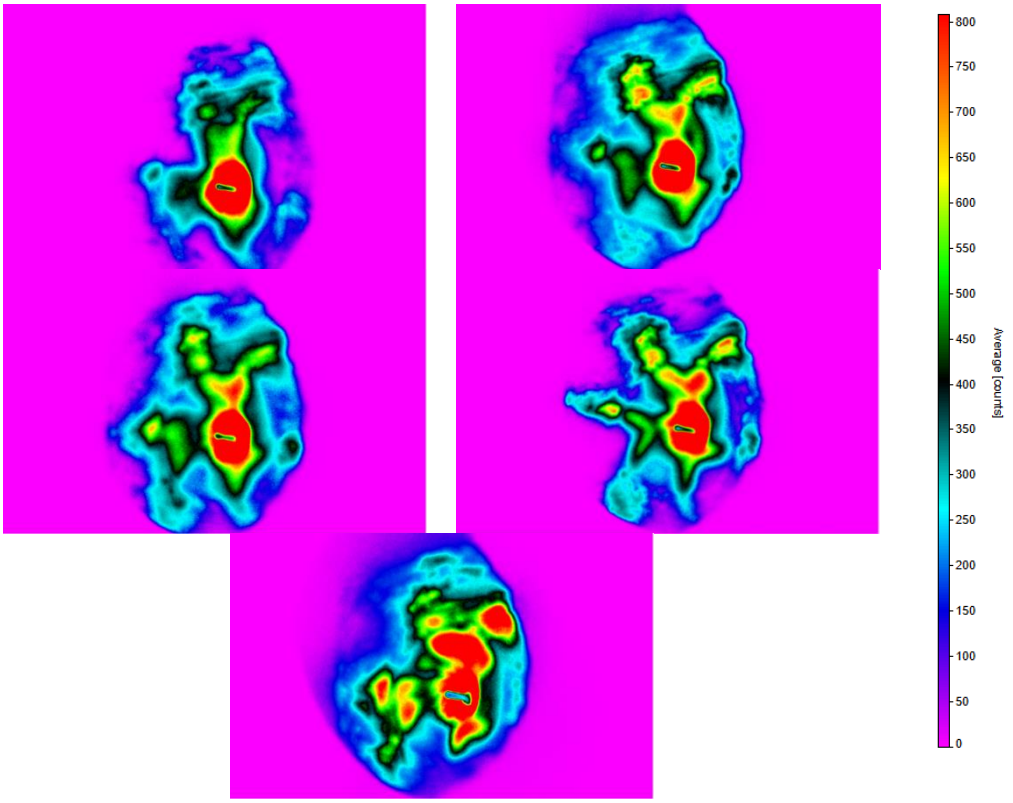

Abbildung 9. UV-Aufnahmen des Brennersteins im Betrieb mit reinem Erdgas (o.l.), 20 Vol.-% H_2 (o.r.), 40 Vol.-% H_2 (m.l.), 60 Vol.-% H_2 (m.r.) und mit reinem Wasserstoff (unten)

Zusammenfassung
Die Prozessindustrie hat in den vergangenen Jahren hohe Investitionen getätigt, um eine möglichst energieeffiziente Produktion mit hohen Sicherheitsstandards zu erreichen. Beim Wechsel von vertrauten Energieträgern zu nachhaltigen Alternativen müssen Sicherheit und Produktivität gewährleistet bleiben. Da grüne Energieträger z.T. mit hohen Kosten einhergehen, ist ein effizienter Betrieb ebenfalls sicherzustellen. Insbesondere beim Einsatz von Wasserstoff ist die Flamme bereits bei niedrigen Temperaturen nahezu unsichtbar, so dass Untersuchungen im industriellen Maßstab erschwert werden. Das wassergekühlte UV-Kamerasystem ermöglicht eine systematische Untersuchung der Flammenstruktur, die u.a. zur Erstellung von Prozessmodellen oder zur Diagnostik bereits im Einsatz befindlicher Brennersysteme eingesetzt werden kann.

Danksagung
Die hier vorgestellten Ergebnisse der Projekte H2-HotRoll und H2-DisTherPro wurden im Rahmen von, durch das BMWE, geförderten Verbundvorhaben erarbeitet:
FKZ 03EN2077A-D: **H2-DisTherPro** – „Vermeidung von CO_2-Emissionen in der Stahlindustrie durch Einsatz von Wasserstoff an diskontinuierlich betriebenen Thermoprozessanlagen am Beispiel von Haubenglühen“. Weitere Partner: thyssenkrupp Rasselstein GmbH, DSD-Automation GmbH, thyssenkrupp Steel Europe AG
FKZ 03EN2091A-B: **H2-HotRoll** – „Vermeidung von CO_2-Emissionen in der Stahlindustrie durch Einsatz von H_2 an kontinuierlich betriebenen Thermoprozessanlagen am Beispiel von Wiedererwärmungsöfen“. Weiterer Partner: Deutsche Edelstahlwerke Witten/Krefeld GmbH & Co. KG
Die Ergebnisse des Projektes **H2-Ziegel** wurden erarbeitet im Rahmen des vom Land NRW (progress.nrw – Innovation) geförderten Verbundvorhabens FKZ: EFO 0058: „Energieeffizienz und Emissionsreduzierung – Einsatz von Wasserstoff in der Ziegelindustrie (H2-Ziegel)“ Weitere Projektpartner: Institut für Ziegelforschung Essen e. V. (IZF), Essen; KELLER HCW GmbH, Ibbenbüren; Klinkerwerk Hagemeister GmbH & Co. KG, Nottuln, Kueppers Solutions GmbH, Dortmund

Wir danken den Projektträgern sowie den Konsortialpartnern für die Unterstützung und das hohe Engagement bei der Umsetzung von Maßnahmen zur Defossilisierung, für eine nachhaltige Produktion.

Literatur

[1] Adler W., Rigo R, Rimpel E., Feller B., Schlegel S.: *Einsatz von Wasserstoff zur Dekarbonisierung der Ziegelindustrie – Herausforderungen und Machbarkeit*, 4. Aachener Ofenbau- und Thermoprozess-Kolloquium (AOTK), Aachen, 2023.
[2] Giese R., Adler W., Wallat S.: *Using hydrogen to decarbonize the brick an tile industry*, 3rd International sustainable energy conference (ISEC), Graz, Austria, 2024.
[3] Adler W., Bialek S., Schmitt T., Salm C., Suer C.: *Dekarbonisierung der diskontinuierlichen Wärmebehandlung durch den Einsatz von Wasserstoff als Brenngas am Beispiel eines Haubenglühofens*, Jahrestreffen der DECHEMA Fachgruppe Hochtemperaturtechnik, Lindlar, 2024
[4] Schmitt T., Bialek S., Busson E., von der Heide C. *thyssenkrupp Rasselstein – Projekte auf einen Blick*, 15. Brennertechnik & Wärmeerzeugung, Koblenz 2024